Technische Universität München
Fakultät für Physik
Dense and Strange Hadronic Matter

First Measurement of the Proton–Σ^0 Interaction via the Femtoscopy Method

Andreas Mathis

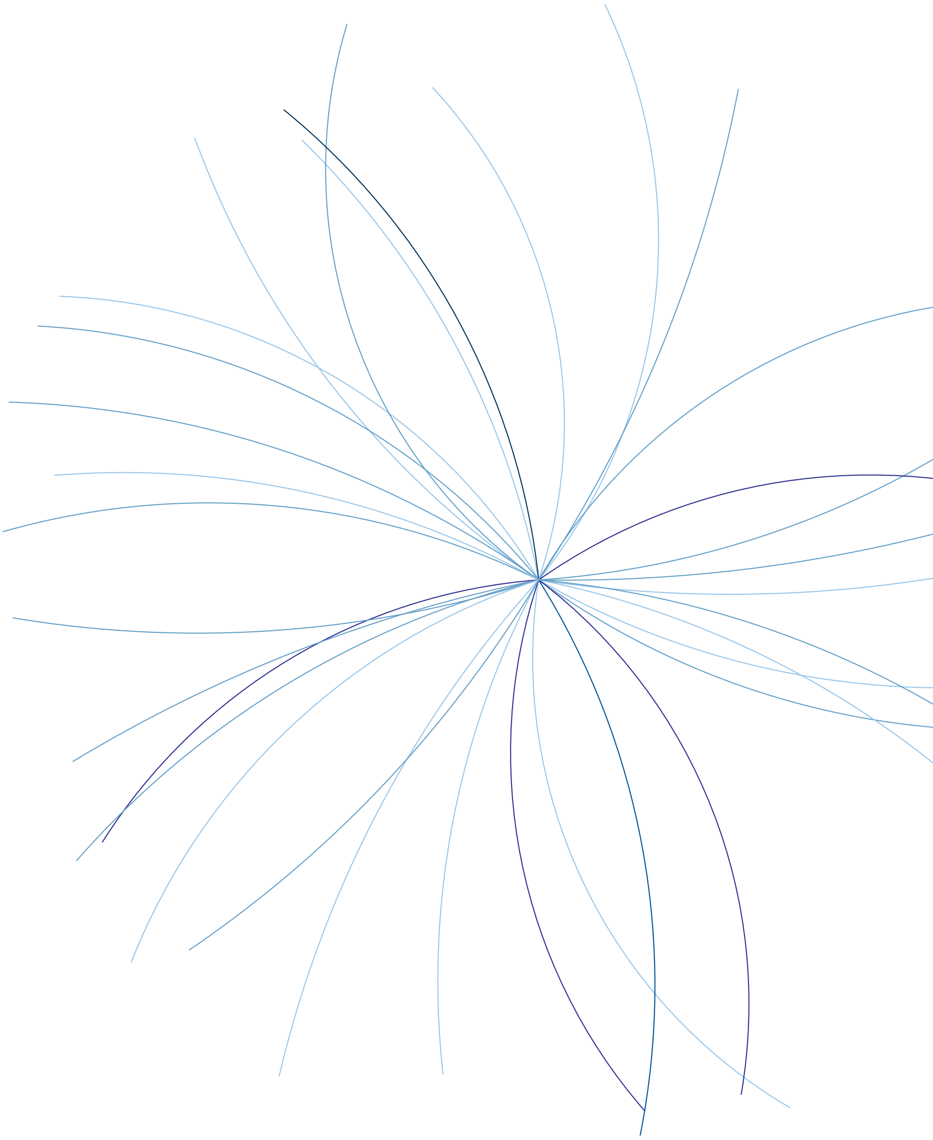

Technische Universität München
Fakultät für Physik
Dense and Strange Hadronic Matter

First Measurement of the Proton–Σ^0 Interaction via the Femtoscopy Method

Andreas Michael Mathis

Vollständiger Abdruck der von der Fakultät für Physik der Technischen Universität München zur Erlangung des akademischen Grades eines

Doktors der Naturwissenschaften (Dr. rer. nat.)

genehmigten Dissertation.

Vorsitzender:		apl. Prof. Dr. Norbert Kaiser
Prüfer der Dissertation:	1.	Prof. Dr. Laura Fabbietti
	2.	Prof. Dr. Stefan Schönert

Die Dissertation wurde am 25.05.2020 bei der Technischen Universität München eingereicht und durch die Fakultät für Physik am 22.07.2020 angenommen.

Abstract

Studies of the interaction among hadrons are a suitable tool to access low-energy features of quantum chromodynamics. A detailed understanding of the interaction among nucleons has been obtained by studies of deuteron properties and scattering experiments. On the contrary, the interaction of baryons containing strange quarks, so-called *hyperons*, is only scarcely known. The production, collection, and reconstruction of large data samples of hyperons is challenging because of the short lifetimes of these particles. The lack of conclusive experimental data is particularly prevalent in the Σ sector. The hyperon–nucleon interaction, however, is relevant for a wide range of applications including hypernuclei and matter at extreme densities, as found for instance in neutron stars. Therefore, experimental constraints are essential in order to obtain a better understanding of such objects, but also of the strong interaction in general.
Recently, significant progress has been made by exploiting femtoscopy to obtain constraints on the hyperon–nucleon interaction. Indeed, the measured two-particle correlations at small relative momenta are sensitive to the final-state interaction, which includes the strong interaction. The latter can be directly measured with high precision circumventing the difficulties associated with producing and handling beams of unstable hadrons. Therefore, the extension of such studies to the Σ sector is natural.

This work presents the first direct measurement of the p–Σ^0 interaction via the femtoscopy method. The experimental correlation function is extracted from a data sample collected by the ALICE experiment in high-multiplicity proton–proton collisions at $\sqrt{s} = 13$ TeV. The Σ^0 is identified exploiting the dominant decay channel $\Sigma^0 \rightarrow \Lambda\gamma$ and the subsequent decay $\Lambda \rightarrow p\pi^-$. The photon is reconstructed relying on conversions to e^+e^- pairs in the detector material. The detection of the Σ^0 is enabled by the unique particle identification and tracking capabilities of the ALICE detector over the full kinematic range down to low transverse momenta.
The p–Σ^0 correlation function is consistent with the baseline within $(0.2 - 0.8)\sigma$, indicating the presence of a shallow potential of the strong interaction. The experimental correlation function is compared to state-of-the-art theoretical predictions for the interaction. The interplay of the four involved spin and isospin channels defines the modeled correlation functions, which is found to be sensitive to the strong interaction. In contrast to the predictions for the p–Λ interaction, the various theoretical approaches yield significantly differing correlation functions for the p–Σ^0 channel. This demonstrates that femtoscopy has the potential to provide conclusive measurements in the N–Σ sector. The precision of the experimental correlation function, however, does not yet allow a discrimination among different models. The same holds for the presently available scattering, Σ atomic, and hypernuclear data, indicating the challenges associated with the reconstruction of the Σ states. This pioneering work demonstrates the feasibility of femtoscopic measurements in the N–Σ sector and paves the way for more detailed studies conducted with the large data samples expected from future runs of the LHC.

Indeed, significant upgrades are under way in order to enhance the rate capabilities of the ALICE detector. Therefore, the second part of this work focuses on several aspects of the upgrade of the main detector for charged-particle tracking and particle identification in ALICE – the Time Projection Chamber. The requirements of the envisaged running conditions imply a replacement of the previously used readout system based on gated Multi-Wire Proportional Chambers. The technology of the upgrade is based on a stack of four large-size Gas Electron Multiplier (GEM) foils in order to enable continuous operation, while retaining the excellent particle identification performance.

A crucial aspect limiting the stable long-term operation of GEM-based detectors is the occurrence of electrical discharges in individual GEMs within the stack. The conditions for discharge ignition are studied employing simulations of the energy deposit and the charge transport in a single-GEM detector. The working hypothesis – that the local charge density drives the stability – is verified by comparison to experimental measurements. The critical charge density igniting the discharge is found to be within $(5-9) \times 10^6$ electrons per GEM hole after amplification, with a modest dependence on the gas mixture.

The increase in interaction rate and the requirements of a trigger-less, continuous readout imply the re-design of the software for the ALICE experiment. The O^2 framework incorporates the code for data taking, reconstruction, calibration, analysis, and simulation. Such Monte Carlo simulations are a commonly used tool for the interpretation of experimental data. The comparison, however, is only valid if detector effects are properly accounted for. Therefore, the simulation of the detector response of the Time Projection Chamber is implemented in the O^2 framework with a particular focus on optimal computing performance. The model for the physics processes leading to the signal formation in the detector is validated using experimental data from beam tests with full-size prototypes.

Zusammenfassung

Studien der Wechselwirkung zwischen Hadronen sind ein geeignetes Werkzeug, um die niederenergetischen Eigenschaften der Quantenchromodynamik zu ergründen. Ein genaues Verständnis der Wechselwirkung zwischen Nukleonen wurde durch Studien des Deuterons und durch Streuexperimente gewonnen. Im Gegensatz dazu ist über die Wechselwirkung von Baryonen die *strange* Quarks enthalten, so genannten *Hyperonen*, nur wenig bekannt. Aufgrund der kurzen Lebensdauer von Hyperonen stellt die Produktion, Erfassung und Rekonstruktion großer Datenmengen dieser Teilchen eine Herausforderung dar. Im Σ-Sektor ist der Mangel an experimentellen Daten besonders ausgeprägt. Die Hyperon–Nukleon-Wechselwirkung ist jedoch für ein breites Spektrum von Anwendungen relevant, einschließlich Hyperkernen und Materie bei extremen Dichten, wie sie beispielweise in Neutronensternen vorkommt. Um ein besseres Verständnis solcher Objekte zu erhalten, aber auch der starken Wechselwirkung im Allgemeinen, sind experimentelle Eingrenzungen unerlässlich.
In jüngster Zeit wurden durch Femtoskopie bedeutende Fortschritte bei der Messung der Hyperon–Nukleon-Interaktion erzielt. In der Tat sind die gemessenen Zwei-Teilchen-Korrelationen bei kleinen Relativimpulsen sensitiv auf die Wechselwirkung im Endzustand, zu der auch die starke Wechselwirkung beiträgt. Diese kann so mit großer Präzision direkt gemessen werden, wodurch die mit der Erzeugung und Handhabung von Strahlen instabiler Hadronen verbundenen Schwierigkeiten umgangen werden. Daher ist die Ausweitung solcher Studien auf den Σ-Sektor nur logisch.

Diese Arbeit stellt die erste direkte Messung der p–Σ^0-Interaktion mittels der Femtoskopie-Methode vor. Die experimentelle Korrelationsfunktion wird aus Daten extrahiert, die von dem ALICE Experiment in Proton–Proton-Kollisionen mit hoher Multiplizität bei $\sqrt{s} = 13$ TeV aufgenommen wurden. Das Σ^0 wird unter Verwendung des dominanten Zerfallskanals $\Sigma^0 \rightarrow \Lambda\gamma$ und des anschließenden Zerfalls $\Lambda \rightarrow p\pi^-$ identifiziert. Das Photon wird mittels der Konversion in e^+e^--Paare im Detektormaterial rekonstriuiert. Der Nachweis des Σ^0 wird durch das einzigartige Teilchenidentifizierungs- und Spurrekonstruktionsvermögen des ALICE Detektors über den gesamten kinematischen Bereich auch bei niedrigen Tranversalimpulsen ermöglicht.
Die p–Σ^0-Korrelationsfunktion stimmt innerhalb von $(0{,}2 - 0{,}8)\sigma$ mit der Referenz überein, was auf das Vorhandensein eines schwachen Potentials der starken Wechselwirkung hinweist. Die experimentelle Korrelationsfunktion wird mit aktuellen theoretischen Vorhersagen der Interaktion verglichen. Die modellierte Korrelationsfunktion erweist sich als sensitiv auf die starke Wechselwirkung und ist durch das Zusammenspiel der vier beteiligten Spin- und Isospinkanäle definiert. Im Gegensatz zu den Vorhersagen der verschiedenen theoretischen Ansätze für die p–Λ-Wechselwirkung unterscheiden sich die Korrelationsfunktionen im p–Σ^0-Kanal stark. Dies zeigt, dass Femtoskopie die Möglichkeit bietet, im N–Σ-Sektor aussagekräftige Messungen zu liefern. Die Präzision der experimentellen Korrelationsfunktion erlaubt jedoch noch keine Unterscheidung zwischen den verschiedenen Modellen. Das Gleiche gilt für die derzeit verfügbaren Daten aus Streu-, Σ-Atom- und Hyperkernexperimenten. Dies zeigt die Herausforderungen auf, die mit der Rekonstruktion der Σ-Zustände verbunden sind. Diese wegweisende Arbeit demonstriert die Durchführbarkeit femtoskopischer Messungen im N–Σ-Sektor und ebnet den Weg für detailliertere Studien, die mit den erwarteten großen Datenmengen von zukünftigen Läufen des LHC durchgeführt werden.

Tatsächlich werden derzeit bedeutende Upgrades zur Erhöhung der maximalen Datenrate des

ALICE Detektors durchgeführt. Daher konzentriert sich der zweite Teil dieser Arbeit auf mehrere Aspekte des Upgrades des Time Projection Chamber. Dieser Detektor spielt eine zentrale Rolle bei der Spurrekonstruktion geladener Teilchen und deren Identifizierung. Die Anforderungen der geplanten Betriebsbedingungen erfordern den Ersatz des bisher verwendeten Auslesesystems, das auf gepulsten Vieldraht-Proportionalkammern basiert. Die Technologie des Upgrades basiert auf einer Anordnung von großflächigen Gas Electron Multiplier (GEM) Folien in vier Lagen. Diese ermöglichen einen kontinuierlichen Betrieb und bewahren gleichzeitig das ausgezeichnete Teilchenidentifizierungsvermögen.

Das Auftreten von elektrischen Entladungen in einzelnen GEMs innerhalb der Anordnung ist ein entscheidender Aspekt, der den stabilen Langzeitbetrieb von GEM-basierten Detektoren einschränkt. Die Bedingungen für das Zünden solcher Entladungen werden mithilfe von Energiedepositions- und Ladungstransportssimulationen in einem einzelnen GEM-Detektor untersucht. Die Arbeitshypothese – dass die lokale Ladungsdichte die Stabilität bestimmt – wird durch einen Vergleich mit experimentellen Messungen verifiziert. Die kritische Ladungsdichte, bei der die Entladung zündet, liegt nach der Verstärkung innerhalb von $(5-9) \times 10^6$ Elektronen pro GEM-Loch, wobei eine mäßige Abhängigkeit von der Gasmischung besteht.

Die Erhöhung der Interaktionsrate und die Anforderungen an eine triggerlose, kontinuierliche Auslese fordern die Neugestaltung der Software des ALICE Experiments. Das O^2 Framework beinhaltet den Code für die Datennahme, Rekonstruktion, Kalibration, Analyse und Simulation. Solche Monte-Carlo-Simulationen werden häufig für die Interpretation experimenteller Daten verwendet. Entscheidend hierfür ist jedoch die korrekte Berücksichtigung von Detektoreffekten. Daher wird die Simulation der Detektorreaktion der Time Projection Chamber mit besonderem Augenmerk auf die optimale Nutzung der Rechenleistung in das O^2-Framework implementiert. Die Modellierung der physikalischen Prozesse, die zur Signalbildung im Detektor führen, wird mit experimentellen Daten aus Strahltests mit Prototypen validiert.

Contents

1 Introduction

Physics with strange hadrons lies at the intersection of particle and nuclear physics. Studying the spectrum of hadrons and their interactions allows the assessment of fundamental properties of the underlying force, the strong interaction. Indeed, detailed studies of the interaction among hadrons are a suitable tool to benchmark and extend the understanding of the strong interaction.

1.1 Quantum Chromodynamics

The theory of the strong interaction is *quantum chromodynamics* (QCD) [1–3], a non-Abelian SU(3) gauge theory with quarks and gluons as fundamental degrees of freedom. Together with the electromagnetic and the weak force it builds up the SU(3) × SU(2) × U(1) standard model of particle physics. The Lagrangian density of QCD is given by [4–6]

$$\mathcal{L} = \overline{\psi} \left(i\gamma^{\mu} D_{\mu} - m \right) \psi - \frac{1}{4} G^{a}_{\mu\nu} G^{\mu\nu}_{a} , \tag{1.1}$$

with the quark spinor fields ψ that occur in six flavors and $N_c = 3$ colors. The bare quark masses are incorporated in the matrix m. The gauge covariant derivative $D_{\mu} = \partial_{\mu} - ig\mathcal{A}^{a}_{\mu}\lambda_{a}$ describes quark propagation and the quark–gluon coupling. The λ_a correspond to the Gell-Mann matrices modifying the quarks' color charge upon interaction with a gluon and $g = \sqrt{4\pi\alpha_s}$ to the QCD coupling constant. In total $N_c^2 - 1 = 8$ different gluon fields $\mathcal{A}^{a}_{\mu}$ exist, with color index a. Finally, the gluon field tensor $G^{a}_{\mu\nu}$ is given by

$$G^{a}_{\mu\nu} = \partial_{\mu}\mathcal{A}^{a}_{\nu} - \partial_{\nu}\mathcal{A}^{a}_{\mu} - g_s f^{abc} \mathcal{A}^{b}_{\mu}\mathcal{A}^{c}_{\nu}, \tag{1.2}$$

where the f^{abc} are the structure constants of the SU(3) group. Especially intriguing is the fact that the last term corresponds to self-couplings of the exchange bosons, which is a unique feature of QCD. Accordingly, gluons can not only create virtual quark–antiquark pairs, leading to a screening of the color charge, but also split into gluon pairs which has the opposite effect and thus diminishes the coupling constant of QCD.

Indeed, the running coupling constant α_s of QCD exhibits a complex behavior. As displayed in Fig. 1.1, the overall trend of α_s as a function of the energy scale is experimentally well established. On the one hand, for larger energy transfers, corresponding to smaller distances, the running coupling constant decreases, giving rise to a phenomenon called *asymptotic freedom*. The strong force weakens and the quarks and gluons can be considered as asymptotically free particles. Accordingly, perturbation theory can be employed to provide quantitative predictions for QCD processes. At particularly large temperatures and/or densities a transition to a phase of deconfined quarks and gluons is expected, the so-called *quark–gluon plasma*. It is an interesting research field of its own, however is not further discussed here.

On the other hand, the coupling constant becomes increasingly large at lower energies, corresponding to larger distances. By separating a quark–antiquark pair further and further, the energy contained in the gluon field in-between them increases to the point at which the creation of another quark–antiquark pair becomes energetically favorable. Accordingly, at low energies the

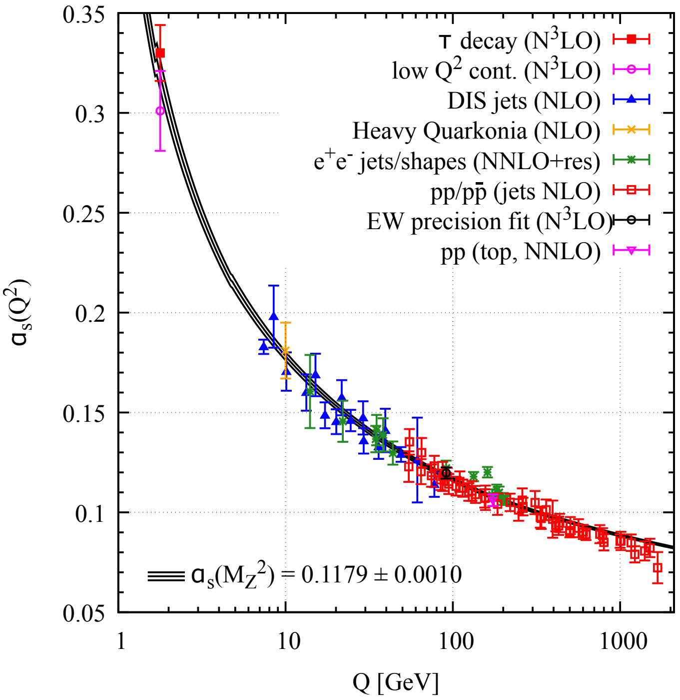

Figure 1.1: Summary of measurements of α_s as a function of the energy scale Q [7].

quarks and gluons are subject to *confinement* and the relevant degrees of freedom are the colorless hadrons that transform as singlets under the gauge group SU(3). Since the dynamics of the quarks and gluons in this energy regime are strongly coupled, a perturbative approach is no longer feasible. The natural mass scale of QCD, $\Lambda_{\mathrm{QCD}} \approx 200\,\mathrm{MeV}$, defines the threshold below which perturbative approaches diverge. Up to now, no analytical approach to low-energy QCD exists. Instead, effective field theories [8, 9] or numerical solutions of the QCD Lagrangian have to be employed. Accordingly, many of the features of low-energy QCD are not solidly understood and experimental studies of fundamental hadron properties, such as their interactions, can provide valuable input.

The current quark masses m are input parameters to QCD and generated via the Higgs mechanism [10–12]. Considering the energies and masses involved in nuclear physics, out of the six quarks only the u, d, and s quarks are relevant. Current estimates for their masses are $(2.16^{+0.49}_{-0.26})$ MeV for the u quark, $(4.67^{+0.48}_{-0.17})$ MeV for the d quark, and (93^{+11}_{-5}) MeV for the s quark [7]. It is obvious that the hadron masses are significantly larger than those of the corresponding current quarks. Therefore, an important aspect of QCD is the generation of hadron masses.

In the *chiral limit* of zero quark masses, the QCD Lagrangian is invariant under unitary transformations of the left- and right-handed quark fields. Accordingly, the QCD Lagrangian exhibits exact $\mathrm{SU}(3)_R \times \mathrm{SU}(3)_L \times \mathrm{U}(1)_V$ symmetry, where the $\mathrm{U}(1)_V$ subgroup generates the conservation of baryon number. It should be noted that the $\mathrm{SU}(3)_R \times \mathrm{SU}(3)_L$ chiral symmetry is only a symmetry of the Lagrangian but not of the ground state – the QCD vacuum $\langle 0|q\bar{q}|0\rangle$. Experimental observations of large mass differences between chiral partners in the hadron spectrum, e.g. between the ρ and the a_1 meson [7], suggest that chiral symmetry is *spontaneously* broken. Correspondingly, the ground state is characterized by a quark condensate with non-vanishing expectation value $\langle 0|q\bar{q}|0\rangle \approx (-250\,\mathrm{MeV})^3$ [13]. The quark condensate $\langle 0|q_L\bar{q}_R + q_R\bar{q}_L|0\rangle$ then connects left- and right-handed quark fields and thus leads to the breaking of chiral symmetry. The quarks propagating through the QCD vacuum are accordingly dressed by their interactions, which generates an increase in mass. Additionally, the introduction of small, non-vanishing quark masses results in a mixing of left- and right-handed quark fields as well. Accordingly, chiral symmetry is also *explicitly* broken. Since the quark masses are rather small, the effect of *spontaneous* chiral symmetry breaking is dominant for the generation of hadron masses. At larger temperatures or densities, however, the quark condensate $\langle 0|q\bar{q}|0\rangle$ is expected to melt, correspondingly leading to the restoration of chiral symmetry [13, 14].

Exploiting the flavor SU(3) symmetry of QCD, the hadrons are conveniently organized in multiplets of irreducible representations [15, 16]. Figure 1.2 depicts exemplarily the octet of baryons relevant for this work, organized by the strangeness quantum number S and the third component of the isospin I_3. Hyperons are baryons containing at least one s quark and therefore characterized by $|S| > 0$. The $|S| = 1$ sector contains the isoscalar Λ and the isovector Σ states. The masses and most important properties of the corresponding baryons are given in Table 1.1. The observed mass differences of the Σ states are interpreted as the pattern of SU(3) symmetry breaking. In contrast to the Λ, the Σ^-, and the Σ^+, which decay via the weak interaction, the Σ^0 decays electromagnetically. The neutral Λ and Σ^0 differ only in isospin and have a mass splitting of about $77\,\mathrm{MeV}/c^2$ [7]. Above threshold, the production ratio approaches $\Sigma^0/\Lambda \approx 1/3$ as expected from isospin considerations [17–25].

Due to the small mass difference and almost equal quantum numbers, a significant entanglement of the Λ and Σ states is expected, which is also relevant for the study of their interaction.

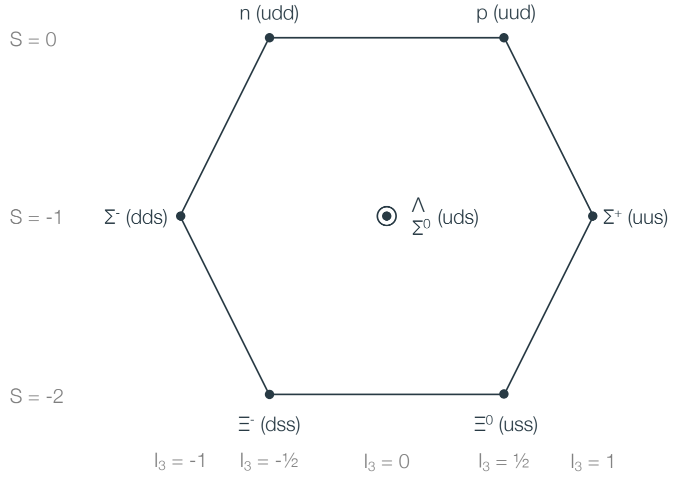

Figure 1.2: The baryon octet with $J^P = 1/2^+$.

Table 1.1: Properties of the $|S| = 1$ baryons [7]. Only the most important decay modes are quoted.

	Λ	Σ^-	Σ^0	Σ^+
Mass (MeV/c^2)	1115.683 ± 0.006	1197.449 ± 0.030	1192.642 ± 0.024	1189.37 ± 0.07
Decay length (cm)	7.89 ± 0.06	4.44 ± 0.03	$(22 \pm 2) \times 10^{-10}$	2.405 ± 0.008
Decay mode	$p\pi^-$ (63.9%) $n\pi^0$ (35.8%)	$n\pi^-$	$\Lambda\gamma$	$p\pi^0$ (51.6%) $n\pi^+$ (48.3%)
Isospin (I, I_3)	(0, 0)	(1, −1)	(1, 0)	(1, 1)

1.2 Hyperon–Nucleon interaction

The study of hadron–hadron interactions provides a valuable benchmark of the symmetries and the theoretical description of low-energy QCD. In the following, the interactions of the $J^P = 1/2^+$ baryons in the irreducible octet, shown in Fig. 1.2, are discussed. Indeed, studies of baryon–baryon interactions can be used a probe of SU(3) symmetry. Under the premise of exact flavor SU(3) symmetry, the pairs of octet baryons can be grouped in six irreducible multiplets [26–28],

$$\mathbf{8} \otimes \mathbf{8} = \mathbf{27} \oplus \mathbf{8}_s \oplus \mathbf{1} \oplus \mathbf{10}^* \oplus \mathbf{10} \oplus \mathbf{8}_a, \tag{1.3}$$

where the first three terms are flavor symmetric and the last three anti-symmetric. Depending on the baryon pair under study different elements of the decomposition contribute.

The nucleon–nucleon (N–N) interaction is very well known, with a vast data base of 4301 p–p and n–p data points collecting the data of various scattering experiments [29]. The long and intermediate-range interaction is mediated by mesons, which was already established in 1935 [30]. For the short-range repulsion, however, a detailed understanding of QCD is required because the relevant degrees of freedom are the quarks and gluons.

Similar arguments hold for the hyperon–nucleon (Y–N) interaction, where experimental constraints are scarce. The Y–N interaction can be exploited to explore the part of $\mathbf{8} \otimes \mathbf{8}$ phase space not accessible with studies of the N–N interaction. Moreover, the N–Σ ($S = 0,\ I = 3/2$) and the the N–N ($S = 0,\ I = 1$) component belong to the same **27** irreducible representation. Therefore, a comparison of the corresponding interaction strengths is a benchmark of the symmetry breaking of SU(3). This underlines, that studies of the Y–N provide valuable input for the understanding of low-energy QCD. Finally, the Y–N interaction is also relevant in the context of hypernuclear physics and for astrophysical objects such as neutron stars.

1.2.1 Experimental Results on the Hyperon–Nucleon Interaction

In contrast to the N–N interaction, the difficulties in handling beams of unstable hyperons are reflected in the fact that only little is experimentally known about the Y–N interaction. For recent reviews of the current situation see e.g. [31–35].

In particular for the case of the Λ, the available scattering data [36–40] and measurements of hypernuclei across the periodic table [41–43] established the attractive character of the Λ–N interaction with a nuclear potential depth $U_\Lambda \approx -30\,\mathrm{MeV}$. The $|S| = 2$ sector is especially intriguing since the so-called H-dibaryon, a deeply bound 6-quark state, is predicted to appear in the coupled $\Lambda\Lambda - \Xi\mathrm{N} - \Sigma\Sigma$ system [44]. The Ξ–N interaction is characterized by the rather scarce scattering data for $\mathrm{p}\Xi^- \rightarrow \mathrm{p}\Xi^-$ and $\mathrm{p}\Xi^- \rightarrow \Lambda\Lambda$ reactions [45, 46]. Hints for an attractive Ξ–N interaction stem from observations of a bound state in the $\Xi^- - {}^{14}\mathrm{N}$ system [47]. Similarly, observations of a ${}^{6}_{\Lambda\Lambda}\mathrm{He}$ double hypernucleus point towards a weakly attractive Λ–Λ interaction [48].

Recently, significant progress has been made for the mentioned systems using the femtoscopy technique. The method and the most important results are revised in Sec. 1.3.

1.2.1.1 Results on the Σ–Nucleon Interaction

Only very little is known about the N–Σ interaction since the decay of all Σ states involves neutral decay products [7], thus requiring experimentalists to build high-resolution calorimeters or employ missing-mass techniques. Due to the small mass difference between the Λ and the Σ states and since they possess the same quantum numbers, a sizable coupling between the N–Λ and the N–Σ channels is expected. A review of the available Σ data and the relevant experimental methods to study interactions is presented in the following.

Scattering Experiments Scattering data have been collected in experiments in the sixties and seventies using the Saclay 81 cm hydrogen bubble chamber [36, 37, 49]. The Σ candidates are produced by stopping a secondary K^- beam in the active medium of the bubble chamber via a *strangeness exchange* reaction $\mathrm{K}^-\mathrm{p} \to \Sigma^{\pm}\pi^{\mp}$. The capture reaction of the K^- results in Σ momenta not exceeding 200 MeV/c, with the lower limit of about 100 MeV/c imposed by the detection limit of the system. In this kinematic regime, the interaction in the S-wave is expected to dominate the Σp cross sections. The elastic scattering of $\Sigma^+\mathrm{p}$, in the isospin ($I = 3/2$) state, and $\Sigma^-\mathrm{p}$ with the isospin ($I = 1/2,\ 3/2$) configuration are studied [36, 49]. Additionally, also the inelastic scattering cross sections for the processes $\Sigma^-\mathrm{p} \to \Lambda\mathrm{n}$ ($I = 1/2$) and $\Sigma^-\mathrm{p} \to \Sigma^0\mathrm{n}$ ($I = 1/2,\ 3/2$) are measured [37]. A few hundred events of each type are identified, resulting in seven (four) data points for elastic $\Sigma^-\mathrm{p}$ ($\Sigma^+\mathrm{p}$) scattering, as depicted in the left (right) panel of Fig. 1.3. The main caveat of this type of experiments, however, is the low-rate capability severely limiting the number of accumulated events and thus the statistical uncertainties.

A new method for the study of such scattering events is conducted using active scintillating fiber targets with digital image readout for the production and detection of short-lived hyperons [50–52]. An exemplary $\Sigma^-\mathrm{p}$ scattering event obtained with this detection system is depicted in Fig. 1.4 demonstrating the excellent spatial resolution of the method. The Σ candidates are produced by a secondary $\pi^{\pm}$ beam impinging on the target via the *associate production* reaction, $\pi^{\pm}\mathrm{p} \to \Sigma^{\pm}\mathrm{K}^{+}$. The K^+ escaping the reaction is tracked using a dedicated spectrometer arm, whose kinematic acceptance defines the accessible momentum regime of the experiment, ranging from about 300 MeV/c to 700 MeV/c. The measurement technique is complementary to bubble chamber

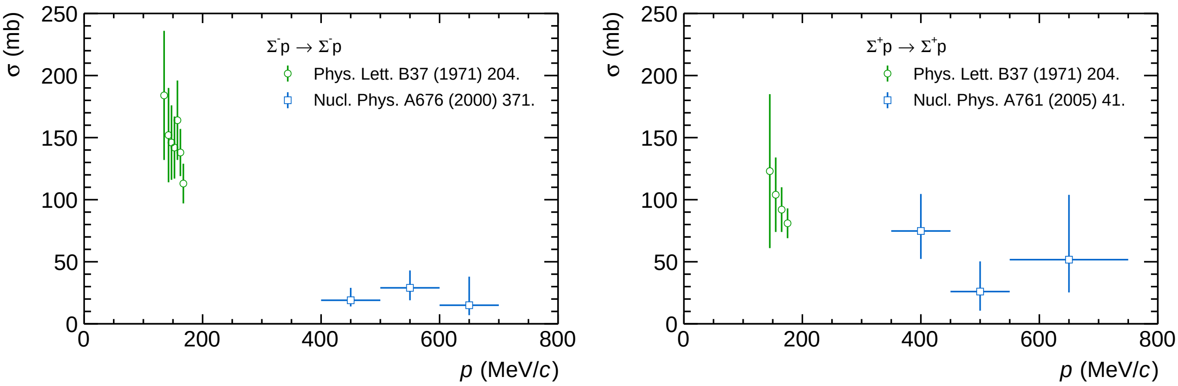

Figure 1.3: Experimental cross sections for the elastic $\Sigma^-\mathrm{p}$ (*left*) and $\Sigma^+\mathrm{p}$ (*right*) scattering [36, 50, 51]. The green data points correspond to the results from K-induced reactions, while the blue data points are obtained using π-induced reactions.

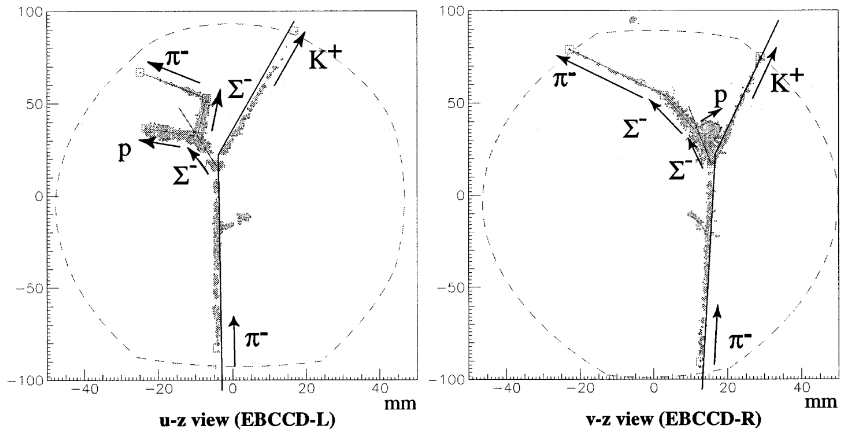

Figure 1.4: Exemplary Σ^-p elastic scattering event [50]. The solid lines depict the incoming π^- and outgoing K^+ tracks obtained with external wire chambers. The lines from the (π^-, K^+) vertices correspond to the predicted momentum vectors of the initial Σ^-.

experiments and enables studies of higher partial waves. For both elastic channels, three data points could be extracted, depicted by the blue data points in Fig. 1.3. As in the case of the bubble chamber data, rather large statistical uncertainties prevent any conclusion on structures appearing in the distribution of scattering angles.

The scattering parameters extracted from these data have sizable uncertainties regarding magnitude and sign [53]. In addition, there are no experimental data for $p \to 0$ and no dedicated phase shift analyses. Therefore, the interaction cannot be constrained relying on scattering data alone. In order to improve the situation, new measurements in these channels are under way [54].

Σ^- Atomic Data Hadronic atoms are formed by capture of a stopped, negatively charged hadron in one of the outer atomic orbits of a target atom. The cascade of the hadron down within the atomic orbits is typically accompanied by the emission of Auger electrons and radiative transitions involving the emission of x-rays [55]. The lower atomic orbitals have a sizable overlap with the nucleus and therefore the strong interaction modifies the atomic levels before the hadron is eventually absorbed by the nucleus.

The strong interaction between the hadron and the nucleus causes a shift of the energy of the last x-ray transition before absorption from the pure electromagnetic value. In addition, the reduced lifetime of the final atomic state leads to a broadening. Hence, analyses of the x-ray energy spectrum allow the determination of the energy shift and width. In the simplest case, the interaction with the nucleus can be described by an optical potential in addition to the Coulomb contribution. It should be noted though, that the overlap of the atomic orbitals with the nucleus probes a wide range of nuclear densities [56]. This introduces a significant model dependence on the exact treatment of the nuclear density distribution for studies of the strong interaction. Nevertheless, analyses of hadronic atoms have be exploited for measurements of the strong interaction of π^-, K^-, Σ^- and $\overline{p}$ with the nucleus [55, 56].

The Σ^- is typically formed in *strangeness exchange* reactions employing stopped K^- beams. Therefore, the x-ray spectra are considerably contaminated by kaonic atoms. This is well visible in the exemplary spectrum of Σ^- and kaonic atoms shown in the left panel of Fig. 1.5. Nevertheless,

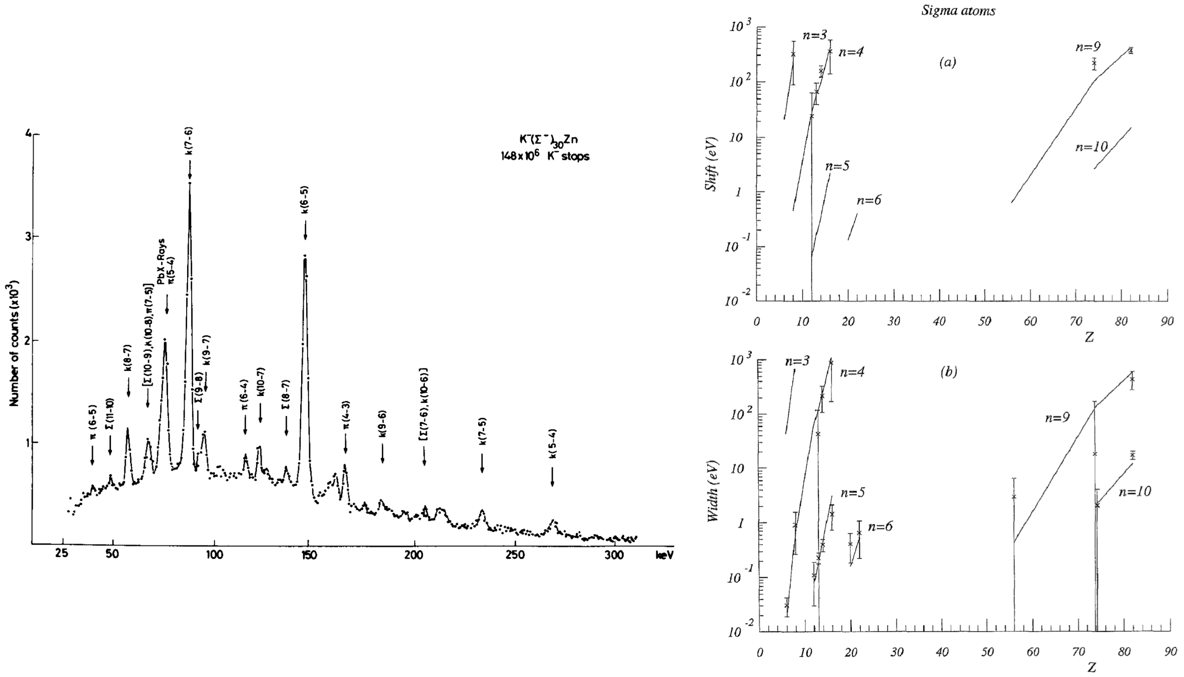

Figure 1.5: (*Left*) Exemplary x-ray spectrum from K, Σ, and π atoms obtained by stopping K⁻ in ^{30}Zn [57]. The Σ transitions in brackets indicate the expected position obscured by other lines. (*Right*) Shift and width values for various Σ atoms [56]. The continuous lines join points calculated with the best-fit optical potential.

multiple Σ^- x-ray lines could be extracted. The compendium of Σ^- atomic data contains in total 23 strong level shifts and widths from target atoms ranging from C to Pb [57–59], as depicted in the right panel of Fig. 1.5.

A satisfactory description of the experimental data could be achieved with a phenomenological *density-dependent* (DD) isoscalar potential [60, 61], or a *geometrical* potential *F* [35, 62]. The resulting potential for Ca and Pb Σ^- atoms is shown in the left and right panel of Fig. 1.6. While the overall shape of the two potentials differs significantly, both models yield a weak attraction at large radii, that turns into repulsion approximately one fm beyond the half-density radius of the charge distribution. The magnitude and shape of the repulsive component within the nucleus,

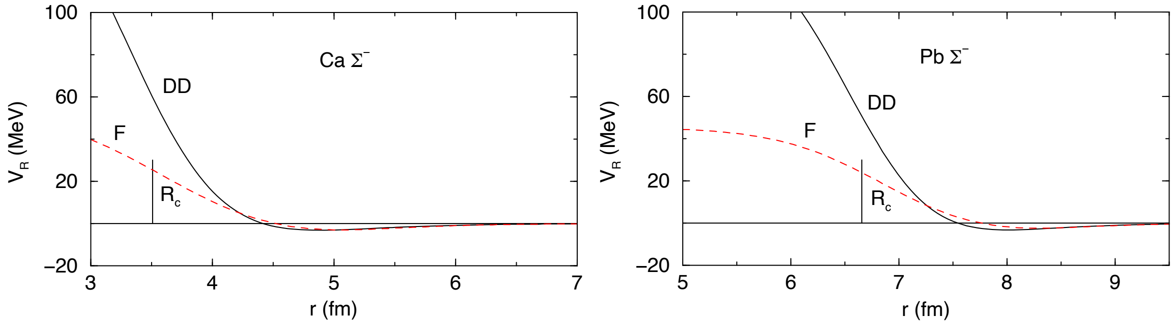

Figure 1.6: Re$V_{\text{opt}}(V_R)$ for two different parametrizations of the Σ^- nuclear potential, DD (solid lines) and F (dashed). Modified from Ref. [35]. The vertical bars indicate the half-density radius of the nuclear charge distribution.

however, cannot be determined by these data. Similar results are obtained by Relativistic Mean Field (RMF) calculations [62] where the Σ–nucleus interaction is generated by scalar (σ) and vector (ω, ρ) mean field contributions. The corresponding coupling constants are determined by a fit to the Σ^- data in Si and Pb atoms. The resulting potential yields a satisfactory description of the available data and is, as well as the phenomenological potentials, attractive far outside the nucleus and turns repulsive at the nuclear surface.

Σ Hypernuclei A hypernucleus is produced when strangeness content is implanted to an ordinary nucleus, resulting typically in one of the nucleons being replaced by a hyperon. When the hyperon is bound to the nuclear system, the resulting hypernucleus then generally deexcites to the ground state in which all baryons reside in their lowest single-particle levels [32]. The corresponding nuclear transitions are accompanied by gamma rays or Auger emission of nucleons. The attractive interaction leading to the bound state can be characterized by measuring the binding energy

$$-B = M_B - (M_{A-1} + M_Y), \tag{1.4}$$

where the mass of the hypernucleus M_B is obtained via a kinematic analysis of the decay products. The mass of the core nucleus M_{A-1} and of the hyperon M_Y require a unique identification of the reaction. The hyperon can be used as a selective probe of the nuclear medium, as it remains distinguishable within the nucleus [32]. The hyperon can also be produced in unbound, continuum states from which it escapes the nuclear potential. In these so-called *quasi-free* processes, the hyperon–nucleus interaction modifies the spectra and can therefore be studied. Nevertheless, the interpretation of hypernuclear measurements introduces a sizable model-dependence.

Hypernuclear Σ states are generally not expected to feature narrow peaks due to the conversion N–Σ → N–Λ [63]. The energy released in the conversion $m_\Sigma - m_\Lambda \approx 80\,\text{MeV}$ dominantly induces nuclear breakup and therefore broadens the widths of the corresponding states. In lighter systems at low energies, however, the selectivity of the conversion process to the ($S = 1$, $I = 1/2$) component may lead to a substantial reduction of the expected widths [63]. Therefore, Σ hypernuclei may be only detectable in these kind of systems.

Indeed, the only Σ hypernucleus found to present day is ${}^4_\Sigma\text{He}$, detected as a quasi-bound state in (K^-, π^-) reactions [64, 65]. In this reaction, both the Σ^0 and Σ^+ states are produced, populating the isospin states ($I = 1/2,\ 3/2$). In the companion reaction (K^-, π^+), however, the Σ^- is produced in the isospin ($I = 3/2$) state. Both excitation spectra are displayed in Fig. 1.7. The quasi-free Σ production is clearly visible in both spectra for $B_\Sigma > 0\,\text{MeV}$. The (K^-, π^-) spectrum, however, displays a clear peak which is interpreted as a quasi-bound state.

Since the structure appears only in the (K^-, π^-) reaction, the quasi-bound state is assigned $I = 1/2$ [64]. An analysis of the peak yields a binding energy of $B_\Sigma = 4.4 \pm 0.3\,(\text{stat.}) \pm 1.2\,(\text{syst.})\,\text{MeV}$ and a width of $\Gamma = 7.0 \pm 0.7\,(\text{stat.})^{+1.2}_{-0.0}\,(\text{syst.})\,\text{MeV}$ [64]. These values are in line with predictions from Ref. [66], where the quasi-bound state occurs in the $I = 1/2$, $S = 0$ channel. In these calculations, the N–Σ interaction exhibits a strong isospin dependence, with attraction in the $I = 1/2$ channel and repulsion for $I = 3/2$ [66].

The strong isospin dependence of the N–Σ interaction is typically incorporated in the Σ–nucleus

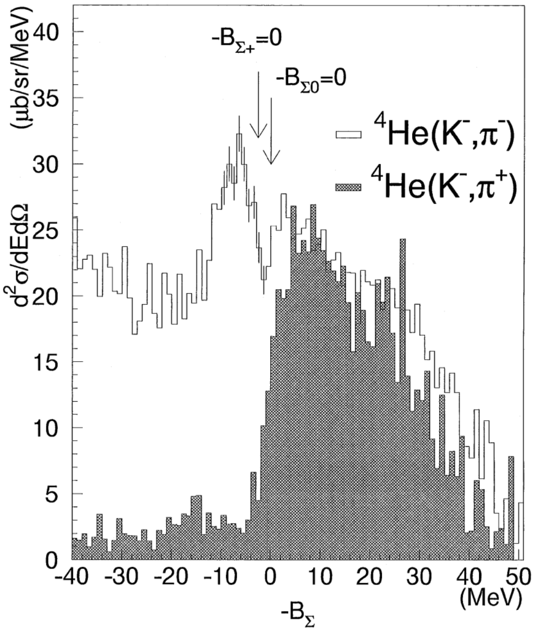

Figure 1.7: Excitation energy spectra for ^{4}He(K$^-$, π^-) and ^{4}He(K$^-$, π^+) reactions at 600 MeV/c K$^-$ momentum [64]. The binding energy threshold for the former reaction corresponds to the Σ^0 threshold, as depicted in the figure, and to the Σ^- threshold for the latter.

potential as

$$U_\Sigma(r) = U_0^\Sigma(r) + \frac{1}{A} U_1^\Sigma(r)(\mathbf{T}_C \cdot \mathbf{t}_\Sigma), \tag{1.5}$$

where $\mathbf{T}_C$ is the isospin operator of the core nucleus with the z projection $(Z - N)/2$, and $\mathbf{t}_\Sigma$ is the Σ isospin operator with $\mathbf{t}_{\Sigma,\,z} = +1,\ 0,\ -1$ for the Σ^+, Σ^0, Σ^- states. The interplay of the isoscalar U_0^Σ and isovector U_1^Σ (*Lane* term [67]) components generate the quasi-bound $^4_\Sigma$He state [66]. For larger A, however, the Lane term is strongly suppressed and therefore it is unlikely that Σ bound states are produced on heavier nuclei.

Indeed, the spectra obtained from *associate* Σ^- production on heavier targets (CH$_2$, Si, Ni, In, and Bi) using π^- beams exhibit the features expected from *quasi-free* processes [68, 69]. The result of an exemplary analysis of the ^{28}Si(π^-, K$^+$) spectrum is shown in Fig. 1.8. The yield in the bound state region ($B_\Sigma > 0$) exceeds the expectations from the combination of the Coulomb and nuclear interaction, and therefore indicates the pattern of the strong Σ–nucleus interaction [68]. A clear peak indicating a bound state, however, is not observed.

In the initial analyses [68, 69], the spectra are fitted with Woods-Saxon–type potentials for the Σ–nucleus interaction in the framework of the Distorted Wave Impulse Approximation (DWIA) [71]. In this formulation, the target is considered as a collection of nucleons in single-particle levels. The elementary production reaction on one of the nucleons in the target is assumed to proceed as in free space, while the remaining spectator nucleons generate an overall nuclear optical potential distorting the wave function of the incoming and outgoing particles. The best fit of the data yields a repulsive real part $U_0^\Sigma \approx 100$ MeV and $W_0^\Sigma = -40$ MeV for the imaginary part. It should be noted that the data are in general less sensitive to the absorptive component. More sophisticated analyses come to similar conclusions, albeit finding a weaker repulsion of the order of 10 MeV

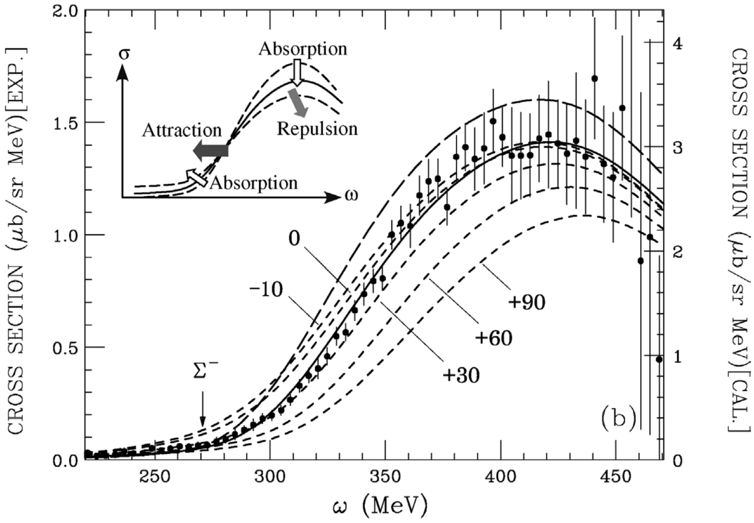

Figure 1.8: Measured ^{28}Si(π^-, K^+) spectrum from Ref. [69], and a comparison to DWIA calculations [70]. The dashed lines correspond to Woods-Saxon potentials with strengths of $U_0^\Sigma = -10$, 0, 30, 60, 90 MeV for the real, and $W_0^\Sigma = -40$ MeV for the imaginary part. The solid line denotes the spectrum with the DD potential obtained from fitting Σ^- atomic data [60, 61]. The inset depicts the effect of different types of interaction on the measured spectra.

to 50 MeV [70, 72–74]. In addition, the spectra have been employed to benchmark different Σ–nucleus potentials. In particular, the potentials found from fits to Σ^- atomic data [60–62], as discussed above, yield a satisfactory description of the spectra [70, 72]. Irrespective of the detailed approach, however, a fully attractive Σ–nucleus potential seem not to conform with the data.

Summary of the Experimental Findings In general, apart from the results of scattering experiments, the available data yields information about the Σ–nucleus interaction and therefore its extraction and interpretation features a significant model dependence. The best description of the available data is obtained by a Σ–nucleus potential that is repulsive inside the nuclear surface and attractive outside.

The general pattern arising from the measurements points towards an overall repulsive interaction with a strong isospin dependence. Indeed, the available data indicate an attractive interaction in the isospin $I = 1/2$ channel and repulsion in the $I = 3/2$ component. Nevertheless, it is clear that more experimental constraints are crucial to clarify the situation.

1.2.2 Theoretical Treatment of the Hyperon–Nucleon Interaction

From a theoretical point of view, the baryon–baryon interaction is fully determined by the corresponding quark–gluon dynamics. In the low-energy regime of QCD, however, the coupling constants are too large to employ perturbative approaches. For this reason, the modeling of the baryon–baryon interaction is typically conducted employing effective theories and phenomenological approaches [8], where the relevant degrees of freedom are hadrons and the interaction is mediated via meson exchange. In the following, the most successful approaches are briefly introduced before discussing the corresponding results for the N–Σ interaction.

Meson-Exchange Models In meson-exchange models the interaction among two baryons is mediated via scalar, pseudoscalar, and vector mesons. A one-meson-exchange potential model is constructed from the couplings of the meson fields to those of the baryon. The coupling constants are determined by relating them, where applicable, to the N–N values employing broken SU(3) symmetry, and fits to the available scattering data. The short-range behavior at the meson-baryon exchange vertices is incorporated in phenomenological form factors that are meant to consider the extended hadron structure. Most successful examples are different versions of the Jülich [75, 76] and Nijmegen [77–81] models. These models differ particularly in the treatment of the scalar-isoscalar meson sector and the modeling of the form factors.

Chiral Effective Field Theory (χEFT) χEFT is a systematic approach that employs the symmetries and symmetry breaking patterns of QCD at low energies. Instead of the quarks and gluons, however, hadrons constitute the relevant degrees of freedom [9]. A power counting scheme allows a systematical choice of the order of the expansion and correspondingly of the involved processes. Accordingly, at leading order (LO) the considered processes are one-meson-exchange and non-derivative four-baryon contact terms [82], while at next-to-leading order (NLO) two-meson-exchanges and contact interactions with two derivatives contribute additionally [83, 84]. The short-range dynamics are incorporated in contact terms with so-called low-energy constants that can be constrained employing SU(3) symmetry and the available scattering data. Results have been obtained at LO [82] and NLO [83, 84].

Quark models Constituent quark models explicitly incorporate essential features of QCD [85]. Baryons are considered as three-quark clusters in the framework of the resonating-group method [86] taking into account the quarks' color degrees of freedom and anti-symmetrization. The short-range part of the effective qq interaction is modeled with a phenomenological quark-confining potential and the one-gluon exchange Fermi-Breit interaction. Longer-ranged effects are included as effective meson-exchange potentials acting between quarks. The SU(3) relations of the relevant coupling constants emerge naturally from the SU(6) quark model. The most significant difference among different approaches concerns the effective meson-exchange potential. The FSS model [87] incorporates scalar and pseudo-scalar meson exchanges, while the more recent fss2 model [88] includes also vector mesons.

Lattice QCD Lattice QCD is relying on first principles to extract the baryon–baryon interaction. The full QCD Lagrangian is numerically solved on a four-dimensional lattice with spacing a, which therefore acts as a non-perturbative regularization scheme. The continuum is approximated in the limit $a \to 0$, to which the observables are extrapolated. It should be noted, however, that the numerical simulations are based on Monte Carlo techniques. Due to the significant computational resources required for these calculations, the reduction of the associated statistical uncertainties, especially important for lighter particles, is not trivial. Recent approaches to the Y–N interaction have been attempted by the HAL QCD [89] and the NPLQCD [90] Collaborations, employing different methods to obtain their results.

1.2.2.1 Results on the Σ–Nucleon Interaction

Due to the modest quality of the available experimental data in the Y–N sector, theoretical approaches lack stringent constraints. Additionally, SU(3) symmetry can be exploited, where in the case of the N–Σ the ($S = 0,\ I = 3/2$) and the N–N ($S = 0,\ I = 1$) component belong to the same **27** irreducible representation.

All discussed models yield a consistent description of the available scattering data in the $|S| = 1$ sector. This is exemplarily depicted for the case of the N–Σ interaction for results from elastic Σ^-p and Σ^+p scatterings in the left and right panel of Fig. 1.9, together with results from χEFT and the Jülich meson-exchange model. The corresponding scattering parameters for the p–Σ^+ channel are shown in Table 1.2 in the scattering sign convention, where a negative scattering length corresponds to an attractive interaction. The results from χEFT are given throughout this work for a cutoff value of $\Lambda = 600\,\mathrm{MeV}$. Even though clear deviations among the values can be observed, most models reflect the experimental evidence of a strong repulsion in the ($S = 0$, $I = 1/2$) and ($S = 1$, $I = 3/2$) component and an overall attraction in the remaining channels.

In strong contrast to this, the NSC97f model features attraction also in the ($S = 1$, $I = 3/2$) component. In general, the Nijmegen meson-exchange models seem to lack repulsion in the N–Σ sector. Therefore, additional Pauli-blocking effects, in line with the findings of Ref. [85], are introduced in the latest version ESC16. Moreover, in this model no bound states are allowed in the $S = -1$ sector. Concerning the results from χEFT, the available Y–N scattering data can be equally well described with repulsion or attraction in ($S = 1$, $I = 3/2$) component of the N–Σ interaction, which appears to be the dominant contribution [83]. To conform with the experimental findings, the repulsive version was chosen. For the updated version of the NLO calculations, NLO2019, SU(3) symmetry is exploited more strictly to constrain the low-energy constants. While scattering observables are equivalently well described, the strength of the

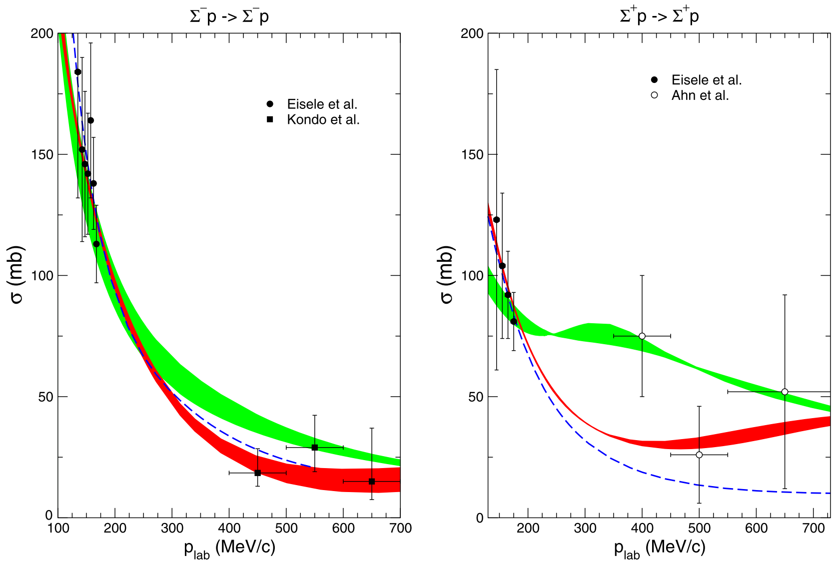

Figure 1.9: Elastic $\Sigma^-\mathrm{p} \to \Sigma^-\mathrm{p}$ (*left*) and $\Sigma^+\mathrm{p} \to \Sigma^+\mathrm{p}$ (*right*) scattering cross sections σ as a function of p_{lab} [83]. The green (red) band depicts the results from χEFT at LO [82] (NLO [83]). The data at higher momenta were not included in the fit. The dashed curve corresponds to the result of the Jülich J04 meson-exchange potential [76].

Table 1.2: Scattering parameters for the p–Σ^+ interaction.

Model		$S = 0$		$S = 1$	
		a_s **(fm)**	r_s **(fm)**	a_t **(fm)**	r_t **(fm)**
fss2	[85]	−2.48	5.03	0.73	−1.31
χEFT (LO)	[82]	−2.32	3.60	0.65	−2.78
χEFT (NLO)	[83]	−3.56	3.54	0.49	−5.08
χEFT (NLO2019)	[84]	−3.62	3.50	0.47	−5.77
ESC16	[81]	−4.30	3.25	0.57	−3.11
NSC97f	[78]	−4.35	3.16	−0.25	−28.9
J04	[76]	−3.60	3.24	0.31	−12.2

N–$\Lambda \rightarrow$ N–Σ coupling is significantly enhanced in the NLO2019 version. This gives rise to sizable differences for the in-medium properties [9, 84]. The fss2 model features very strong repulsion in the ($S = 1,\ I = 3/2$) channel induced from the Pauli principle at quark level [85]. Results for the N–Σ interaction are also available from the HAL QCD Collaboration [91, 92]. The central potential of the N–Σ ($S = 0, I = 3/2$) component, evaluated at the almost physical point $m_\pi = 146\,\mathrm{MeV}/c^2$, is shown in Fig. 1.10 and displays a repulsive core and an attractive well. The results agree with the general pattern of the interaction in the different spin and isospin components, although the statistical uncertainties are still rather large. The same holds for results on the n–Σ^- interaction from the NPLQCD Collaboration, extrapolated to the physical pion mass using χEFT [93].

The resulting in-medium properties of the N–Σ interaction, however, differ significantly among the models. It should be noted, that the extrapolation of theoretical calculations to finite density, via e.g. the G-matrix approach [95, 96], introduces a significant model dependence. The different partial wave contributions to the resulting single-particle potential of various models are summarized in Table 1.3. Recent calculations from fss2, χEFT, and Lattice QCD extract an overall repulsive U_Σ ranging from 10 MeV to 17 MeV [83–85, 94], with significantly differing

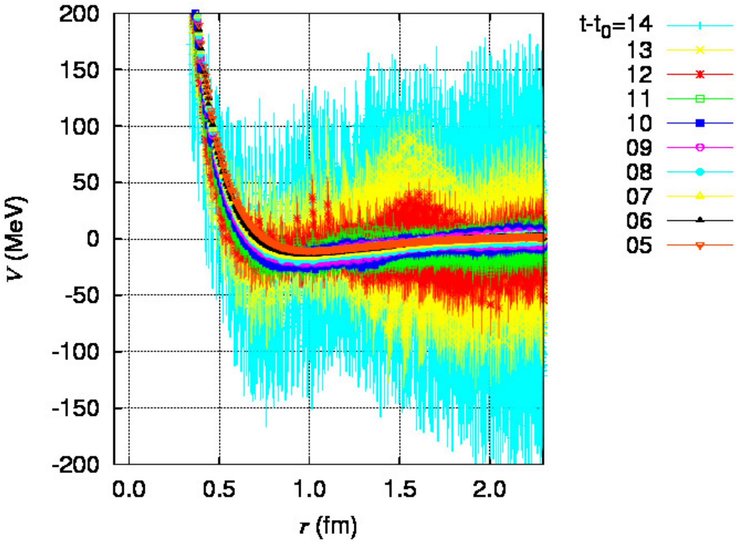

Figure 1.10: The central potential of the N–Σ ($S = 0, I = 3/2$) component from Lattice QCD evaluated at the almost physical point $m_\pi = 146\,\mathrm{MeV}/c^2$ for different euclidean times [91].

Table 1.3: Partial wave contributions to U_Σ in symmetric nuclear matter at saturation density. All values are in MeV. When marked with an asterisk the corresponding value contains additionally a contribution from the $^3D_1$ channel.

Model		$I = 1/2$ $^1S_0$	$^3S_1$	$I = 3/2$ $^1S_0$	$^3S_1$	**Total**
HAL QCD	[94]	7.4	−9.3	−5.0	21.8	14.6
fss2	[85]	6.7	−23.9*	−9.2	41.2*	7.5
χEFT (NLO)	[83, 84]	5.0	−22.7*	−10.1	43.6*	17.1
χEFT (NLO2019)	[84]	5.0	−20.0*	−9.9	40.2*	16.6
ESC16	[81]	10.2	−24.7	−13.1	29.5	−3.3
NSC97f	[78, 84]	15.0	−8.8*	−12.6	−6.4*	−16.1
J04	[76, 84]	4.2	−15.0*	−12.0	11.7*	−22.2

contributions from the individual partial waves. On the contrary, the meson-exchange models yield slightly attractive Σ single-particle potentials, ranging from ~ -22 MeV for the Jülich model J04 [76, 84] and ~ -16 MeV for NSC97f [78, 84] to -3 MeV for ESC16 [81]. Studies of the Σ–nuclear interaction have also been conducted using chiral perturbation theory [97, 98], resulting in a moderately repulsive real single-particle potential of $U_\Sigma = 59$ MeV.

Figure 1.11 depicts the momentum dependence of the Σ single-particle potential. The Lattice QCD calculations, shown in the right panel of Fig. 1.11, feature sizable statistical uncertainties and predict an overall repulsive U_Σ. For χEFT, shown in the left panel, the momentum dependence is similar for different densities, but the magnitude of U_Σ varies strongly. In particular, the Σ single-particle potential may even become attractive at low densities. For larger momenta, a significant difference between the results from χEFT at ρ_0 and from Lattice QCD arises. This once again demonstrates the need for further experimental constraints.

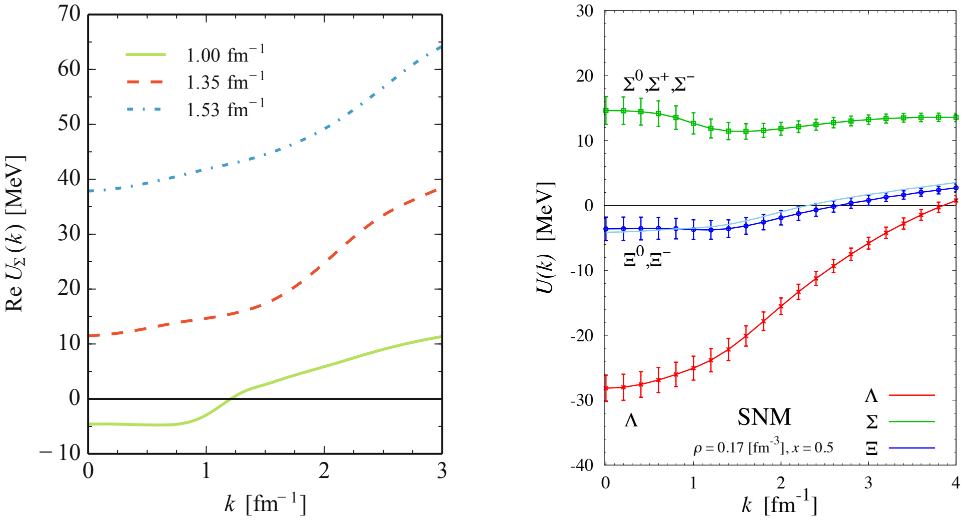

Figure 1.11: Momentum dependence of the Σ single-particle potential in symmetric nuclear matter. (*Left*) The real part of U_Σ from χEFT at NLO for different Fermi momenta corresponding to densities of about $\rho = (0.4, 1.0, 1.5)\,\rho_0$ [99] and (*right*) U_Y for different hyperons from HAL QCD at ρ_0 [94].

1.2.3 Implications for Neutron Stars

Experimentally, the largest densities can be achieved in heavy-ion collisions at intermediate energies of few GeV per nucleon. In such reactions, densities of about $2-3$ times the nuclear saturation density ρ_0 and moderate temperatures can be reached [100]. Similar or even larger densities at albeit significantly lower temperatures are believed to be realized in astrophysical objects, and in particular in neutron stars [101, 102]. The latter are extremely compact, massive objects with typical masses of $1-2\,M_\odot$ and radii of about 10 km. Their large density renders them suitable laboratories for QCD at extreme conditions. The interactions among the constituents are encoded in the Equation of State (EoS) connecting temperature, pressure and baryon density $p(\rho, T)$. Traditionally, the content of neutron stars is thought to be composed of neutron-rich matter in equilibrium against weak interaction processes, since weak decays are Pauli-blocked. Nevertheless, because the content of especially the inner core of neutron stars is not precisely known, a hypothetical EoS can only be tested if linked to observable quantities.

This can be accomplished employing the Tolman-Oppenheimer-Volkoff equations [103, 104], describing the hydrostatic and gravitational equilibrium of isotropic matter. This means, that a stable configuration is realized when the pressure among the constituents, given by the EoS, counterbalances the gravitational force. Accordingly, the Tolman-Oppenheimer-Volkoff equations link a given EoS to observable quantities such as the mass–radius relation of a star. Assuming only a degenerate Fermi gas of neutrons, the maximal neutron star mass would be only $\sim 0.7\,M_\odot$ [104], indicating the impact of the interaction among the constituents. The importance of properly modeling the EoS is well demonstrated in Fig. 1.12. The left panel depicts state-of-the-art EoS and in the right panel the resulting mass-radius curves are shown. It is clear that the predicted neutron star properties differ significantly. The strongest experimental constraints stem from astrophysical mass measurements of the heaviest neutron stars observed to date, yielding masses of about $2\,M_\odot$ [105–108]. Additional constraints come also from the recent observation of gravitational waves from neutron star mergers that provide limits for the tidal deformability [109, 110].

The large densities in the inner core of the neutron star can have an intriguing consequence. With the increasing Fermi pressure also the chemical potential of the nucleons increases, and it may

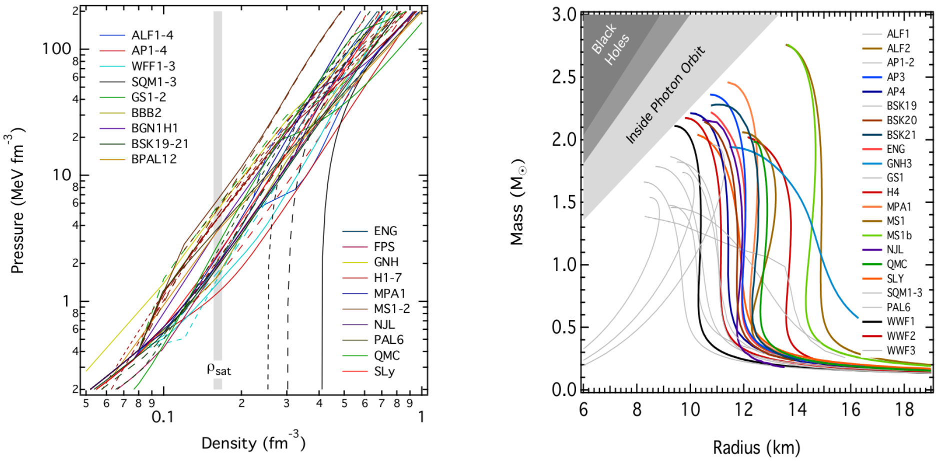

Figure 1.12: State-of-the art equations of state (*left*) and the corresponding mass–radius curves for neutron stars (*right*) [101]. Curves not fulfilling the $2\,M_\odot$ constraint are depicted in gray.

become energetically favorable to convert nucleons into hyperons [111]. A naïve introduction of Λ hyperons as additional degrees of freedom, however, softens the EoS to an extent that the neutron star can no longer sustain the two solar mass limit [112]. This is commonly referred to as the *hyperon puzzle* – the appearance of hyperons as additional degrees of freedom seems energetically favored, however leads due to the strong softening of the EoS to maximum masses not compatible with astrophysical observations [113].

It should be stressed though, that the precise onset of hyperons depends significantly on the Y–N and Y–Y interactions. In general, the more attractive the interaction, the earlier hyperons start to appear. This leads to a further softening of the EoS, and therefore to a lower maximum mass of the neutron star, while the opposite is true for a repulsive interaction. Thus, the two solar mass observations can be reconciled with the hypothesis of hyperon appearance by introducing additional repulsion that provides the required stiff EoS.

One important aspect is the inclusion of further hyperons in the EoS. This is especially important, as negatively charged hyperons such as the Σ^- or Ξ^- can replace an electron together with a neutron via processes such as $\mathrm{n} + \mathrm{e}^- \rightarrow \Sigma^- + \nu_e$ [111]. In RMF calculations, the baryon–baryon interaction is mediated via scalar (σ) and vector (ω), and isovector (ρ) mesons, while the hyperon-hyperon interaction is incorporated through strange scalar (ω^*) and vector (ϕ) mesons [115]. Results of such a calculation are depicted in the left panel of Fig. 1.13. The Σ^- appears even at lower densities than the Λ for an attractive N–Σ interaction [114]. Assuming a repulsive N–Σ interaction in line with the experimental observations, however, the onset is shifted to significantly larger densities and the Σ states are not expected to appear in neutron stars [114].

In RMF calculations, a repulsive component in the hyperonic sector can be introduced via the exchange of ϕ mesons for the Y–Y interaction [116]. The effect on the mass-radius relation for different values of the single-particle potential U_Σ is shown in the right panel of Fig. 1.13. In general, the dependence on U_Σ is rather modest, with a slight softening of the EoS for more

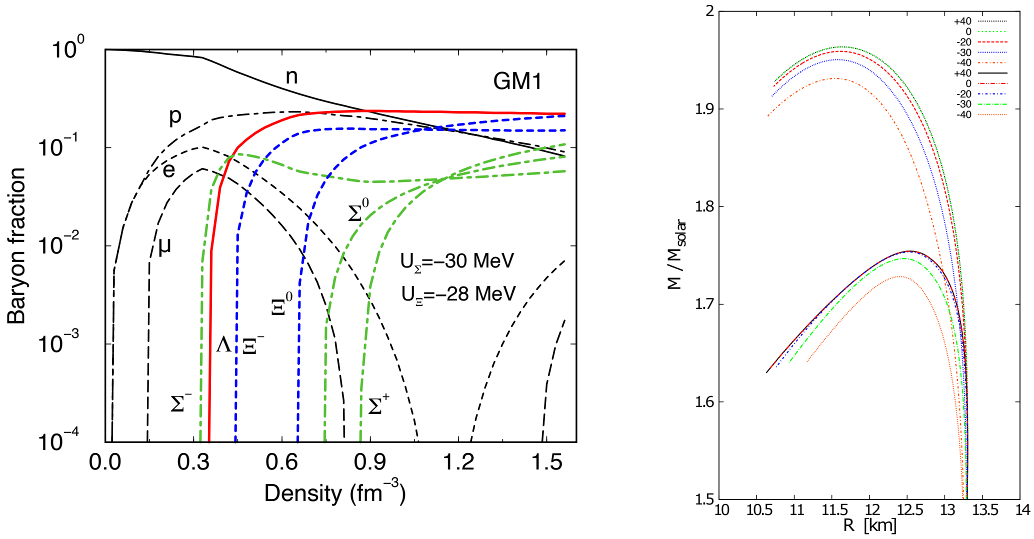

Figure 1.13: (*Left*) The composition of neutron star matter as a function of baryon density assuming an attractive N–Σ and N–Ξ interaction [114, 115]. (*Right*) Mass-radius relation for neutron stars for different variations of U_Σ [116]. The lower branch corresponds to a model including $\sigma\omega\rho$ mesons. The experimental mass limits can only be reached when additionally the exchange of ϕ mesons is considered (upper branch).

attractive values. Most intriguing, the EoS and correspondingly the mass-radius relation does not differ for $U_\Sigma \geq 0\,\mathrm{MeV}$, since in this case the Σ states simply do not appear and the EoS becomes insensitive to the actual value [116]. The inclusion of the ϕ meson has a sizeable influence, since it leads to a significant stiffening of the EoS and thus to larger achievable neutron star masses. It should be noted though, that the results depend strongly on the ϕ–N coupling strength [117]. Nevertheless, the curves for a repulsive U_Σ including the repulsion mediated via the ϕ meson come close to the $2\,M_\odot$ limit.

Moreover, the dynamics of the N–Λ interaction are strongly affected by the conversion process N–Λ ↔ N–Σ, occurring in the $I = 1/2$ channel due to the close kinematic threshold between the two systems [118]. Figure 1.14 depicts the phase shift of p–Λ in the $^3S_1$ channel with and without considering the coupling in the left and right panel. Although the exact behavior of the different models varies, the coupling consistently contributes to the overall attraction. Instead, the p–Λ phase shift turns repulsive for the χEFT results when the coupling is switched off. This is particularly interesting since hypernuclear results suggest that at larger densities the coupling is indeed suppressed. Therefore, a repulsive N–Λ interaction arises quite naturally at larger densities. Indeed, the resulting N–Λ and N–Σ interactions are expected to be repulsive to an extend that hyperon appearance in neutron stars is disfavored [9].

Finally, in Quantum Monte Carlo simulations [119] the required stiff EoS could be accomplished by introducing a phenomenological, repulsive three-body ΛNN force constrained to binding energies of hypernuclei. This is accomplished, however, at the expense that the interaction is as repulsive that no hyperons appear at the densities expected in neutron stars. Similar conclusions on the three-body ΛNN force are obtained in a recent study within χEFT [120].

Whatever the solution to the *hyperon puzzle* is, it is essential to include a precise modeling of all relevant interactions and couplings for the modeling of a realistic hypernuclear EoS. Therefore, it is crucial to provide further experimental input and pin down the interactions in the Y–N sector. This concerns especially the Σ sector, where experimental results are scarce and theoretical approaches diverge.

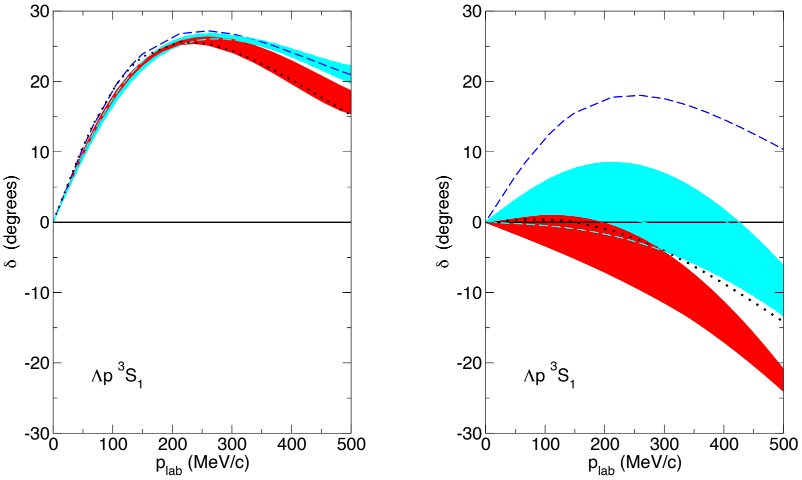

Figure 1.14: $^3S_1$ p–Λ phase shift with (*left*) and without (*right*) the N–Λ ↔ N–Σ coupling. Modified from Ref. [84]. The red band represents the result from χEFT NLO [83] and the cyan band that of the alternative version NLO2019 [84]. The dashed curve corresponds to the result of the Jülich '04 meson-exchange model [76] and the dotted curve to that of the NSC97f potential [78].

1.3 Femtoscopy

The femtoscopcy method is based on intensity interferometry techniques developed for measurements of angular dimensions of stars, the so-called *Hanbury-Brown and Twiss* (HBT) interferometry [121, 122]. In particle physics, measurements of two-particle correlations at small relative momenta have been employed since the 1960s [123–127]. Depending on the particle pair under study, quantum statistics, the Coulomb, and strong final-state interactions may give rise to a correlation signal. Under the prerequisite that the interaction among the studied particle pairs is known, the space-time evolution of the particle-emitting source in elementary and heavy-ion collisions can be characterized [124–127]. Due to the typical length scale of such sources, the method is commonly referred to as *femtoscopy*.

By inverting the paradigm of femtoscopy, however, the interaction among particles can be studied. The benefit of this method is that any detectable particle pair produced in elementary or heavy-ion collisions can be investigated. This enables measurements of interactions that are not accessible via scattering experiments and circumvents the difficulties associated with producing and handling beams of unstable hadrons as discussed above.

1.3.1 Framework of Femtoscopy

Hereafter, the underlying mathematical framework of femtoscopy is briefly sketched following Refs. [125, 128, 129]. In general, the two-particle correlation function is constructed as the ratio of the two-particle spectrum and the product of the single-particle spectra [126],

$$C(\mathbf{p}_1,\ \mathbf{p}_2) = \frac{N(\mathbf{p}_1,\ \mathbf{p}_2)}{N(\mathbf{p}_1)\,N(\mathbf{p}_2)} = \frac{E_1 E_2\, \mathrm{d}N/(\mathrm{d}^3p_1\mathrm{d}^3p_2)}{E_1\, \mathrm{d}N/\mathrm{d}^3p_1\ E_2\, \mathrm{d}N/\mathrm{d}^3p_2}. \tag{1.6}$$

In absence of any correlations, the two-particle spectrum factorizes $N(\mathbf{p}_1,\ \mathbf{p}_2) = N(\mathbf{p}_1)\ N(\mathbf{p}_2)$ and therefore the correlation function is equal to unity. The correlation function can be related to the particle emission and the interaction of the particle pair via [125]

$$C(\mathbf{p}_1,\ \mathbf{p}_2) = \frac{\int \mathrm{d}^4x_1\mathrm{d}^4x_2\, s_1(p_1,\ x_1)\, s_2(p_2,\ x_2)\, |\Psi(p_1,\ x_1,\ p_2,\ x_2)|^2}{\int \mathrm{d}^4x_1\, s_1(p_1,\ x_1)\ \int \mathrm{d}^4x_2\, s_2(p_2,\ x_2)} \tag{1.7}$$

where the emission function $s(p,\ x)$ describes the probability to emit a particle with momentum p from a space-time point x. The square of the Bethe-Salpeter amplitude $\Psi(p_1,\ x_1,\ p_2,\ x_2)$ serves as a weight for the two-particle emission [125, 130]. Assuming equal emission times for the particles, the Bethe-Salpeter amplitude can be replaced by the relative wave function $\psi(\mathbf{k}^*,\ \mathbf{r}^*)$, where $\mathbf{r}^*$ denotes the relative distance of the two particles upon their emission and the *reduced relative momentum* $\mathbf{k}^* = (m_2\mathbf{p}_1^* - m_1\mathbf{p}_2^*)/(m_1 + m_2)$ with the momenta of the two particles, $\mathbf{p}_1^*$ and $\mathbf{p}_2^*$, in the pair rest frame denoted by the *. With further assumptions regarding e.g. the smoothness of the source functions $s(p,\ x)$ in momentum space [125, 130] one arrives at the *Koonin–Pratt equation* [131, 132]

$$C(\mathbf{k}^*) = \int \mathrm{d}\mathbf{r}^*\ S(\mathbf{r}^*)|\psi(\mathbf{r}^*,\mathbf{k}^*)|^2, \tag{1.8}$$

with the relative source distribution in the pair rest frame $S(\mathbf{r}^*)$. This formulation underlines the two necessary ingredients for the interpretation of an experimentally determined correlation function – the source function and the relative wave function. Femtoscopy in its traditional meaning relies on particles of known interaction to constrain the particle-emitting source. In the following, however, the paradigm of femtoscopy is inverted and the correlation function is exploited to study the interaction among hadron pairs.

Depending on the particle pair under study, different contributions to the correlation function may arise. In general, a correlation signal can emerge from quantum statistics, Coulomb and the strong interaction, or a combination thereof. In case a pair of identical particles is studied, quantum statistics gives rise to a correlation signal – for a boson pair, the wave function must be symmetrized, while the opposite holds for a pair of fermions. The left panel of Fig. 1.15 depicts exemplarily the resulting correlation functions of π–π and p–p pairs, neglecting any other contribution to the correlation function. The signal emerging from quantum statistics is particularly sensitive to the geometric extension of the emission source. Indeed, the effect of quantum statistics acts like a Fourier transformation of the source distribution and therefore, the width of the signal is inversely proportional to the width of the source function. Studies of the size of the colliding system are most prominently conducted with π–π and K–K pairs.

Correlations among charged particles are additionally affected by the Coulomb interaction. In general, the Coulomb potential decays as r^{*-1} and therefore introduces a correlation signal even at large pair separations. Oppositely-charged particles are attracted by one another, which leads to a correlation signal $C(k^*) > 1$. The opposite holds for particle pairs of the same charge. The right panel of Fig. 1.15 depicts exemplarily the resulting correlation functions of same and opposite charge combinations of π–π pairs, neglecting the contribution of quantum statistics. It is clearly visible that the Coulomb interaction acts most prominently at low k^* and that the size of the particle-emitting source has a negligible effect.

Finally, the contribution most relevant for this work arises from the strong interaction. The effect of quantum statistics and the Coulomb interaction defines, if applicable to the particle pair of interest, the baseline of the measurement. Due to the short range of the strong force, the

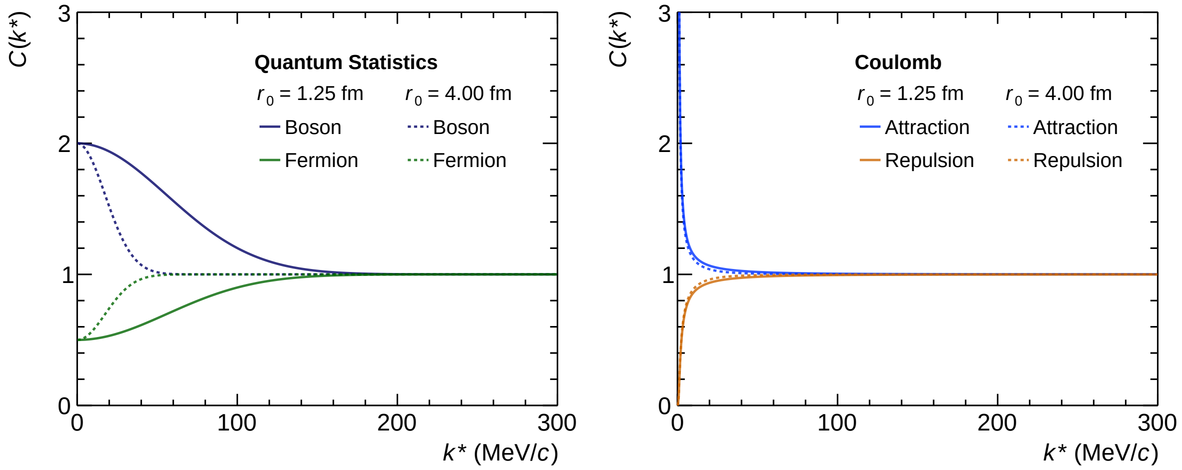

Figure 1.15: Exemplary correlation functions arising from quantum statistics (*left*) and the Coulomb interaction (*right*). The correlation functions are obtained for a femtoscopic radius r_0 equivalent to a small (pp, *solid lines*) and large (Pb–Pb, *dotted lines*) collision system.

interaction takes place mainly in the S-wave. A number of convenient simplifications enables one to obtain an analytical expression for Eq. 1.8. The asymptotic solution of the wave function for an elastic scattering problem is given as the sum of the incoming plane wave and a modified outgoing spherical wave,

$$\psi(\mathbf{k}^*,\, \mathbf{r}^*) = e^{i\mathbf{k}^*\cdot\mathbf{r}^*} + f(k^*)\, \frac{e^{ik^*r^*}}{r^*}, \tag{1.9}$$

where the modification is incorporated in the *scattering amplitude* $f(k^*)$. It should be noted that in femtoscopy the scattering problem occurs in reversed direction in time, so the final state particles are in the entrance channel and $\mathbf{k}^* \rightarrow -\mathbf{k}^*$. The effect of the final-state interaction is encoded in the S-wave scattering amplitude,

$$f_S(k^*) = \frac{e^{2i\delta_0} - 1}{2ik^*} = \left(\frac{1}{K_S} - ik^*\right)^{-1} \approx \left(\frac{1}{f_0} + \frac{1}{2}d_0 k^{*2} - ik^*\right)^{-1}, \tag{1.10}$$

where δ_0 is the S-wave phase shift. In the last step, the *effective range approximation* was applied, introducing two so-called *scattering parameters*, the scattering length $f_0 = \lim_{k^*\to 0} f_S(k^*)$ and the effective range of the potential d_0. Furthermore, the two-particle source function is assumed to be static, spherically symmetric, and described by a Gaussian distribution with a single-particle width r_0,

$$S(r^*) = \frac{1}{(4\pi r_0^2)^{3/2}}\, e^{-\frac{r^{*2}}{4r_0^2}}. \tag{1.11}$$

Then, the integration of Eq. 1.8 can be carried out analytically and one arrives at the Lednický–Lyuboshits formula [133] to model the correlation function as

$$\begin{aligned} C(k^*) = 1 + \sum_S \rho_S \Bigg[&\frac{1}{2}\left|\frac{f_S(k^*)}{r_0}\right|^2 \left(1 - \frac{d_0^S}{2\sqrt{\pi} r_0}\right) \\ &+ \frac{2\Re f_S(k^*)}{\sqrt{\pi} r_0} F_1(2k^* r_0) - \frac{\Im f_S(k^*)}{r_0} F_2(2k^* r_0) \Bigg], \end{aligned} \tag{1.12}$$

where the analytical functions $F_1(2k^*r_0)$ and $F_2(2k^*r_0)$ result from the approximation of isotropic emission from a Gaussian-shaped source. The factor ρ_S corresponds to the fraction of pairs emitted into a certain spin state S, where typically unpolarized emission is assumed.
According to Eq. 1.8, the correlation function is obtained as the integration of the square of the wave function over the source distribution. Depending on the source distribution, a sizable amount of particle pairs may be emitted within the range of the strong potential where $V(r^*) \neq 0$. In this case, the wave function deviates significantly from its asymptotic form. Therefore, an approximate correction is introduced in the Lednický–Lyuboshits approach by subtracting the term $d_0^S |f_S(k^*)|^2/(2\sqrt{\pi} r_0{}^3)$ from the asymptotic solution [133]. For particularly small sources, however, the approximation might break down resulting in unphysical correlation functions.

Exemplary strong interaction correlation functions for distinguishable particles computed with the Lednický–Lyuboshits approach are shown in Fig. 1.16. Smaller source sizes result in more particle pairs emitted within the range of the strong potential and therefore typically in a more pronounced correlation function. For this reason, elementary collision systems with femtoscopic

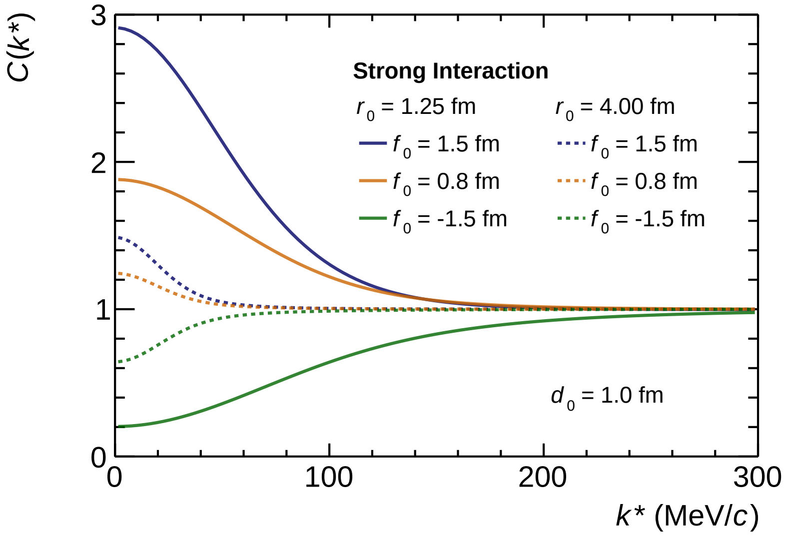

Figure 1.16: Exemplary strong interaction correlation functions for distinguishable particles computed with the Lednický–Lyuboshits approach [133] for an effective range $d_0 = 1$ fm and different scattering lengths f_0. The correlation functions are obtained for a femtoscopic radius r_0 equivalent to a small (pp, *solid lines*) and large (Pb–Pb, *dotted lines*) collision system.

radii of the order of 1 fm constitute an especially suitable environment to study hadron–hadron interactions with the femtoscopy method. The displayed correlation functions exhibit the general pattern – for an attractive interaction the correlation function demonstrates an enhancement $C(k^*) > 1$, while for a repulsive interaction the opposite is true. Here, the femtoscopy sign convention for the scattering length f_0 is employed, where a positive scattering length corresponds to an attractive interaction. A stronger attraction results in a more pronounced enhancement of the correlation function. The formation of bound states or coupled-channel effects, however, may alter the correlation function in a way that the conclusions made above do not hold any longer.

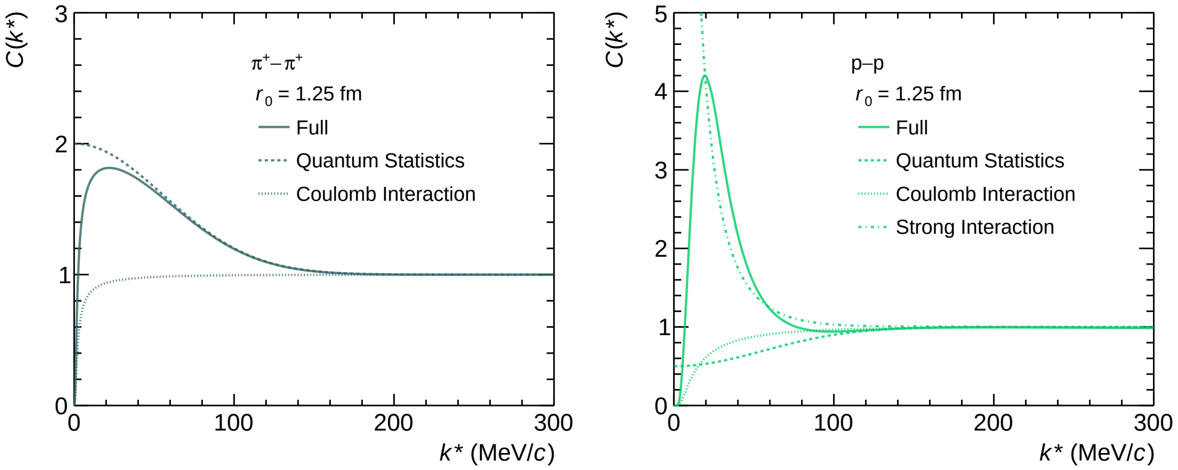

Figure 1.17: Correlation functions of π–π (*left*) and p–p (*right*) pairs, defined by the interplay of quantum statistics (*dashed*), the Coulomb (*dotted*) and the strong interaction (*dash-dotted*). The contribution of the strong interaction in the p–p channel is obtained employing the Argonne v_{18} potential [134] and the *Correlation Analysis Tool using the Schrödinger equation* [135].

Realistic correlation functions are then defined by the interplay of the relevant contributions. For π^+–π^+ pairs, the signal emerges from the combination of quantum statistics and the Coulomb interaction, as depicted in the left panel of Fig. 1.17. At very low k^* the repulsion due to the Coulomb interaction drives the correlation function, while at larger k^* the signal is solely due to quantum statistics. For p–p pairs, in addition to quantum statistics and the Coulomb interaction, also the strong interaction contributes, as displayed in the right panel of Fig. 1.17. The contribution of the strong interaction is modeled employing the Argonne v_{18} potential [134] and the *Correlation Analysis Tool using the Schrödinger equation* [135]. In this case, both quantum statistics and the Coulomb interaction cause a depletion of the correlation function at low k^*, with the signal for $C(k^* \to 0) \to 0$. The attractive strong interaction in the S-wave of the p–p channel, on the other hand, drives the behavior of the correlation function in the intermediate k^* regime. The bump structure in the overall correlation function emerges from the interplay of all three contributions.

1.3.2 Coupled-Channel Effects

In general, inelastic transitions due to coupled-channel effects occur between particle pairs with the same quantum numbers that are close in mass [136, 137]. In the Y–N sector, this occurs prominently in the $\Lambda\mathrm{N} - \Sigma\mathrm{N}$ system in the $|S| = 1$ sector, with the thresholds separated by about $80\,\mathrm{MeV}/c^2$. In scattering experiments, the initial state of the reaction is fixed by the selected beam projectile and the target. Coupled-channel effects occurring in the scattering process lead to the population of different final states. The contrary holds for femtoscopy, where the experimental detection of the outgoing particles defines the final state, to which different initial states can contribute via their coupling [138]. For the exemplary case of the p–Σ^0 correlation function, the relevant inelastic contributions come from p–$\Lambda \to$ p–Σ^0 ($I = 1/2$) and n–$\Sigma^+ \to$ p–Σ^0 ($I = 1/2,\ 3/2$).

The resulting correlation function is then given by [138, 139],

$$C(\mathbf{k}^*) = \int \mathrm{d}\mathbf{r}^* S(r^*) \sum_j \omega_j |\psi_j(\mathbf{r}^*, \mathbf{k}^*)|^2, \tag{1.13}$$

where the sum runs over all contributions that couple to the final state, including the elastic transition p–$\Sigma^0 \to$ p–Σ^0. It should be noted, that the source functions for the different channels could be different [140], with the sum running accordingly over the full integral. For the sake of simplicity, however, the same source is assumed for all channels hereafter. The wave functions $\psi_j(\mathbf{r}^*, \mathbf{k}^*)$ are weighted by the factor ω_j considering the population of the initial state and the coupling strength to the measured final state. The former can be obtained from either measured particle spectra or statistical hadronization models [141], while for the latter a theoretical description of the interaction is necessary. The wave functions of the coupled system are obtained by solving a multi-channel Schrödinger equation [138],

$$\begin{pmatrix} \mathcal{H}_{\mathrm{p}\Sigma^0 \to \mathrm{p}\Sigma^0} & \mathcal{H}_{\mathrm{p}\Sigma^0 \to \mathrm{n}\Sigma^+} & \mathcal{H}_{\mathrm{p}\Sigma^0 \to \mathrm{p}\Lambda} \\ \mathcal{H}_{\mathrm{n}\Sigma^+ \to \mathrm{p}\Sigma^0} & \mathcal{H}_{\mathrm{n}\Sigma^+ \to \mathrm{n}\Sigma^+} & \mathcal{H}_{\mathrm{n}\Sigma^+ \to \mathrm{p}\Lambda} \\ \mathcal{H}_{\mathrm{p}\Lambda \to \mathrm{p}\Sigma^0} & \mathcal{H}_{\mathrm{p}\Lambda \to \mathrm{n}\Sigma^+} & \mathcal{H}_{\mathrm{p}\Lambda \to \mathrm{p}\Lambda} \end{pmatrix} \begin{pmatrix} \psi_{\mathrm{p}\Sigma^0}(\mathbf{r}^*, \mathbf{k}^*) \\ \psi_{\mathrm{n}\Sigma^+}(\mathbf{r}^*, \mathbf{k}^*) \\ \psi_{\mathrm{p}\Lambda}(\mathbf{r}^*, \mathbf{k}^*) \end{pmatrix} = E \begin{pmatrix} \psi_{\mathrm{p}\Sigma^0}(\mathbf{r}^*, \mathbf{k}^*) \\ \psi_{\mathrm{n}\Sigma^+}(\mathbf{r}^*, \mathbf{k}^*) \\ \psi_{\mathrm{p}\Lambda}(\mathbf{r}^*, \mathbf{k}^*) \end{pmatrix}. \tag{1.14}$$

The momenta in the channels j are given by $k_j^* = \sqrt{2\mu_j(E - \Delta_j)}$, with the reduced mass μ_j and the difference of the threshold energy Δ_j with respect to the measured channel in the final state.

Accordingly, all momenta in the individual channels can be related to the measured k^* of the elastic transition. The Schrödinger equation is then solved under the boundary condition that the outgoing waves are normalized and that the outgoing channel is the measured final state.

Since a multi-channel Schrödinger equation is solved, the presence of coupled channels also influences the elastic single-channel wave function $\psi_{\mathrm{p}\Sigma^0}(\mathbf{r}^*, \mathbf{k}^*)$. Simple arguments from scattering theory can be exploited to qualitatively sketch the effect of the presence of coupled channels on the correlation function. Since open coupled channels constitute essentially another source of particle pairs, the additional feeding leads to an enhancement of the studied correlation function. At the same time, in any kind of scattering problem the total particle flux must be conserved. Accordingly, the yield in the elastic channel is depleted and so is the correlation function. It should be noted, however, that details of the interplay of the enhancement due to the presence of open coupled channels and the corresponding depletion of the elastic channel are significantly influenced by the final-state interaction. Therefore, only a full treatment of all relevant channels enables meaningful conclusions on the interaction of the particle pair under study.

1.3.3 Studies of the Final-State Interaction of Strange Hadrons

Hyperons, in particular the Λ, have been employed to determine the size of the particle-emitting source [142–147] using either phenomenological potentials [148] or scattering parameters from theoretical approaches to model the interaction. Detailed studies of hadron–hadron interactions can be conducted by reversing the paradigm of femtoscopy and under the premise that the particle-emitting source is well constrained. Recently, significant progress was made in the Y–N sector by exploiting the particular sensitivity of the femtoscopy method to the final-state interaction for small particle-emitting sources.

Studies of the p–Λ correlation function in small collision systems, such as pp, p–Pb, and p–Nb, at various energies enabled detailed tests of state-of-the-art theoretical models of the interaction and demonstrated the feasibility of the method [128, 150–152]. Figure 1.18 depicts exemplarily the p–Λ correlation function obtained from high-multiplicity pp collisions at $\sqrt{s} = 13$ TeV. The measured correlation function reflects at low k^* the pattern of the attractive strong p–Λ interaction. Additionally, the correlation function exhibits a peak-like structure at $k^* \sim 280\,\mathrm{MeV}/c$. The k^* value is consistent with the threshold of the p–Σ^0 channel opening at $k^* = 282.8\,\mathrm{MeV}/c$ and of the n–Σ^+ channel at $k^* = 279.0\,\mathrm{MeV}/c$, corresponding to the respective mass difference between the Λ and the Σ states. Therefore, the precision of these data enables quantitative studies of the coupling N–$\Sigma \rightarrow$ N–Λ. In fact, the available scattering data lack the precision to resolve the opening of the p–Σ^0 channel at $p_{\mathrm{lab}} = 642.2\,\mathrm{MeV}/c$ and of the n–Σ^+ channel at $p_{\mathrm{lab}} = 633.1\,\mathrm{MeV}/c$ [36–40]. The overall agreement of the theoretical correlation functions, modeled using χEFT at leading and next-to-leading order order, depends on the precise treatment of the non-femtoscopic baseline. Regardless of this, the description of the structure at the opening of the N–Σ channel cannot be described satisfactorily. This demonstrates, that femtoscopic measurements can provide decisive measurements to constrain the p–Λ interaction and the corresponding coupling to the N–Σ channel.

The Λ–Λ correlation function has been determined in elementary [128, 150, 152, 153] and heavy-ion collisions [154, 155]. In the first case, results from pp collisions at $\sqrt{s} = 7$ TeV and 13 TeV and from p–Pb collisions at $\sqrt{s_{\mathrm{NN}}} = 5.02$ TeV are combined to constrain the scattering parameters of the Λ–Λ interaction. Employing the Lednický–Lyuboshits approach, the scattering parameter

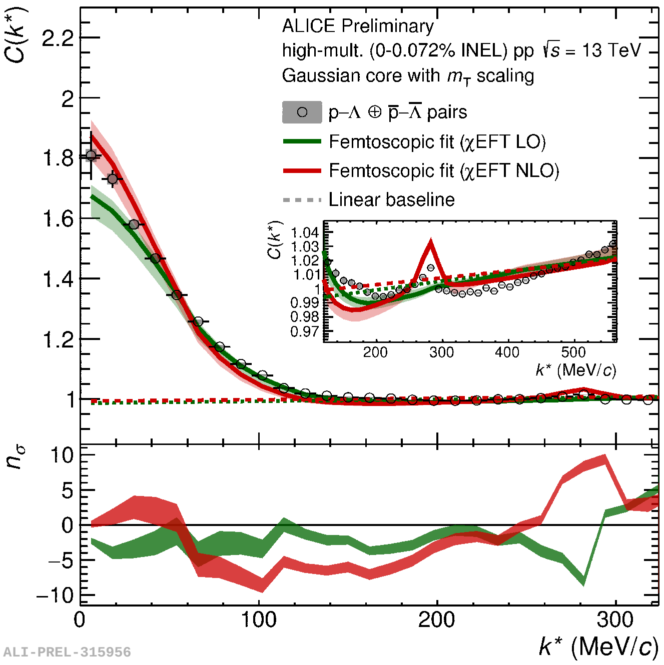

ALI-PREL-315956

Figure 1.18: Correlation function of p–Λ measured in pp collisions at $\sqrt{s} = 13$ TeV [149, 150]. The data are compared to χEFT at LO [82] and NLO [83]. The width of the bands corresponds to one standard deviation of the systematic uncertainty of the fit. The inset shows a zoom to the opening of the N–Σ channel at intermediate k^*.

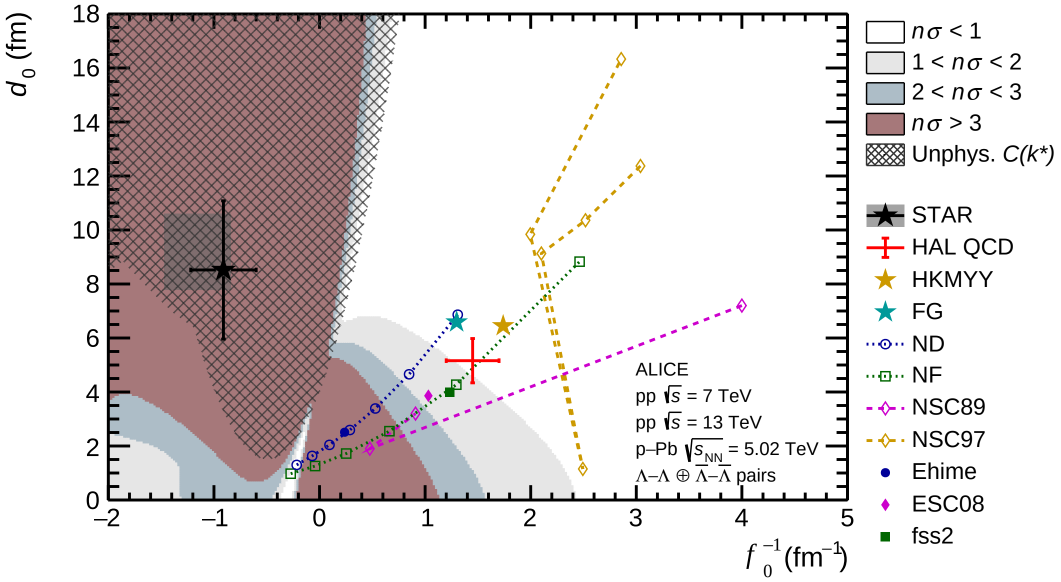

Figure 1.19: Exclusion plot for the Λ–Λ scattering parameter phase space obtained using data from pp collisions at $\sqrt{s} = 7$ TeV and $\sqrt{s} = 13$ TeV and from p–Pb collisions at $\sqrt{s_{\mathrm{NN}}} = 5.02$ TeV [153]. The degree of consistency n_σ is expressed by the color code. The gray-shaded region denotes the part of the phase space in which the Lednický–Lyuboshits approach produces an unphysical correlation function.

phase space (f_0^{-1}, d_0) is scanned and the resulting modeled correlation functions are compared to the data. The degree of consistency is expressed in number of standard deviations n_σ. As depicted in Fig. 1.19, a significant fraction of the phase space is excluded with more than 3σ. Indeed, the data indicate a shallow attractive interaction. Nevertheless, the region of phase space at large negative f_0 and small d_0 is in line with the data as well. This is particularly intriguing, since in this part of the phase space a Λ–Λ bound state – the H-dibaryon [44] – is expected to arise. The allowed scattering parameters can be related to the binding energy of the Λ–Λ state using the effective-range expansion [156, 157]. Accordingly, a value of $B_{\Lambda\Lambda} = 3.2^{+1.6}_{-2.4}\,(\mathrm{stat.})^{+1.8}_{-1.0}\,(\mathrm{syst.})\,\mathrm{MeV}$ is obtained, which is the most stringent experimental constraint to date.

For heavier baryon pairs the reduced signal-to-noise ratio of Lattice QCD computations enables the comparison of the corresponding results to experimental data. Measurements of the p–Ξ^- correlation function in pp and p–Pb collisions established for the first time the attractive nature of the strong interaction in the N–Ξ sector [158–161] and allowed the validation of the corresponding Lattice QCD potentials [89].

Finally, the first measurement of the p–ϕ interaction is under way [162]. Figure 1.20 depicts the resulting correlation function measured in high-multiplicity pp collisions at $\sqrt{s} = 13$ TeV. The background from minijets and residual p–($\mathrm{K}^+\mathrm{K}^-$) correlations is in an oversimplified manner described by a second order polynomial. Nevertheless, a clear correlation signal arises above the background, indicating an attractive interaction. The data are well described with a fit employing the Lednický–Lyuboshits approach. The resulting scattering parameters shall not be discussed here due to the oversimplified description of the background. Nevertheless, this study demonstrates the feasibility to study the interaction in a channel that cannot be accessed otherwise.

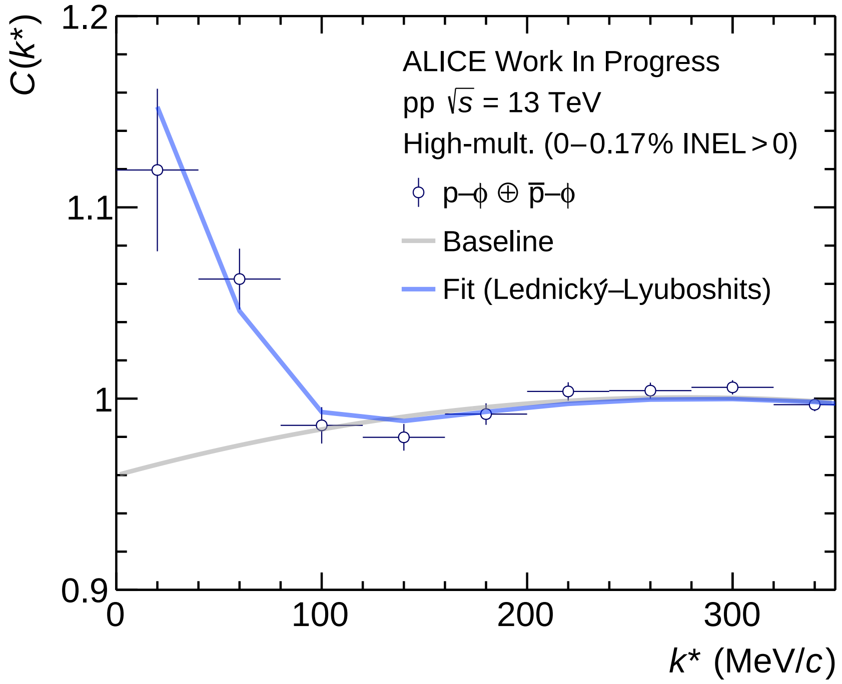

Figure 1.20: Measured correlation function of p–ϕ fitted employing the Lednický–Lyuboshits approach. Reproduced from Ref. [162]. The background is described by a second order polynomial.

In summary, the discussed measurements indicate that femtoscopy is a suitable tool to constrain interactions that are very difficult, if not impossible, to access via other methods. One particular advantage is that the interaction is studied in vacuum and therefore the comparison to theoretical predictions is far less model-dependent as in the case of hypernuclei or hyperonic atoms. Accordingly, the extension of such studies to the Σ sector, as presented in this work, is a logical step.

2 ALICE – A Large Ion Collider Experiment

This work is focused around A Large Ion Collider Experiment (ALICE) located at the Large Hadron Collider (LHC) at the Organisation Européenne pour la Récherche Nucléaire (CERN). In this Chapter, the accelerator, the detector, and the data processing chain are introduced.

2.1 The Large Hadron Collider

The LHC [163] at CERN is a particle accelerator and collider installed in the existing 26.7 km tunnel of the Large Electron–Positron Collider (LEP). During Run 2 (2015–2018), the center-of-mass energy reached up to $\sqrt{s} = 13$ TeV for pp collisions at a maximal design luminosity of about $\mathcal{L} = 10^{34}\,\mathrm{cm}^{-2}\,\mathrm{s}^{-1}$, and $\sqrt{s_{\mathrm{NN}}} = 5.02$ TeV per p–Pb and Pb–Pb nucleon pair at $\mathcal{L} = 10^{27}\,\mathrm{cm}^{-2}\,\mathrm{s}^{-1}$. For the upcoming Run 3 of the LHC, starting in 2021, the energy is planned to be further increased to the nominal design value of $\sqrt{s} = 14$ TeV in pp and $\sqrt{s_{\mathrm{NN}}} = 5.5$ TeV in p–Pb and Pb–Pb collisions.
The accelerator comprises eight straight sections with a length of 528 m each, where the experimental facilities are located, and eight arcs where the beams are deflected by superconducting dipole magnets with a field strength of up to 8.33 T. Since the accelerated particles are of the same charge, two magnet configurations are necessary to deflect the counter-rotating beams. Due to the space limitation in the tunnel, this has been accomplished by a twin-bore magnet design. Additional quadrupole, sextupole, octupole and decapole magnets serve to focus the beams. The latter are made of discrete packets of particles, so-called *bunches* that contain $\sim 1.15 \times 10^{11}$ protons each. In total, up to 2808 bunches with a bunch spacing of 25 ns can be stored in each of the two beams.
The CERN accelerator complex is employed to subsequently accelerate the hadrons to the injection energy of the LHC. The LHC is linked to this injector chain via two transfer tunnels, as schematically depicted in Fig. 2.1. The accelerator chain for protons starts in the linear accelerator (Linac 2), in which the particles reach energies of 50 MeV. The resulting beam is then further accelerated to 1.4 GeV in the Proton Synchrotron Booster (PSB) and to 25 GeV in the Proton Synchrotron (PS). Finally, the protons are brought to an energy of 450 GeV in the Super Proton Synchrotron (SPS) before injection into the LHC. The injection systems are located close to interaction point (IP) 2 for beam 1, and close to IP 8 for beam 2.

All four IPs of the LHC are instrumented with experiments. The two high-luminosity spectrometers ATLAS (A Toroidal LHC Apparatus) [165] and CMS (Compact Muon Solenoid) [166] are located at IP 1 and 5. Even though both detector systems have been designed and optimized for the search of the Standard Model Higgs boson, the physics program ranges from precision measurements of Standard Model parameters to the search of new physics beyond the Standard Model. Therefore, both experiments are designed as general-purpose detectors with high rate capabilities, aiming at detecting particles at large transverse momenta (p_{T}). The LHCb (Large Hadron Collider beauty) [167] experiment, located at IP 8, is dedicated to the search for indirect evidence of charge conjugation symmetry and parity symmetry violating physics beyond the Standard Model in decays of beauty and charm hadrons. The detector is a single-arm spectrometer with a forward angular coverage to benefit from the Lorentz-boost the charm ($c\tau \sim 150\,\mu\mathrm{m}$ [7]) and beauty mesons ($c\tau \sim 450\,\mu\mathrm{m}$ [7]) experience when emitted in forward direction. The forth

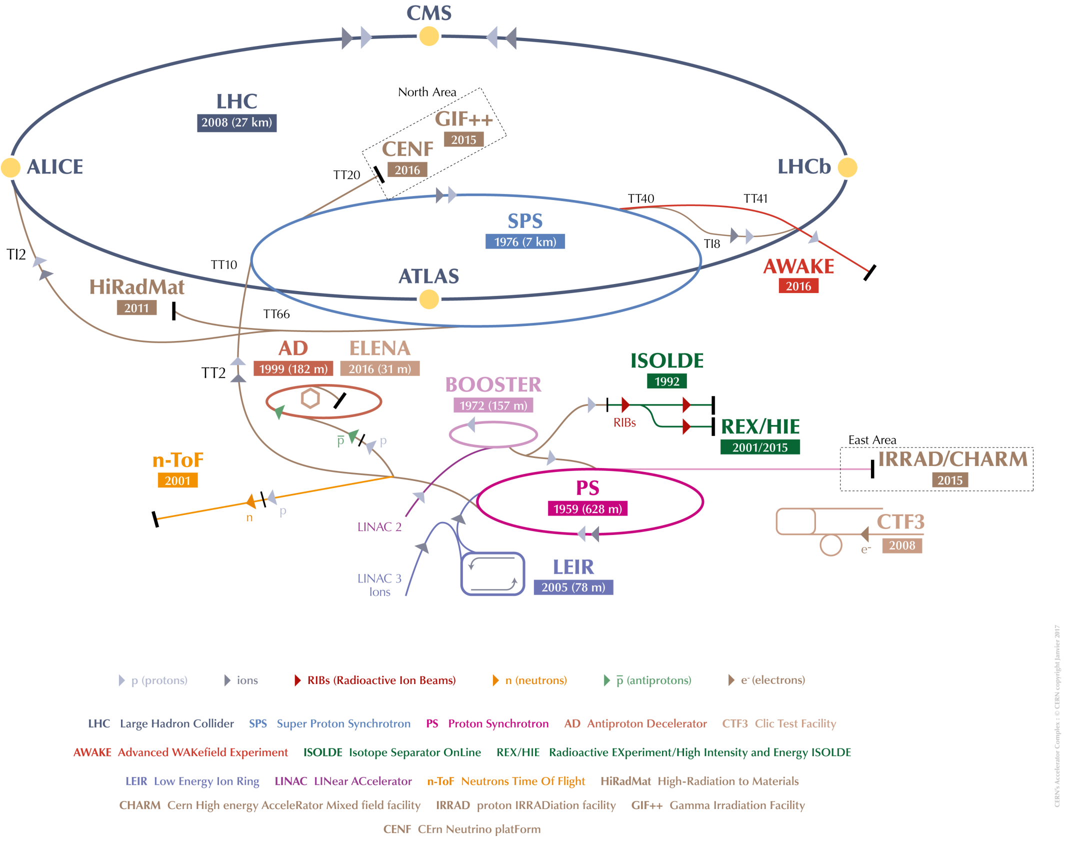

Figure 2.1: Overview of the CERN accelerator complex [164]. The LHC is the last in the complex injector chain of the CERN accelerators. See text for details.

large LHC experiment ALICE is located at IP 2 and is discussed in detail in the next Section. In addition, several smaller detectors complement the LHC physics program. Among these, the TOTEM (Total Elastic and Diffractive Cross Section Measurement) [168] experiment studies elastic and diffractive pp scattering and measures the total pp cross section. The detector system consists of several forward detectors placed up to 220 m on either side of IP 5. Similarly, the LHCf (Large Hadron Collider forward) [169] experiment has placed forward detectors at 140 m on either side of IP 1 with the aim to measure neutral particles to calibrate hadron interaction models employed in the study of high-energetic cosmic rays. Finally, the MoEDAL (Monopole and Exotics Detector at the LHC) [170] experiment is instrumented with largely passive detector material surrounding the intersection region at IP 8 and dedicated to the direct search for magnetic monopoles.

2.2 The ALICE Detector

The ALICE spectrometer [171–174] is located at the IP 2 of the LHC. The main goals of the ALICE collaboration are studies of the hot and dense phase of strongly interacting matter created in ultra-relativistic heavy-ion collisions [172]. The overall dimensions of the ALICE apparatus are $16 \times 16 \times 26\,\mathrm{m}^3$ with a total weight of about 10 000 t. The detector consists of a central system of sub-detectors for measurements at mid-rapidity covering the full azimuthal angle, a muon spectrometer, and multiple forward systems. A schematic view of the detector is shown in Fig. 2.2. The spectrometer is optimized to provide high-resolution tracking capabilities in high-multiplicity environments up to $\mathrm{d}N_{\mathrm{ch}}/\mathrm{d}\eta \approx 8000$ [172] at mid-rapidity. One unique feature of the ALICE experiment is its excellent particle identification (PID) capabilities down to low p_{T}.

In general, PID can be accomplished by either searching for unique decay patterns inherent to a particle, or by determining the particle mass via the relation

$$m = \sqrt{E^2 - p^2} = \frac{p}{\beta\gamma}, \tag{2.1}$$

where p corresponds to the momentum of the particle, E to its energy, β to its velocity, and $\gamma = 1/\sqrt{1-\beta^2}$. One method to determine the mass of the particle is by measuring its total energy in conjunction with its momentum. This kind of measurement is typically conducted using calorimeters, where the particles are fully stopped. The full energy of the particle is contained in, depending on the particle species, electromagnetic or hadronic showers. Accordingly, this is a destructive measurement, and calorimeters are usually located in the outer layers of a detector. On the other hand, multiple complementary techniques can be employed for PID via the

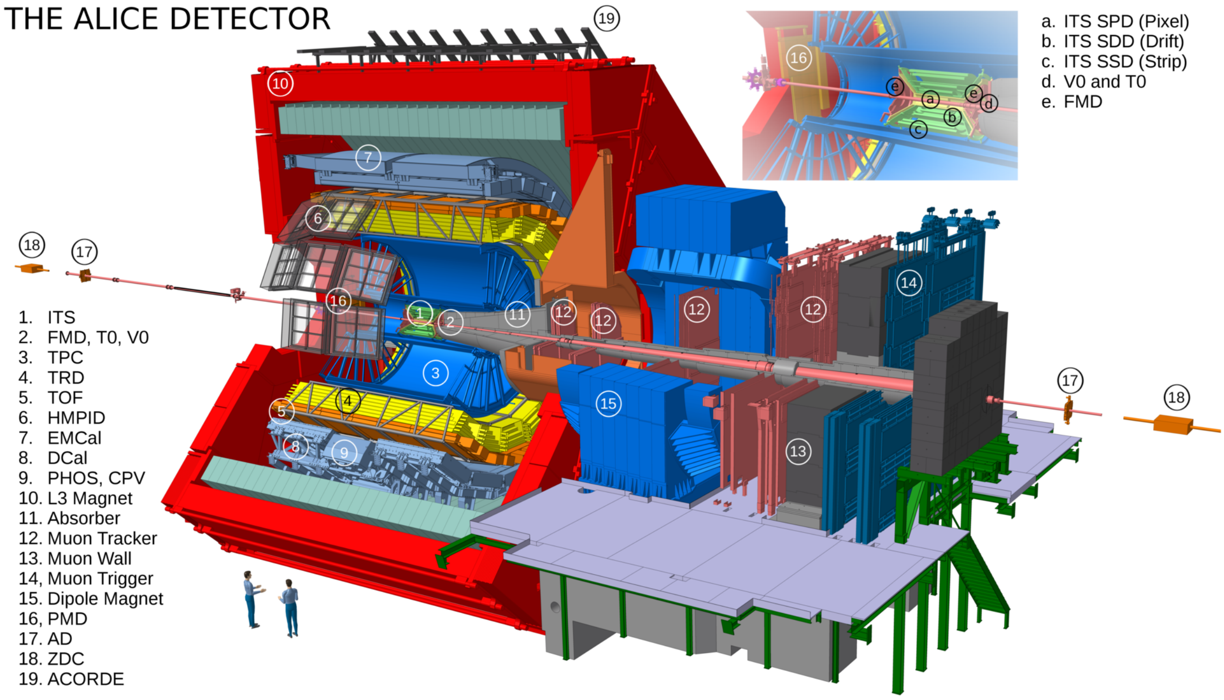

Figure 2.2: Schematic view of the ALICE spectrometer during the LHC Run 2 [149]. The inset shows a zoomed view of the sub-systems located around the nominal interaction point.

determination of the factor $\beta\gamma$ [175]. Commonly used methods comprise measurements of Cherenkov [176] and transition radiation [177]. The two following methods have been employed in this work

- The specific energy loss $\mathrm{d}E/\mathrm{d}x$ per unit path length for inelastic collisions of a charged particle traversing a medium is in a wide kinematic range given by the Bethe-Bloch equation [178, 179],

  $$\left\langle \frac{\mathrm{d}E}{\mathrm{d}x} \right\rangle = \frac{4\pi N e^4}{mc^2} \frac{1}{\beta^2} z^2 \left(\ln \frac{2mc^2}{I} \beta^2\gamma^2 - \beta^2 - \frac{\delta(\beta)}{2} \right), \tag{2.2}$$

  where mc^2 is the rest energy of the electron, z the charge of the incident particle, N the number density of electrons in the material traversed, e the elementary charge and I the mean excitation energy of the atom. The correction term $\delta(\beta)$ describes the *density effect* that leads to a shielding of the electric field of the incident particle by the electric polarization of the medium [180]. Notable is, that the mean energy loss depends on the velocity β of the incident particle, and not on its mass. Therefore, a measurement of the specific energy loss in conjunction with the particle momentum allows for particle identification. Exemplary measurements with several sub-systems of ALICE are discussed in the next Sections.

- Measuring the time of flight t of a particle along its trajectory of length L in conjunction with the particle momentum allows the mass computation via

  $$m = \frac{p}{c}\sqrt{\frac{c^2t^2}{L^2} - 1}. \tag{2.3}$$

Additionally, the decay pattern of certain particles can be exploited to obtain a unique identification. This includes the tagging of secondary decay vertices of charmed hadrons, weak decays of hyperons and photon conversions in the detector material. In some cases, a kinematic analysis of the decay children can lead to a unique particle identification in the Armenteros-Podolanski [181] space spanned by the longitudinal momentum asymmetry of positive and negative child tracks $\alpha = (p_L^+ - p_L^-)/(p_L^+ + p_L^-)$ and the transverse momentum component of the child momentum, p, with respect to the parent momentum $q_\mathrm{T} = p \sin\theta_{\mathrm{parent-child}}$.
For the case of of photon conversions, the opening angle of the decay children is negligible and accordingly $q_\mathrm{T} = 0$, which can well be observed in Fig. 2.3. Additionally, the decay children, electron and positron, are of the same mass, hence the distribution is symmetric in α. This is also the case for $\mathrm{K}^0_\mathrm{S} \rightarrow \pi^+\pi^-$, where due to the mass difference of the parent and the children the value of q_T is offset from zero. For the case of $\Lambda \rightarrow \pi^-\mathrm{p}$ the momenta are due to the mass difference of the decay children not split equally resulting in an asymmetric distribution in α. Hence, the particles can clearly be separated in a large part of the Armenteros-Podolanski space. ALICE is exploiting all of the above-mentioned concepts in its different sub-systems.

The so-called *central barrel* detectors of ALICE are immersed in the 0.5 T solenoidal magnetic field of the L3 magnet [182] and include, from the interaction point outwards, high-resolution silicon tracking detectors (Inner Tracking System), the main charged-particle tracking system of the apparatus, the Time Projection Chamber (TPC), a transition radiation detector (TRD) for pion/electron separation, and a time of flight detector array (TOF). Additionally, several sub-systems instrument a fraction of the space angle, in particular a Cherenkov detector (High Momentum Particle Identification Detector) extending the PID capabilities to larger p_T, and

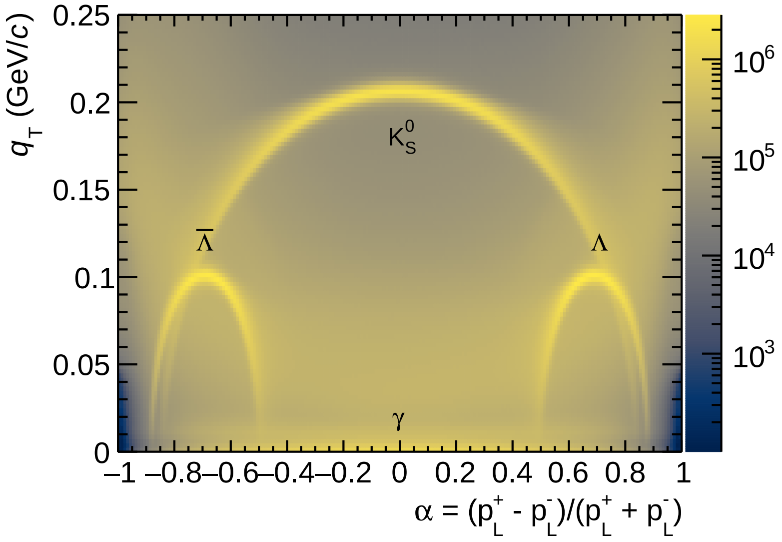

Figure 2.3: Armenteros-Podolanski distribution for weak decay and photon conversion candidates. In a large part of the phase space the individual contributions can be well separated.

several calorimeters optimized for studies of soft photons (PHOS) and jet physics (EMCal, DCal). The muon spectrometer is dedicated to measurements of quarkonia and light vector meson production at forward rapidity $-4.0 < y < -2.4$. It consists of five tracking stations with two pad chambers each (Muon Chambers), a hadron absorber of $\sim 10\,\lambda_{\mathrm{int}}$ and a dipole magnet of 3 Tm. Dedicated single-muon and muon-pair triggers are provided by two further stations (Muon Trigger) located behind an additional $7\,\lambda_{\mathrm{int}}$ absorber.

The Forward Multiplicity Detector (FMD) and the Photon Multiplicity Detector (PMD) are dedicated to the measurement of charged particles and photons in forward direction, respectively. Triggering and event characterization is conducted using the T0 and V0 system.

In the following, the sub-systems of ALICE relevant for this work are discussed.

2.2.1 The Inner Tracking System

The main tasks of the Inner Tracking System (ITS) [171] are the precise localization of the interaction vertex, the measurement of low p_{T} tracks, and the reconstruction of secondary vertices from the decay of short-lived hyperons, and charm and beauty mesons. It comprises six cylindrical layers of different types of lightweight silicon detectors that surround the beam pipe which is a 800 µm thin Beryllium cylinder with an outer radius of 3 cm. The active detector layers are located at radii ranging from 3.9 cm to 43.0 cm and are organized in three sub-systems, as depicted in the left panel of Fig. 2.4. Since for both the momentum and impact parameter resolution of low momentum particles multiple scattering contributes significantly, the material budget of the detector is minimized to 7.18% of a radiation length X_0[1] (7.26% including air), as depicted in the right panel of Fig. 2.4. Variations of the traversed material budget as a function of the azimuthal angle are well within the requirements.

The four outer detector layers (SDD and SSD) feature an analogue readout that allows the

---

[1] The radiation length X_0 is defined as both $7/9$ of the mean free path for pair production of a high energetic photon, and the mean distance over which a high energetic electron has lost all but $1/e$ of its energy via bremsstrahlung.

measurement of the specific energy loss dE/dx complementing the PID capabilities of the apparatus especially at low p_{T}.

Silicon Pixel Detector (SPD) The innermost part is the SPD [183], optimized for robust tracking and vertex reconstruction capabilities in a high particle-density environment of up to 50 particles/cm^2. Two detector layers located at $r = 3.9$ cm and 7.6 cm hold the highly granular silicon sensors. The detector comprises a total of about 9.8×10^6 individual reverse-biased silicon detector diodes with a size of 50 µm ($r\varphi$) by 425 µm (z) each. The pixel size is driving the spatial resolution of 12 µm ($r\varphi$) and 100 µm (z). The readout time is 300 ns corresponding to 12 LHC bunch crossings.

Silicon Drift Detector (SDD) The SDD features two detector layers at $r = 15.0$ cm and 23.9 cm [183]. The sensitive detector area is divided into two drift regions by a central cathode. The ionization electrons created by the incident particle move in opposite directions under the applied drift field. The front-end electronics are mounted on either side providing the position along the drift coordinate ($r\varphi$) by measuring the drift time with respect to the trigger. The z coordinate is obtained by computing the centroid of the collected charge along the anodes. The spatial resolution is 35 µm ($r\varphi$) and 25 µm (z), and the overall readout time due to the electron drift 6.4 µs.

Silicon Strip Detector (SSD) The two layers of the SSD at $r = 38$ cm and $r = 43$ cm [183] are essential for the matching of the measured tracks from the TPC to the ITS. The SDD comprises double-sided silicon detectors with 768 strips on each side with a pitch of 95 µm. The sensors are mounted with the strips in parallel to the z axis. The strip pitch and the charge-sharing among neighboring strips drive the spatial resolution of 27 µm ($r\varphi$) and 830 µm (z). The readout time of the SSD is about 1 µs.

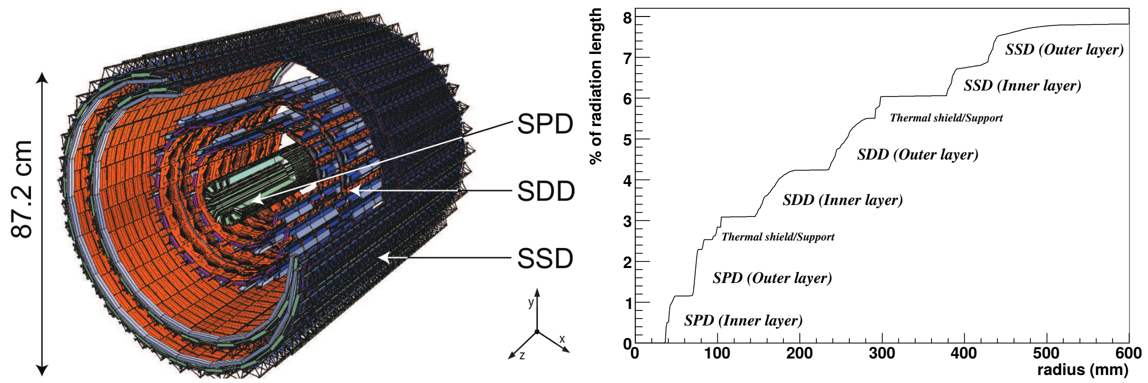

Figure 2.4: Schematic view of the ALICE ITS (*left*) [183] and the integrated material budget as a function of the transverse radius (*right*) [171].

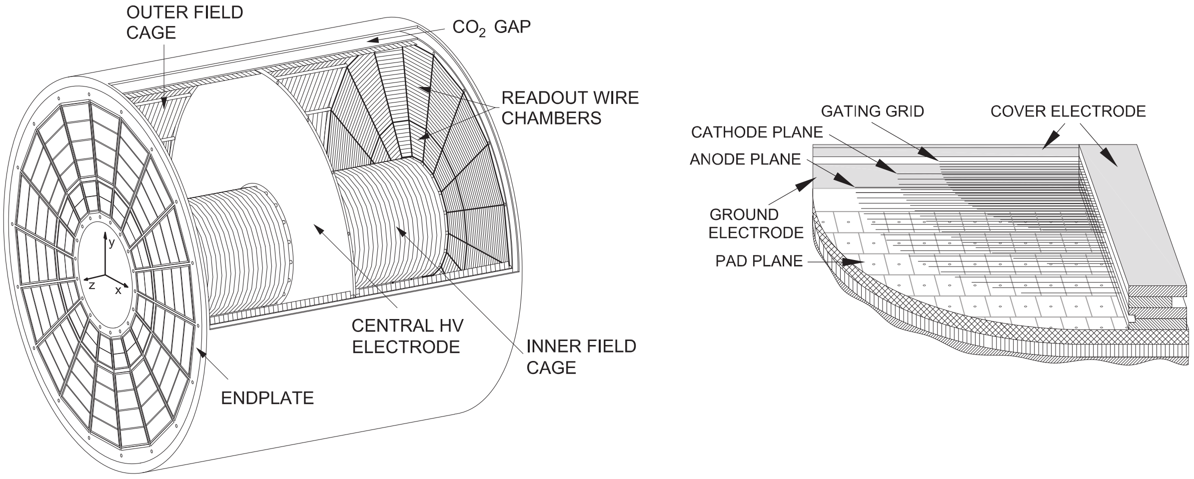

Figure 2.5: Schematic view of the ALICE TPC [184] (*left*). The active detector volume is divided by the high voltage electrode located at its center. The endplates are segmented into 18 sectors and 36 readout chambers on each side. Each readout chamber is equipped with a pad plane and multiple wire planes for electron amplification and ion blocking (*right*) [184].

2.2.2 The Time Projection Chamber

The main device for tracking and particle identification in the ALICE central barrel is a large TPC [184, 185]. Details of the physics processes relevant for the signal formation are discussed in Sec. 5.1, whereas a general overview is given in the following. The active volume of the detector is a cylindrical vessel with a inner (outer) radius of 84.8 cm (246.6 cm) that extends 500 cm along the beam direction with the IP in its center. Accordingly, the TPC covers the full azimuth and pseudorapidity $|\eta| < 0.9$ for tracks radially fully contained within. The detector volume is filled with the active detection medium, Ar-CO$_2$ (88-12) in 2016 and 2018, and Ne-CO$_2$-N$_2$ (90-10-5) in 2017, and divided into two halves by the central cathode, as depicted in the left panel of Fig. 2.5. Together with a lightweight field cage, the cathode defines a homogeneous drift field of 400 V/cm. Ionization electrons liberated by the incident particles from the primordial collision and the constituents of the detector gas drift in this field towards the readout chamber located on either side of the TPC, while the ions drift towards the central electrode. The maximal drift time of the electrons defines the integration time of the detector of about 100 μs with a slight dependence on the gas mixture. The total yield of ionization electrons is typically of the order of $30 - 40\,\mathrm{e}^-/\mathrm{cm}$ per minimum ionizing particle (MIP), and therefore too low to obtain a detectable signal. For this reason, charge amplification has to occur on the endplates on both sides of the TPC. The endplates are segmented into 18 sectors in φ, where one sector is subdivided into Inner (IROC) and Outer (OROC) ReadOut Chamber due the different requirements as a function of the track density which is trivially reduced for larger radii. Multi-Wire Proportional Chambers (MWPC) [186] with cathode pad readout operated at typical gains ranging from 7000 to 8000 were employed for charge amplification in the ALICE TPC during Run 1 and Run 2 of the LHC. As depicted in the right panel of Fig. 2.5 the readout chambers feature a segmented cathode pad plane above which the anode wire plane, where the charge amplification occurs, is mounted. The following cathode wire plane separates the drift volume from the amplification region and neutralizes a large fraction of the ions produced in the avalanche amplification at the anode wires. This is particularly important since ions penetrating the active detection medium accumulate as space charge due to their low mobility and accordingly cause distortions of the drift field. In order to further suppress ion leakage from the amplification region an additional wire plane is introduced – the gating grid. Upon a L1 trigger (6.5 µs after the collision, see Sec. 2.2.5) the gating grid is opened and thus transparent for incoming ionization electrons from the drift volume. After one full drift time of 100 µs the gating grid is closed in order to electrically separate the amplification region from the drift volume. Accordingly, no ionization electrons can enter the amplification region, and no ions escape from it. In this way, the ions created in the amplification process that were not collected at the cathode wires are neutralized. With a closure time of about 200 µs the overall ion leakage to the active detector volume is reduced to a level of $\mathcal{O}(10^{-4})$ [171]. On the other hand, the overall turnover time of about 300 µs leads to a rate limitation of few kHz for the TPC with the present readout system.

The readout plane is of one sector is organized in 159 pad rows, and for the whole detector amounts to 557,568 channels covering a total area of about 32.4 m^2. This enables a projective measurement of the particle trajectory in the xy plane. Since additionally the drift velocity in the detector medium and the time of the initial collision is well known, the z-component of the trajectory can be inferred and therefore the TPC provides a three-dimensional measurement of the flight path of the particle.

As discussed above, a TPC can perform particle identification via a measurement of the specific energy loss dE/dx which can be related to $\beta\gamma$ via the Bethe-Bloch formula [178, 179]. The corresponding measurement of the specific energy loss as a function of the momentum with the ALICE TPC is shown in Fig. 2.6 and demonstrates the performance of the system which allows particle identification on a track-by track basis in a wide kinematic range. The lines correspond to a parametrization of the Bethe-Bloch formula by a function initially proposed by the ALEPH collaboration [179],

$$f(\beta\gamma) = \frac{P_1}{\beta^{P_4}} \cdot \left\{ P_2 - \beta^{P_4} - \ln\left[P_3 + \frac{1}{(\beta\gamma)^{P_5}} \right] \right\}, \tag{2.4}$$

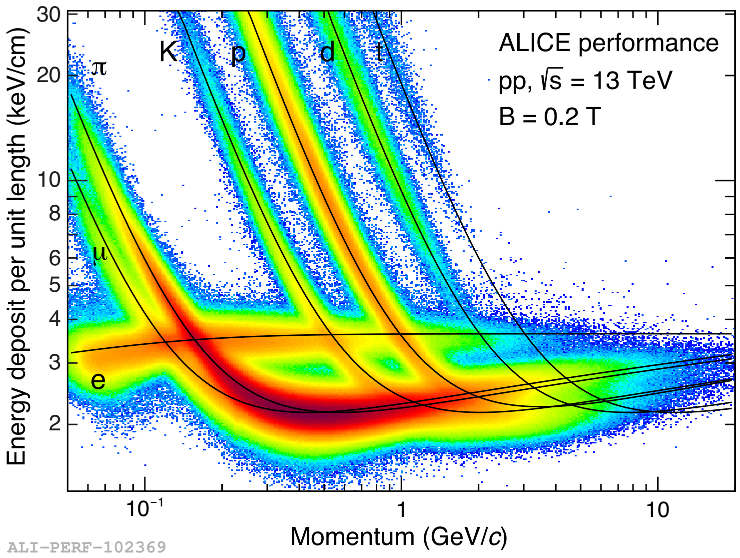

Figure 2.6: Specific energy loss dE/dx measured with the TPC at a reduced magnetic field of 0.2 T as a function of the momentum of the incident particle measured in pp collisions at $\sqrt{s} = 13$ TeV [149].

where P_i are parameters obtained from a fit to data. The $\mathrm{d}E/\mathrm{d}x$ resolution of the ALICE TPC features a modest dependence on the occupancy due to the increasing cluster overlap and slightly worsens from about 5.2% in isolated pp collisions to about 6.5% in central Pb–Pb collisions [174].

2.2.3 The Time Of Flight Detector

The Time Of Flight sub-system (TOF) [187] extends the reach of particle identification in the central barrel towards intermediate momenta by using a complementary technique with respect to the measurement of the specific ionization energy loss in ITS and TPC. Measuring the arrival time of the particles in conjunction with the time of the initial collision allows one to infer the time of flight and thus directly determine β as discussed above. The TOF array is positioned at radii from 370 cm to 399 cm from the beam axis covering pseudorapidity $|\eta| < 0.9$, the full azimuth, and an active area of 141 m^2. The rather large transverse distance from the IP introduces in combination with the nominal magnetic field of 0.5 T a rigidity cutoff at about 300 MeV/c. The detector is composed of in total 1593 Multi-gap Resistive Plate Chambers (MRPC) [188, 189], that each provide a sensitive area of $7.4 \times 120\,\mathrm{cm}^2$. With a pad size of $2.5 \times 3.5\,\mathrm{cm}^2$ this amounts to 152,928 electronic channels in total. The MRPC technology is based on a parallel-plate chamber design where the drift gap is subdivided by inserting multiple, electrically floating, resistive plates. High voltage applied across the drift gap generates a high, uniform electric field in which ionization charges produced by traversing charged particles is amplified. Due to the insertion of the resistive plates, however, the charge drift in the intermediate gaps is severely restricted, which significantly reduces the time jitter and thus improves the resolution of the detector. The TOF array of ALICE provides a time resolution of ∼80 ps [174] with a modest multiplicity dependence, as depicted in the right panel of Fig. 2.7. The resulting β distribution is shown in the left panel of Fig. 2.7 and demonstrates how the TOF detector extends the separation power among different particle species to intermediate momenta. The readout time of TOF is 500 ns, corresponding to 20 LHC bunch crossings.

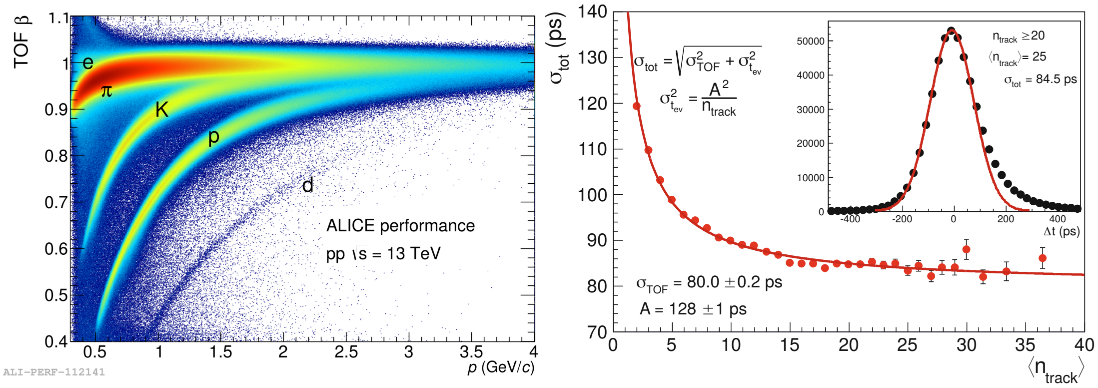

Figure 2.7: Velocity β measured with TOF as a function of the momentum of the incident particle p in pp collisions at $\sqrt{s} = 13$ TeV [149] (*left*), and the corresponding TOF time resolution for charged π tracks with $0.95 < p < 1.05\,\mathrm{GeV}/c$ employed to define the start time of the event t_{ev} [187] (*right*).

2.2.4 Trigger Detectors

ALICE features multiple detectors at forward direction, that are mainly used to obtain a trigger signal and to measure event characteristics such as the centrality in p–Pb and Pb–Pb collisions. Additionally, these detectors extend the reach of the measurement of particle multiplicities beyond that of the central barrel. In the following, two relevant sub-systems are discussed.

V0 The V0 [190] detector consists of two plastic-scintillator arrays, V0A and V0C, placed on both sides of the IP. The V0A is located at $z = 3.29\,\mathrm{m}$ from the nominal vertex position and covers the pseudorapidity $2.8 < \eta < 5.1$. Due to the space constraints imposed by the hadronic absorber, the V0C is placed at $z = -0.88\,\mathrm{m}$ and covers $-3.7 < \eta < -1.7$. The sum of the measured signal amplitude in both detectors is referred to as V0M and is a proxy of the charged-particle multiplicity. As discussed in Sec. 2.2.5, the V0 contributes to the trigger scheme of ALICE. Additionally, the V0 is employed for the measurement of the luminosity during the so-called *Van Der Meer* scans [191]. Exploiting the time difference of signals detected in both detectors, interactions of the beams with residual gas in the beam pipe, or with mechanical structures of the beam line can be efficiently rejected as demonstrated in Fig. 2.8.

T0 The T0 [192] detector comprises two arrays of Cherenkov counters with a quartz radiator, called T0A and T0C, that are located on either sides of the IP. The T0A is placed at at $z = 3.75\,\mathrm{m}$ and covers the pseudorapidity range of $4.61 < \eta < 4.92$, while the T0C is located at $z = -0.727\,\mathrm{m}$ and covers $-3.28 < \eta < -2.97$. The detectors are mounted as close as feasible in radial direction to the beam pipe to maximize the trigger efficiency. Accordingly, the T0 can provide a trigger signal redundant to that of the V0. Its main task, however, is to provide the start time t_0 for the TOF detector. Depending on the multiplicity of the event, the measured time resolution for single events ranges between 50 ps at low and 25 ps at high multiplicities.

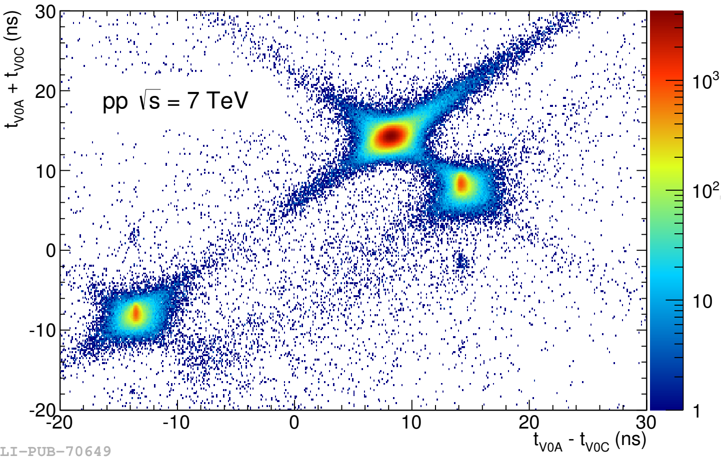

Figure 2.8: Correlation between the sum and difference of signal times in V0A and V0C [174]. Genuine beam–beam collisions (8.3 ns, 14.3 ns) can clearly be differentiated from background from beam 1 (−14.3 ns, −8.3 ns) and beam 2 (14.3 ns, 8.3 ns).

2.2.5 Data Taking and Operation during LHC Run 2

The data employed in this work was collected during the Run 2 of the LHC, after the long shutdown one (LS1) during which major consolidation works on the accelerator were conducted. This enabled an almost twofold increase of the center of mass energy for pp collisions from $\sqrt{s} = 7$ TeV in Run 1 (2009–2013) to $\sqrt{s} = 13$ TeV, at a tighter bunch spacing of 25 ns and an accordingly increased instantaneous luminosity of up to $\mathcal{L} = 2 \times 10^{34}\,\mathrm{cm}^{-2}\,\mathrm{s}^{-1}$ [163, 193]. For ALICE, the transition from Run 1 to Run 2 marked in particular the installation of the remaining five super modules of the TRD and an extension of the geometrical acceptance of the calorimeters.

The first year of pp collisions during the Run 2 was characterized by rather low interaction rates of $\mathcal{O}(10\,\mathrm{kHz})$. Due to the resulting low yield this data set is not considered in this work. Figure 2.9 shows a summary of the data taking conditions of ALICE in pp collisions at $\sqrt{s} = 13$ TeV during 2016–2018. In order to provide interaction rates suited for the running conditions of ALICE [174] and in particular for the gated operation of the TPC, the instantaneous luminosity in pp collisions is adjusted (*leveled*). A reduction of the instantaneous luminosity can be achieved by optimizing *i*) the number of colliding bunches, *ii*) the value of the β^* which is related to the transverse size of the particle beam at the IP, and *iii*) a wide geometrical separation of the two intersecting beams. Accordingly, the probability of an inelastic pp collision upon a bunch crossing μ is very low. These beam conditions typically result in interaction rates not exceeding 250 kHz. The beginning of each year is characterized by a gradual increase of the number of colliding bunches. The mitigation of beam losses in the 16L2 section of the LHC between ALICE and ATLAS required a modified filling scheme during the second half of 2017 allowing for fewer bunches stored in the accelerator [193, 194]. A warm-up of the LHC sector 1–2 to room temperature and an improved filling scheme lead to a significant increase of the number of colliding bunches in 2018.

The ALICE data taking scheme is based on multiple trigger classes, aiming at inspecting simultaneously vastly different observables ranging from jet physics with the calorimeters to single and di-muon physics with the MUON arm. All detectors with fast trigger capabilities contribute input to the hardware trigger (T0, V0, SPD, TOF, TRD, PHOS, EMCal, MCH, MTR, and ACORDE) [171]. Depending on the trigger type, different combinations and observables from these inputs are employed. These information are collected and inspected by the Central Trigger Processor (CTP) from which the trigger decision is distributed to all sub-systems. Three levels of hierarchical hardware triggers are issued to consider the timing requirements of the different detectors – level zero (L0, 0.9 µs after the collision), one (L1, 6.5 µs) and two (L2). Only upon a L2 trigger after the end of the drift time in the TPC, at about 100 µs, the detectors are read out and the event is sent to the Data Acquisition (DAQ) and the High Level Trigger (HLT) for event building and data compression.

The unique capability of the ALICE central barrel detectors to measure particles at low p_{T} motivates the data taking with a so-called *minimum bias* trigger (`kINT7`) aiming at reading out all inelastic pp collisions without introducing a significant selection bias. This is particularly important since traditional trigger strategies cannot be employed at low p_{T}. The trigger requires coincident hits in both V0 detectors synchronous with the LHC bunch crossing time. In order to inspect collective phenomena in small systems, a significant fraction of the data taking of ALICE in Run 2 was dedicated to a *high-multiplicity* trigger (`kHighMultV0`). This trigger additionally requires the sum of the measured signal amplitudes in both V0 (V0M) to exceed a threshold defined as a multiple of the average value in the case of minimum bias, which was typically at around $5 \cdot \langle \mathrm{V0M} \rangle$. Accordingly, the multiplicity range with respect to the minimum bias trigger

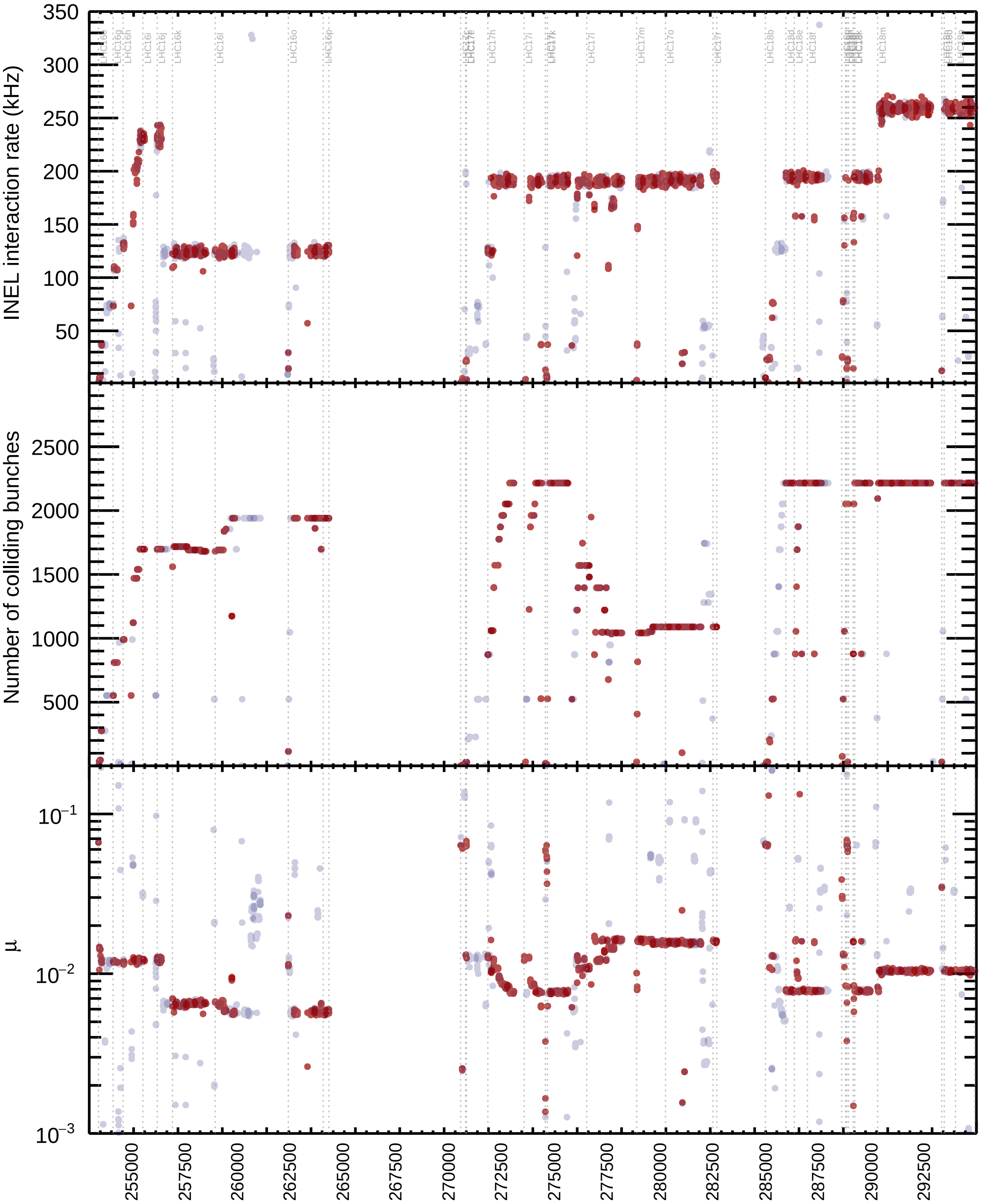

Figure 2.9: ALICE data taking conditions in pp collisions at $\sqrt{s} = 13$ TeV as a function of the run number during 2016–2018. The top panel shows the inelastic interaction rate, the middle panel the number of colliding bunches stored inside the LHC and the bottom panel the mean number of inelastic pp collisions per bunch crossing. The vertical lines indicate the limits of the so-called LHC periods of the ALICE experiment – periods in time of stable accelerator and detector conditions. Runs considered as good for analysis are denoted by the red markers, while the remaining runs are shows in blue. Breaks between different periods are due to running at a different beam composition (p–Pb, Xe–Xe or Pb–Pb), or energy. Obtained using data from Ref. [195].

is significantly enhanced, as illustrated in the left panel of Fig. 2.10. This can be translated to the highest 0.17% multiplicity interval with respect to all inelastic collisions with at least one charged particle in $|\eta| < 1$ (INEL > 0).

The collected integrated luminosity of all relevant triggers of ALICE is shown in the right panel of Fig. 2.10, and demonstrates that a significant fraction of high-multiplicity events has been collected in pp collisions during the data taking periods from 2016–2018.

2.2.6 Data Reconstruction and Analysis

After the data taking of a run has finished, the compressed raw data are shipped to permanent storage. Further processing is conducted asynchronously with the data taking by the ALICE offline framework AliRoot [196]. AliRoot is based on the ROOT [197] software, and is responsible for handling all relevant tasks for the preparation of the data for analysis such as simulation, reconstruction, calibration, alignment and visualisation.

In order to compare the measured quantities to different Monte Carlo (MC) event generators, and assess e.g. reconstruction efficiencies, full-scale simulations are filtered through the detector and the reconstruction algorithms. The modularity of the framework makes it possible to employ various event generators, such as different versions of PYTHIA [198–201] for pp, DPMJET [202] for p–Pb and HIJING [203] for Pb–Pb collisions. The EPOS event generator [204] can be used for all systems. These generators simulate the particle collision and provide the kinematic information of the outgoing particles. These are then filtered through the detector using transport codes such as GEANT3 [205] or GEANT4 [206], which simulate the energy deposit of the traversing particles in the individual detectors, the so-called *hits*. Within AliRoot, also the signal formation and processing in the corresponding sub-systems is simulated, resulting in *digits* that are equivalent to the output of the front-end electronics of the detector. From then on, the simulated data is processed and reconstructed in the same way as real raw data.

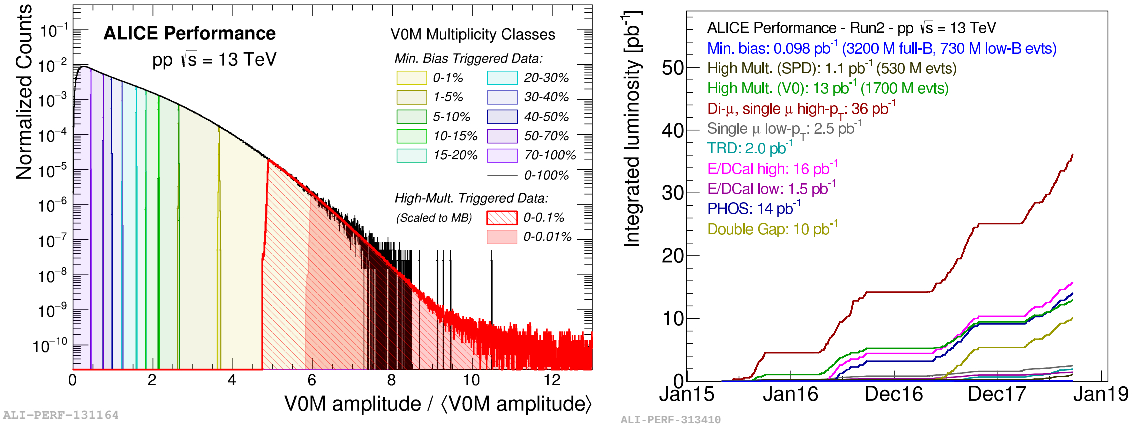

Figure 2.10: (*Left*) The V0M/⟨V0M⟩ distributions measured in pp collisions at $\sqrt{s} = 13$ TeV compared between the minimum bias (`kINT7`) and high-multiplicity trigger (`kHighMultV0`) [149]. The distributions for the high-multiplicity trigger is scaled to the corresponding fraction in minimum bias. (*Right*) Integrated luminosity for various triggers in pp collisions at $\sqrt{s} = 13$ TeV during Run 2 [149].

The reconstruction of the raw data starts by combining adjacent digits in time and space to so-called *clusters* for each sub-system individually. The tracking starts by a preliminary determination of the interaction vertex with the SPD [174]. The strategy for track finding is thoroughly described in Refs. [171, 174, 207] and based on a Kalman filter [208]. The track finding starts in the outermost pad row of the TPC in the inward direction and is conducted with and without a constraint to the primary vertex. The such found tracks are labelled as *TPC-only* tracks. The tracks are propagated to the ITS, and subsequently refitted outwards using also the information of the outer detectors, such as TOF. Finally, the tracks are refitted inwards, resulting in *global* tracks. The interaction vertex is additionally determined using the information of global tracks. As shown in Fig. 2.11, already with the vertex constraint on TPC-only tracks a p_{T}-resolution compatible with that of global tracks is achieved up to transverse momenta $p_{\mathrm{T}} \approx 10\,\mathrm{GeV}/c$.

After the track finding procedure is accomplished, a search for secondary vertices from weak decays and photon conversion begins, as described in Refs. [173, 174]. Topological selections, as sketched in Fig. 2.12, serve to eliminate combinatorial background. In order to suppress the contribution from primary tracks, a minimal Distance of Closest Approach (DCA) with respect to the interaction vertex of 0.5 mm (1 mm) in pp (Pb–Pb) is required [174]. From this sample of tracks, unlike-sign combinations are constructed, the so-called V^0 candidates. The distance between the two child tracks at their point of closest approach (PCA) is requested to be smaller than 1.5 cm and the reconstructed secondary decay vertex, the PCA, is requested to be closer to the primary vertex than the innermost hit of any of the child tracks. Finally, the Cosine of the Pointing Angle (CPA) between the V^0 momentum and the vector pointing from the vertex to the decay vertex is required to be CPA > 0.9, which is relaxed for candidates with $p_{\mathrm{T}} < 1.5\,\mathrm{GeV}/c$. A similar procedure is conducted to find cascade-like decays of Ξ^- and Ω^- candidates [173, 174]. Two different implementations of V^0 finding algorithms are employed in ALICE during the data processing. At first, V^0 candidates are reconstructed during the tracking procedure (*on-fly*), where the full information about the cluster positions is still available. Accordingly, the tracks can be

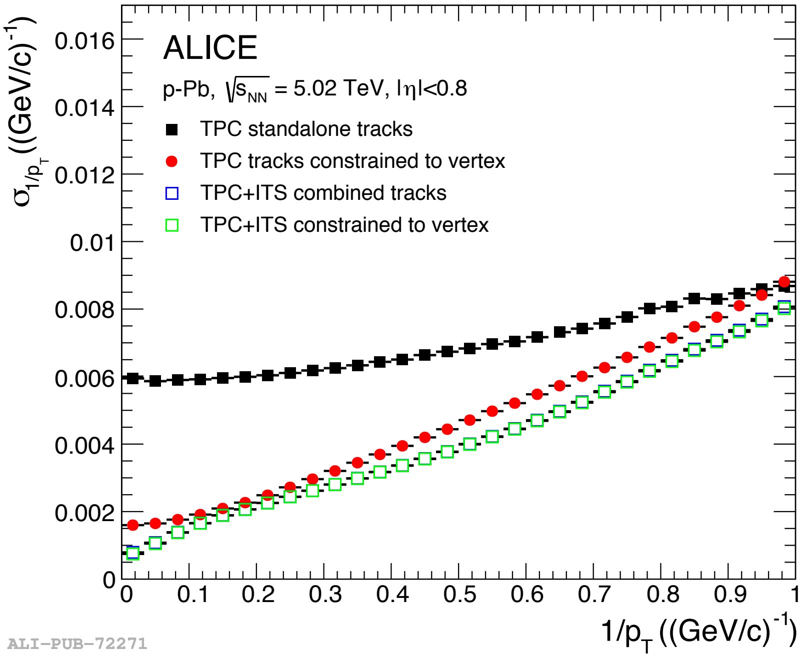

Figure 2.11: The p_{T} resolution of standalone TPC and ITS–TPC matched tracks [174].

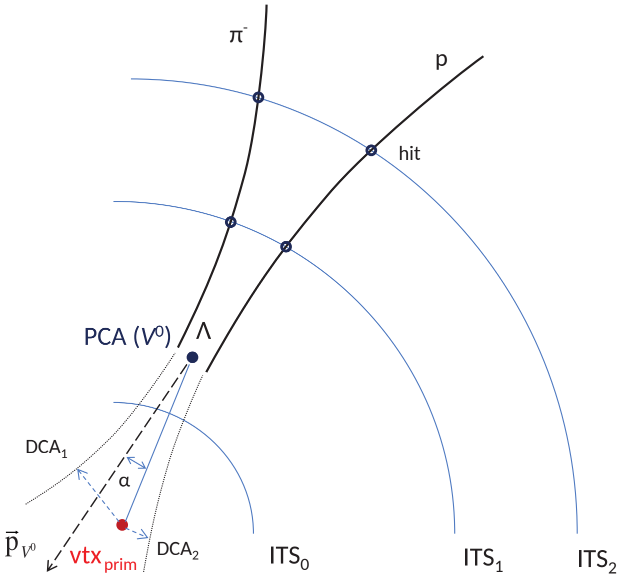

Figure 2.12: Illustration of the secondary vertex reconstruction exemplary showing the weak decay of a Λ (modified from Ref. [174]). Reconstructed charged particle tracks as shown as solid lines, while extrapolations to the primary vertex and auxiliary vectors are depicted as dashed lines.

refitted considering the position of the secondary decay vertex, which improves the precision and invariant mass resolution of the V^0 candidates. The *offline* V^0 finder, on the other hand, uses fully reconstructed tracks as input, and for this reason can be re-run anytime.

The such obtained entities, such as tracks and V^0 candidates, are then stored in Event Summary Data (ESD) files. A further filtering removes information not relevant for most analyses. The resulting data are stored in Analysis Object Data (AOD) files. In order to further reduce the data size, and accordingly the turnover time of the analysis, only the information relevant for individual sub-groups of analyses, such as for femtoscopy, is stored in so-called NanoAODs. The final data analysis is then conducted using the AliPhysics [209] framework.

2.3 The Upgrade of the ALICE Experiment beyond LHC Run 2

The heavy-ion program of the LHC during Run 3 (2021–2023) and Run 4 (2026–2029) foresees running at instantaneous luminosities of $\mathcal{L} = 6 \times 10^{27}\,\mathrm{cm}^{-2}\,\mathrm{s}^{-1}$ in Pb–Pb. This corresponds to interaction rates of about 50 kHz which is beyond the rate limitations of some of the sub-systems of ALICE. Therefore, a dedicated upgrade campaign is currently taking place during the Long Shutdown 2 (LS2, 2019–2021) [210].

The main physics goals of the ALICE heavy-ion campaign beyond Run 2 focus on rare probes and the study of their coupling with the medium and hadronisation processes [210], such as precise measurements of heavy flavour hadrons, low-momentum quarkonia and low mass di-leptons. Since these probes involve soft momentum scales and are characterised by small signal-to-background ratios, accumulation of large data samples are required. In addition, the concept of dedicated triggering cannot be applied. Therefore, the current strategy foresees the collection of all Pb–Pb collisions at $\sqrt{s_{\mathrm{NN}}} = 5.5$ TeV, i.e. accumulating in total $13\,\mathrm{nb}^{-1}$ [211]. In addition, a pp reference sample of $6\,\mathrm{pb}^{-1}$ at $\sqrt{s} = 5.5$ TeV will be collected, and $200\,\mathrm{pb}^{-1}$ at $\sqrt{s} = 14$ TeV with high-multiplicity triggers.

The most important ingredients of the upgrade are listed below and are essentially based on *i*) improving the tracking resolution, *ii*) increasing the readout rate, while *iii*) consolidating the PID performance. A schematic overview of the upgraded ALICE apparatus is shown in Fig. 2.13.

- The new ITS [212] consists of seven layers of Monolithic Active Pixel Sensors, in particular improving the material budget of the first three layers from 1.1% to 0.3% X_0. The first layer is significantly closer to the beam pipe – 23 mm instead of 39 mm in Run 1 and Run 2. Notably, this is expected to increase the transverse impact parameter resolution by about a factor of three.
- The gated readout of the TPC implies rate limitation of few kHz which are not compatible with the running scenario. Additionally, the typical electron drift time of about 100 μs at

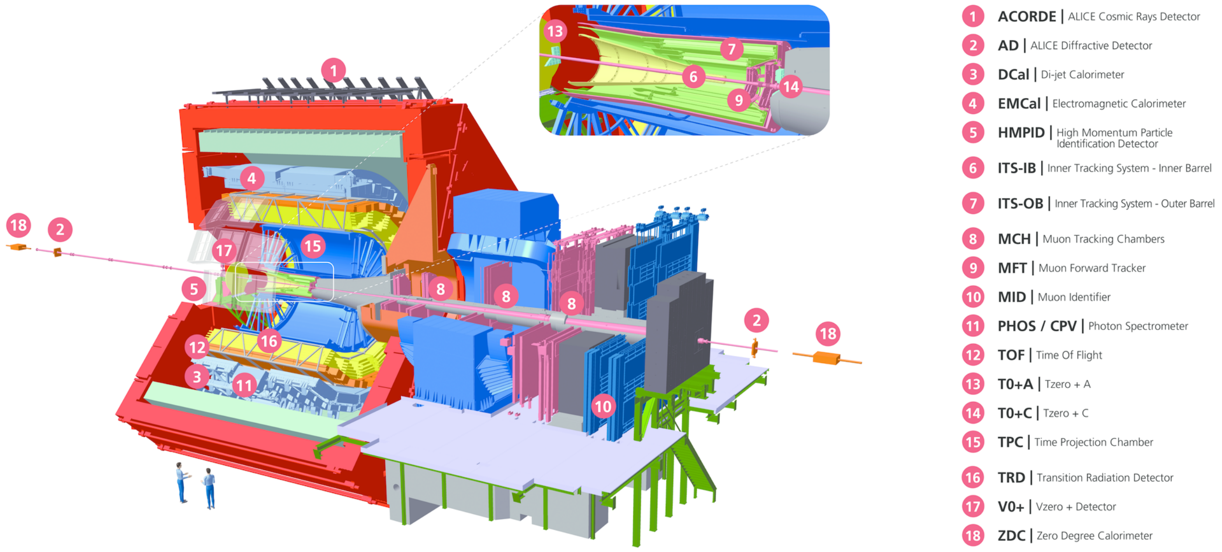

Figure 2.13: Schematic view of the ALICE spectrometer in the LHC Run 3 [149]. The inset shows a zoomed view of the sub-systems located around the nominal interaction point.

interaction rates of 50 kHz implies an average event pile-up of five within the active volume of the TPC, prohibiting the usage of gating structures. Therefore, the upgraded readout chambers [213–215] are based on the Gas Electron Multiplier (GEM) [216]. This enables ungated, continuous readout while retaining the current tracking and PID capabilities of the apparatus. Details of the TPC upgrade are discussed in Sec. 4.

- Continuous data taking at 50 kHz in Pb–Pb collisions results in data rates exceeding those from Run 1 and Run 2 by several orders of magnitude. The data processing relies on synchronous reconstruction of the data, therefore dissolving the separation between the current online/offline data handling with asynchronous reconstruction of the data, and the integration of both into a new common system called O^2 [217–219]. An outline of the data flow is discussed in Sec. 4.2.4.

3 Investigation of the Proton–Σ^0 Interaction via the Femtoscopy Method

This Chapter describes the first direct measurement of the p–Σ^0 interaction via the femtoscopy method in pp collisions, as published in Ref. [220]. The most important analysis steps and the interpretation of the data are reviewed. The p–p correlation function is extracted from the data and employed to constrain the particle-emitting source. A detailed study of the p–Σ^0 correlation function is conducted and the data are compared to several theoretical models describing the interaction.

3.1 Data Set and Event Selection

The analysis is conducted employing the pp data sample collected at $\sqrt{s} = 13$ TeV by ALICE during the LHC Run 2. The data are reconstructed as outlined in Sec. 2.2.6, and filtered from the ESD data format to AODs and subsequently to NanoAODs produced for femtoscopic analyses. The data sample employed for this work was collected with a high-multiplicity trigger based on the measured signal amplitudes in the V0 detectors (`kHighMultV0`), as discussed in Sec. 2.2.4. At the analysis level, this corresponds to the highest multiplicity interval containing the top 0.17% of all inelastic collisions with at least one charged particle in $|\eta| < 1$ (referred to as INEL > 0). As mentioned above, only the data from 2016–2018 are used due to the low interaction rates and the lack of a high-multiplicity trigger in 2015.

This data set represents a good environment for femtoscopic studies since the larger charged-particle multiplicity significantly increases the probability to detect particle pairs. Additionally, in such events the production of strange particles is enhanced with respect to low multiplicity events [221], therefore resulting in larger yields of the particles of interest, such as the Σ^0.

In order to ensure the integrity of the collected data, several event selection criteria are imposed as depicted in Table 3.1. Background events stemming from the interaction of beam particles with residual gas in the beam line, or with mechanical structures of the latter are suppressed using timing measurement with the V0 detectors [190]. Multiple inelastic pp interactions within a single bunch crossing are rejected by evaluating the presence of additional event vertices [174], with an upper limit of 1.4% for the residual pile-up contamination of the sample.

As discussed in Sec. 2.2.6, the primary vertex (PV) is reconstructed employing two different approaches using the SPD standalone, and with the combined global track information. In case both vertex reconstruction methods yield a vertex candidate with a sufficient number of tracks pointing to it, the difference among the corresponding z-coordinates is required to be smaller than 5 mm. Poorly reconstructed SPD vertices are rejected by demanding that their resolution, obtained from the covariance matrix, is better than 0.25 cm. The maximal deviation between the reconstructed PV and the nominal interaction point in the center of the detector is required to be smaller than 10 cm to ensure a uniform detector coverage.

After application of these selection criteria, a total of 1.0×10^9 high-multiplicity events are used for the analysis.

Table 3.1: Event selection criteria.

Selection criterion	**Value**
Trigger	`kHighMultV0`
Physics selection	default
Incomplete DAQ	check
Contributors to track vertex	$N_{\mathrm{contrib,track}} > 1$
Contributors to SPD vertex	$N_{\mathrm{contrib,SPD}} > 0$
Distance between track and SPD vertex	$\Delta z_{\mathrm{vtx,track-SPD}} < 0.5\,\mathrm{cm}$
SPD vertex z resolution	$\sigma_{\mathrm{SPD},z} < 0.25\,\mathrm{cm}$
z-vertex	$\lvert vtx_z \rvert < 10\,\mathrm{cm}$

3.2 Proton Reconstruction

The proton candidates are selected among the reconstructed particles employing the unique PID capabilities of ALICE. In order to ensure the quality of the candidates in the sample, particle tracks which are poorly reconstructed or detector or reconstruction artefacts (*fakes*) need to be removed from the sample. The selection criteria follow the analysis methods employed for minimum bias pp collisions at $\sqrt{s} = 7$ TeV [128, 152] and $\sqrt{s} = 13$ TeV [153, 159], and are applied both for the proton and antiproton candidates. Therefore, in the following the term protons refers to both unless specified otherwise. All proton selection criteria are summarized in Table 3.2.

The candidates are selected among the charged particles in $\lvert\eta\rvert < 0.8$ reconstructed with the TPC (*TPC-only* tracks) and constrained to the PV. A selection on the number of assigned TPC clusters ensures that only tracks of proper quality and good p_{T} resolution are considered in the analysis. Tracks that share at least one cluster with another track are rejected. In order to reduce the contribution of secondary particles that were not produced in the primordial inelastic pp collision, a strict selection is imposed on the Distance of Closest Approach (DCA) to the PV, both in radial direction ($\mathrm{DCA}_{xy} < 0.1\,\mathrm{cm}$) and along the beam line ($\mathrm{DCA}_z < 0.2\,\mathrm{cm}$). Particles with a low transverse momentum have an increased probability to stem from interactions with the detector material and therefore only tracks with $p_{\mathrm{T}} > 0.5\,\mathrm{GeV}/c$ are accepted [222].

Table 3.2: Selection criteria for the proton candidates.

Selection criterion	**Value**
Transverse momentum	$0.5 < p_{\mathrm{T}} < 4.05\,\mathrm{GeV}/c$
Pseudorapidity	$\lvert\eta\rvert < 0.8$
TPC clusters	$n_{\mathrm{cluster}} > 80$
Findable TPC clusters	$n_{\mathrm{crossed}}/n_{\mathrm{findable}} > 0.83$
Tracks with shared TPC clusters	rejected
Distance of closest approach to PV	$\mathrm{DCA}_{xy} < 0.1\,\mathrm{cm}$ $\mathrm{DCA}_z < 0.2\,\mathrm{cm}$
Particle identification	$\lvert n_{\sigma,\mathrm{TPC}}\rvert < 3$ for $p < 0.75\,\mathrm{GeV}/c$ $\sqrt{n^2_{\sigma,\mathrm{TPC}} + n^2_{\sigma,\mathrm{TOF}}} < 3$ for $p > 0.75\,\mathrm{GeV}/c$

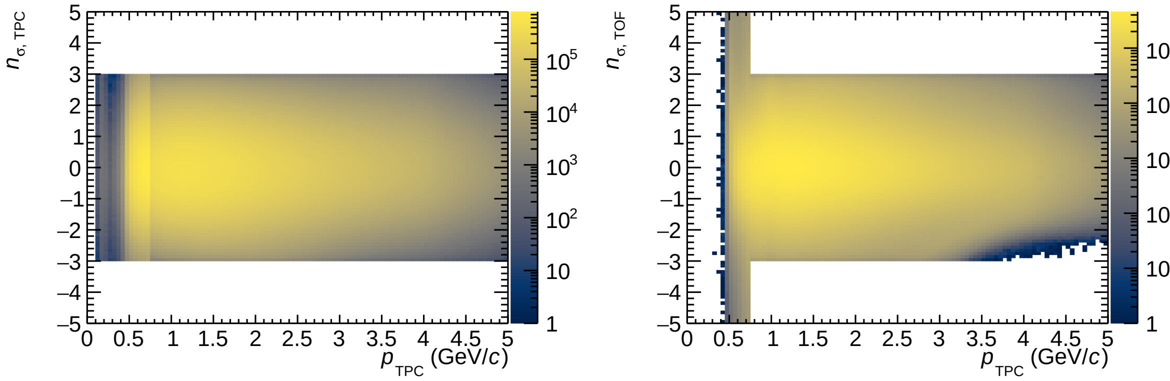

Figure 3.1: The proton n_σ distributions in the TPC (*left*) and TOF (*right*).

The resolution of the detector PID response depends on the p_{T} of the particle and is related to effects of the intrinsic detector resolution. In order to obtain a p_{T}-independent observable, the deviation between the signal hypothesis for a given particle species i, $\mu_{\mathrm{expected},i}$, and the experimental measurement μ_{measured} is calculated and normalized by the detector resolution σ,

$$n_{\sigma,\,i} = \frac{\mu_{\mathrm{measured}} - \mu_{\mathrm{expected},i}}{\sigma}. \tag{3.1}$$

The expected PID response is computed employing Eqs. 2.3 or 2.4, depending on the observable. For the proton sample, PID is conducted employing only the TPC information for $p < 0.75\,\mathrm{GeV}/c$ requiring $|n_{\sigma,\mathrm{TPC}}| < 3$. For larger momenta the PID information of TPC and TOF are combined and a circular selection $\sqrt{n^2_{\sigma,\mathrm{TPC}} + n^2_{\sigma,\mathrm{TOF}}} < 3$ is applied. The threshold between the two methods is defined by the momentum at which protons can no longer be uniquely identified by the TPC dE/dx signal as shown in Fig. 2.6. At larger momenta, however, also the TOF β does not provide the separation power required for a unique identification as shown in Fig. 2.7, and a contamination is introduced to the sample. In order to ensure that the purity is better than about 80% within the full p_{T} range, only proton candidates with $p_{\mathrm{T}} < 4.05\,\mathrm{GeV}/c$ are considered.

The n_σ distributions for protons in the TPC and TOF are shown in the left and right panel of Fig. 3.1 and demonstrate the purity of the sample. The resulting p_{T} distribution is shown in the left panel of Fig. 3.2. The momentum threshold of $p = 0.75\,\mathrm{GeV}/c$ above which additionally the TOF PID is employed is prominently visible in the spectrum.

The purity of the proton sample is investigated using MC simulations generated with the PYTHIA 8.2 [201] event generator which are, as discussed in Sec. 2.2.6, filtered through the ALICE detector [205] and reconstruction algorithm [171]. As shown in the right panel of Fig. 3.2, the p_{T}-weighted purity is better than 99%, and decreases towards the upper p_{T} threshold applied in the analysis.

In order to employ the femtoscopy method to study the interaction among particle pairs, the genuine correlation function of primary particles produced in the initial collisions needs to be extracted from the experimental data. Only in this case, the particle pairs carry the pattern of the strong interaction. On the other hand, secondary particles that stem from weak decays, or particles produced in interactions with the detector material represent a contamination to the

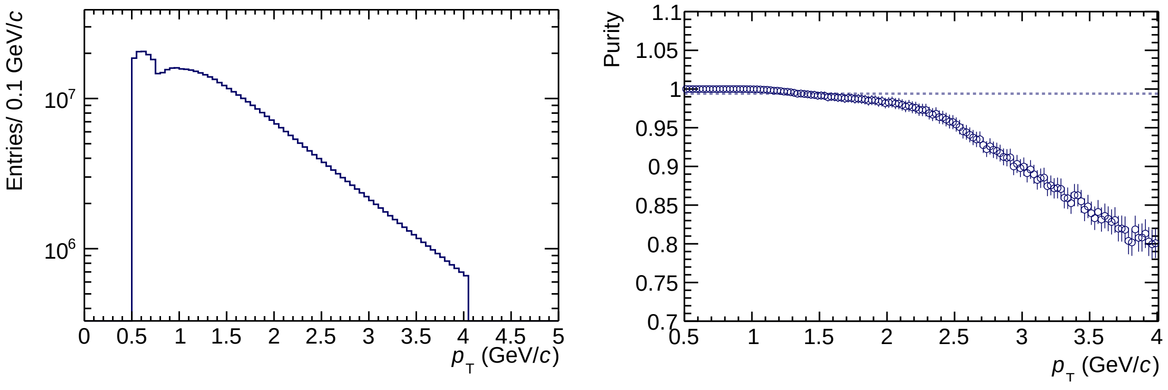

Figure 3.2: The proton p_T distribution after all selection criteria (*left*) and the resulting purity extracted from MC simulations (*right*). The dashed line indicates the p_T-weighted averages of the purity.

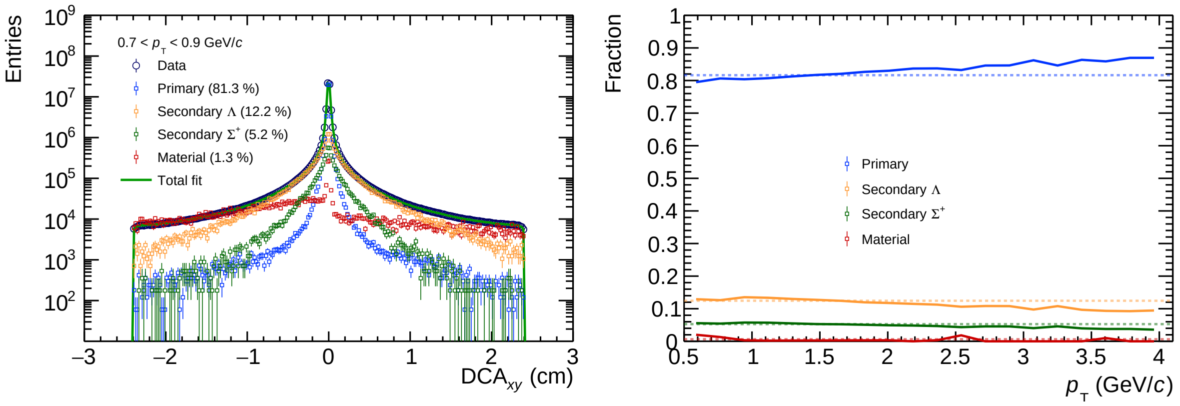

Figure 3.3: An exemplary DCA$_{xy}$ template fit (*left*) and the resulting fractions of protons as a function of p_T (*right*). The dashed lines indicate the p_T-weighted average of the respective observables.

signal. In particular in the former case an additional correlation signal from the parent may arise and contribute to the total experimental correlation function.

In order to quantify the contribution of these particles MC template fits of the DCA$_{xy}$ distributions are employed, which have been proven to be sensitive to the different contributions [152]. Four different templates are used to separate the different contributions. Primary protons originate from the initial collision and are therefore expected to have a narrow DCA distribution. On the other hand, secondary protons from the decays of Λ or Σ^+ have a significantly broadened distribution due to their decay length of few cm, while for protons produced in the detector material the distribution is basically flat. The template fit of the experimental distribution determines the individual weights of these contributions. The left panel of Fig. 3.3 shows the result of such a template fit in an exemplary p_T interval, and in the right panel the resulting fractions are shown as a function of p_T. As displayed in the right panel of Fig. 3.3, protons have a p_T-weighted primary fraction of 82%, with the remaining fraction associated to weak decays of Λ and Σ^+ in the ratio 70%/30%. The contribution from protons from the detector material is found to be negligible.

After all track quality and PID selection criteria applied, in total about 5.2×10^8 (4.6×10^8) proton (antiproton) candidates with a purity larger than 99% are available for analysis.

3.3 Σ^0 Reconstruction

The Σ^0 particle mainly decays via the channel $\Sigma^0 \rightarrow \Lambda\gamma$ with a branching ratio of almost 100% [7], which is therefore exploited for its reconstruction. The electromagnetic decay is characterized by a short life time with $c\tau = (22 \pm 2) \times 10^{-12}\,\mathrm{m}$ [7] and accordingly the decay products are indistinguishable from primary particles produced in the initial collision. Thus, the reconstruction of the Σ^0 relies on the independent reconstruction of the two decay children and the subsequent combination of all $\Lambda\gamma$ pairs in a given event.

3.3.1 Λ Reconstruction

The Λ candidates are identified via the subsequent decay $\Lambda \rightarrow \mathrm{p}\pi^-$ with a branching ratio of 63.9% and a $c\tau = 7.89\,\mathrm{cm}$ [7]. For the $\overline{\Lambda}$, the charge-conjugate decay is exploited and therefore in the following the term Λ refers to both particles, unless specified otherwise. The reconstruction is based on the procedures applied for the analysis of minimum bias pp collisions at $\sqrt{s} = 7$ TeV [128, 152] and $\sqrt{s} = 13$ TeV [153]. The selection criteria have been optimized for the reconstruction of Λ stemming from the decay of Σ^0, as specified at the end of this Section. All Λ selection criteria are summarized in Table 3.3.

The reconstruction is based on the V^0 candidates identified after the tracking procedure (*offline* V^0) as discussed in Sec. 2.2.6 and Ref. [173]. The charged children of the decay are reconstructed with the TPC and the ITS within $|\eta| < 0.9$. A selection on the number of associated TPC clusters ensures the quality of the employed tracks. By requesting a minimal DCA_{xy} to the PV, primary particles are effectively suppressed. In order to achieve a high yield of Λ candidates, only a loose PID selection in the TPC within a broad window of $|n_\sigma| < 5$ is applied as depicted in Fig. 3.4.

Table 3.3: Selection criteria for the Λ candidates.

Selection criterion	**Value**
Child track selection criteria	
Pseudorapidity	$\|\eta\| < 0.9$
TPC cluster	$n_{\mathrm{cluster}} > 70$
Distance of closest approach to PV	$\mathrm{DCA}_{xy} > 0.05\,\mathrm{cm}$
Particle identification	$\|n_{\sigma,\mathrm{TPC}}\| < 5$
V^0 selection criteria	
V^0 finder	*Offline*
Transverse momentum	$p_\mathrm{T} > 0.3\,\mathrm{GeV}/c$
Pointing angle α	$\cos\alpha > 0.999$
Λ decay vertex	$\|i_{\mathrm{vertex}_\Lambda}\| < 100\,\mathrm{cm}$, i=x,y,z
Transverse radius of the decay vertex r	$0.2 < r < 100\,\mathrm{cm}$
DCA of the tracks at the decay vertex	$\mathrm{DCA}(\|p,\pi\|) < 1.5\sigma$
K^0_S rejection	$493 < \mathrm{M}_{\pi^+\pi^-} < 504\,\mathrm{MeV}/c^2$
Λ selection	$\|\mathrm{M}_{\mathrm{p}\pi} - \mathrm{M}_{\Lambda,\mathrm{PDG}}\| < 6\,\mathrm{MeV}/c^2$
Out-of-bunch pile-up suppression	Either of the two tracks has a hit in ITS (SPD or SSD) or TOF timing

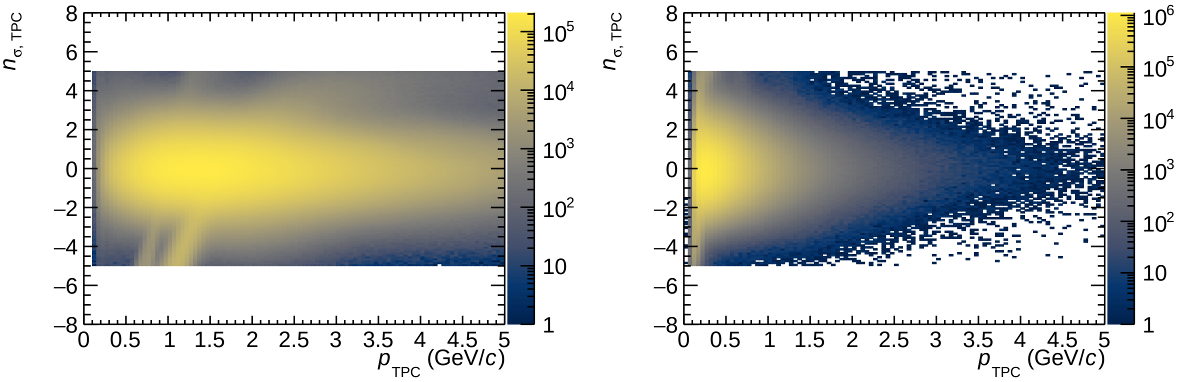

Figure 3.4: The n_σ distribution for the positive (*left*) and negative (*right*) child tracks of the Λ. A residual contamination of the sample is clearly visible.

In both cases a clear contamination of the sample is visible, which however can be effectively reduced by applying further selection criteria on the V^0 candidates.

The resulting Λ candidate is obtained as the combination of the child tracks, assuming nominal PDG values [7] for their masses. The secondary decay vertex is defined as the point of closest approach between the two tracks. The DCA of the two child tracks at the decay vertex is used as an additional selection criterion to suppress combinatorial background. Requiring a minimum $p_\mathrm{T} > 0.3\,\mathrm{GeV}/c$ for the Λ candidates serves a similar purpose and rejects fake candidates. The purity of the Λ sample is further enhanced by topological selections on the radial distance of the decay vertex with respect to the detector center and on the CPA. Since the PID selection on the child tracks is rather broad, a residual K^0_S contamination is present in the sample due to the misidentification of a π as a proton. Therefore, the invariant mass of the V^0 is evaluated assuming a decay into $\pi^+\pi^-$ and depicted in the left panel of Fig 3.5. The resulting K^0_S contamination is removed by a 1.5σ rejection, where σ corresponds to the width of a Gaussian fitted to the invariant mass signal.

Since the tracks are required not to point to the primary vertex, a contribution from out-of-bunch

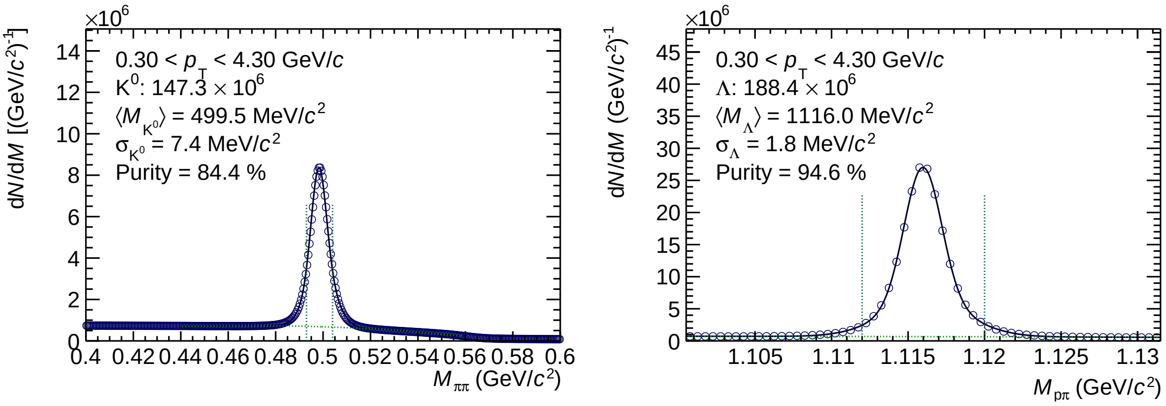

Figure 3.5: The residual K^0_S contamination of the Λ sample before the rejection in the p_T-integrated $\pi^+\pi^-$ invariant mass spectrum (*left*), and the resulting Λ p_T-integrated invariant mass spectrum (*right*). The dashed lines denote the limits for the selection (rejection) of the Λ (K^0_S) candidates.

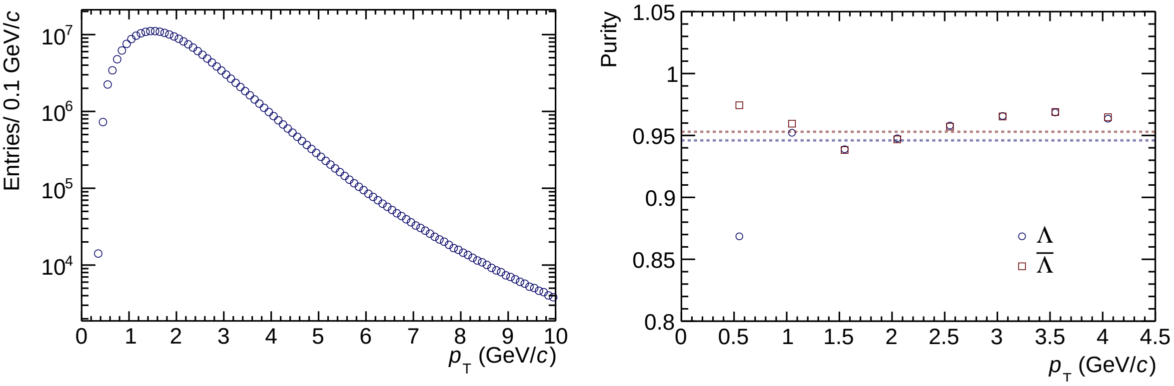

Figure 3.6: The p_T distribution of the Λ candidates (*left*) and the purity of the Λ and $\overline{\Lambda}$ candidates as a function of p_T (*right*). The dashed lines denote the respective p_T-weighted average value.

pile-up, i.e. further inelastic pp collisions within the integration time of the detector, may be present in the sample. In addition to the tight selection on the CPA of the V^0, the fast timing detectors are employed to suppress tracks stemming from such events. One of the two child tracks is requested to have an associated hit in either the SPD, SSD, or the TOF detector. Finally, a selection on the $p\pi^-$ ($\bar{p}\pi^+$) invariant mass is employed to extract the Λ candidates.

The Λ invariant mass signal, depicted in the right panel of Fig. 3.5, is described by two Gaussian functions for the signal and a second order polynomial to emulate the combinatorial background. The results for the combined mean and width of the two Gaussians are evaluated as the weighted arithmetic average. For the p_T-integrated invariant mass spectrum, the mean of the Λ peak is 1116 MeV/c^2 and its width, driven by the detector resolution, is found to be 1.8 MeV/c^2.

As shown in the right panel of Fig. 3.6, the dependence of the purity on p_T is rather weak, with a p_T-weighted average of 94.6% (95.3%) for the Λ ($\overline{\Lambda}$) candidates. For the Λ candidates an additional combinatorial background at low p_T is present due to the contribution of protons produced in the interaction of primary particles with the detector material, which is not present for the antiprotons. Accordingly, in the first p_T interval the purity decreases for the Λ candidates to about 87%.
The optimization of the selection criteria with respect to the Λ analyses [128, 152, 153] concern the timing requirements and the pseudorapidity of the child tracks, a more stringent CPA selection and a more loose rejection of K^0_S candidates. Additionally, the rather broad selection ($\approx 3.5\sigma$) is motivated to enhance the Σ^0 yield. The resulting p_T spectrum is shown in the left panel of Fig. 3.6.

After the selection criteria are applied, about 188×10^6 (178×10^6) Λ ($\overline{\Lambda}$) candidates with a purity of 94.6% (95.3%) are available for further processing.

3.3.2 Photon Reconstruction

Copious sources for photons exist in pp collisions and are conceptually distinguished as *i*) prompt photons and *ii*) photons from the decays of resonances. The first case is particularly interesting since these photons are dominantly produced in hard scattering processes of the partons from the colliding hadrons, such as $q\bar{q} \rightarrow \gamma g$ or $qg \rightarrow \gamma q$ [223]. In addition, higher-order processes such as fragmentation or bremsstrahlung contribute as well [224]. Accordingly, studying their production enables detailed tests of perturbative QCD and constrains the parton distribution functions.

On the other hand, numerous resonances have decay channels with a photon in the final state [7]. The decays of π^0 and η mesons have the largest contribution to the photon spectrum. Since this study aims at the reconstruction of the Σ^0 via the decay channel $\Sigma^0 \rightarrow \Lambda\gamma$, all of the above mentioned sources contribute to the combinatorial background of the measurement. In order to assess the respective contributions, the photon spectrum generated by PYTHIA 8.2 [201] is investigated. This is shown in the left panel of Fig. 3.7, while the right panel depicts the fractional contribution of photons from various sources to the total spectrum.

It is clearly visible that photons from the π^0 decay have a contribution of about $85-90\%$ to the total spectrum, followed by the η with about $5-10\%$. Contributions from the Σ^0 are at the sub-percent level and fall off steeply with increasing momentum as depicted by the solid dark blue line in Fig. 3.7. This is not surprising since in the rest frame of the Σ^0 the photon is monochromatic with its momentum determined by the mass difference between the Σ^0 and the Λ, and accordingly about 77 MeV/c [7]. The left panel of Fig. 3.7 demonstrates that due to the boost into the lab frame, the photon obtains typical momenta of only few hundreds of MeV/c, peaking slightly below 300 MeV/c.

The major challenge of the Σ^0 identification is therefore to reconstruct low-energetic photons and to handle the combinatorial background introduced by the various sources.

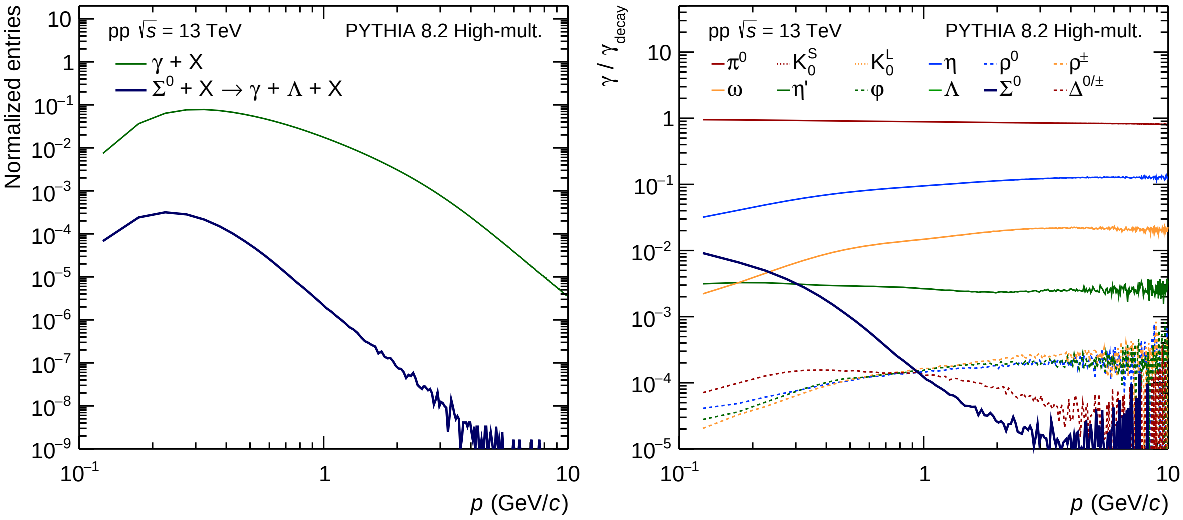

Figure 3.7: (*Left*) Photon spectrum generated with PYTHIA 8.2 [201] for pp collisions at $\sqrt{s} = 13$ TeV separating the contribution from Σ^0 decays and (*right*) ratio of decay photons from copious sources to the integrated photon spectrum.

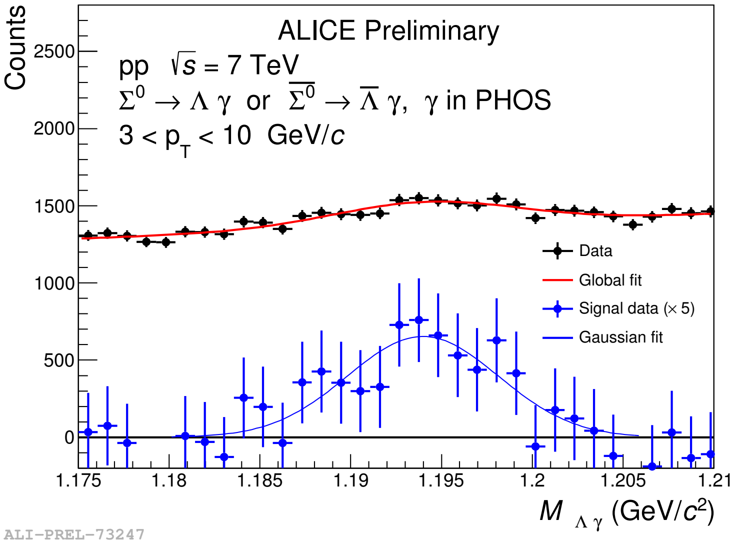

Figure 3.8: Invariant mass distribution of $\Lambda\gamma$ in pp collisions at $\sqrt{s} = 7$ TeV, with the photon reconstructed in the PHOS detector [149].

A first attempt to reconstruct such photons from the Σ^0 decay was carried out within ALICE by employing the PHOS calorimeter [225]. This exploratory reconstruction of the Σ^0 was conducted using data from pp collisions at $\sqrt{s} = 7$ TeV [25]. The resulting $\Lambda\gamma$ invariant mass spectrum is shown in Fig. 3.8. The invariant mass peak of the Σ^0 is barely visible due to the overwhelming combinatorial background, which therefore is, in addition to the limited geometrical acceptance of the PHOS detector, prohibitive for femtoscopic measurements.

Hence, the photon is reconstructed relying on conversions to e^+e^- pairs in the detector material within the central barrel. Depending on the energy scale, the interaction of photons with matter can occur via the photoelectric effect, Compton and Rayleigh scattering, pair production and photonuclear absorption. The total photon cross section on carbon is shown in Fig. 3.9 and depicts the relevant energy regimes for the corresponding processes.

At low energies up to $\sim 100\,\mathrm{keV}$, the photoelectric effect is the dominant process. The photon is absorbed by a bound electron which is subsequently ejected from the atom. When thresholds for photoionization of atomic levels are reached, the corresponding cross section exhibits discontinuities (*absorption edges*), which are clearly visible in Fig. 3.9. For larger photon energies, the cross section corresponds approximately to [226]

$$\sigma_{\mathrm{p.e.}} \sim E_\gamma^{-1}. \tag{3.2}$$

At intermediate energies from several 10 keV to few MeV the Compton effect becomes dominant, and the photon scatters off a quasi-free electron and is deflected. The corresponding cross section can be approximated for photon energies $E_\gamma \gg m_e c^2$ as [226]

$$\sigma_{\mathrm{Compton}} \sim \frac{\ln E_\gamma}{E_\gamma}. \tag{3.3}$$

Finally, and most relevant for this work, for energies larger than few MeV, pair production takes

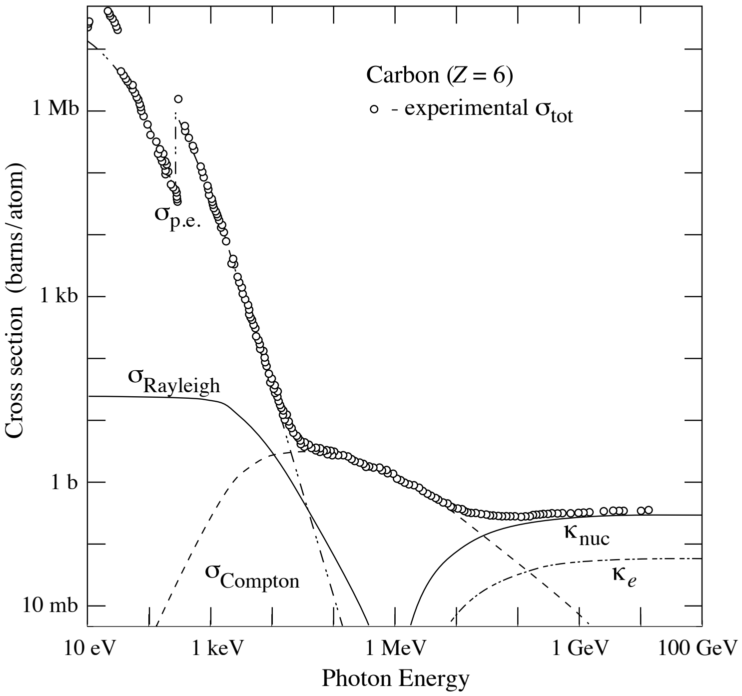

Figure 3.9: Photon total cross section as a function of energy in Carbon, modified from Ref. [7]. The individual contributions of the processes are:

$\sigma_{\text{p.e.}}$:	Atomic photoeletric effect (photon absorption, electron ejection),
σ_{Rayleigh}:	Rayleigh (coherent) scattering – atom neither ionized nor excited,
σ_{Compton}:	Incoherent scattering (Compton scattering off an electron),
κ_{nuc}:	Pair production, nuclear field,
κ_e:	Pair production, electron field.

over as the dominant process. Due to energy and momentum conservation this can only occur in the presence of the Coulomb field of a nucleus (κ_{nuc}) or an electron (κ_e). The energy thresholds differ slightly for the two cases. The cross section of the process is closely related to that of bremsstrahlung due to the similarity of the corresponding Feynman diagrams and given in the high-energy limit by [227]

$$\sigma \sim \frac{7}{9}\frac{A}{X_0}, \tag{3.4}$$

where A is the mass number of the traversed material and the radiation length X_0. The probability for the conversion process to occur for a high energetic photon traversing the distance l is given by [7]

$$P(l) = 1 - e^{-\frac{7}{9}\frac{l}{X_0}}. \tag{3.5}$$

For the ALICE detector, and within the acceptance of the central barrel ($|\eta| < 0.9$), the material budget amounts to (11.4 ± 0.5) % of a radiation length X_0 for transverse radii $r < 180\,\text{cm}$ [228]. This corresponds to a plateau value of the conversion probability of (8.6 ± 0.4) % [228]. Details of the photon conversion analysis and the corresponding selection criteria are described in Refs. [228, 229]. All γ selection criteria are summarized in Table 3.4 and have been optimized to enhance the yield of Σ^0 candidates.

Table 3.4: Selection criteria for the γ candidates.

Selection criterion	**Value**
Child track selection criteria	
Transverse momentum	$p_{\mathrm{T}} > 0.05\,\mathrm{GeV}/c$
Pseudorapidity	$\lvert\eta\rvert < 0.9$
Ratio findable TPC cluster	$n_{\mathrm{cluster}}/n_{\mathrm{findable}} > 0.35$
Particle identification	$-6 < n_{\sigma,\mathrm{TPC}} < 7$
Pion rejection	$n_{\sigma_\pi,\mathrm{TPC}} < -10$ for $p_{\mathrm{T}} > 0.5\,\mathrm{GeV}/c$
V^0 selection criteria	
V^0 finder	*On-fly*
Transverse momentum	$p_{\mathrm{T}} > 0.02\,\mathrm{GeV}/c$
Pseudorapidity	$\lvert\eta\rvert < 0.9$
Pointing angle α	$\cos\alpha > 0.999$
Transverse radius of the decay vertex r	$5 < r < 180\,\mathrm{cm}$
Armenteros-Podolanski selection	2-D selection with $q_{\mathrm{T}} < 0.06\,\mathrm{GeV}/c$
Opening angle in B-field	2-D χ^2 and ψ_{pair} cut with $\chi^2 < 30$ and $\lvert\psi_{\mathrm{pair}}\rvert < 0.2$
Distance of closest approach to PV	$\mathrm{DCA}_z < 0.5\,\mathrm{cm}$ $\mathrm{DCA}_{xy} < 0.75\,\mathrm{cm}$

The reconstruction is based on the V^0 candidates identified during the tracking procedure (*on-fly* V^0) as discussed in Sec. 2.2.6 and Ref. [173]. Since the spatial information of the clusters is still available at this point, an improved reconstruction efficiency can be achieved for low-p_{T} tracks. Additionally, the tracks can be refitted considering the fact that the decay children stem from a secondary vertex, however without an additional mass constraint on the V^0.

The charged children of the decay are reconstructed with the TPC and the ITS within $\lvert\eta\rvert < 0.9$. A selection on the fraction of associated TPC clusters with respect to the distance traversed ensures the quality of the employed tracks. No selection on a fixed minimum amount of associated TPC clusters is required as the number of reconstructable clusters depends on the position of the secondary vertex. On average, however, about 120 clusters are associated to the child tracks. A loose PID selection of $-6 < n_{\sigma,\mathrm{TPC}} < 7$ with the TPC is applied to the resulting child tracks, while for larger momenta, where a better pion-electron separation can be accomplished with the TPC, an additional pion rejection criterion is applied. Since the TPC alone does not provide the required identification capabilities for electrons over the full momentum range, a clear contamination can be observed in the sample, as displayed in the left panel of Fig. 3.10. Further selection criteria on the V^0 candidates lead to a significant improvement of the purity of the sample.

The γ candidate is then obtained as the combination of the child candidates, assuming nominal PDG values for the masses [7]. The V^0 finder associates the secondary decay vertex to the point of closest approach of the two child tracks. For the case of photon conversions, this estimate can be significantly improved by requiring that the child tracks are collinear at their origin. The procedure is described in detail in Refs. [230, 231] and results in a spatial resolution of the conversion point sufficient to resolve details of the detector geometry when used for tomographic purposes as depicted in Fig. 3.11.

Only photon candidates with $p_{\mathrm{T}} > 0.02\,\mathrm{GeV}/c$ and within $\lvert\eta\rvert < 0.9$ are accepted. The resulting

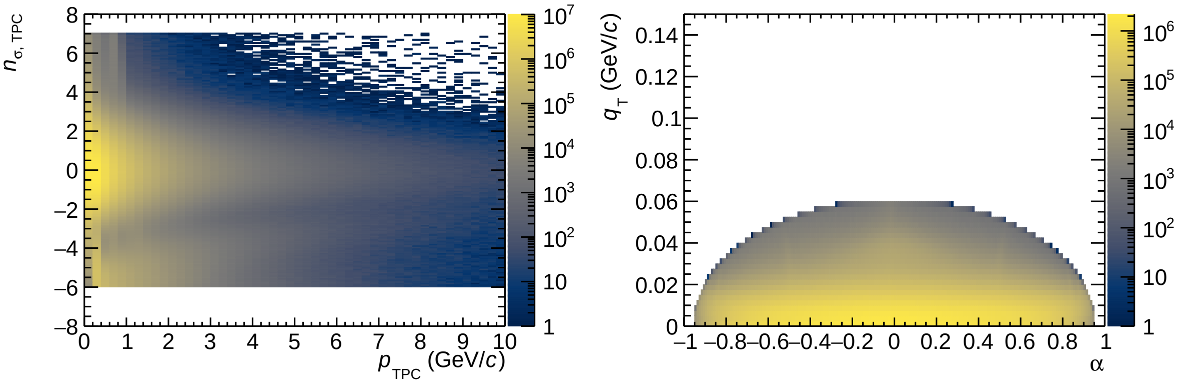

Figure 3.10: The n_σ distribution for the positive and negative child tracks of the γ (*left*) and the resulting distribution in the Armenteros-Podolanski space (*right*). While the single-track observable displays a residual contamination of the sample, the selection in the Armenteros-Podolanski space efficiently removes the contribution from Λ and K^0_S.

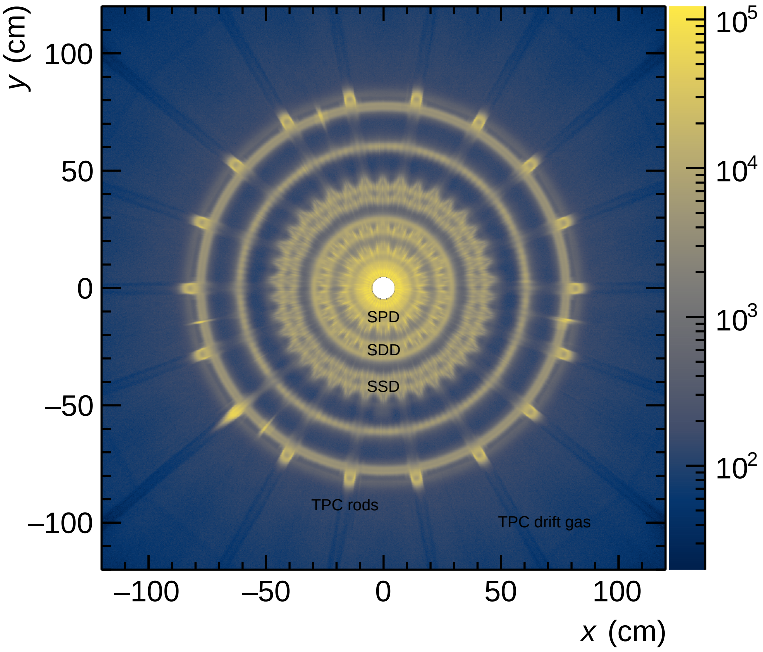

Figure 3.11: Reconstructed conversion vertices in the inner part of the ALICE central barrel. Detailed structures of the ITS and TPC auxiliary systems can be resolved.

photon sample still contains contaminations from uncorrelated or correlated primary e^+e^- pairs, or from Dalitz decays of the short-lived π^0 ($c\tau \sim 2.6 \times 10^{-8}$ m [7]) or η mesons ($c\tau \sim 1.5 \times 10^{-10}$ m [7]). The child tracks from these contributions cannot be distinguished from primary particles, however may be ill-reconstructed as a V^0 with a decay vertex very close to the PV. For this reason, the transverse radius of the conversion point is restricted to $5 < r < 180$ cm. The upper limit is introduced to enforce for a reasonable track length of the decay children within the TPC.

Since in a considerable fraction of the covered momentum range the pion–electron and proton–electron separation of the $\mathrm{d}E/\mathrm{d}x$ measurement within the TPC does not impose a strict rejection, combinatorial background and remaining K^0_S and Λ candidates may contaminate the sample. As discussed in Sec. 2.2, a selection in the Armenteros-Podolanski space [181, 229] enables an efficient suppression of these contributions while leaving the photon conversion sample intact. A two-dimensional selection reduces the contamination, as displayed in the right panel of Fig. 3.10.

The e^+e^- pair resulting from the conversion process has a vanishing intrinsic opening angle. The solenoidal magnetic field, however, leads to a bending of the tracks perpendicular to the magnetic field, while it does not act in the direction along the field. The tracks stemming from decays of massive particles, on the other hand, are randomly oriented with respect to the magnetic field. Therefore, a selection on the angle ψ_{pair} [232] between the plane defined by the e^+e^- pair and the magnetic field efficiently suppresses combinatorial background and particle pairs from decays. This is conducted in combination with a selection on the reduced χ^2 of a refit of the reconstructed V^0 assuming that it originates from the primary vertex and has $M_{V^0} = 0$. This selection has been developed in Ref. [229] and proven to efficiently suppress the contamination from decays of massive particles.

The CPA of the remaining γ candidates is required to be CPA > 0.999. Additionally to the tight CPA selection, γ stemming from out-of-bunch pile-up are suppressed by enforcing a strict DCA_z along the beam direction of the photon. The resulting p_{T} spectrum is depicted in the left panel of Fig. 3.12. The corresponding purity is evaluated using Pythia 8.2 [201] MC simulations and shown in the right panel of Fig. 3.12.

After the application of all selection criteria, about 946×10^6 γ candidates with a purity of about 95.4% are available for further processing.

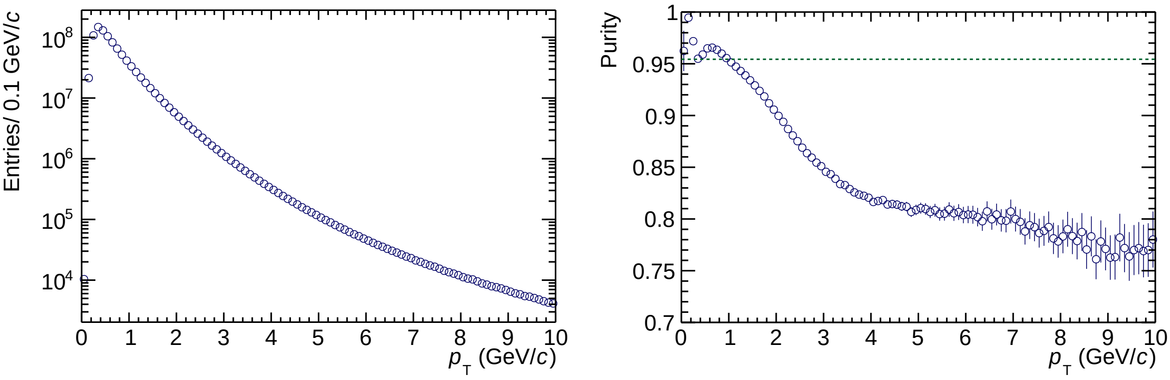

Figure 3.12: The p_{T} distribution of the γ candidates (*left*) and the corresponding purity as a function of p_{T} (*right*). The dashed line denotes the respective p_{T}-weighted average value.

3.3.3 Σ^0 Identification

The Σ^0 ($\overline{\Sigma^0}$) candidates are constructed by combining all Λ ($\overline{\Lambda}$) and γ candidates from the same event. Nominal particle masses [7] are assumed for the decay children. When a track is used more than once for the construction of the γ, Λ, or $\overline{\Lambda}$, the resulting V^0 with the smaller CPA is removed from the sample. As depicted in Figs. B.1 and B.2 in the appendix, the rejection acts on the sub-percent level for all involved particle species.

The resulting p_{T}-integrated invariant mass spectra of $\Lambda\gamma$ and $\overline{\Lambda}\gamma$ are displayed in Fig. 3.13. For transverse momenta $p_{\mathrm{T}} < 1\,\mathrm{GeV}/c$ the sample is composed only of combinatorial background. Therefore, this kinematic region is excluded in order to further optimize the yield and the purity of the Σ^0 candidates. The overall purity is rather modest due to the overwhelming combinatorial background in particular from the γ. The yield and purity of the resulting candidates is extracted by fitting the spectra with a single Gaussian for the signal and a third-order polynomial for the background.

The $\Lambda\gamma$ and $\overline{\Lambda}\gamma$ invariant mass spectra in slices of p_{T} are depicted in Figs. 3.14 and 3.15, together with the individual fits. The corresponding results are discussed in the following. The resulting parameters of the Σ^0 and $\overline{\Sigma^0}$ invariant mass peaks are depicted in Fig. 3.16, and demonstrate consistency. Both the mean value M_{Σ^0} and the width σ_{Σ^0} of the signal exhibit a strong dependence on p_{T}. The mean value decreases with p_{T} and is for $p_{\mathrm{T}} \gtrsim 5\,\mathrm{GeV}/c$ in agreement with the nominal value [7]. The width of the peak is driven by the detector resolution and is about $2\,\mathrm{MeV}/c$ in the first p_{T} interval from which is decreases. In both cases, the trend is well reproduced in MC

Table 3.5: Selection criteria for the Σ^0 candidates.

Selection criterion	**Value**
Transverse momentum	$p_{\mathrm{T}} > 1\,\mathrm{GeV}/c$
Mass selection Σ^0 candidates	$\lvert M_{\Lambda\gamma} - M_{\Sigma^0}(p_{\mathrm{T}})\rvert < 3\,\mathrm{MeV}/c^2$
Mass selection $(\Lambda\gamma)$ candidates	$5 < \lvert M_{\Lambda\gamma} - M_{\Sigma^0}(p_{\mathrm{T}})\rvert < 50\,\mathrm{MeV}/c^2$

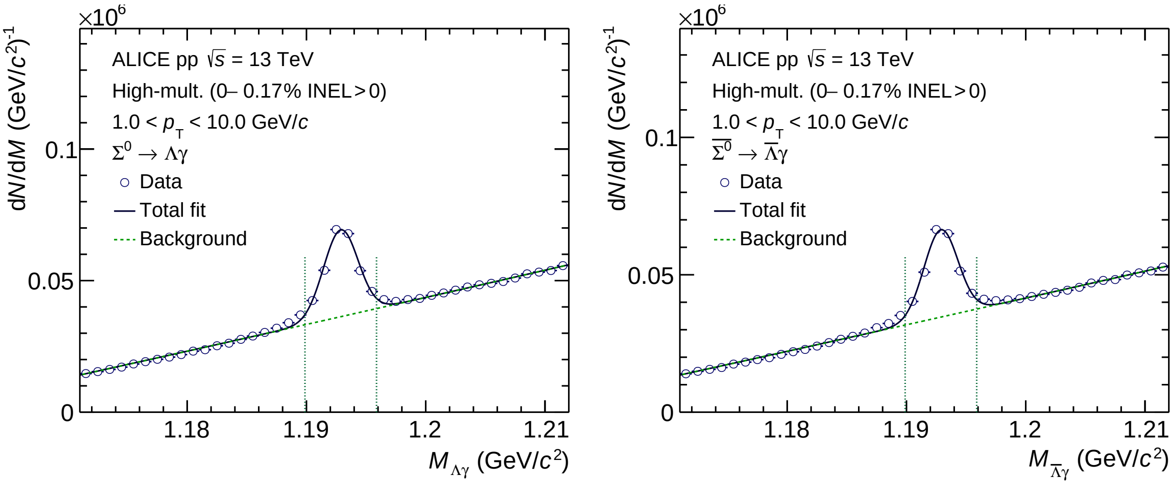

Figure 3.13: Invariant mass distribution of the $\Lambda\gamma$ (*left*) and $\overline{\Lambda}\gamma$ (*right*) candidates, integrated over the p_{T} range from $1.0 - 10.0\,\mathrm{GeV}/c$. The signal is described by a single Gaussian, and the background by a polynomial of third order.

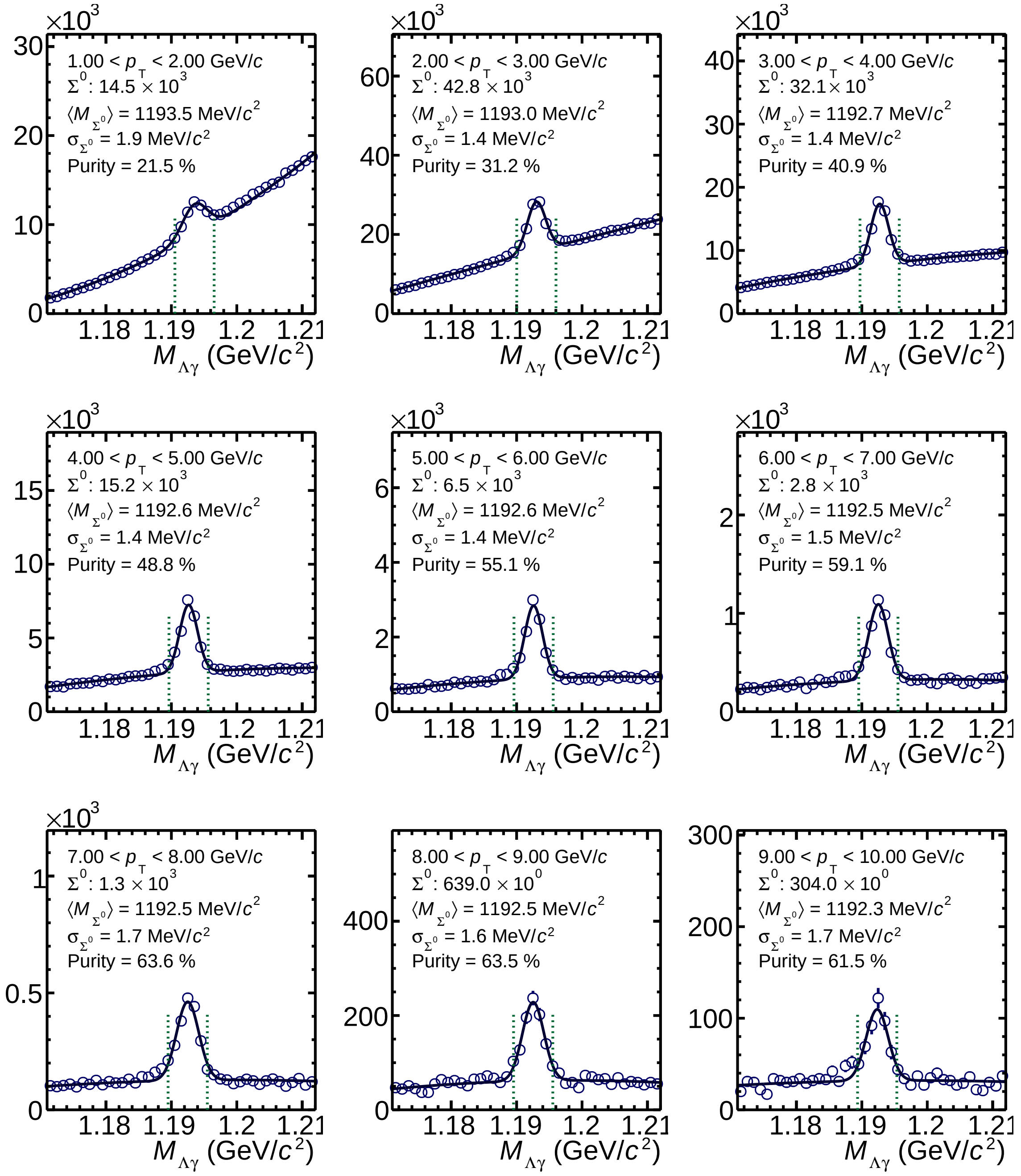

Figure 3.14: The Σ^0 invariant mass spectra in p_{T} slices with a width of 1 GeV/c. The signal is described by a single Gaussian, and the background by a polynomial of third order.

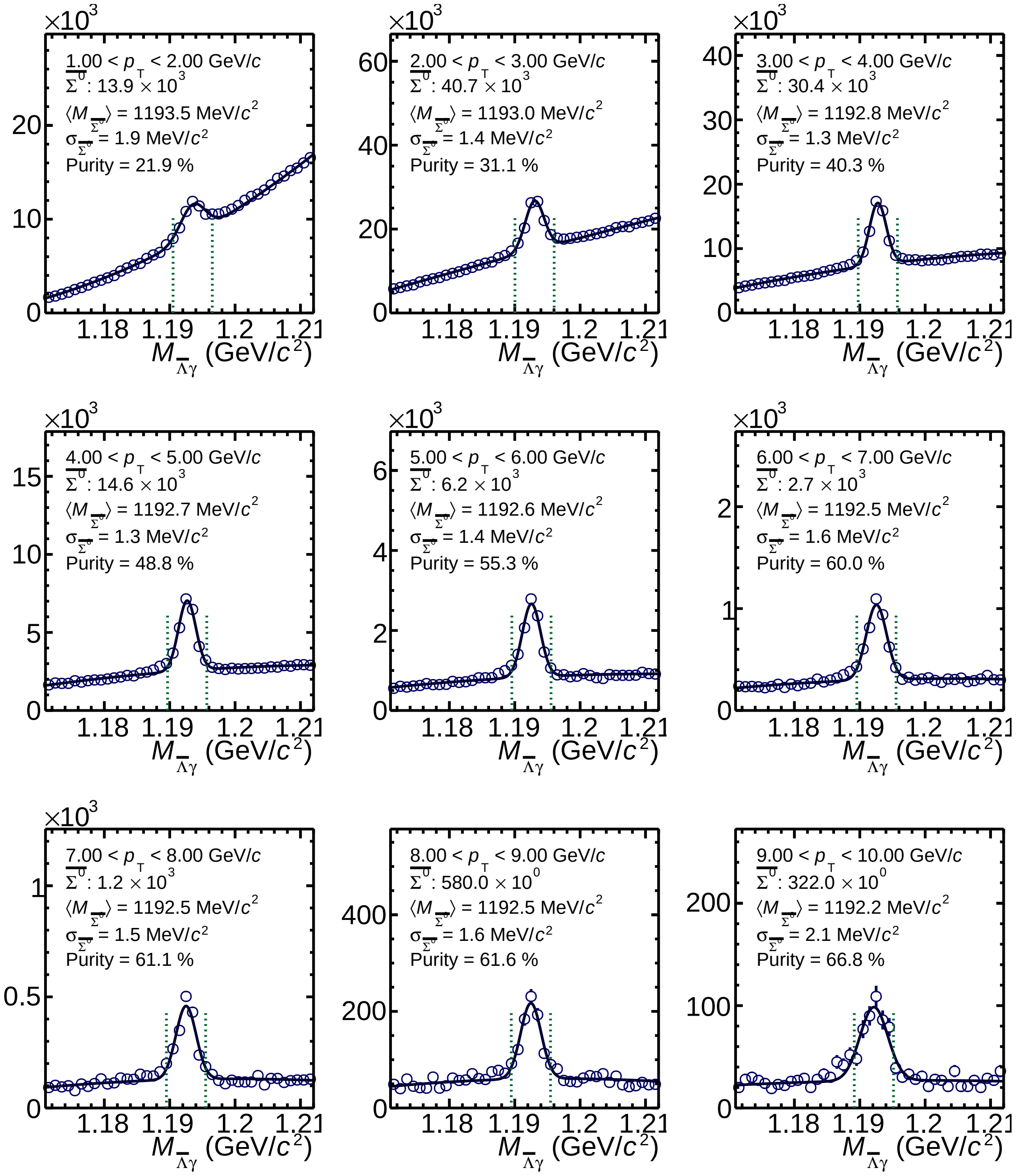

Figure 3.15: The $\overline{\Sigma^0}$ invariant mass spectra in p_{T} slices with a width of 1 GeV/c. The signal is described by a single Gaussian, and the background by a polynomial of third order.

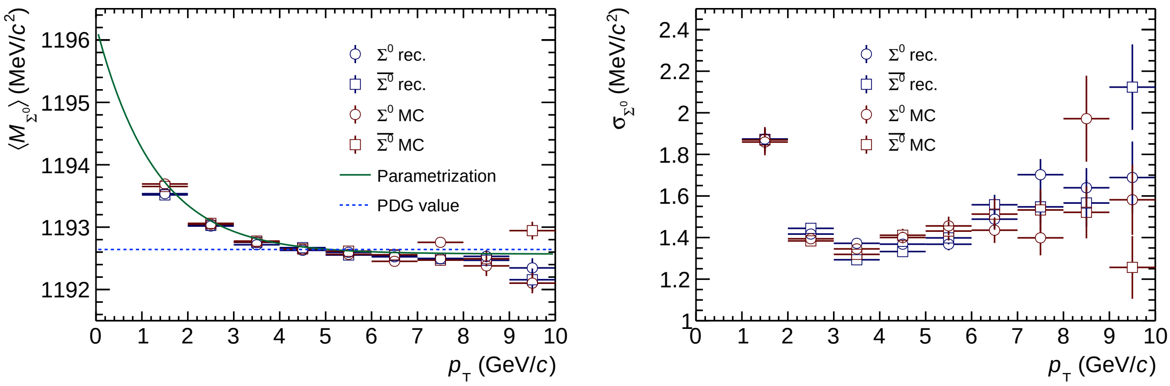

Figure 3.16: The Σ^0 and $\overline{\Sigma^0}$ invariant mass peak parameters as a function of p_T. The mean value of the Gaussian function to describe the signal (*left*) and its width (*right*). The trend is well reproduced by MC simulations.

simulations and can be attributed to the momentum resolution of the spectrometer. In particular the γ candidates, which are formed from soft tracks, are especially affected by the momentum resolution at very low p_T.

In order to extract the Σ^0 candidates for the femtoscopic analysis, the observed drift of M_{Σ^0} with p_T is considered by applying a p_T-dependent mass selection. The p_T dependence of the reconstructed Σ^0 mass is parametrized as

$$M_{\Sigma^0}(p_T) = a + b \cdot e^{c \cdot p_T}, \tag{3.6}$$

where the parameters are obtained by a fit, as shown in the left panel of Fig. 3.16. The Σ^0 ($\overline{\Sigma^0}$) candidates for femtoscopy are then selected around $M_{\Sigma^0}(p_T)$ as outlined in Table 3.5. The width of the interval is optimized to maximize both the candidate counts and the corresponding purity. Only one candidate per event is used, and is randomly selected in the very rare case in which more than one is available. The resulting p_T distribution is depicted in the left panel of Fig. 3.17.

The dependence of the purity as a function of p_T is shown in the right panel of Fig. 3.17. The enhanced combinatorial background at lower p_T is mainly related to the presence of soft photons, and leads to a purity of about 20% at the lower p_T threshold. Above 5 GeV/c, the purity reaches its saturation value of about 60%. The p_T-weighted purity of the sample if 34.6% for both the Σ^0 and the $\overline{\Sigma^0}$.

Due to the modest purity of the Σ^0 sample, a significant contamination of combinatorial $\Lambda\gamma$ combinations contributes to the p–Σ^0 correlation function. In order to benchmark residual correlations, genuine $(\Lambda\gamma)$ combinations without a contribution from Σ^0 are selected from the sidebands of the invariant mass spectrum. The selection criteria for the Σ^0 and $(\Lambda\gamma)$ candidates are summarized in Table 3.5.

Only for the Λ candidates the timing detectors are employed to suppress out-of-bunch pile-up, while for the γ a tight DCA$_z$ selection is used. In this way, the Σ^0 candidates are anchored to the right event by the Λ, and photons from out-of-bunch pile-up contribute only to the combinatorial background, but not to the signal. Therefore, the remaining contamination of the Σ^0 candidates by out-of-bunch pile-up can be estimated by studying the purity as a function of the LHC periods, which are time intervals of stable detector and LHC conditions as shown in Fig. 2.9. The resulting

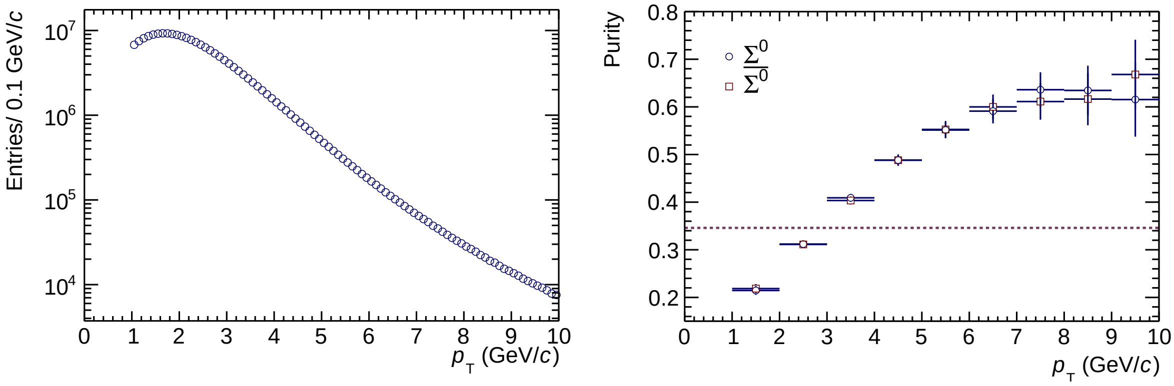

Figure 3.17: The p_T distribution (*left*) and purity (*right*) of the Σ^0 and $\overline{\Sigma^0}$ candidates. The dashed lines denote the p_T-weighted average value.

purity, shown in Fig. 3.18, is consistent within the uncertainties with the average value of 34.6%. In particular, the purity of the LHC periods with low interaction rates at the beginning of each year does not deviate systematically from the average value. Therefore, it can be concluded that the contamination of the sample is not significant.

Relevant for femtoscopy are primary particles produced in the initial collision since only these contribute to particle pairs carrying the pattern of the strong interaction. On the other hand, secondaries from weak decays are a contamination to the signal. Since only strong resonances are feeding to the Σ^0 [7], a 100% primary fraction is assumed.

Finally, the full efficiency $A \times \varepsilon \times \mathrm{BR}$ of the Σ^0 measurement is computed, considering the geometrical acceptance (A), the Σ^0 detection efficiency (ε) and the branching ratio of Λ to $\mathrm{p}\pi^-$ (BR) [7]. To this end, the raw yield as a function of p_T is extracted from MC simulations generated with the PYTHIA 8.2 [201] event generator which are, as discussed in Sec. 2.2.6, filtered through the ALICE detector [205] and reconstruction algorithm [171]. The procedures to extract the

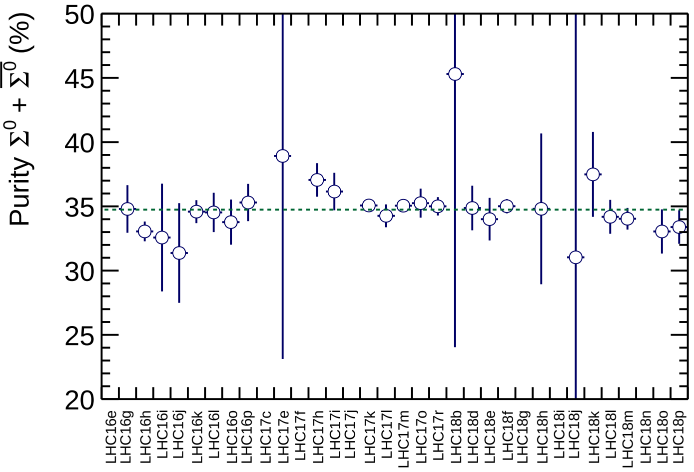

Figure 3.18: The purity of the combined Σ^0 and $\overline{\Sigma^0}$ candidates as a function of the LHC period. No significant deviations from the average value are observed.

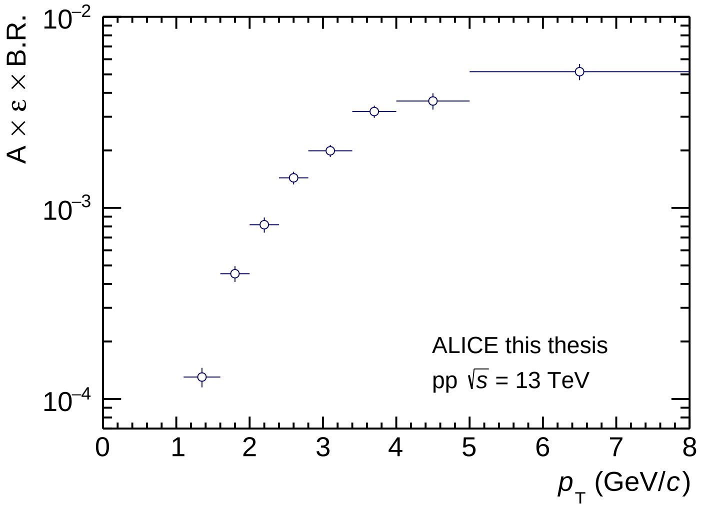

Figure 3.19: The acceptance × efficiency × branching ratio correction for the Σ^0 and $\overline{\Sigma^0}$ candidates.

signal are the same as discussed above. At the same time, MC events allow the extraction of the true number of Σ^0 particles produced by the event generator. The overall efficiency is then defined as the ratio of both and depicted in Fig. 3.19. In particular at low p_{T} the small conversion probability and the reconstruction efficiency of low energetic photon child tracks hampers the overall efficiency of the measurement. However, even at large p_{T} the overall efficiency remains significantly below one percent.
This clearly underlines the challenges of this particular measurement.

In total, about 115×10^3 (110×10^3) Σ^0 ($\overline{\Sigma^0}$) candidates are found at a purity of about 34.6% for both.

3.4 The Experimental Correlation Function

In order to relate the correlation function as discussed in Sec. 1.3 to experimentally accessible quantities, the experimental correlation function is defined as [125, 126]

$$C(k^*) = \mathcal{N} \cdot \frac{N_{\mathrm{same}}(k^*)}{N_{\mathrm{mixed}}(k^*)} \xrightarrow{k^* \to \infty} 1. \tag{3.7}$$

The relative momentum of the pair k^* is defined as $k^* = \frac{1}{2} \cdot |\mathbf{p}_1^* - \mathbf{p}_2^*|$ with the momenta of the two particles in the pair rest frame (PRF, denoted by the *) $\mathbf{p}_1^*$ and $\mathbf{p}_2^*$. The ratio of the k^* distribution of particle pairs from the same (N_{same}) and mixed (N_{mixed}) events is obtained and normalized in the interval $k^* \in [240, 340]$ MeV/c for p–p and $k^* \in [250, 400]$ MeV/c for p–Σ^0. In these kinematic regimes, effects of final-state interactions are absent and therefore the correlation function approaches unity. The different size of the normalization window for the p–p and the p–Σ^0 correlation function is due to the different bin sizes.

The uncorrelated control sample N_{mixed} is obtained using event mixing techniques, in which the particle pairs are combined from single particles stemming from different events. In order to avoid acceptance effects of the detector system, the mixing procedure is conducted only between particles stemming from events with similar z-position of the primary vertex and multiplicity [125]. The bin width for the z-vertex position is 2 cm and the multiplicity is grouped in classes of $[1-4]$, $[5-8]$, ..., $[93-96]$, $[97-100]$, $[>101]$. The latter is estimated by using the reference multiplicity `RefMult08`, counting the number of charged particles N_{ch} in $|\eta| < 0.8$, as shown in Fig. 3.20. The mixed event distributions $N_{\mathrm{mixed}}(k^*)$ are reweighted so the corresponding multiplicity distribution describes the one from the same event.

p–p Correlation Function In total 1.7×10^6 (1.3×10^6) p–p ($\overline{\mathrm{p}}$–$\overline{\mathrm{p}}$) pairs contribute to the respective correlation function in the region $k^* < 200$ MeV/c. The correlation functions of p–p and $\overline{\mathrm{p}}$–$\overline{\mathrm{p}}$ pairs demonstrate consistency with one another and are therefore combined to enhance the statistical significance of the results. Hence, in the following p–p denotes the combination p–p $\oplus$ $\overline{\mathrm{p}}$–$\overline{\mathrm{p}}$.

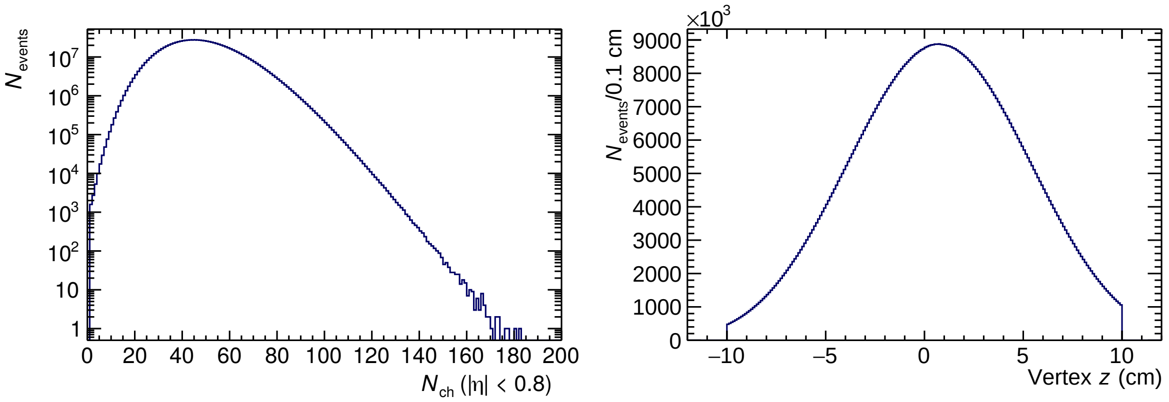

Figure 3.20: The observables used for the event mixing, the multiplicity N_{ch} (*Ref08*) in $|\eta| < 0.8$ (*left*) and the z-vertex distribution (*right*).

The resulting experimental correlation function is shown in the left panel of Fig. 3.21. The pattern of the relevant final-state interactions can be clearly observed. For $k^* < 100\,\mathrm{MeV}/c$ the attractive strong interaction leads to an enhancement of the correlation function, while at very low k^* the repulsive Coulomb interaction and quantum statistics lead to a depletion. Since the p–p interaction is theoretically well understood and experimentally constrained, these precise data enable detailed studies of the particle-emitting source.

The right panel of Fig. 3.21 depicts the p–p correlation function obtained from PYTHIA 8.2 [201] simulations, filtered through the ALICE detector [205] and reconstruction algorithm [171]. The multiplicity of the events is adjusted to mimic the effect of the `kHighMultV0` trigger. In MC simulations, effects of the final-state interaction are not incorporated, and for this reason the correlation function should be flat by construction. The resulting p–p correlation function does not deviate from unity within uncertainties, and therefore it can be concluded that detector-related effects do not introduce a bias to the measurement.

p–Σ^0 Correlation Function A total number of 587 (539) p–Σ^0 ($\overline{\mathrm{p}}$–$\overline{\Sigma^0}$) pairs contribute to the correlation function in the region $k^* < 200\,\mathrm{MeV}/c$. When the track of a primary proton is also employed as the child track of the γ or the Λ, the corresponding Σ^0 candidate is rejected. As depicted in Fig. B.3 in the appendix, this occurs in less than one per mille of the cases. The number of contributing particle pairs in the respective k^* bins are listed in Table 3.6. In general, only few counts contribute to the femtoscopic signal. This, folded with the modest experimental purity and primary fractions, leads to about 10 genuine p–$\Sigma^0 \oplus \overline{\mathrm{p}}$–$\overline{\Sigma^0}$ pairs contributing to the first bin of the correlation function.

The baryon–baryon correlation function of p–Σ^0 is compared to its antibaryon–antibaryon counterpart $\overline{\mathrm{p}}$–$\overline{\Sigma^0}$, as shown in Fig. 3.22. While for the largest part of the k^* range the behavior is fully consistent, at low k^* deviations arise. As summarized in Table 3.6, only few pairs contribute to the measured correlation function. In order to obtain a more thorough understanding of the deviation, the Σ^0 and $\overline{\Sigma^0}$ invariant mass distributions of the candidates contributing to the pairs at $k^* < 200\,\mathrm{MeV}/c$ are analyzed. The two panels of Fig. 3.23 show the selected invariant

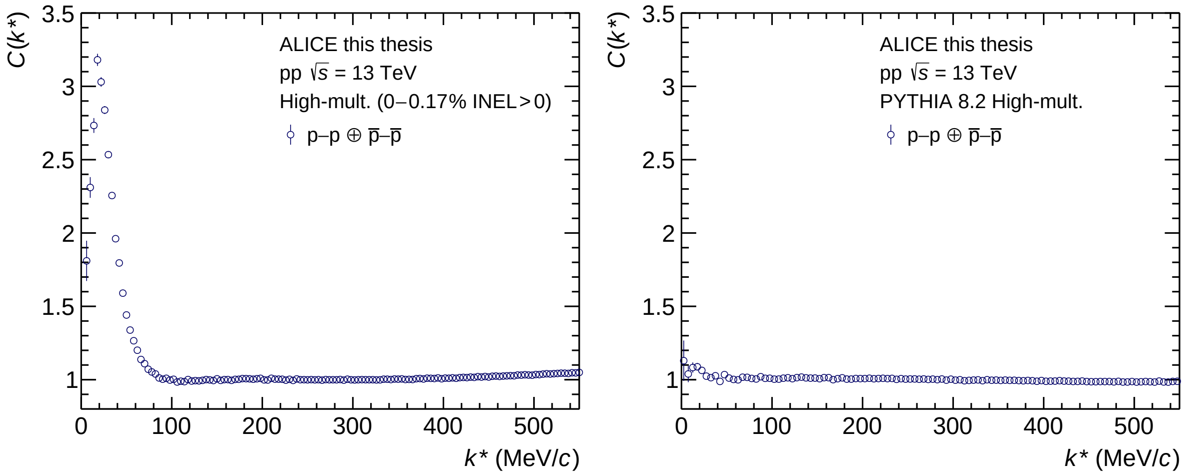

Figure 3.21: p–p $\oplus$ $\overline{\mathrm{p}}$–$\overline{\mathrm{p}}$ correlation functions obtained from data (*left*) and PYTHIA 8.2 simulations with a comparable multiplicity as the data (*right*).

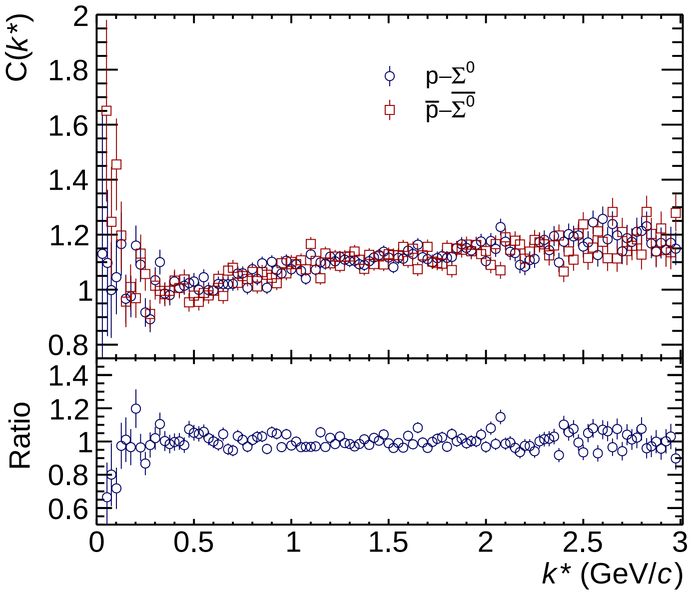

Figure 3.22: The measured p–Σ^0 and $\overline{\text{p}}$–$\overline{\Sigma^0}$ correlation functions with the corresponding ratio.

Table 3.6: Number of particle pairs for the p–Σ^0 and $\overline{\text{p}}$–$\overline{\Sigma^0}$ correlation function in the respective k^* bins and the corresponding $\langle k^* \rangle$ of the combined same event distribution $N_{\text{same}}(k^*)$.

k^* (MeV/c)	$\langle k^* \rangle$ (MeV/c)	p–Σ^0	$\overline{\text{p}}$–$\overline{\Sigma^0}$
15 – 65	48.3	22	32
65 – 115	92.4	93	105
115 – 165	139.7	226	188
165 – 215	190.7	421	328
215 – 265	238.7	609	525
265 – 315	289.3	844	705
315 – 365	338.0	1208	950

mass distributions of the Σ^0 and $\overline{\Sigma^0}$ candidates and it is clearly visible that the purity of the Σ^0 candidates is significantly lower than the one of the $\overline{\Sigma^0}$ candidates. As expected, the correlation signal of $\overline{\text{p}}$–$\overline{\Sigma^0}$, with larger purity, is more enhanced compared to the p–Σ^0 correlation function. Therefore, in the first case the correlation function demonstrates stronger sensitivity to the N–Σ interaction. It should be noted though, that the average p_{T} of the Σ^0 candidates that contribute to the correlation function at $k^* < 200\,\text{MeV}/c$ is with about $2\,\text{GeV}/c$ lower than the $\langle p_{\text{T}} \rangle$ of all inclusive Σ^0 candidates, which is about $3\,\text{GeV}/c$. This is particularly relevant, since the purity exhibits a strong p_{T} dependence. Considering the reduced average p_{T}, the Σ^0 purity relevant for the correlation function is 27.4%. In contrast to this, the p_{T}-integrated purity of the Σ^0 and $\overline{\Sigma^0}$ candidates is 34.6%. At the same time, the invariant mass spectra of the Σ^0 and $\overline{\Sigma^0}$ candidates contributing to the pairs at $k^* < 200\,\text{MeV}/c$, shown in Fig. 3.23, can be employed to study the relevant purity. The statistical uncertainties and fluctuations of the invariant mass spectra, however, introduce significant challenges in extracting a reliable purity. For this reason, the invariant mass spectra of Σ^0 and $\overline{\Sigma^0}$ are combined and the background is described by a first order polynomial. The resulting purity is, albeit with large uncertainties, found to be about 27% and therefore consistent with the purity extracted at the $\langle p_{\text{T}} \rangle$ of the Σ^0 candidates for the

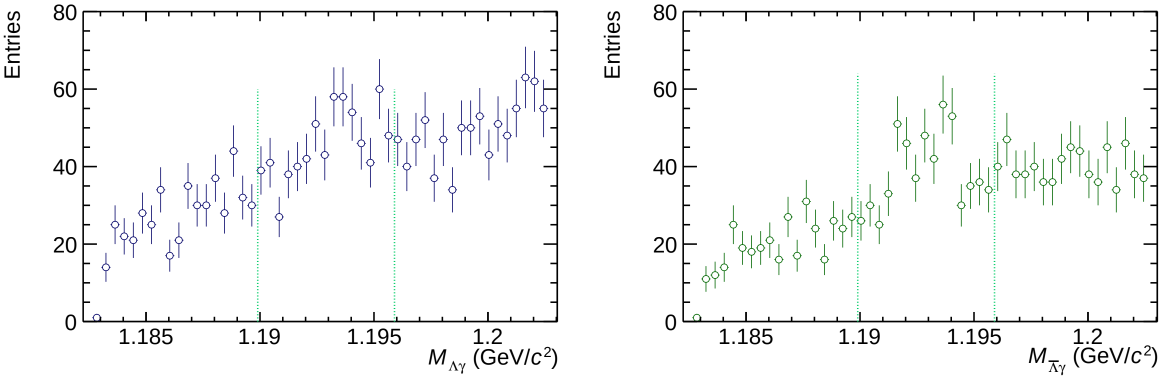

Figure 3.23: Invariant mass distributions of the Σ^0 (*left*) and $\overline{\Sigma^0}$ (*right*) candidates to construct the correlation function at $k^* < 200\,\text{MeV}/c$. The dashed lines sketch the selection used for the analysis.

correlation function. Thus, the correlation functions are combined, and in the following p–Σ^0 denotes the combination of p–$\Sigma^0 \oplus \overline{\text{p}}$–$\overline{\Sigma^0}$. The low number of pair counts in the first few bins and the rather wide bin size of 50 MeV/c introduces another complication, namely that the $\langle k^* \rangle$ of the data points of the experimental correlation function may be shifted with respect to the bin center. Indeed, especially in the first bin the lack of counts at low k^* significantly shifts the $\langle k^* \rangle$ of the same event distribution with respect to the bin center, as shown in Fig. 3.24. Therefore, the data points are drawn at the $\langle k^* \rangle$ of the same event distribution of the respective bin, as summarized in Table 3.6.

The final p–$\Sigma^0 \oplus \overline{\text{p}}$–$\overline{\Sigma^0}$ correlation function is shown in the left panel of Fig. 3.25. Albeit the rather large statistical uncertainties, a deviation from unity can be observed in the first two k^* intervals. In general, this could be interpreted as the pattern of an attractive p–Σ^0 interaction, however, due to the rather modest purity of the Σ^0 candidates, also a possible contribution from the combinatorial p–$(\Lambda\gamma)$ background needs to be considered. This is discussed throughout the remainder of this Chapter. In order to check the possible contribution from detector or

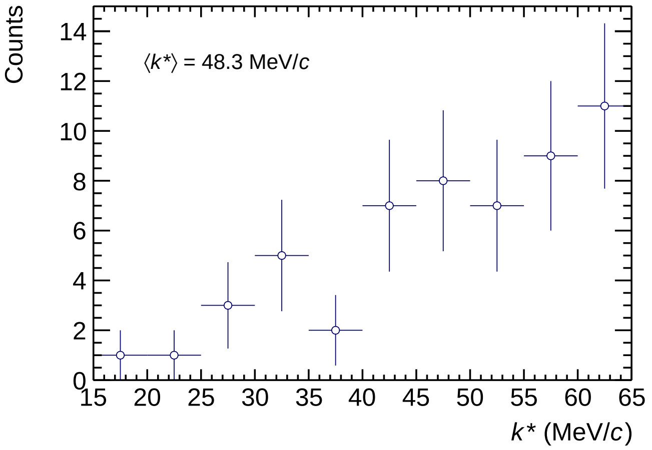

Figure 3.24: The same event p–$\Sigma^0 \oplus \overline{\text{p}}$–$\overline{\Sigma^0}$ k^* distribution before rebinning to what becomes the first bin of the correlation function ($15 < k^* < 65\,\text{MeV}/c$). It is clearly visible that the mean of the distribution is shifted with respect to the bin center at 40 MeV/c.

reconstruction effects the correlation function obtained from PYTHIA 8.2 [201] simulations, filtered through the ALICE detector [205] and reconstruction algorithm [171], is extracted and shown in the right panel of Fig. 3.25. Within the statistical uncertainties the correlation function is consistent with unity, and therefore no sign of kinematic effects influencing the profile at low k^* are observed.

As discussed, the purity of the Σ^0 sample is rather modest. In order to assess whether the uncorrelated $\Lambda\gamma$ ($\overline{\Lambda}\gamma$) background in the Σ^0 ($\overline{\Sigma^0}$) sample contributes to the measured p–Σ^0 correlation function, an invariant mass selection of $5 < |M_{\Lambda\gamma} - M_{\Sigma^0}(p_\mathrm{T})| < 50\,\mathrm{MeV}/c^2$ is chosen, as outlined in Table 3.5. The selection in the sidebands of the invariant mass spectrum ensures that no Σ^0 candidates are present in the sample. The such obtained background candidates are paired with protons, conducting the same checks for shared tracks as in the case of signal candidates. Unlike for the case of the p–Σ^0, the particle–particle and antiparticle–antiparticle correlation functions with $(\Lambda\gamma)$ candidates from left and right of the Σ^0 invariant mass peak demonstrate good agreement, as depicted in Fig. B.6 in the appendix. This underlines further the conclusions made above about different purities as the origin of the discrepancy between the p–Σ^0 and the $\overline{\mathrm{p}}$–$\overline{\Sigma^0}$ correlation function. The two p–$(\Lambda\gamma)$ correlation functions with $(\Lambda\gamma)$ candidates from left and right of the Σ^0 invariant mass peak also demonstrate reasonable agreement with each other and are therefore combined in the following to enhance the statistical significance. Thus, in the following p–$(\Lambda\gamma)$ refers to p–$(\Lambda\gamma) \oplus \overline{\mathrm{p}}$–$(\overline{\Lambda}\gamma)$. By default, the mass intervals of the candidates are chosen as $5 < |M_{\Lambda\gamma} - M_{\Sigma^0}(p_\mathrm{T})| < 50\,\mathrm{MeV}/c^2$, but are varied in the evaluation of the systematic uncertainties as discussed in Sec. 3.4.2. The correlation signal, however, does not depend on the choice of the mass interval within a reasonable invariant mass range around the Σ^0 peak. The resulting correlation function is shown in the left panel of Fig. 3.26. Clearly visible is that a significant correlation signal is present at low k^*. This can be explained by a contribution of the residual p–Λ correlation which is smeared by an uncorrelated γ and is discussed further in Sec. 3.5.3. This conclusion is underlined by the fact that the correlation signal vanishes when studying the correlation function obtained from MC simulations, as depicted in the right panel of Fig. 3.26. Apart from the first bin which has only limited significance due to the low number of counts, no sign of kinematic effects is present within the statistical uncertainties at low k^*.

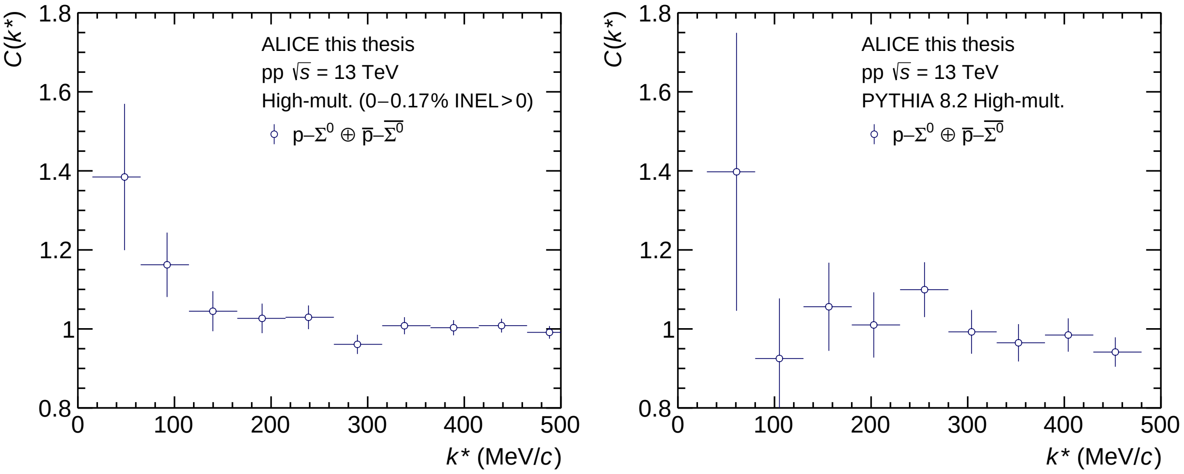

Figure 3.25: p–Σ^0 $\oplus$ $\overline{\mathrm{p}}$–$\overline{\Sigma^0}$ correlation function obtained from data (*left*) and PYTHIA 8.2 simulations with a comparable multiplicity as the data (*right*).

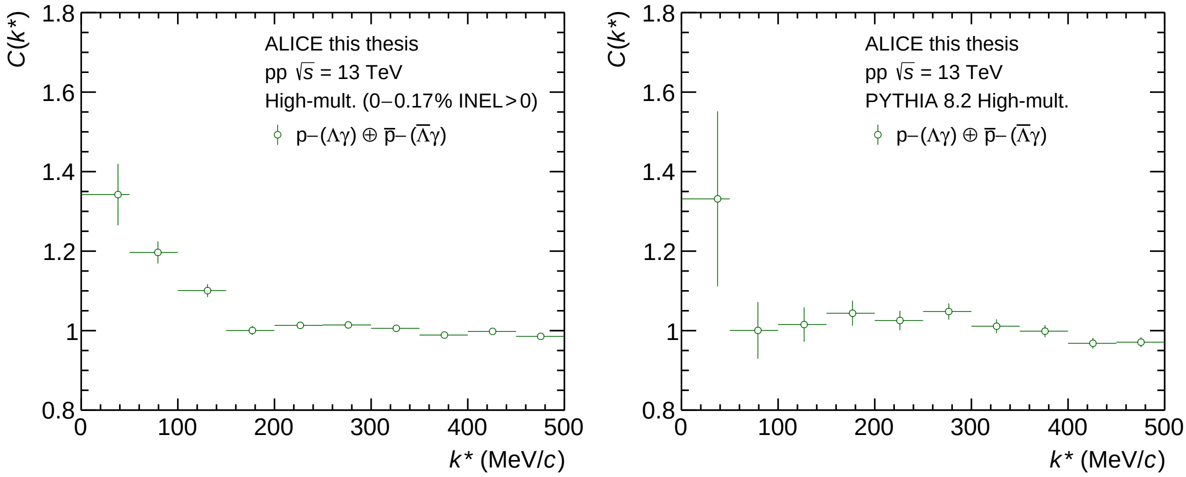

Figure 3.26: p–$(\Lambda\gamma) \oplus \bar{\text{p}}$–$(\bar{\Lambda}\gamma)$ correlation function obtained from data (*left*) and PYTHIA 8.2 simulations with a comparable multiplicity as the data (*right*).

3.4.1 Detector Effects

The finite momentum resolution of the reconstructed particles affects the measured correlation function. This effect needs to be considered when comparing modeled correlation functions to the data. The momentum resolution is obtained from MC simulations generated using PYTHIA 8.2 [201] and shown in the left and right panel of Fig. 3.27 for p–p and p–Σ^0 pairs. At low k^*, the momentum resolution of p–p and p–Σ^0 pairs is about 4 MeV/c and well in agreement with one another. This demonstrates the performance of the reconstruction of the γ and Λ candidates. For the case of the Σ^0, the momentum resolution is mainly defined by the Λ which carries due to its mass most of the momentum after the Σ^0 decay. Therefore, the momentum resolution of the p–Σ^0 is mostly driven by the resolution of p–Λ.

The effect of the momentum resolution on different theoretical models of the p–p and p–Σ^0 interaction, as described in Sec. 3.5.2, is shown in the left and right panel of Fig. 3.28. Apart from modifications at $k^* < 50\,\text{MeV}/c$ the theoretical correlation functions remain unaffected by the finite momentum resolution of the detector.

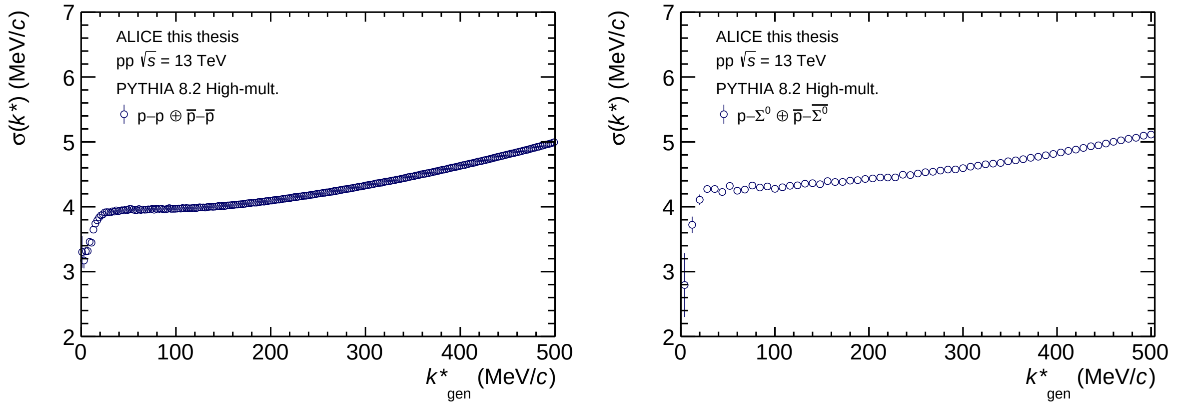

Figure 3.27: Relative momentum resolutions $\sigma(k^*)$ for p–p (*left*) and p–Σ^0 pairs (*right*) obtained from PYTHIA 8.2 simulations.

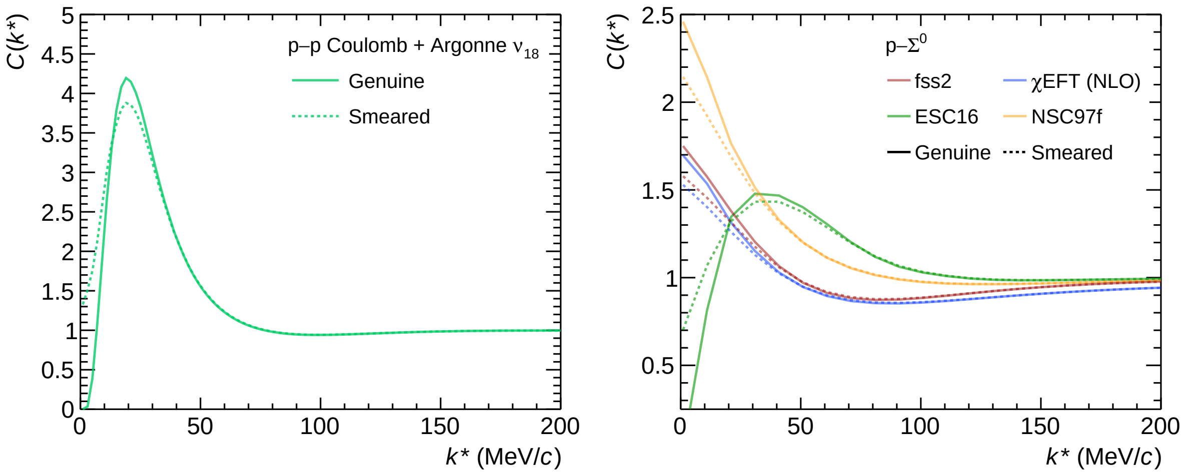

Figure 3.28: Effect of the momentum smearing on the theoretical p–p (*left*) and p–Σ^0 (*right*) correlation functions. Details of the models are discussed in Sec. 3.5.2.

When the trajectories of two particles of the same charge are almost co-linear, i.e. have a low k^*, the finite granularity of the readout, the spatial resolution of the spectrometer, and the precision of the tracking algorithm might introduce detector effects [233]. These include *track splitting*, where one track is incorrectly reconstructed as two, or *track merging*, where two tracks are reconstructed as one. The result is an enhancement (depletion) of the yield of particle pairs at a given k^* for track splitting (merging), and therefore introduces artificial correlations. The trivial modification of the angular differences in φ due to the track bending in the magnetic field is corrected for using the variable

$$\varphi^* = \varphi + \arcsin\left(\frac{0.3 \cdot rBe}{2p_{\mathrm{T}}}\frac{1}{\mathrm{Tm}}\right), \tag{3.8}$$

where B corresponds to the magnitude of the magnetic field, r is the transverse radius at which the value of φ^* is evaluated, and e the charge of the particle. The angular difference both in η and in φ^* is evaluated using MC simulations where effects of the final-state interaction are absent and thus only detector effects can influence the distribution. The result for p–p pairs is shown in Fig. 3.29, and demonstrates that a modest depletion is present for close pairs. For this reason, a circular rejection of $\sqrt{\Delta\eta^2 + \Delta\varphi^{*\,2}} < 0.012$ is applied for this specific pair.

For the p–Σ^0, however, the number of particle pairs is too small to study correlations in the $\Delta\eta\Delta\varphi^*$ space. Therefore, the effect of such a selection is studied in a more direct way. The same circular close pair rejection $\sqrt{\Delta\eta^2 + \Delta\varphi^{*\,2}} < 0.012$ as for the p–p correlation function is introduced and the resulting correlation function is compared to the default one, as depicted in the left panel of Fig. 3.30. The two correlation functions are fully consistent, and therefore no sign of track splitting or merging is observed. For this reason, no dedicated rejection is applied for the p–Σ^0 case in order to maximize the pair yield. Additionally, since four decay tracks are involved, effects of track splitting or merging are smeared over the full range of k^* for the p–Σ^0 correlation function.

As discussed above, residual out-of-bunch pile-up may contribute to the combinatorial background below the Σ^0 invariant mass peak, and accordingly to the p–Σ^0 correlation function. In order to study this effect beyond the sensitivity of the purity of the Σ^0 shown in Fig. 3.18, the

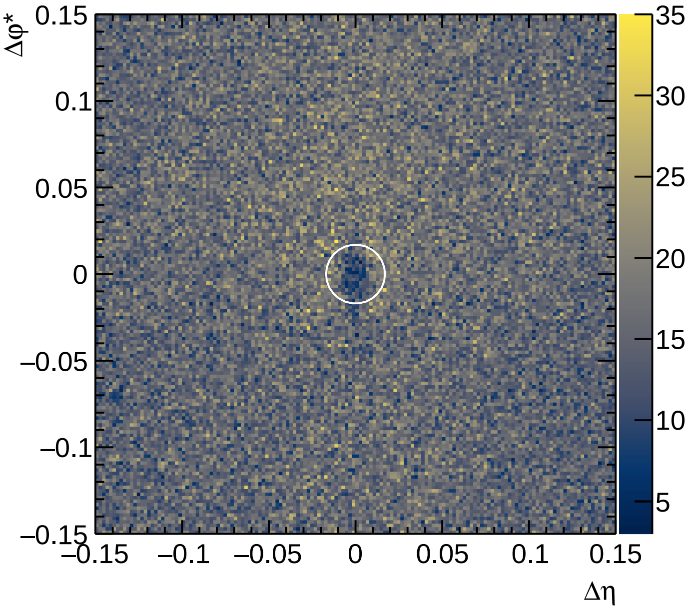

Figure 3.29: Angular difference in the ΔηΔφ* space between p–p pairs. The applied rejection is depicted by the white circle.

correlation function is constructed with timing cuts on the photon child tracks. As shown in the right panel of Fig. 3.30, the resulting correlation function is fully consistent albeit demonstrating significantly larger uncertainties.

This underlines the conclusion that the contribution of residual out-of-bunch pile-up is not relevant for the measurement.

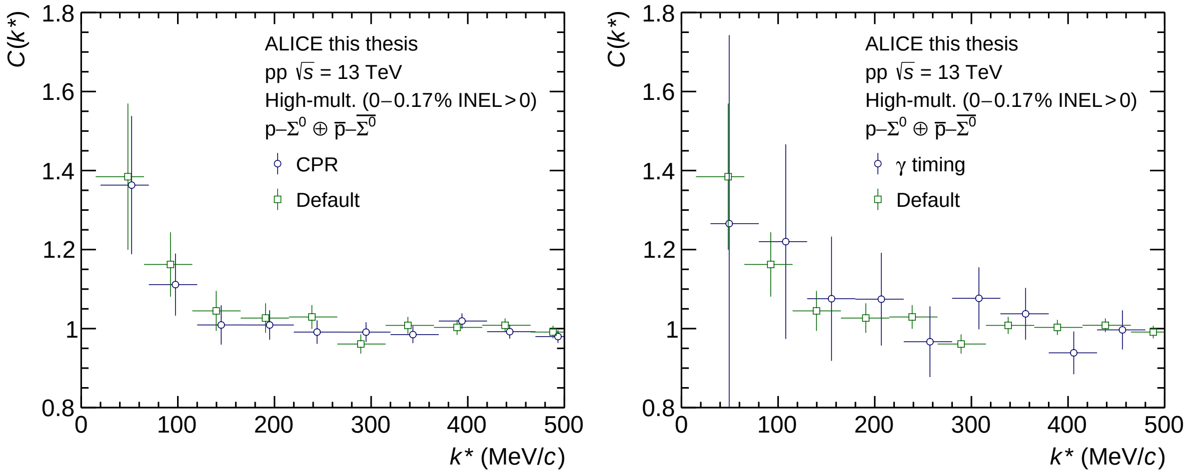

Figure 3.30: Effect of the rejection in the ΔηΔφ* space (*left*), and timing cuts on the photon child tracks (*right*) on the p–Σ^0 correlation function. No significant differences are observed.

3.4.2 Systematic Uncertainties

The systematic uncertainties of the experimental data are evaluated by choosing random combinations of variations of the proton, Λ, γ, and Σ^0 single-particle selection criteria by up to 20% around the default values. The employed variations of the selection criteria of the particle candidates are outlined in Table 3.7. Only choices that modify the pair yield by less than 20% for p–p and 10% for p–Σ^0 with respect to the default choice are considered. Modifications of the Σ^0 purity need to be less than 5%.

To reduce the impact of statistical fluctuations due to the low number of particle pairs at low k^* the systematic uncertainties are evaluated in k^* intervals of 20 MeV/c for the p–p correlation function and 100 MeV/c for p–Σ^0. The individual variations are assumed to follow a flat distribution, and the resulting systematic uncertainties are parametrized by an exponential function and interpolated to obtain the final point-by-point uncertainties. At the respectively lowest k^*, the total systematic uncertainty is of the order of 2.5% for both the p–p and the p–Σ^0 correlation function. The p–Σ^0 correlation function with the systematic uncertainties is shown in Fig. 3.31, the corresponding Figs. B.7 and B.8 for the p–p and the p–($\Lambda\gamma$) correlation functions can be found in the appendix.

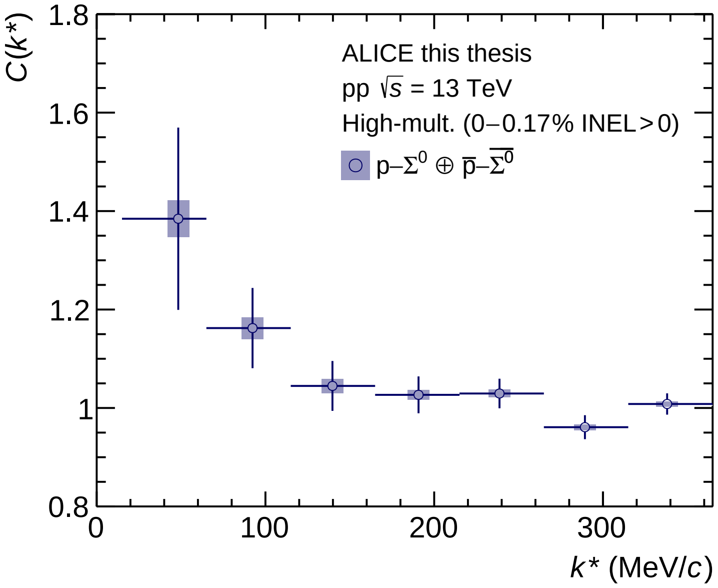

Figure 3.31: Experimental p–Σ^0 $\oplus$ $\overline{\text{p}}$–$\overline{\Sigma^0}$ correlation function with systematic uncertainties.

Table 3.7: Variations of the selection criteria for the p, Λ, γ and Σ^0 candidates to evaluate the systematic uncertainties.

Selection criterion			**Default**	**Variation**
Proton candidates				
Min. p_T		(GeV/c)	0.5	0.4, 0.6
Max. $\lvert\eta\rvert$			0.8	0.75, 0.85
Min. $n_\text{Cluster, TPC}$			80	70, 90
Particle identification n_σ			3	2.5, 3.5
Λ *candidates*				
Min. p_T		(GeV/c)	0.3	0.24, 0.36
Min. $\cos(\alpha)$			0.999	0.995, 0.99925
$\lvert M_{p\pi} - M_{\Lambda,\mathrm{PDG}}\rvert$		(MeV/c^2)	6	8
Max. $\lvert\eta\rvert$ child tracks			0.9	0.85
Min. $n_\text{Cluster, TPC}$ child tracks			70	80, 60
PID child tracks $n_{\sigma,\ \mathrm{TPC}}$			5	4, 6
γ *candidates*				
Min. p_T		(GeV/c)	0.02	0, 0.15
Min. $\cos(\alpha)$			0.999	0.995, 0.99925
Armenteros-Podolanski selection q_T		(GeV/c)	0.06	0.05, 0.1
Opening angle in B-field $\lvert\psi_\mathrm{pair}\rvert$			0.2	0.15, 0.3
Min. p_T child tracks		(GeV/c)	0.05	0, 0.075
Max. $\lvert\eta\rvert$ child tracks			0.9	0.85
Ratio findable TPC cluster child tracks			0.35	0.3, 0.5
PID child tracks $n_{\sigma,\ \mathrm{TPC}}$	up		7	8, 6
	low		−6	−7, −5
Σ^0 *candidates*				
Sideband mass selection	up	(MeV/c^2)	50	35, 75
	low	(MeV/c^2)	5	3.5, 7.5
p–p pairs				
Close pair rejection			0.012	0.010, 0.014

3.5 The Modeled Correlation Function

As already indicated above, the measured correlation function contains the genuine signal of the final-state interaction under study, but also contributions from residual correlations due to impurities, feed-down and detector effects. The approach chosen in this work is leave the measured correlation function without any corrections, and instead include all relevant contributions to the modeled correlation function.

3.5.1 Decomposition of the Correlation Function

The experimental correlation function is distorted by two mechanisms. On the one hand, the sample of particle pairs can include misidentified particles. On the other hand, particles stemming from the weak decay of resonances (*feed-down*) may contribute as well. In this case, the correlation signal is caused by the parent particle instead of the particle of interest. Accordingly, the measured correlation function carries information from different, misidentified particle pairs or from the decay parent of one of the two or both particles. These effects are included by modeling the total correlation function as the sum of all these contributions,

$$C_{\mathrm{model}}(k^*) = 1 + \sum_i \lambda_i \cdot (C_i(k^*) - 1). \tag{3.9}$$

The $C_i(k^*)$ are the corresponding genuine or residual contributions to the measured correlation function transformed into the momentum frame of the corresponding pair, as explained later in this Section. The information about the relative contribution is given by the λ parameters, and obtained in a data-driven way from single-particle properties such as the purity $\mathcal{P}$ and channel fraction f_i of particle species X and Y as $\lambda_{ij} = \mathcal{P}_i(\mathrm{X})f_i(\mathrm{X})\mathcal{P}_j(\mathrm{Y})f_j(\mathrm{Y})$ [128, 152]. In order to compare the data to theoretical models of the interaction of the particle pair of interest, all relevant contributions need to be properly modeled and accounted for.

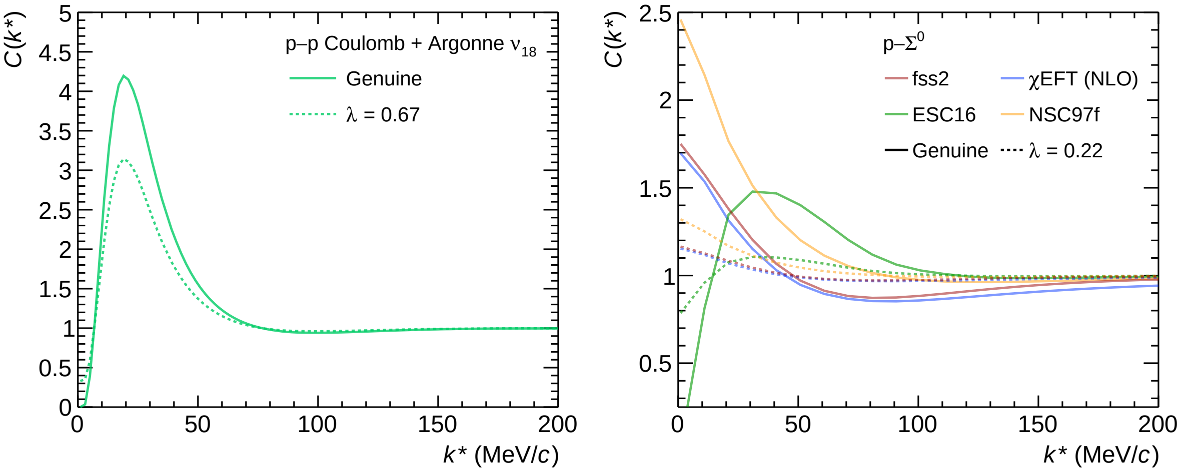

Figure 3.32: Effect of the finite experimental purity and the contribution from secondaries on the theoretical p–p (*left*) and p–Σ^0 (*right*) correlation functions. Details of the models are discussed in Sec. 3.5.2.

p–p Correlation Function For the case of the p–p correlation function the following contributions are to be considered

$$\begin{aligned}\{\mathrm{p–p}\} = {} & \mathrm{p–p} + \mathrm{p–p}_{\Lambda} + \mathrm{p}_{\Lambda}\mathrm{–p}_{\Lambda} + \mathrm{p–p}_{\Sigma^+} + \mathrm{p}_{\Sigma^+}\mathrm{–p}_{\Sigma^+} \\ & + \mathrm{p}_{\Lambda}\mathrm{–p}_{\Sigma^+} + \tilde{\mathrm{p}}\mathrm{–p} + \tilde{\mathrm{p}}\mathrm{–p}_{\Lambda} + \tilde{\mathrm{p}}\mathrm{–p}_{\Sigma^+} + \tilde{\mathrm{p}}\mathrm{–}\tilde{\mathrm{p}},\end{aligned} \tag{3.10}$$

where $\tilde{\mathrm{X}}$ refers to misidentified particles of species X. Since, for instance, the parent correlation function Λ–Σ^+ is unconstrained and contributes only weakly to the total correlation function, it is assumed to be flat. Only the genuine p–p and the residual p–Λ correlation functions are explicitly modeled, while the contribution from misidentifications and other residual correlation function are assumed to be flat. Thus, the number of contributions reduces to only four. The contribution of primary and feed-down particles is determined by the DCA template fits as discussed in Sec. 3.2. In particular, a significant contribution of 20.3% arises from Λ decays. The corresponding λ parameters are displayed in Table 3.8, and the effect on the theoretical correlation function is shown in the left panel of Fig. 3.32. The genuine p–p correlation function contributes with 67% to the measured signal.

Table 3.8: Weight parameters of the individual components of the p–p correlation function.

Pair	**λ (%)**		**Treatment**
p–p	67.0		Genuine
p–p_{Λ}	20.3		p–Λ
p_{Λ}–p_{Λ}	1.5	11.6	Feed-down (flat)
p–p_{Σ^+}	8.5		
p_{Σ^+}–p_{Σ^+}	0.3		
p_{Λ}–p_{Σ^+}	1.3		
$\tilde{\mathrm{p}}$–p	0.9	1.1	Misidentification (flat)
$\tilde{\mathrm{p}}$–p_{Λ}	0.1		
$\tilde{\mathrm{p}}$–p_{Σ^+}	0.1		
$\tilde{\mathrm{p}}$–$\tilde{\mathrm{p}}$	0		

p–Σ^0 Correlation Function For the case of the p–Σ^0 correlation function the following contributions have to be taken into account

$$\{\mathrm{p–}\Sigma^0\} = \mathrm{p–}\Sigma^0 + \mathrm{p}_{\Lambda}\mathrm{–}\Sigma^0 + \mathrm{p}_{\Sigma^+}\mathrm{–}\Sigma^0 + \tilde{\mathrm{p}}\mathrm{–}\Sigma^0 + \mathrm{p–}\tilde{\Sigma^0} + \mathrm{p}_{\Lambda}\mathrm{–}\tilde{\Sigma^0} + \mathrm{p}_{\Sigma^+}\mathrm{–}\tilde{\Sigma^0} + \tilde{\mathrm{p}}\mathrm{–}\tilde{\Sigma^0}, \tag{3.11}$$

where the misidentified $\tilde{\Sigma^0}$ refers to the uncorrelated $\Lambda\gamma$ background in the invariant mass spectrum of the Σ^0. The contributions of the proton are constrained by the template fits. On the other hand, only strongly decaying resonances feed to the Σ^0 [7], hence a primary fraction of 100% is assumed. The Σ^0 purity at the average p_{T} of the candidates that contribute to the correlation function at $k^* < 200\,\mathrm{MeV}/c$ yields about 27.4%. This value is used for the evaluation of the λ parameters. The parent correlation functions, such as Λ–Σ^0, are unconstrained and contribute only weakly to the total correlation function. Therefore, they are assumed to be flat and the number of contributions reduces to only four. The resulting λ parameters are displayed in Table 3.9, and the effect on the different theoretical curves is shown in the right panel of Fig. 3.32. Due to the rather modest purity of the Σ^0 candidates, the genuine p–Σ^0 correlation function contributes with 22% to the measured signal and the by far dominating contribution arises from the combinatorial p–$(\Lambda\gamma)$ background.

Table 3.9: Weight parameters of the individual components of the p–Σ^0 correlation function.

Pair	λ (%)		Treatment
p–Σ^0	22.0		Genuine
p–$\tilde{\Sigma^0}$	59.8	73.1	p–$(\Lambda\gamma)$
p_Λ–$\tilde{\Sigma^0}$	9.1		
p_{Σ^+}–$\tilde{\Sigma^0}$	3.8		
$\tilde{\mathrm{p}}$–$\tilde{\Sigma^0}$	0.4		
p_Λ–Σ^0	3.3	4.7	Feed-down (flat)
p_{Σ^+}–Σ^0	1.4		
$\tilde{\mathrm{p}}$–Σ^0	0.2		Misidentification (flat)

3.5.2 Genuine Correlation Function

In case the interaction of the particle pair under study is well known, the correlation function can be employed to extract information about the particle-emitting source. On the other hand, if the particle-emitting source is reasonably well constrained, the correlation function can also be used to extract information about the final-state interaction of a given particle pair, or to compare different theoretical models to the data.

p–p Correlation Function For the modeling of the p–p correlation function, in addition to the strong interaction, also Coulomb and quantum statistics need to be considered. The strong interaction in the N–N sector is theoretically well understood, and a state-of-the-art model – the Argonne v_{18} potential [134] – is employed. The *Correlation Analysis Tool using the Schrödinger equation* (CATS) [135] allows one to use either a local potential $V(r)$ or directly the two-particle wave function and additionally any source distribution as an input to compute the correlation function. For the computation of the correlation function with CATS the *S*-, *P*-, and *D*-waves are considered according to their statistical weights. The resulting genuine correlation function is depicted e.g. in the left panel of Fig. 3.32.

p–Σ^0 Correlation Function The N–Σ interaction can be modeled employing various theoretical approaches, as discussed in Sec. 1.2.2. Accordingly, the measured correlation function can be used as a benchmark for these different approaches. In general, the total p–Σ^0 correlation is defined by the sum of the correlation functions obtained for each of the four available spin and isospin states, taking into account the statistical weights

$$\begin{aligned} C_{\mathrm{p}-\Sigma^0} = \frac{1}{12}\, C_{\mathrm{p}-\Sigma^0}(I=1/2,\ S=0) + \frac{1}{4}\, C_{\mathrm{p}-\Sigma^0}(I=1/2,\ S=1) \\ + \frac{1}{6}\, C_{\mathrm{p}-\Sigma^0}(I=3/2,\ S=0) + \frac{1}{2}\, C_{\mathrm{p}-\Sigma^0}(I=3/2,\ S=1). \end{aligned} \tag{3.12}$$

This approach assumes an unpolarized emission with a weight of $1/4$ for the spin singlet and $3/4$ for the spin triplet. The corresponding correlation functions are already expressed in the particle basis due to the presence of coupled channels in the p–Σ^0 system. The contribution from n–$\Sigma^+ \rightarrow$ p–Σ^0 ($I = 1/2,\ 3/2$) is especially relevant, since the mass of the n–Σ^+ system is due to isospin breaking only about $2\,\mathrm{MeV}/c^2$ below the p–Σ^0 threshold [7]. An additional contribution from p–$\Lambda \rightarrow$ p–Σ^0 ($I = 1/2$) is less important since it is about 77 MeV/c^2 below threshold [7]. Since coupled-channels are known to have a sizeable impact on the correlation function [138, 139], a meaningful comparison can only be conducted when properly including the respective contributions.

The correlation function is modeled employing either CATS or the Lednický–Lyuboshits approach [133]. The latter relies on the effective-range expansion using scattering parameters as input to evaluate the correlation function. In both cases only the interaction in the S-wave is considered. Details of the employed models are discussed in Sec. 1.2.2.1.

For χEFT at next-to-leading order (NLO) [83], NSC97f [78], and ESC16 [81] the correlation function is computed using CATS from the isospin-averaged wave functions including the coupling of the n–Σ^+ and the p–Λ system to the p–Σ^0 correlation function. The weights of the contributions from n–Σ^+ and p–Λ are, lacking the knowledge of the coupling strength and conversion rate, assumed to be unity. Figure 3.33 depicts a decomposition of the correlation functions and displays for both χEFT (left) and the NSC97f model (right) a strong influence of the coupling n–$\Sigma^+ \rightarrow$ p–Σ^0 leading to a sizable enhancement of the correlation function. The inclusion of the p–$\Lambda \rightarrow$ p–Σ^0 channel has, as expected, an almost negligible effect. The inclusion of the relevant couplings leads to an enhancement of the correlation signal of about 50% (30%) for χEFT (NSC97f), demonstrating their importance.

For fss2 [85], on the other hand, the Lednický–Lyuboshits approach [133] is employed. The effect of the p–$\Lambda \rightarrow$ p–Σ^0 coupled channel is incorporated via complex scattering parameters, while the coupling of n–$\Sigma^+ \rightarrow$ p–Σ^0 is explicitly included by means of a coupled-channel approach considering the isospin breaking due to the mass splitting [234]. Therefore, the only required ingredients are the scattering parameters for all spin and isospin channels. For the $(I = 1/2,\ S = 0)$ component the coupling of p–$\Lambda \rightarrow$ p–Σ^0 in fss2 is expected to be rather weak [234] and therefore the elasticity coefficient $\eta(k^*) = 1$. Accordingly, Eq. 1.10 can be employed to extract the scattering parameters from the phase shift [85, 234]. On the other hand, the $(I = 1/2,\ S = 1)$ component is significantly affected by the p–$\Lambda \rightarrow$ p–Σ^0 coupling. This is reflected in sizable

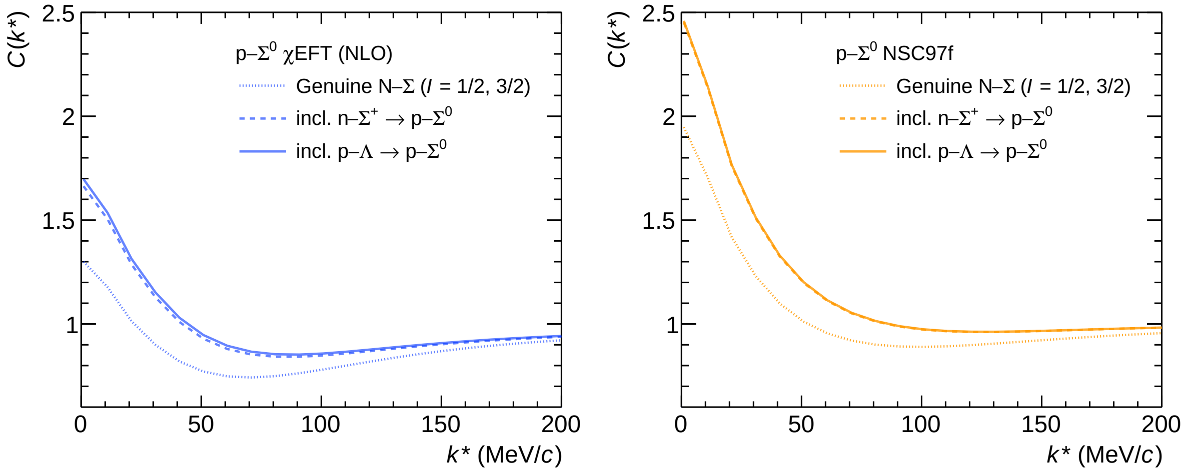

Figure 3.33: The influence of the coupled channels of n–Σ^+ and p–Λ to the p–Σ^0 correlation function modeled using χEFT [83] (*left*) and NSC97f [78] (*right*). The dotted line denotes the genuine N–Σ correlation function. The dashed line includes the n–$\Sigma^+ \rightarrow$ p–Σ^0 contribution, while the solid line includes additionally the p–$\Lambda \rightarrow$ p–Σ^0 component.

imaginary parts of the scattering parameters. The effective range approximation is expanded to obtain the scattering parameters from a fit of the elasticity coefficient η and the phase shifts δ [85, 234]. Finally, for the $I = 3/2$ component only the N–Σ components are relevant and the scattering parameters can be readily extracted from Ref. [85] in the isospin basis. The resulting scattering parameters [85, 234] are shown in Table 3.10 in the femtoscopy sign convention where a positive scattering length corresponds to an attractive interaction.

In general, it should be noted that the theoretical descriptions of the N–Σ interaction are not well constrained due to a lack of experimental data. The resulting correlation functions for the p–Σ^0 case are shown e.g. in the right panel of Fig. 3.32. The strength of this specific channel is that the models differ significantly among each other, permitting to conduct decisive measurements. Details of the resulting correlation functions are discussed in Sec. 3.7.

3.5.3 Residual Correlations

In addition to the correlation function of interest, a sizeable feed-down from other channels can be present in the sample and this may distort the measurement. Following the strategy outlined before, these contributions are included in the modeled correlation function which is compared to the data.

p–p Correlation Function A significant contribution of the p–Λ correlation feeds into the measurement of the p–p correlation function. The genuine p–Λ is modeled using χEFT at NLO [83], as discussed in Sec. 1.2.2. Since experimental constraints on the p–Λ interaction are rather scarce, different approaches exist to model it. This is considered in the evaluation of the systematic uncertainties of the fitting procedure. The correlation function resulting from χEFT (NLO) is shown in the right panel of Fig. 3.34. It is transformed into the momentum basis of the p–p pair by applying the corresponding decay matrices [128, 235], shown in the left panel of Fig. 3.34. Finally, the weighting with the corresponding λ parameter is performed. As depicted in the right panel of Fig. 3.34, the resulting correlation function deviates only slightly from unity.

Accordingly, all further contributions to the p–p correlation function are assumed to be $C(k^*) \sim 1$.

p–Σ^0 Correlation Function The main contribution to the measured p–Σ^0 correlation function stems from combinatorial $\Lambda\gamma$ background in the invariant mass spectrum of the Σ^0. These candidates are obtained by pairing the copiously produced uncorrelated Λ and γ. Due to the vanishing mass of the γ, the kinetic properties of the $\Lambda\gamma$ candidate are mainly defined by the Λ. Accordingly, if the Λ candidate underwent final-state interactions with the proton, the resulting modification of the relative momenta of the two particles is propagated to the $\Lambda\gamma$ candidate as well. Therefore, the measured p–$(\Lambda\gamma)$ correlation function is expected to inherit from the p–Λ

Table 3.10: Scattering parameters of the p–Σ^0 interaction extracted from the fss2 model [85, 234].

	$S=0$		$S=1$	
I	f_0 (fm)	d_0 (fm)	f_1 (fm)	d_1 (fm)
1/2	−1.1	−1.5	$-1.1 + i4.3$	$-2.2 - i2.4$
3/2	2.51	4.92	−0.73	−1.22

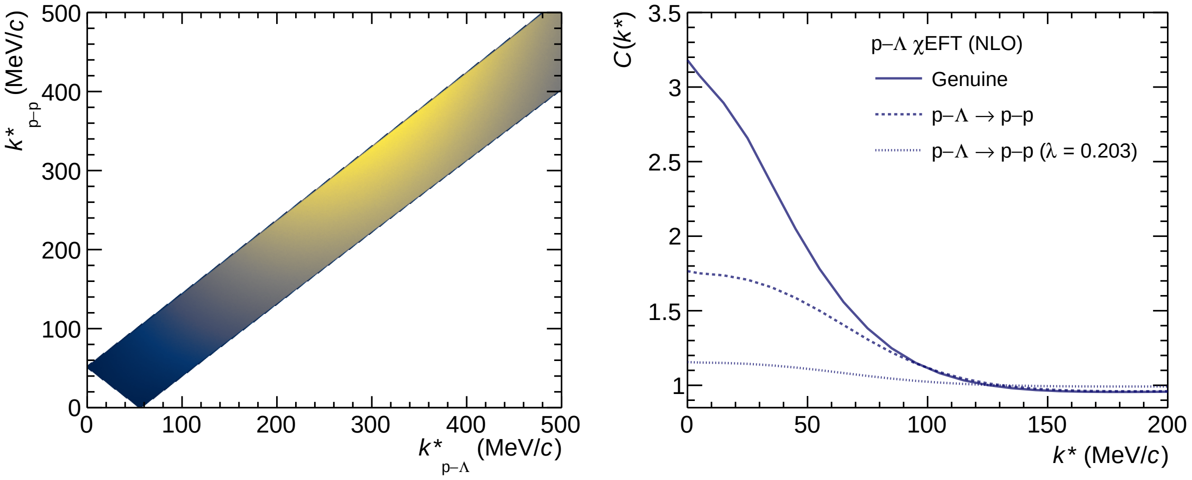

Figure 3.34: The transformation matrix from the p–Λ momentum base to that of the p–p correlation function (*left*) and the effect of the transformation, the finite experimental purity, and feed-down fractions on the p–Λ correlation function modeled using χEFT at NLO [83] (*right*).

correlation function. Indeed, as depicted in Fig. 3.26, the p–$(\Lambda\gamma)$ correlation function reflects the pattern of an attractive interaction at low k^*. The attractive nature of the p–Λ interaction is well established from theoretical predictions [78, 81–83, 85] and experimental observations [36–43, 128, 152]. Therefore, the signal in the measured p–$(\Lambda\gamma)$ correlation function can be attributed to the residual correlation of the p–Λ interaction. Due to the rather modest purity of the Σ^0 candidates, a sizeable contribution from the p–$(\Lambda\gamma)$ baseline is also present in the measured p–Σ^0 correlation function, as outlined in Table 3.9. Correspondingly, a residual p–Λ contamination of the measured p–Σ^0 signal is expected as well.

The resulting contamination of the p–Σ^0 correlation function is modeled employing the p–Λ interaction. The benchmark for this procedure is the signal in the measured p–$(\Lambda\gamma)$ sideband correlation function itself, where no p–Σ^0 final-state interactions are present. The construction of the $\Lambda\gamma$ candidate leads to a smearing of the p–Λ correlation by the additional γ. The transformation from the p–Λ system to the p–Σ^0 or the p–$(\Lambda\gamma)$ momentum basis is accordingly conducted by considering the kinematics of the uncorrelated γ, and by computing the relative momentum in the p–Σ^0 or p–$(\Lambda\gamma)$ momentum basis. The separate treatment of the Σ^0 signal region and the $(\Lambda\gamma)$ sidebands is necessary since the invariant mass selection significantly influences the kinematics. In principle, the transformation matrix can be obtained from MC simulations, where the effect of final-state interactions is not present. Due to the severely limited number of pair candidates, however, this approach is not feasible. For this reason, phase space simulations are employed where the particle candidates are constructed by sampling from the experimental p_{T}, η and φ distributions of the protons, Λ, and γ. The invariant mass selection of the Σ^0 and $(\Lambda\gamma)$ candidates is conducted according to the employed cuts outlined in Table 3.5. The k^* in the p–Λ and the p–Σ^0 or p–$(\Lambda\gamma)$ momentum basis is computed for the resulting pair candidates.

The resulting transformation matrix for p–Σ^0 pairs is depicted in the left panel of Fig. 3.35. The strict selection on the invariant mass of the Σ^0 candidates and the large mass difference between the Λ and the γ result in a linear correlation between the p–Λ and the p–Σ^0 system. The spread is larger for the p–$(\Lambda\gamma)$ system due to the broader invariant mass window. The effect of the transformation of the p–Λ correlation function to the p–Σ^0 and the p–$(\Lambda\gamma)$ system

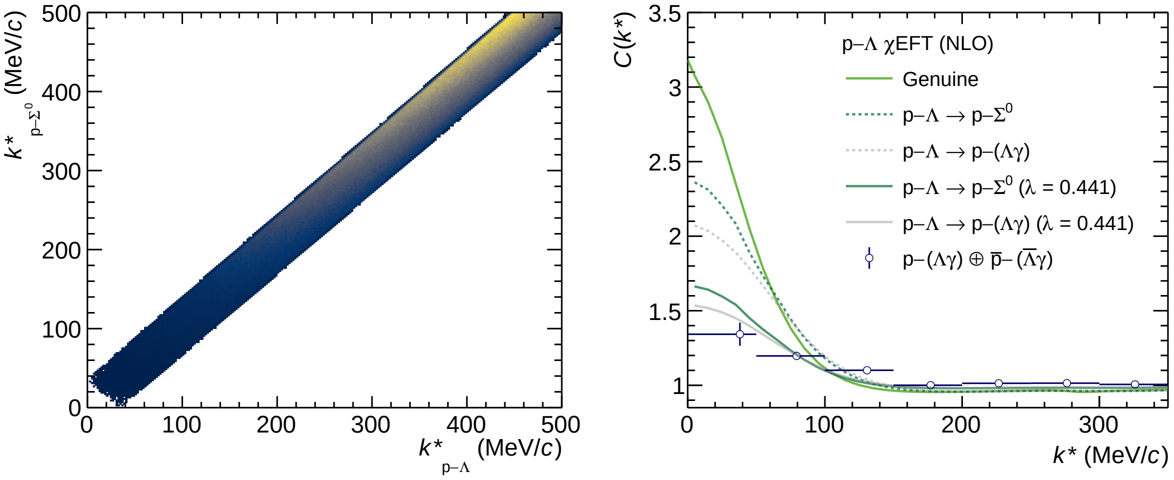

Figure 3.35: (*Left*) The transformation matrix from the p–Λ momentum basis to that of the p–Σ^0. (*Right*) The effect of the transformation of the p–Λ correlation function modeled using χEFT at NLO [83] to the p–Σ^0 (*teal*) and the p–$(\Lambda\gamma)$ (*gray*) momentum basis. The dashed lines correspond to the transformation of the genuine p–Λ correlation function, and the full lines consider additionally the finite experimental purity, and feed-down fractions. The data points display the measured p–$(\Lambda\gamma)$ baseline correlation function.

is depicted in the right panel of Fig. 3.35. The genuine p–Λ correlation function is modeled using χEFT at NLO [83]. The dashed lines correspond to the transformation of the genuine p–Λ correlation function to the p–Σ^0 and the p–$(\Lambda\gamma)$ system, including the effect of the finite momentum resolution. The correlation signal after the transformation is quite pronounced in both cases, much more than e.g. in the case p–Λ → p–p shown in Fig. 3.34. Due to the stricter selection in the invariant mass space for the Σ^0, the residual correlation signal is stronger in the p–Σ^0 than the p–$(\Lambda\gamma)$ system.

As in the case of the protons and Σ^0, the experimental Λ sample contains contributions from misidentifications and feed-down from the decay of resonances, that propagate to the experimental p–Λ correlation function. The primary fraction of the Λ candidates is extracted similarly to the case of the protons by MC template fits to the measured CPA distribution [152, 153, 236]. A significant feed-down is found to stem from decays of Σ^0 (19%), $\Xi^\pm$ (11%), and Ξ^0 (11%), with a primary Λ fraction of about 59% [236]. Considering additionally the purity and primary fraction of protons, and the Λ purity, the contribution of the genuine p–Λ correlation function is 44.1%.

The resulting transformation of the experimental p–Λ correlation function to the p–Σ^0 and the p–$(\Lambda\gamma)$ system is depicted by the full lines in the right panel of Fig. 3.35. As expected, the correlation signal is more pronounced in the p–Σ^0 system than the p–$(\Lambda\gamma)$ system. The difference between the two transformations is most prominent at low k^* and remains below 2% for $k^* > 50\,\mathrm{MeV}/c$. The benchmark of the procedure is the comparison of the measured p–$(\Lambda\gamma)$ sideband correlation function to the transformed p–Λ correlation function considering the λ parameters. As depicted by the solid gray line in the right panel of Fig. 3.35, the agreement is not satisfactory, especially at larger k^*. Therefore, the transformed p–Λ correlation function seems not to be sufficient to describe the signal in the p–$(\Lambda\gamma)$ correlation function.

One possible explanation for the observed difference is related to the λ parameter of the genuine p–Λ correlation function. If the reconstruction of the Σ^0 was 100% efficient, the sidebands would contain absolutely no feed-down contribution from the decay of the Σ^0 to the Λ. At the same time, the feed-down would be significantly enhanced in the peak region. In both cases, the primary fraction of the Λ would be modified, and accordingly the λ parameter. Since the efficiency of the Σ^0 reconstruction is significantly below the percent level, the resulting modification of the primary fraction of the Λ is expected to be rather small. A detailed investigation of the primary and feed-down fractions would require to conduct the MC template fits of the CPA distributions of the Λ candidates used to construct the Σ^0 and $(\Lambda\gamma)$. With the limited amount of particle candidates, however, this is not feasible.

Additional contributions to the p–$(\Lambda\gamma)$ correlation function might stem from correlations between the γ and the proton, arising e.g. from decays of Δ resonances [7]. The effect of such, rather rare, decays is smeared by the Λ and thus it is questionable whether the signal would be appreciable in the correlation function. The present experimental uncertainties, however, do not allow a more detailed investigation of the p–$(\Lambda\gamma)$ baseline correlation function.

Therefore, the shape is parametrized with a Gaussian distribution fitted to the experimental p–$(\Lambda\gamma)$ correlation function. As depicted in Fig. 3.36, this yields a good description of the experimental data and, weighted by its λ parameter, defines the baseline of the measurement of the p–Σ^0 correlation function. The width of the fit curve corresponds to one standard deviation of the total systematic uncertainty of the fit, and is significantly larger than the difference originating from the transformation to the p–Σ^0 or the p–$(\Lambda\gamma)$ system discussed above.

All other contributions stemming from misidentified protons or from feed-down are assumed to be flat $C(k^*) \sim 1$.

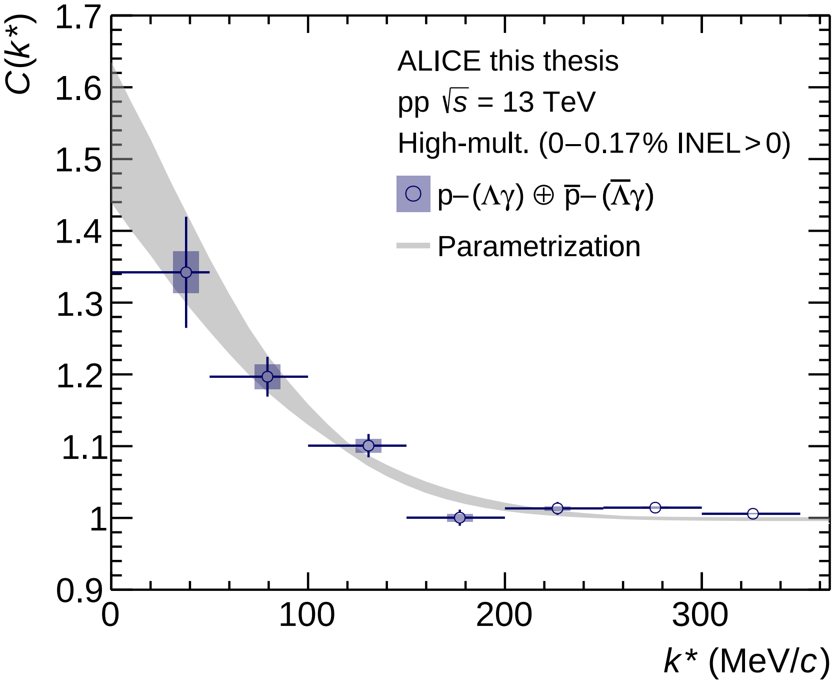

Figure 3.36: Measured correlation function of p–$(\Lambda\gamma)$ $\oplus$ $\overline{\mathrm{p}}$–$(\overline{\Lambda}\gamma)$. Statistical (bars) and systematic uncertainties (boxes) are shown separately. The gray band denotes the parametrization employing a Gaussian function. The width of the band corresponds to one standard deviation of the systematic uncertainty of the fit.

3.5.4 Total Correlation Function

The total correlation function incorporating all ingredients according to Eq. 3.9 is multiplied by a polynomial baseline $C_{\mathrm{non-femto}}(k^*)$ yielding,

$$C(k^*) = C_{\mathrm{non-femto}}(k^*) \cdot C_{\mathrm{model}}(k^*), \tag{3.13}$$

to account for the normalization and non-femtoscopic background effects [152]. Indeed, all measured correlation functions exhibit an increase for $k^* > 200\,\mathrm{MeV}/c$, where final-state interactions among the particles are suppressed and therefore the correlation function is expected to approach unity. Such non-femtoscopic effects are more pronounced in systems with lower multiplicities [125] and caused by momentum and energy conservation [152]. An additional contribution might arise from mini-jets, which significantly contribute in pion analyses [237], but is found to be suppressed in the analysis of baryon pairs [128, 152]. Energy and momentum conservation, on the other hand, leads to a contribution to the signal which can be modeled using a linear function [238], which is therefore used in this work.

p–Σ^0 Correlation Function Since the uncertainties of the p–Σ^0 correlation function even at larger k^* are sizable, the parameters of the baseline are obtained from a fit to the p–$(\Lambda\gamma)$ correlation function in $k^* \in [250, 600]\,\mathrm{MeV}/c$. In this region, the p–$(\Lambda\gamma)$ correlation function is consistent and kinematically comparable with the p–Σ^0 correlation function, however features significantly smaller uncertainties. This leads to a more precise constraint on the parameters of the baseline.

3.5.5 Systematic Uncertainties

In order to assess the systematic uncertainties associated with the femtoscopic fit, all correlation functions resulting from the variations of the selection criteria are fitted individually. Furthermore, several input parameters of the fit are modified.

p–p Correlation Function The range of the femtoscopic fit is varied as outlined in Table 3.11. Furthermore, the input to the λ parameters is modified by $\pm 20\%$, while maintaining a constant sum of the primary and secondary fractions. As discussed above, non-femtoscopic correlations arising from energy and momentum conservation can lead to a non-flat baseline. To cover this possibility, in addition to the normalization constant, the fit is performed with a linear and quadratic slope.

Since the p–Λ is experimentally not very well constrained, different models for the interaction exist. Therefore, additionally to χEFT at next-to-leading order [83], further models of the p–Λ interaction are considered. As a systematic variation, the p–Λ feed-down to p–p is modeled using χEFT at leading order (LO) [82] and the Usmani potential [148]. The resulting fit curves have a width corresponding to one standard deviation of the total systematic uncertainty of the fit.

Table 3.11: Systematic variations of the parameters for the femtoscopic fit of the p–p correlation function. Details are explained in the text.

Parameter		Default	Variation
Femtoscopic fit	(MeV/c)	375	350, 400
Non-femtoscopic slope		constant	linear quadratic
Composition of secondaries	$\Lambda \to \mathrm{p}$	0.7	0.56, 0.84
	$\Sigma^+ \to \mathrm{p}$	$1 - (\Lambda \to \mathrm{p})$	
p–Λ interaction		χEFT (NLO) [83]	χEFT (LO) [82] Usmani potential [148]

p–Σ^0 Correlation Function The range of the femtoscopic fit and the parametrization of the p–$(\Lambda\gamma)$ baseline is varied, as outlined in Table 3.12. The input to the λ parameters is modified by $\pm 20\%$, while maintaining a constant sum of the primary and secondary fractions. The parameters of the baseline are varied within 1σ of their uncertainties considering their correlation, including the case of a constant baseline. As outlined in Sec. 3.6, the femtoscopic radius obtained from the p–p correlation function is employed to model the p–Σ^0 correlation function. It is varied according to its uncertainties. Moreover, as discussed in the next Section, strong decays may influence the source size of p–Σ^0. Therefore, such variations are incorporated by decreasing r_0 additionally by 15%. The width of the resulting model bands is computed as the 1σ confidence interval around the central value. The correlated absolute uncertainty from the modeling of the p–$(\Lambda\gamma)$ baseline correlation function is common to all models, and therefore shown separately.

Table 3.12: Systematic variations of the parameters for the femtoscopic fit of the p–Σ^0 correlation function. Details are explained in the text.

Parameter		Default	Variation
Femtoscopic fit	(MeV/c)	550	500, 600
Sideband fit	(MeV/c)	650	600, 700
Non-femtoscopic slope		Fit within $250 - 600\,\mathrm{MeV}/c$	$\pm 1\sigma$ of the parameters
Composition of secondaries	$\Lambda \to \mathrm{p}$	0.7	0.56, 0.84
	$\Sigma^+ \to \mathrm{p}$	$1 - (\Lambda \to \mathrm{p})$	
Femtoscopic radius	(fm)	1.249	1.033, 1.281

3.6 The Femtoscopic Source

In order to study the interaction among a given baryon–baryon pair using the femtoscopy formalism, the size of the particle-emitting source needs to be constrained. This can be accomplished employing pairs of known interaction, such as N–N. Due to the difficulties associated with the reconstruction of neutral particles, the measured p–p correlation function is used for this purpose.

The p–p correlation function, including the systematic uncertainties, is shown in Fig. 3.37 and demonstrates the interplay of the involved final-state interactions and quantum statistics. The attractive strong interaction is reflected in an enhancement of the correlation function for $k^* < 100\,\mathrm{MeV}/c$, while at very low k^* the repulsive Coulomb interaction and quantum statistics lead to a depletion. The repulsive contribution of higher partial waves at intermediate k^* becomes apparent in the inset. The modeled theoretical correlation function including all these contributions, and in addition also considering impurities and feed-down, is fitted to the data under the premise of a one-dimensional Gaussian source. The width of the latter is in the following referred to as the femtoscopic radius r_0 and left as a free parameter for the fit to determine. The fit with the Argonne v_{18} potential [134] for the strong final-state interaction yields a good description of the data. Following the premise of a Gaussian source, the resulting femtoscopic radius is obtained as $r_0 = 1.249 \pm 0.008\,(\mathrm{stat.})\,^{+0.024}_{-0.021}\,(\mathrm{syst.})\,\mathrm{fm}$. The small size of the particle-emitting source gives rise to a pronounced correlation signal, and thus enables detailed studies of the strong final-state interaction. Assuming that the particle-emitting source is the same for any baryon–baryon pair, the resulting constraint can be used as an input for the modeling of the p–Σ^0 correlation function.

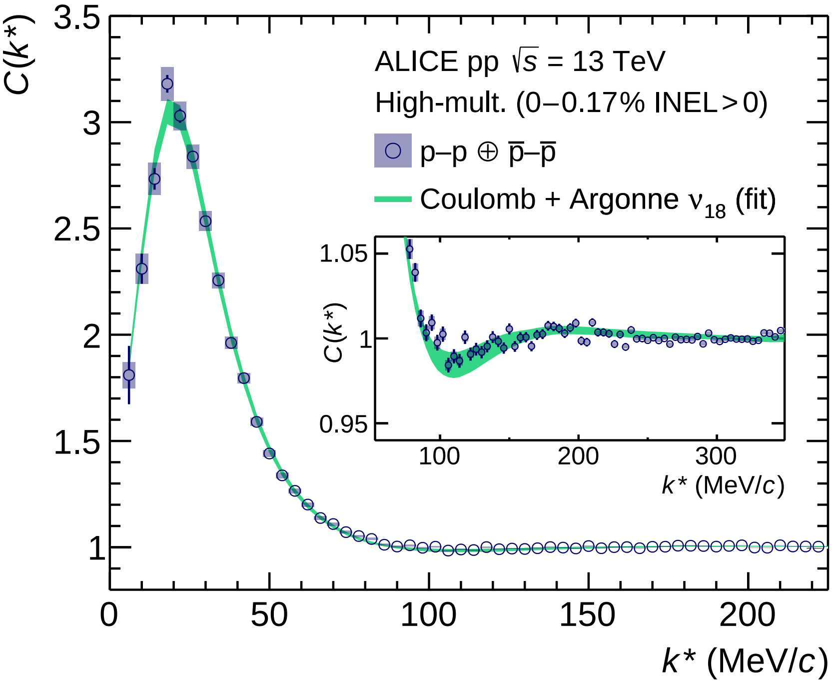

Figure 3.37: Measured correlation function of p–p ⊕ $\overline{\mathrm{p}}$–$\overline{\mathrm{p}}$ [220]. Statistical (bars) and systematic uncertainties (boxes) are shown separately. The data are fitted with the correlation function modeled using the Argonne v_{18} potential [134] and a Gaussian source distribution. The width of the band corresponds to one standard deviation of the systematic uncertainty of the fit. The inset shows a zoom at intermediate k^*, where the effect of repulsion becomes apparent.

There are, however, several aspects of the source size and shape to be considered. First of all, femtoscopic analyses of π–π and K–K pairs at ultrarelativistic energies in elementary [239] and heavy-ion collisions [240] observe a source shape significantly deviating from a Gaussian distribution. Indeed, the appearance of Lévy-stable distributions [241–243] as source functions is expected in expanding systems due to considerations of a generalized form of the central limit theorem and the occurrence of generalized random walk or anomalous diffusion phenomena [240]. The one-dimensional Lévy distribution is the generalization of the Gaussian distribution with an additional stability parameter α [241]. For the case $\alpha = 2$ the Gaussian shape is recovered, while for $\alpha = 1$ a Cauchy distribution arises. The most important feature in the context of femtoscopic sources is the fact that for $\alpha < 2$ significant power-law like tails arise, as depicted in Fig. 3.38 where source distributions for different values of α are shown.

The CATS framework allows one to use any source shape with a given potential to compute the correlation function, including Lévy-stable distributions [135, 150]. When attempting to fit the p–p correlation function with both the femtoscopic radius and the stability parameter α left as free parameters for the fit, α is found to be close to two and accordingly points towards a Gaussian-type source for baryon–baryon pairs. Enforcing a Cauchy-type source distribution significantly increases the overall χ^2/NDF by almost one order of magnitude and thus significantly deteriorates the agreement of the model with the data. The tails observed in the particle-emitting source of π–π and K–K pairs are accordingly significantly less pronounced for p–p pairs. Indeed, such exponential tails arise in the source distribution due to strongly decaying resonances, which influences in particular π–π correlations [244–247]. Studies employing MC simulations of heavy-ion collisions to extract the π–π source size with and without the contribution of strongly decaying resonances yield differences of about 1 fm for the two source types [248]. Accordingly, the source distribution can be decomposed into a Gaussian core and a non-Gaussian halo. The latter contribution becomes especially significant when the $c\tau$ of the feeding resonances is comparable to the source size, and is thus even more important in small collision systems.

In order to estimate the impact of strongly decaying resonances feeding to the particles of interest in the construction of the correlation function, the statistical hadronization model in the canonical

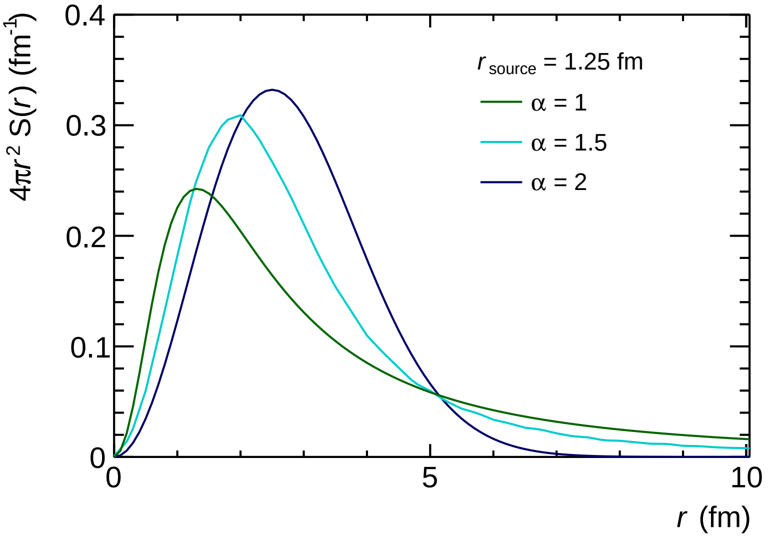

Figure 3.38: Lévy-stable source distributions for $\alpha = 1,\ 1.5$, and 2 with a femtoscopic radius $r_{\mathrm{source}} = 1.25$ fm obtained with CATS [135].

approach [141] is employed to compute the corresponding yields. For the case of pions, only about 28.0% are of primordial origin, with the remainder stemming from resonances such as the ρ and ω. The weighted average of the $c\tau$ of the resonances is 17.8 fm.

The contribution of resonances is also considerable for the case for baryons [236]. About 32.4% of the protons are primary particles, thus resulting in a substantial contribution from secondaries. In total 57 different resonances with lifetimes $0.5 < c\tau < 13$ fm are considered, with a dominant contribution from Δ resonances. Indeed, 22% of all protons originate from the decay of Δ^{++} resonances, 15% from Δ^{+} resonances, and 7.2% from Δ^{0} resonances. Feed-down from heavier N^{*}, Δ and Λ resonances contributes individually with less than 2%. The weighted average of the $c\tau$ of the contributing resonances is 1.65 fm with a weighted average of the their masses of 1.36 GeV/c^2 [236].

For the case of the Σ^0, the primordial contribution is with 62.7% significantly larger than for the protons. Feed-down stems from 23 different excited Λ and Σ states with lifetimes of $0.5 < c\tau < 13$ fm. Most prominently the $\Lambda(1405)$ and $\Lambda(1520)$ contribute with about 6.7% and 5%, respectively. In total, the weighted average of the $c\tau$ of the resonances is 4.28 fm, while the weighted average of the their masses is 1.58 GeV/c^2.

The average $c\tau$ and the masses of the resonances feeding to baryon–baryon pairs are significantly smaller than in the case of π–π pairs. Therefore, it is not surprising that the source distributions of baryon–baryon pairs feature less pronounced tails and can be well described by a Gaussian.

A more quantitative understanding of the source shape and the specific contributions of the different baryonic resonances can be obtained employing a model based on MC techniques [150, 160, 236]. The main assumption is that all primordial particles or resonances are emitted from a common Gaussian source with radius r_{core}. The Gaussian core incorporates possible collective effects, such as hydrodynamic flow, that are known to modify the source radii in heavy-ion collisions at LHC energies [125]. Indeed, a collective expansion of the system in such collisions

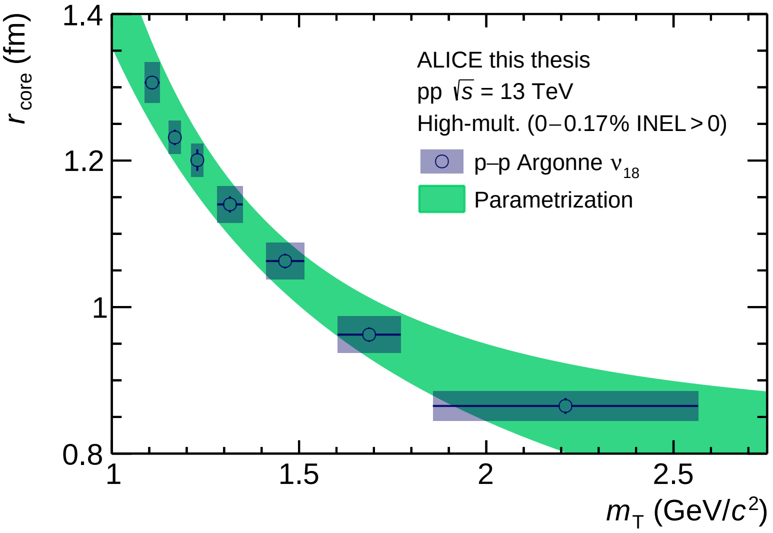

Figure 3.39: Source radius r_{core} as a function of m_T extracted from the p–p correlation function with the MC source including the effect of strongly decaying resonances [150, 160, 236]. Reproduced from Ref. [149, 236]. Statistical (lines) and systematic (boxes) uncertainties are shown separately. The width of the band corresponds to 3σ. For details see text.

is typically reflected in a decrease of the measured source radii with increasing pair transverse momentum $k_{\mathrm{T}} = 0.5 \cdot |p_{\mathrm{T},1} + p_{\mathrm{T},2}|$ and transverse mass $m_{\mathrm{T}} = \sqrt{k_{\mathrm{T}}^2 + m^2}$ with m being the average mass of the particle pair [125]. Since hadronization in pp collisions is believed to occur on a similar time scale for all particles, a possible collective expansion would be reflected in a common m_{T} scaling of the source size. The available studies with π–π and K–K pairs at the LHC are conducted at rather low values of m_{T} and indeed point to a consistent decrease of the source size with increasing pair m_{T} [239, 249–251].

Accordingly, the source size of the Gaussian core in the model exhibits a dependence on the pair m_{T}. The strongly decaying resonances feeding to the particle pair of interest are then incorporated in the MC source according to the primary fractions and decayed considering the average masses and lifetimes. The kinematics of the emission are fixed with results of the EPOS transport model [204] using simulated high-multiplicity pp events at $\sqrt{s} = 13$ TeV. Details of the model and the sampling procedure are explained in detail in Refs. [150, 160, 236].

The p–p correlation function is fitted with this prescription of the source in slices of m_{T} and the radii are extracted [150, 160, 236]. The result is shown in Fig. 3.39 and demonstrates the decrease of the source radii with increasing m_{T}. In order to interpolate the value of r_{core} the behavior is parametrized as

$$r_{\mathrm{core}} = a \cdot m_{\mathrm{T}}^{b} + c, \tag{3.14}$$

with $a = (0.74^{+0.12}_{-0.05})\,\mathrm{fm}(\mathrm{GeV}/c^2)^{-\mathrm{b}}$, $b = (-1.85^{+0.54}_{-0.70})$, and $c = (0.69^{+0.14}_{-0.19})$ fm.

In order to construct the overall p–p source distribution, the corresponding m_{T}-integrated correlation function is fitted with the same prescription of the source yielding a radius of $r_{\mathrm{core}} = 1.173 \pm 0.008\,(\mathrm{stat.})\,^{+0.026}_{-0.009}\,(\mathrm{syst.})$ fm. The resulting source distribution is shown in Fig. 3.40. The parametrization of the p–p MC source with an effective Gaussian source distribution yields

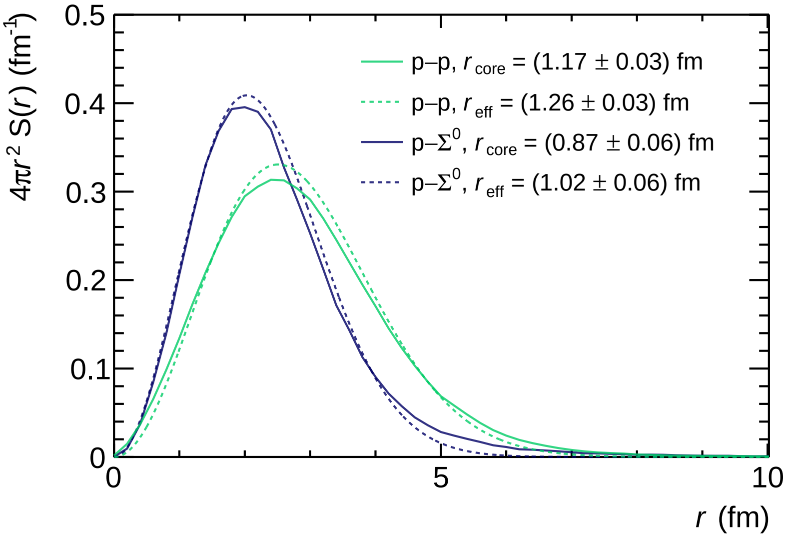

Figure 3.40: Source distributions of p–p (*teal*) and p–Σ^0 (*blue*). The source distributions obtained with the MC source including the effects of m_{T} scaling and feed-down from strongly decaying resonances [150, 160, 236] (*solid lines*) are in good agreement with fits employing an effective Gaussian source distribution (*dotted lines*).

good agreement in particular for small r, which are relevant for the study of the strong interaction. The so extracted value of the radius r_{eff} is consistent with $r_0 = 1.25\,\mathrm{fm}$. Therefore, it is not surprising that an effective Gaussian source distribution is sufficient to fit the precise data of the p–p correlation function.

Since the properties of the resonances feeding to p–p and p–Σ^0 pairs are different, the corresponding source distribution may differ accordingly. The core radius of p–Σ^0 is obtained by evaluating Eq. 3.14 at the $\langle m_{\mathrm{T}} \rangle = 2.14\,\mathrm{GeV}/c^2$ of the p–Σ^0 pairs yielding $r_{\mathrm{core}} = (0.87 \pm 0.06)\,\mathrm{fm}$. The resulting source distribution of p–Σ^0 pairs including the effect of strongly decaying resonances is shown in Fig. 3.40. The radius is smaller than for p–p pairs and the parametrization with an effective source distribution yields good agreement, with an extracted value of $r_{\mathrm{eff}} = (1.02 \pm 0.06)\,\mathrm{fm}$.

The femtoscopic radius r_0 used as an input for the fit of the p–Σ^0 correlation function is a conservative combination of the radii obtained above. First of all, assuming a common source for all baryon–baryon pairs the radius r_0 from a fit to the m_{T}-integrated p–p correlation function is employed. In order to incorporate variations of the p–Σ^0 source due to the effect of m_{T} scaling and feed-down from strongly decaying resonances the radius is decreased by 15%, in line with the findings for r_{eff}, in the evaluation of the systematic uncertainties of the fitting procedure.

3.7 Results and Discussion

The final result of this work, the experimental p–Σ^0 $\oplus$ $\overline{\text{p}}$–$\overline{\Sigma^0}$ correlation function, is shown in Fig. 3.41. The correlation function exhibits a deviation from unity in the first two k^* intervals. Due to the modest purity of the Σ^0 candidates, the corresponding reference is the p–$(\Lambda\gamma)$ baseline correlation. Nevertheless, the data are slightly above the baseline. A potential incompatibility with the p–$(\Lambda\gamma)$ baseline can be quantified by the number of standard deviations n_σ obtained from the p-value computed in $k^* < 150\,\text{MeV}/c$. Presently, apart from the rather large uncertainties of the data points themselves, the other main source of uncertainty is the parametrization of the p–$(\Lambda\gamma)$ baseline due to its sizeable statistical uncertainties. The resulting absolute uncertainty is correlated among all models and shown separately as the hatched area at the bottom of Fig. 3.41. The uncertainty is also reflected in a rather broad range of n_σ values shown in Table 3.13.

The data are found to be within $(0.2 - 0.8)\sigma$ consistent with the p–$(\Lambda\gamma)$ baseline. This indicates the presence of an overall shallow strong potential in the p–Σ^0 channel. It should be noted that the slight enhancement of the p–Σ^0 correlation function with respect to the p–$(\Lambda\gamma)$ baseline cannot be directly interpreted as an indication for an attractive interaction, since also the presence of coupled channels can introduce such an effect. This was already discussed in Sec. 1.3. Therefore, it is in general very challenging to make a statement on the character of the p–Σ^0 interaction based on the measured correlation function alone.

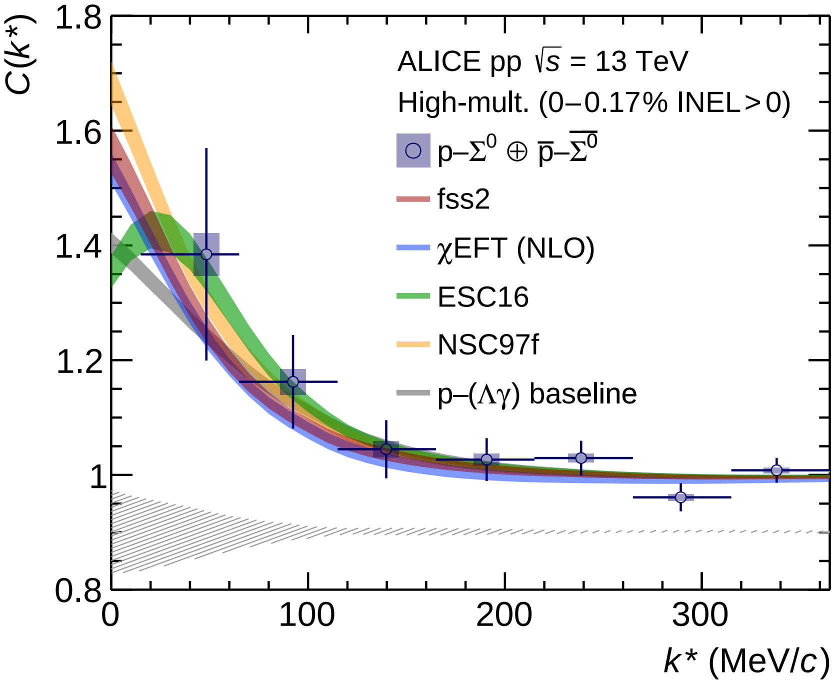

Figure 3.41: Measured correlation function of p–Σ^0 $\oplus$ $\overline{\text{p}}$–$\overline{\Sigma^0}$ [220]. Statistical (bars) and systematic uncertainties (boxes) are shown separately. The gray band denotes the p–$(\Lambda\gamma)$ baseline. The data are compared with different theoretical models such as χEFT [83], NSC97f [78], ESC16 [81], and fss2 [85]. The width of the bands corresponds to one standard deviation of the systematic uncertainty of the fit. The correlated uncertainty due to the modeling of the p–$(\Lambda\gamma)$ baseline is shown separately as the hatched area at the bottom of the figure.

For the same reason and considering the sizable uncertainties of the data, a direct determination of scattering parameters via a femtoscopic fit is not feasible. Instead, the data are employed to benchmark the above discussed models of the interaction. The comparison is depicted in Fig. 3.41. In addition to the uncertainties arising from the fitting procedure and represented by the width of the bands, all modeled correlation functions are affected by the absolute correlated uncertainty arising from the parametrization of the p–($\Lambda\gamma$) baseline. The uncertainties are reflected in the n_σ values shown in Table 3.13. Therefore, a conclusion on individual models cannot be drawn given the present uncertainties of the measured p–Σ^0 correlation function.

The predictions of the different models for the p–Λ interaction yield equivalent results. On the contrary, the modeled correlation functions for the p–Σ^0 interaction differ significantly among each other. The overall shape is defined by the interplay of the involved spin and isospin components. This is particularly evident in the correlation functions from the fss2 model and χEFT, which exhibit similar behavior albeit the corresponding scattering parameters in the isospin $I = 3/2$ channel are rather different as shown in Table 1.2. The significant depletion in the intermediate k^* range, present in both modeled correlation functions, can be attributed to repulsion occurring in the spin singlet $S = 0$, $I = 1/2$ and spin triplet $S = 1$, $I = 3/2$ [83, 85]. At lower k^* of up to 50 MeV/c both models display significant enhancement.
The behavior of the two Nijmegen models NSC97f and ESC16 is characterized by a rather constant attraction over the whole range of k^*, while significant deviations arise at low k^*. Especially intriguing is the shape of the most recent Nijmegen model, ESC16 [81]. In this model, the formation of bound states in the strangeness sector $S = -1$ is not allowed, leading to a repulsive core in all N–Σ channels. This is well reflected in the sizable depletion at small k^*. In contrast to all other discussed models, NSC97f yields attraction in the spin triplet $S = 1$, $I = 3/2$ channel [78]. Accordingly, the corresponding correlation function demonstrates the strongest enhancement at low k^*.

The effect of the interplay of the involved spin and isospin components is best visualized when comparing the resulting correlation function for two different source radii. Figure 3.42 depicts the p–Σ^0 correlation function for a source corresponding to high-multiplicity pp collisions at $\sqrt{s} = 13$ TeV with $r_0 = 1.25$ fm and to a central Pb–Pb collision system with $r_0 = 4$ fm. As expected, the correlation signal is in general less pronounced in the larger system, and arises only at significantly lower k^*. The hierarchy of the modeled correlation functions differs significantly for different radii. While in the smaller system, χEFT and the fss2 model yield comparable predictions for the correlation function, appreciable differences arise in the larger system. Similarly, the strong attraction observed for the NSC97f model is less pronounced in the larger system and the correlation function is compatible with the one from χEFT. Most notably, the ESC16 model exhibits no attraction over the full range of k^* and instead turns fully repulsive.

Table 3.13: Degree of consistency of the different models with the experimental correlation function evaluated in $k^* < 150$ MeV/c.

Model	n_σ
p–($\Lambda\gamma$) baseline	(0.2−0.8)
fss2	(0.2−0.9)
χEFT (NLO)	(0.3−1.0)
ESC16	(0.1−0.5)
NSC97f	(0.2−0.6)

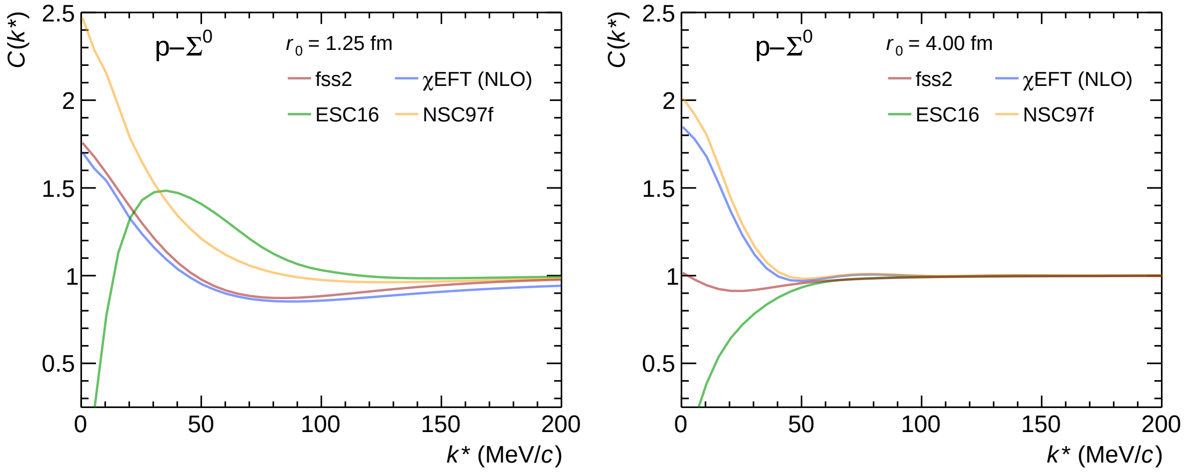

Figure 3.42: The genuine correlation functions for the p–Σ^0 system [78, 81, 83, 85]. The correlation function is computed for a femtoscopic radius r_0 equivalent to a small (pp, *left*) and large (Pb–Pb, *right*) collision system.

This demonstrates that in systems with various involved components, the resulting correlation functions can differ sizably. This holds in particular true for the N–Σ interaction, where the different spin and isospin components have significantly distinct properties. Therefore, studies of the correlation function in diverse collision systems might yield complementary information about the interaction.

As discussed in Sec. 1.2.2, the underlying two-body N–Σ interaction resulting from these models yields significantly different values for the in-medium single-particle potential U_Σ when included in many-body calculations. The available experimental data, discussed in Sec. 1.2.1, suggest an overall repulsive U_Σ. In line with this, both the fss2 model and χEFT yield an overall repulsive U_Σ of around $10-17$ MeV at nuclear saturation density [83–85]. On the contrary, both Nijmegen models result in a slightly attractive Σ single-particle potential, ranging from ≈ -16 MeV for NSC97f [78] to ≈ -3 MeV for ESC16 [81]. It should be noted, however, that both the interpretation of the experimental measurements and the extrapolation of theoretical calculations to finite density via e.g. the G-matrix approach [95, 96] introduce a significant model dependence.

In this respect, one of the clear benefits of employing the femtoscopy method is the significantly reduced model dependence in the interpretation compared to the presently available experimental constraints in the N–Σ sector. Nevertheless, the present uncertainties of the measured p–Σ^0 correlation function do not yet permit a conclusion on individual models. It should be noted, that this is also the case for all available experimental data in the N–Σ sector. Accordingly, the theoretical descriptions of the N–Σ interaction are not well constrained and result in large deviations of the correlation functions at low k^*. That underlines the strength of this specific channel, where decisive measurements can be undertaken, given sufficient pair counts.

This work demonstrates that both the measured and the modeled correlation functions are sensitive to the strong final-state interaction and therefore the feasibility to study the p–Σ^0 interaction with femtoscopic measurements.

3.8 Future Perspectives of the Measurement

As discussed in Sec. 2.3, the data taking rates of ALICE will be significantly increased after completion of the detector and readout upgrades conducted during LS2 (2019–2021). This will result in a data sample of 6 pb^{-1} in pp collisions at $\sqrt{s} = 5.5$ TeV, and of 200 pb^{-1} at $\sqrt{s} = 14$ TeV with dedicated high-multiplicity triggers [211].

In the case of the minimum bias data sample, about 4×10^{11} events are expected to be recorded, however at a significantly reduced average charged-particle multiplicity $\langle N_{\mathrm{ch}} \rangle$ with respect to the high-multiplicity data sample collected in Run 2. In order to estimate the effect of the reduced multiplicity on the number of particle pairs per event, the evolution of the number of p–p pairs per event with the charged-particle multiplicity $\mathrm{d}N_{\mathrm{ch}}/\mathrm{d}\eta$ are extracted from the present Run 2 data set and displayed in Fig. 3.43. Since the observed strangeness enhancement in high-multiplicity collisions is not as pronounced for $|S| = 1$ particles [221], these serve as a good proxy for the evolution of the p–Σ^0 pairs for which the particle count is too low to conduct such extrapolations.

Accordingly, an almost tenfold decrease of the number of particle pairs per event is expected with respect to the high-multiplicity data sample of Run 2 at the $\langle N_{\mathrm{ch}} \rangle$ at $\sqrt{s} = 5.5$ TeV. This results in an overall increase of particle pairs of about a factor of forty considering the larger data sample. In reality, the increase may be less pronounced since this estimate neglects the influence of the reduced collision energy. The left panel of Fig. 3.44 shows the correlation function with statistical uncertainties scaled according to the planned pp reference data sample at $\sqrt{s} = 5.5$ TeV. The projection is obtained on the basis of the Esc16 model [81], which provides the best agreement with the presently measured correlation function. Clearly visible is a sizable reduction of the statistical uncertainties, not only of the correlation function itself, but also of the correlated uncertainty of the models due to the modeling of the p–$(\Lambda\gamma)$ baseline. Nevertheless, a discrimination among the different models may still not be feasible.

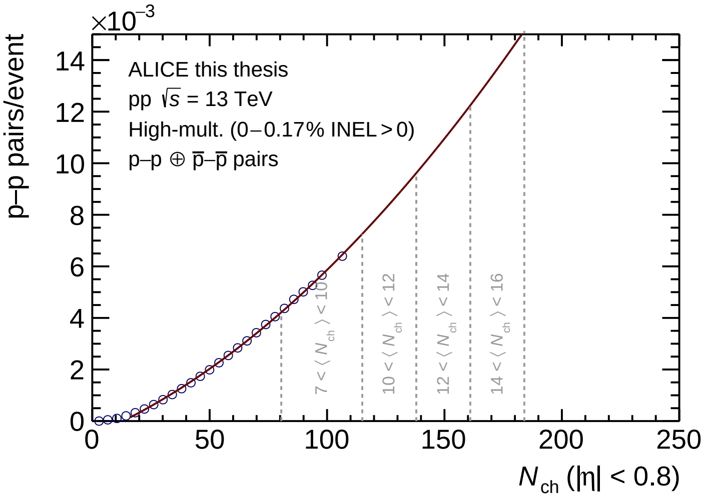

Figure 3.43: Proton–proton pairs with $k^* < 200\,\mathrm{MeV}/c$ per event as a function of the charged-particle multiplicity extracted from the high-multiplicity pp data sample at $\sqrt{s} = 13$ TeV. The vertical dashed lines denote the multiplicity intervals corresponding to Table 3.14.

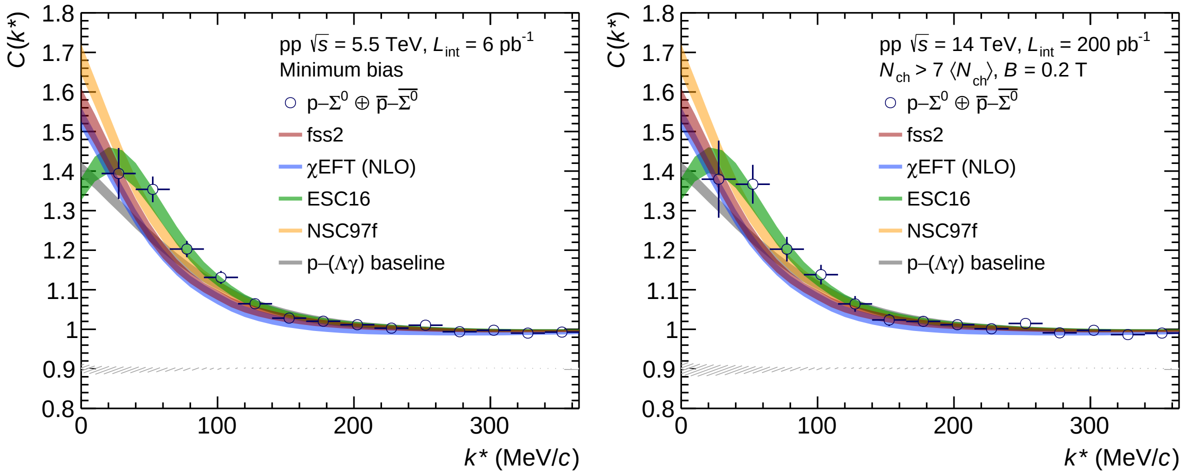

Figure 3.44: Projection of the correlation function of p–$\Sigma^0 \oplus \overline{\text{p}}$–$\overline{\Sigma^0}$ for the $\mathcal{L}_{\text{int}} = 6\,\text{pb}^{-1}$ data sample at $\sqrt{s} = 5.5$ TeV (*left*) and the $\mathcal{L}_{\text{int}} = 200\,\text{pb}^{-1}$ data sample at $\sqrt{s} = 14$ TeV (*right*). In the latter case, full data taking at a reduced magnetic field of 0.2 T is assumed. Only the scaled statistical uncertainties are shown. The gray band denotes the p–$(\Lambda\gamma)$ baseline, the data are compared with the same models as in Fig. 3.41. The width of the bands corresponds to one standard deviation of the systematic uncertainty of the fit. The dashed area denotes the correlated uncertainty due to the modeling of the p–$(\Lambda\gamma)$ baseline which is as well substantially reduced due to the enhanced data sample.

Regarding the high-multiplicity data sample at $\sqrt{s} = 14$ TeV, the trigger scheme foresees a significant downscaling of events with $\langle N_{\text{ch}} \rangle < 7$, extending the reach of multiplicities with respect to the Run 2 data sample. The envisaged number of collected events in the corresponding multiplicity intervals is shown in Table 3.14. Based on the evolution of the number of p–p pairs per event shown in Fig. 3.43, an almost fivefold increase of the number of p–Σ^0 pairs is expected. This is certainly not sufficient to conduct decisive measurements.

The reconstruction efficiency ε of the γ at low momenta deteriorates significantly, which is reflected in the rather poor overall reconstruction efficiency of the Σ^0. A reduction of the magnetic field of the solenoid to 0.2 T would significantly enhance the reconstruction efficiency, as depicted in Fig. 3.45. In particular at low p_{T}, a significant increase in reconstruction efficiency is expected, resulting in an overall improvement of about a factor of four. This is particularly beneficial for femtoscopic measurements since the Σ^0 candidates used to construct the correlation function have a $\langle p_{\text{T}} \rangle$ of about 2 GeV/c. The right panel of Fig. 3.44 shows the resulting correlation function for the expected high-multiplicity data sample at $\sqrt{s} = 14$ TeV assuming full running at a reduced solenoidal field of $B = 0.2$ T. It should be noted, that even in this optimistic scenario, the precision of the minimum bias sample is superior.

Table 3.14: Number of expected pp events at $\sqrt{s} = 14$ TeV in selected high-multiplicity bins [252].

Range	**$\langle \text{d}N_{\text{ch}}/\text{d}\eta \rangle$**	**Events in 200 pb^{-1}**
7–10 $\langle N_{\text{ch}} \rangle$	53.2	2.0×10^9
10–12 $\langle N_{\text{ch}} \rangle$	73.6	1.8×10^7
12–14 $\langle N_{\text{ch}} \rangle$	87.5	7.3×10^5
14–16 $\langle N_{\text{ch}} \rangle$	101.5	2.8×10^4

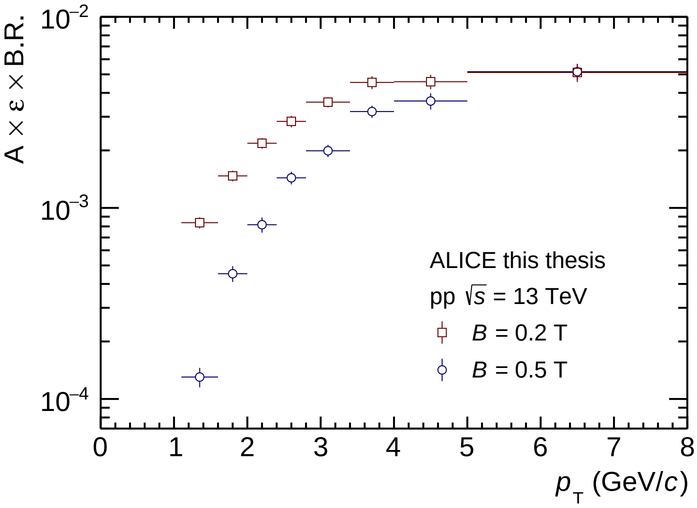

Figure 3.45: Efficiency of the Σ^0 reconstruction at nominal (0.5 T) and reduced (0.2 T) magnetic field setting of the solenoid.

Another perspective might be a measurement in a different collision system such as p–Pb or peripheral Pb–Pb. Since the dependence of the different modeled correlation functions on the radius diverges significantly as demonstrated in Fig. 3.42, such a measurement adds complementary information. The p–$(\Lambda\gamma)$ combinatorial background, however, is even more pronounced in such a collision system, thus strongly damping the observed differences.

A probably more promising option might be to resort to a different channel in the N–Σ sector that is less affected by the combinatorial background introduced by the γ involved in the decay of Σ^0. Particularly interesting is an analysis of the p–Σ^+ correlation function, in which only the $I = 3/2$ channel contributes and coupled channels are not present. Accordingly, more detailed constraints on theoretical models can be obtained.
The Σ^+ decays with a kink topology $\Sigma^+ \rightarrow \mathrm{p}\pi^0$ ($c\tau \sim 2.4\,\mathrm{cm}$, BR $\sim$ 52% [7]), that can be reconstructed with the ITS. The momentum of the Σ^+ could be directly measured using the first few layers of the ITS, and the invariant mass could be reconstructed using the missing mass of the π^0. This way, the tails of the exponential decay of the Σ^+ could be probed. Even more advantageous would be the decay $\Sigma^+ \rightarrow \mathrm{n}\pi^+$ (BR $\sim$ 48% [7]) where the kink is more pronounced due to the larger mass difference of the charged particles involved. Employing the reconstruction based on the identification of the π^+ yields a contamination by $\overline{\Sigma^-} \rightarrow \overline{\mathrm{n}}\pi^+$ decays, which by combination with a proton would probe the same isospin channel of the interaction. This channel, however, introduces quite likely non-femtoscopic effects from mini-jets since a baryon–antibaryon pair is studied.
The situation for the reconstruction of $\Sigma^+ \rightarrow \mathrm{p}\pi^0$ is even better in the upcoming Run 3, where the upgraded ITS is significantly closer to the beam pipe than during Run 1 and 2. In this light, a measurement of the p–Σ^+ correlation function seems promising and could enable decisive studies of the interaction.

Either way, the profile of the modeled correlation functions in the N–Σ sector is sensitive to details of the strong interaction and differs significantly among the employed state-of-the-art models. This work demonstrates the feasibility of the measurement of the p–Σ^0 correlation function, and that more detailed studies can be conducted with the large data samples expected beyond Run 2.

4 The Upgrade of the ALICE Time Projection Chamber

The collection of the large data samples envisaged for the upcoming LHC Run 3 and beyond can only be accomplished by increasing the interaction rates provided by the LHC and the rate capability of the ALICE detector. The latter demands for significant upgrades of several sub-systems of ALICE, as outlined in Sec. 2.3. In particular, the TPC is equipped with GEM-based readout chambers. The key requirements driving the choice of technology are to enable continuous operation without a gating grid while retaining the excellent particle identification capabilities of the detector. This Chapter reviews the most important technical features of the upgrade as described in Refs. [214, 215].

4.1 Gas Electron Multiplier

In general, the high-rate capability of the MWPC is limited by significant gain drops for large radiation fluxes above $10^4\,\mathrm{s}^{-1}\mathrm{mm}^{-2}$ [253]. This is related to modifications of the field around the anode wires by the low-mobility ions accumulating at large rates. The progress in photo-lithographic processing techniques enabled the fabrication of more delicate structures aiming at the substitution of the MWPC wires with finer micro-structures $\mathcal{O}(100\,\mu\mathrm{m})$ and therefore circumventing this downfall. This gave rise to a new generation of gaseous detectors, summarized under the name of Micro Pattern Gaseous Detectors (MPGD) [254], out of which the Gas Electron Multiplier (GEM) [216] and the Micro-Mesh Gaseous Structure (MICROMEGAS) [255] are nowadays the most prominent examples.

Invented by F. Sauli in 1997, the GEM has become a mature technology employed in particular for high-rate tracking detectors [256–260]. The application for GEM-based TPCs has been pioneered in Refs. [261, 262], which lead to the consideration and implementation in ALICE [214, 215]. The

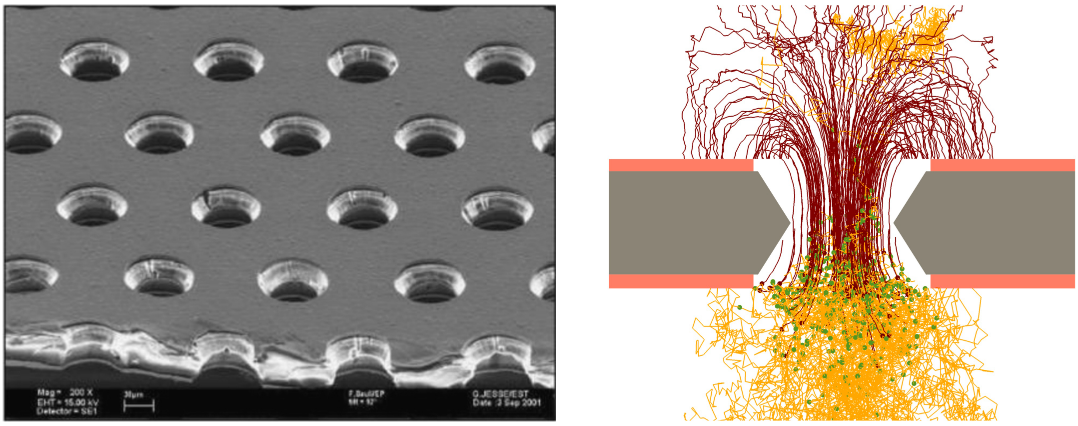

Figure 4.1: (*Left*) Electron microscope image of a typical GEM [256]. (*Right*) A GARFIELD/MAGBOLTZ [263] simulation of the amplification process inside a GEM hole [264]. The electron (ion) paths are depicted by the light (dark) lines and dots mark the locations of ionization processes.

technology is based on a 50 µm thin polyamide foil with a copper coating of about 5 µm on both sides, which is perforated via photo-lithographic processing with the typical hexagonal hole pattern as depicted in the left panel of Fig. 4.1. Depending of the manufacturing process, the cross section of these holes is double-conical [265] and features an inner (outer) diameter of 50 µm (70 µm) at a hole pitch of 140 µm. Other configurations are, however, also possible featuring e.g. a larger hole pitch or different hole geometries. The electric fields arising inside these holes upon application of a moderate potential difference of, depending on the gas mixture employed, 300 V to 400 V are sufficiently large to enable avalanche amplification of electrons. The effective gain of a single GEM is defined as

$$G_{\mathrm{eff}} = \varepsilon_{\mathrm{coll}} \cdot M \cdot \varepsilon_{\mathrm{extr}}, \tag{4.1}$$

where ε corresponds to the electron collection ($\varepsilon_{\mathrm{coll}}$) and extraction ($\varepsilon_{\mathrm{extr}}$) efficiency and M to the absolute gain of the GEM foil. Typical values of G_{eff} are about 100–1000, but can reach up to 1×10^4. The overall gain can be further increased by stacking several foils and thus sharing the gain among several independent elements. The field configurations above and below the respective GEMs in a stack can be optimized so that a large fraction of the ions produced in the amplification process inside the GEM holes are collected on the top GEM electrodes. This is illustrated by the simulation depicted in the right panel of Fig. 4.1, where the avalanche is initiated by two electrons guided by the drift field to the GEM hole and occurs towards the bottom side of the GEM hole. The electrons are efficiently extracted from the GEM hole after amplification. On the other hand, the created ions follow the field lines due to their much lower mobility. Since the drift field is lower than the field inside the GEM hole, most of the ions are neutralized on the top side of the GEM. This effect is referred to as *intrinsic* suppression of the ion backflow (*IB*) inherent to GEMs, defined as

$$IB = \frac{1+\epsilon}{G_{\mathrm{stack}}}, \tag{4.2}$$

where ϵ corresponds to the total number of back-drifting ions per incoming electron, and G_{stack} is the overall effective gain of the stack. For a single GEM, the *IB* is close to the ratio between drift and induction fields [266], and thus typically $\mathcal{O}(10\%)$. With highly optimized field configurations values of about 2.5% [214] and 0.4% [215] in a stack of three and four GEMs have been accomplished. A discussion about how such an optimization can be conducted follows in Sec. 4.2.2.

The stability against electrical discharges is crucial for the successful long-term operation of a detector in particular in the harsh environment of high-rate experiments. Such discharges lead to permanent damage to the detector ranging from enhanced leakage currents to irreversible short circuits rendering the detector blind. The left panel of Fig. 4.2 depicts a microscope image of the evolution of a GEM hole after repeated discharges. It is clearly visible that the copper layer is successively evaporated and the intermediate polyamide significantly carbonized, which may result in an electrical connection of the top and bottom sides of the GEM foil. Depending on the resistance of the connection, the overall gain of the foil is only reduced, or in the worst case the electrodes are short-circuit. Therefore, such events should be mitigated.

In general, the occurrence of discharges is related to the transition of the avalanche to a streamer. During the evolution of the electron avalanche, the ions produced in the ionizing collisions can be assumed as static and remain present as space charge. When the field created by the space charge is comparable to the external field, gas amplification is enhanced in its vicinity. Secondary avalanches initiated by the field of the space charge lead to a fast growth of the ionized region. Due to diffusion phenomena and photon-feedback the streamer can then propagate through the full gas gap and lead to electrical breakdown. Therefore, large charge densities reached due to high irradiation rates and/or heavily ionizing tracks are believed to be the main cause for discharges in GEM-based detectors [267].

For the case of the parallel-plate counter, avalanche sizes of about $10^7 - 10^8$ electron-ion pairs can cause a sudden breakdown, which is referred to as the *Raether limit* [270]. Similar values are believed to hold for GEM-based detectors by comparing the discharge rates upon irradiation with x-rays to those caused by heavily ionizing particles [267, 269, 271].

By cascading several GEMs in a stack, the gain of the individual elements can be reduced while maintaining the same overall gain. Since the applied potential difference has a driving impact on the single-GEM stability, as depicted in the right panel of Fig. 4.2, the stability of the overall system is improved accordingly. Another aspect reducing the discharge rates in multi-GEM systems is the dilution of local charge densities caused by diffusion during the charge transport within the stack. As depicted in the right panel of Fig. 4.2, about two orders of magnitude larger gains can be accomplished in multi-GEM stacks at similar discharge probabilities compared to a single-GEM detector.

The driving factor for the remaining discharge probability is then the voltage configuration applied to the GEM stack [269]. The most stable configuration features an asymmetric configuration where the largest amplification occurs in the first GEM in the stack and is then successively reduced towards the readout anode [256]. This is rather intuitive since the overall stability of the stack is determined by the breakdown limits of the individuals GEMs. The reduction of the voltage of the last GEM in the stack is therefore beneficial since the charge density, and accordingly the discharge probability, is largest at this point.

As shown in the next Section, optimizing the GEM voltages for different applications may significantly compromise the detector stability and the discharge mitigation requires a thorough understanding of the behavior of an individual GEM.

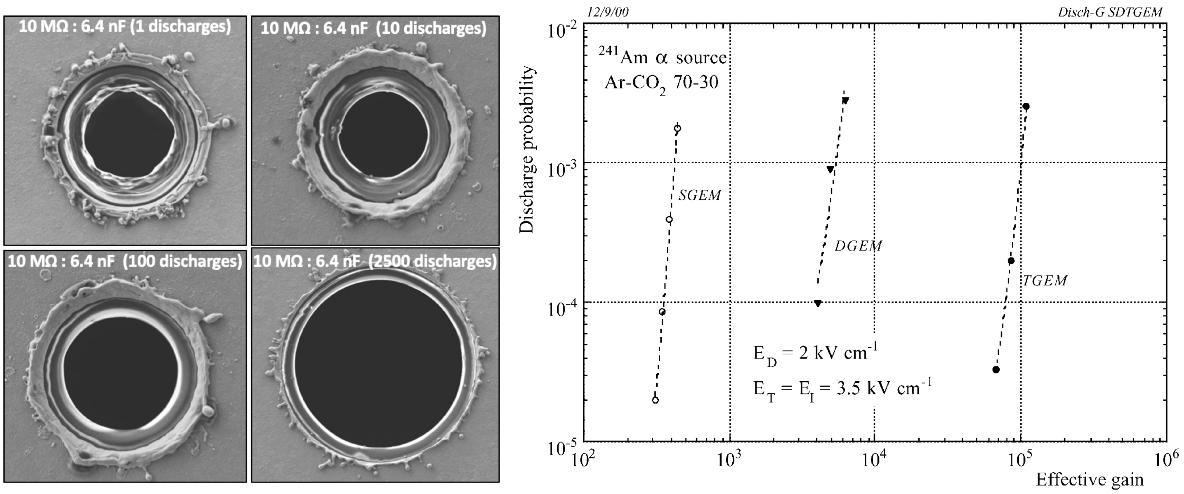

Figure 4.2: (*Left*) Electron microscope image of the evolution of a GEM hole after repeated discharges [268] and (*right*) the discharge probability as a function of total effective gain for single-, double-, and triple-GEM detectors [269].

4.2 The ALICE GEM TPC

The necessity to operate the TPC in a continuous mode motivates the choice of GEMs for the amplification stage due to their capabilities to suppress the *IB* without the necessity for a gating grid. Since the excellent tracking and PID capabilities of the ALICE TPC must be retained after the upgrade, the following requirements were defined [214, 215].

- A total effective gain of 2000 to achieve the required signal-to-noise ratio of at least 20 for the IROC.
- At a gain of 2000, the *IB* must be less than 2% in order to keep the distortions of the drift field at a tolerable level.
- The energy resolution, quantified at the 5.9 keV x-ray peak of ^{55}Fe, is required to be better than $\sigma_E/E = 14\%$ to retain the dE/dx resolution of the TPC.
- Stable operation under the harsh conditions of the LHC.
- A re-design of the front-end electronics to process the negative signal polarity provided by GEMs. The key requirements are low-noise operation and a continuous readout of the anticipated high data rates.
- Significant online data reduction to conform with the limited bandwidth of the data acquisition system.

An extensive R&D program, which is briefly outlined in the following, lead to the baseline solution for the upgrade – a stack of four GEMs containing Standard (S, 140 µm pitch) and Large Pitch (LP, 280 µm pitch) foils in the order S-LP-LP-S [215]. The significant misaligment of the GEM holes introduced by the different hole pitches leads to a geometric blocking of the ions produced in the avalanche multiplication. Figure 4.3 shows a schematic cross section of a readout chamber and depicts the most important elements. The GEMs in the stack are separated by 2 mm thick frames, which also define the distance between the last GEM in the stack (GEM 4) and the readout anode. The drift field $E_{\text{drift}} = 400\,\text{V/cm}$ is defined by the voltage applied to the central electrode of the TPC. The transfer fields ($E_{\text{T}i}$) between the different GEMs in the stack and the induction field (E_{ind}) between GEM 4 and the anode are, as the voltages applied to the GEMs, highly optimized to fulfill the above mentioned requirements.

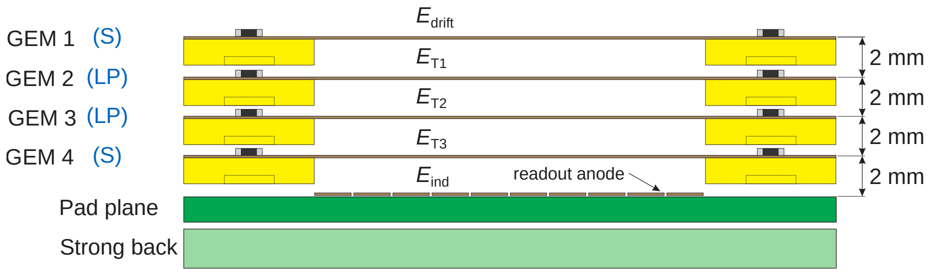

Figure 4.3: Schematic cross section of the 4-GEM stack. Each GEM foil is glued onto a 2 mm Vetronite EGS 103 frame. The nomenclature of the field is depicted, where E_{drift}, $E_{\text{T}i}$ and E_{ind} denote the drift, transfer and induction fields. The drift cathode located about 250 cm away from the pad plane is not shown.

However, even at an *IB* of 1% the space charge created by the ion leakage from the amplification stage causes significant distortions of the drift field. Considerations of the ion mobility lead to the choice of Neon as the noble gas component of the active volume, with the addition of CO_2 and N_2 as quencher in the proportion Ne-CO_2-N_2 (90–10–5) [214]. Nevertheless, the overall drift time of ions from the readout chambers to the central electrode is about 180 ms, which means that on average the ions of 8,000 events accumulate within the active volume of the detector at interaction rates of 50 kHz. The resulting space charge significantly alters the drift field and creates distortions reaching up to 19 cm in r and 7 cm in $r\varphi$ [214]. Employing a multi-step approach with average distortion maps, scaled according to the instantaneous TPC occupancy, and the information of external detectors, the intrinsic detector resolution can be restored [214].

At the interaction rates anticipated for the Pb–Pb data taking campaign, the TPC produces data at rates as high as 3.28 TB/s rendering online reconstruction for data compression by a factor of 20 mandatory.

4.2.1 The GEM-based ReadOut Chambers

The large-size GEM foils for the upgrade of the ALICE TPC [272] are manufactured at the CERN PCB workshop using the single-mask technique [265]. The trapezoidal shape of the outline is owed to the size and shape of the previously used MWPCs. Since the maximal size of the processed raw material is limited, the OROCs are equipped with three independent stacks. Geometrical features of the different GEM types are summarized in Table 4.1.

In order to limit the current flowing in case of a potential electrical discharge, and accordingly mitigating potential harm to the foils [269], the top side of all GEMs is divided so that individual *segments* have an area of about 100 cm^2. The copper layer of adjacent segments is separated by 200 µm, as depicted in Fig. 4.4. An additional 100 µm clearance is introduced between these boundaries and the GEM holes to accommodate possible misaligments of the different masks used for the photo-lithographic processing of the foil during production. The segments on the top side are connected via 5 MΩ SMD[1] 1206 loading resistors to a common high voltage (HV) distribution circuit which has a width of 1 mm and runs along three sides of the foil. The resistors are mounted on so-called SMD pads which are placed in parallel to the segment boundary. Their dimensions are optimized to ensure electrical stability and safe handling of the resistors, and were specified by the producer (CERN PCB workshop): two pads with a size of $1.6 \times 2\,\mathrm{mm}^2$

Table 4.1: Geometrical dimensions and essential features of the GEM foils [272]. The width of the chambers is indicated by the long (short) side of the trapezoid.

GEM type	**Size** **H × W (cm^2)**	**# HV segments**	**Segment area** **Mean (cm^2)**	 **RMS (cm^2)**
IROC	49.7 × 46.7 (29.2)	18	93	4
OROC 1	36.2 × 59.5 (46.8)	20	87	8
OROC 2	38.0 × 73.0 (59.6)	22	105	11
OROC 3	39.8 × 87.0 (73.0)	24	122	13

---

[1] Surface-mount device

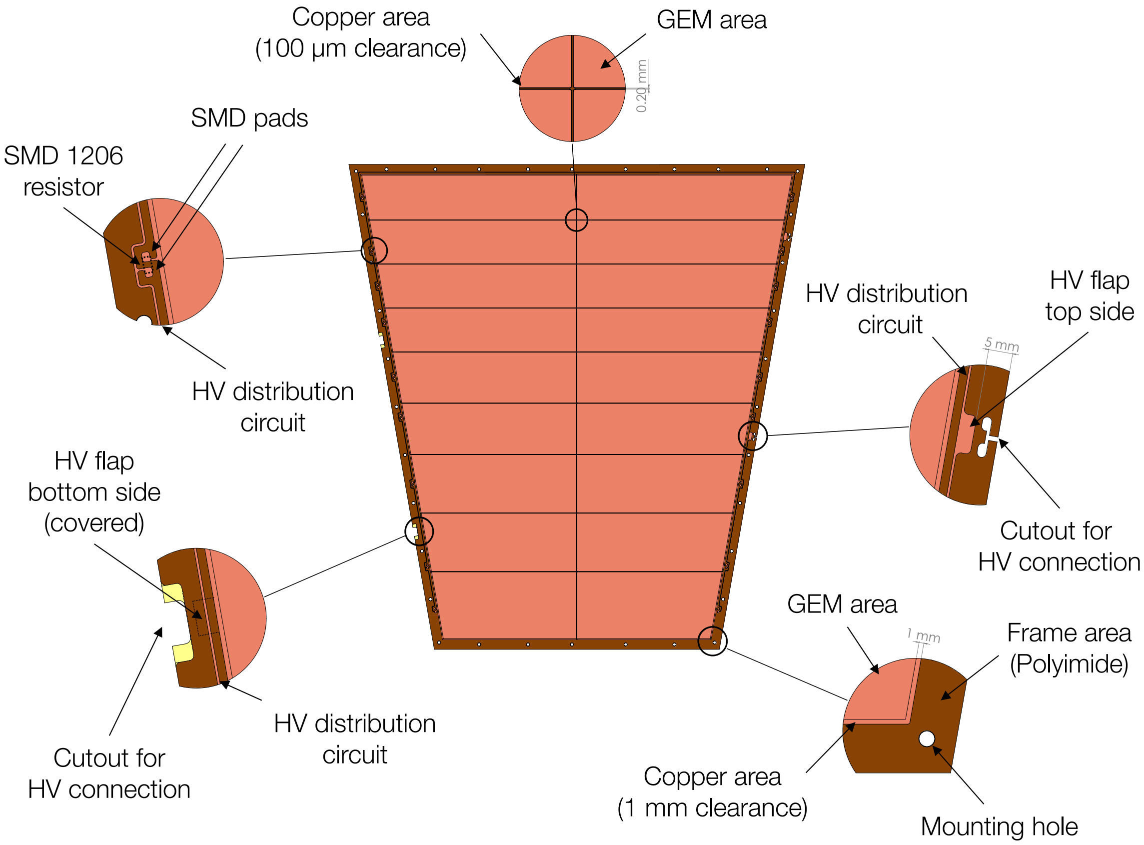

Figure 4.4: Schematic drawing of an IROC GEM foil of the final design with a zoom on the key features [272]. See text for details.

with a 1.2 mm gap in-between. The GEM foils are equipped with loading resistors directly after production and the corrosive content of the solder is removed by cleaning. The HV connection to the outside is provided via flaps that are connected to PEEK-insulated wires. Cutouts in the 2 mm thick Vetronite EGS 103 frames, onto which the foils are glued during the manufacturing process, guide the cables to the flaps. On the top side of the foil, the flap is connected to the HV distribution bus, while on the unsegmented bottom side there is a direct connection.

It is essential to ensure that no electrical discharges can arise from electrically live elements for the operation of the detector as a whole. Therefore, as shown in Fig. 4.4, the corners of all elements are rounded with a radius larger than 0.5 mm to avoid regions of large electric fields. Additionally, all elements have been placed so the distance to any electrical ground is maximized. This concerns in particular also the distance to elements of a neighboring sector. This is a crucial aspect, since in case of a HV trip in one sector a large potential difference of up to 4 kV may occur with respect to the electrical elements of its neighbors. Accordingly, the maximal distance between the HV bus and the chamber boundary is 5 mm. Considering the gap in-between two adjacent ROCs, this results in a minimal distance between electrically live elements of 13 mm. Tests with a mock-up of this configuration, where two parts of an IROC GEM foil were placed as in the final detector, demonstrated the safety of this distance. At the nominal voltage plus an additional 10% safety margin, no discharges were detected upon irradiation with an internal 15 Hz gaseous ^{220}Rn source.

Prior to each manufacturing step the individual foils are subject to a coarse optical inspection and a measurement of the leakage current, where a maximum of 0.5 nA is allowed per HV segment to reject malfunctioning GEM foils [273, 274]. After the GEM production at CERN, a first measurement of the leakage current is conducted and the foils are subsequently shipped to the *Advanced QA* centers, where a high-resolution map of the hole diameters and possible defects is obtained from optical scans [274]. Figure 4.5 shows the distribution of the GEM hole size of all GEMs produced for the upgrade and demonstrates the precision of the manufacturing process.

The first step of the production of the readout chambers consists of the assembly of the frames from four ledges made of 2 mm thick Vetronite EGS 103. In order to support the GEM foils against the electrostatic attraction of adjacent foils, a 1.5 mm wide spacer cross is mounted. Prior to the gluing procedure of the foils onto the pre-assembled frame, the foils are pneumatically stretched with a tension of 10 N/cm. Using an assembly jig, the foils are glued to the frames using the epoxy glue ARALDITE 2011$^{\text{TM}}$ which is cured for 24 hours in dry atmosphere below 30% relative humidity. After that, the foil is sent to the corresponding assembly center for further processing, where the foils are subsequently mounted on the readout chamber bodies, which consist of the pad plane, an additional 5 mm Vetronite EGS 103 insulation plate (*strong back*) and an aluminum frame (*alubody*). The pad plane is the segmented readout anode, a multi-layer Printed Circuit Board (PCB), with a total number of 5280 and 9280 pads for IROC and OROC, respectively. The pad size is depicted in Table 4.2 and depends on the radial coordinate reflecting the different requirements as a function of the track density which is reduced for larger radii. The front-end cards are connected via flexible flat cables on the back side of the pad plane. In a last assembly step the PEEK-coated wires providing HV to the foils are soldered to the flaps. Figure 4.6 shows an exploded view of a fully equipped IROC.

The assembled ROC is then subject to several acceptance tests and is fully characterized with respect to gain and *IB* uniformity. The overall stability of the chamber is tested by irradiation with x-rays resulting in charge densities on the anode of about 10 nA/cm^2. A final load test with an about tenfold increased particle load compared to the expectations for the operation during LHC Run 3 is conducted either at the GIF++ facility [276] or in the ALICE cavern close to the LHC beam pipe. This final test assures the integrity of all GEM foils and the corresponding HV connections. Upon successful completion of the tests, the chamber is stored until its final installation in the TPC.

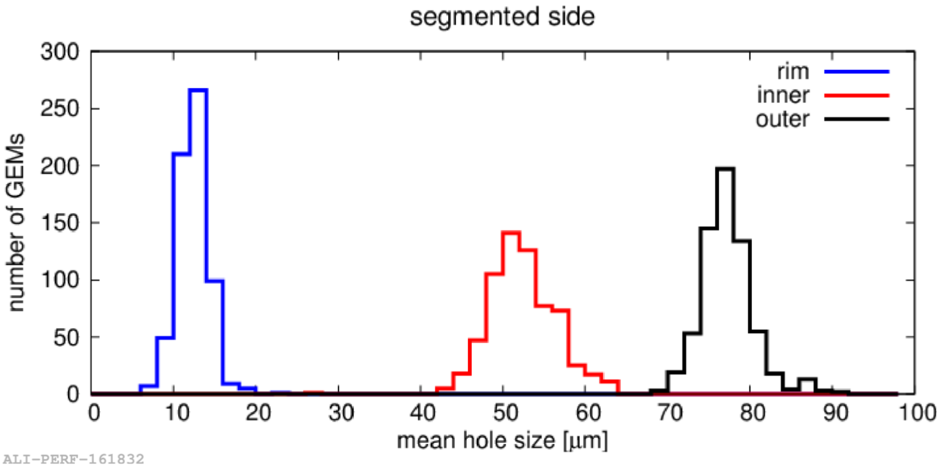

Figure 4.5: Distribution of GEM hole sizes of 647 GEMs produced for the ALICE TPC Upgrade [275].

Table 4.2: Dimensions and parameters of readout planes and pad size [214].

ROC type	r (cm)	Pad size (mm^2)	# pad rows	# pads
IROC	84.1 – 132.1	4×7.5	63	5,280
OROC 1	134.6 – 169.6	6×10	34	2,880
OROC 2	171.6 – 206.6	6×10	30	3,200
OROC 3	208.6 – 246.1	6×15	25	3,200
Sector	84.1 – 246.1		152	14,560
Total				524,160

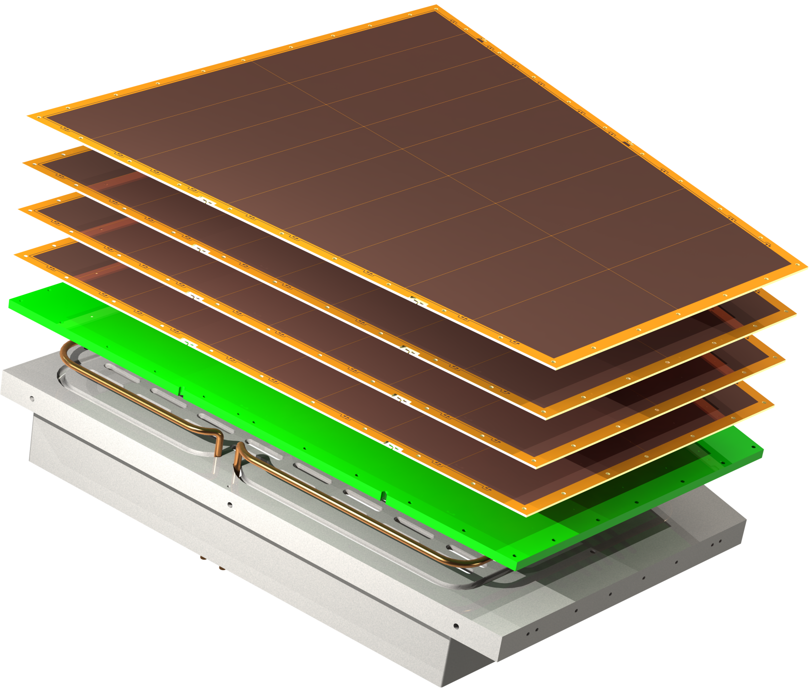

Figure 4.6: Exploded view of an Inner ReadOut Chamber (IROC). See text for details.

4.2.2 High-Voltage Configuration

The demanding requirements of the upgrade can only be fulfilled by employing a stack of four GEMs with a highly optimized HV configuration. In short, the GEM stack needs to provide an energy resolution $\sigma(^{55}\text{Fe}) < 14\%$ and an *IB* $< 2\%$ at a gain of 2000 while ensuring stability against discharges. Since these are competing requirements, a suitable working point can only be found by careful, parallel optimization.

The optimal configuration for suppressing the *IB* is accomplished by successively increasing the gain of the GEMs throughout the stack, so that the largest amplification takes place in the last foil. In this scenario, the largest fraction of ions is produced in GEM 4 and therefore can be effectively blocked while traversing the stack. This effect can be enhanced by employing foils with a larger hole pitch as intermediate layers of the stack for geometric blocking of the ions. The largest contribution to the overall *IB* then stems from GEM 1 of the stack and can be minimized by further reducing the gain of this stage.

At the same time, however, the energy resolution is mainly determined by the transparency of the first amplification stage where the number of incoming electrons is low. Therefore, fluctuations of the avalanche and the collection and extraction statistics can significantly degrade the energy resolution especially for low gains. This correlation is depicted in Fig. 4.7 where the increase of the voltage across GEM 1 at a constant gain of 2000 leads to a significant improvement of the energy resolution, while degrading the *IB* suppression of the stack. The correlation suggests that most of the remaining backflowing ions are indeed produced in the first GEM layers [214]. Nevertheless, some of the HV configurations fulfill the demanding requirements of the upgrade.

It should be noted though, that the large gain in the last GEM, in combination with the larger, already pre-amplified charges leads to a significant enhancement of the discharge probability [277]. Indeed, an increase of the discharge probability over three orders of magnitude has been observed in 3-GEM stacks when going from HV-stable settings ($\mathcal{O}(10^{-10})$) to a configuration optimized for a suppression of the *IB* [277]. The performance of some of the optimized HV configurations for ALICE upon irradiation of a 4-GEM stack with a mixed α nuclide source [278] is shown in Fig. 4.8. At the nominal gain of 2000 only upper limits could be measured, meaning that no discharge was recorded during the time of the measurement. This indicates that the addition of another GEM to the stack yields a significant improvement of the stability. Two different HV configurations are tested with the S-LP-LP–S configuration of the GEM stack – the so-called ALICE *baseline* fulfilling all requirements ($IB \approx 0.7\%$, $\sigma(^{55}\mathrm{Fe}) \approx 12\%$) and one with a very good *IB* suppression ($IB \approx 0.3\%$, $\sigma(^{55}\mathrm{Fe}) \approx 17\%$). The comparison of the two settings demonstrates that an aggressive optimization for *IB* suppression seriously affects the overall stability. The exposure of an IROC equipped with a 4-GEM stack to an intense hadron flux produced by a high-intensity secondary pion beam with a momentum of 150 GeV/*c* impinging on an iron absorber yields a

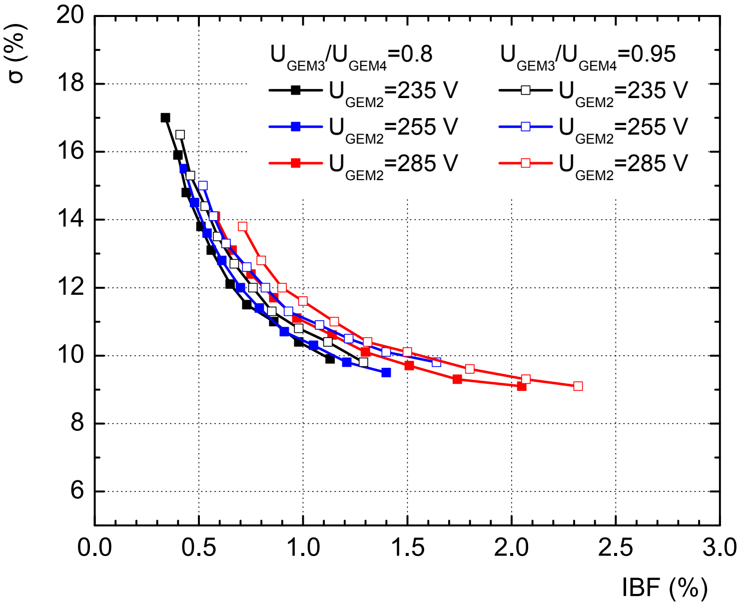

Figure 4.7: Correlation between *IB* and $\sigma(^{55}\mathrm{Fe})$ in a 4-GEM stack of the ALICE TPC Upgrade [215]. The voltage across GEM 1 increases for a given setting from left to right from 225 V to 315 V. The voltages on GEM 3 and 4 are adjusted to achieve a total effective gain of 2000, while keeping their ratio fixed.

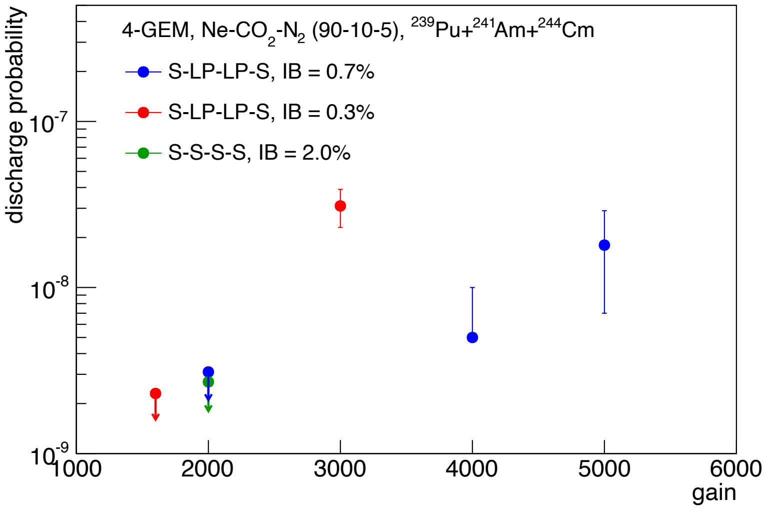

Figure 4.8: Discharge probability of a 4-GEM prototype measured for different stack and HV configurations [277]. Upper limits for discharge probability are indicated by arrows.

measured discharge probability of $(6.4 \pm 3.7) \times 10^{-12}$, which is in line with the requirements for safe operation [215].

The occurrence of a discharge may, under certain circumstances, lead to the breakdown in the gap below that GEM [269, 271], even at electric field values lower than required for amplification [279]. In order to mitigate the occurrence of such events that may be particularly harmful to the GEM and the front-end electronics, the maximal value of the transfer and induction fields is reduced to 3.5 kV/cm. Additionally, the parasitic capacitance of the 80 m long HV cable between the power supply and the GEM stack is decoupled via a 500 kΩ resistor [280].

The currently foreseen HV configuration for the ALICE GEM TPC is summarized in Table 4.3. As discussed above, the gain in GEM 1 drives the energy resolution of the configuration of $\sigma(^{55}\mathrm{Fe}) = 10.8\%$ [281]. GEM 2 has a low effective gain and thus essentially passes the electrons further to GEM 3 and 4, while partially blocking the ions from the lower layers. The low E_{T3} leads to the absorption and neutralization of a large fraction of the the ions produced in GEM 4 on its top side. The further blocking in the intermediate LP foils leads to an overall *IB* performance of $IB = 1.1\%$ [281], fulfilling the requirements of the upgrade.

Table 4.3: The currently foreseen HV configuration for the ALICE GEM TPC [281].

IB (%)	$\sigma(^{55}\mathrm{Fe})$ (%)	$\Delta U_{\mathrm{GEM\,1}}$ (V)	E_{T1} (kV/cm)	$\Delta U_{\mathrm{GEM\,2}}$ (V)	E_{T2} (kV/cm)	$\Delta U_{\mathrm{GEM\,3}}$ (V)	E_{T3} (kV/cm)	$\Delta U_{\mathrm{GEM\,4}}$ (V)	E_{ind} (kV/cm)
1.1	10.8	270	3.5	230	3.5	320	0.1	320	3.5

4.2.3 Front-End Electronics

Due to the negative signal amplitude induced on the pad plane by the electron avalanche in the GEM-based readout chambers, a re-design of the PASA (PreAmplifier ShAper)/ALTRO (ALice Tpc Read Out)-based front-end electronics became necessary. The new front-end cards are based on the SAMPA ASIC[1] which was designed for the ALICE TPC and the Muon Chambers [282, 283]. The chip is made in a 130 nm CMOS[2] technology and features 32 channels with a selectable input polarity and three different combinations of conversion gain and shaping time. As shown in the block diagram of the chip in Fig. 4.9, the first stage of each channel features a charge-sensitive amplifier (CSA) and a shaper, where the current induced on the pads of the readout plane is transformed into differential semi-Gaussian voltage signals. The 10-bit ADC digitizes these signals continuously. The resulting signal can be handled by the digital signal processor featuring zero suppression and different correction procedures for fast and slow variations of the baseline. For the application with the TPC, however, the data are passed without further processing after digitization, to ensure maximal flexibility for the signal processing in the further chain. Finally, the data are encoded by the GBTx ASIC [284] from which it is transferred via optical links for further processing. One front-end card houses 5 SAMPA chips and therefore 160 channels. The specifications of the new system and a comparison with the performance of the previous PASA/ALTRO system are shown in Table 4.4. Notable is the decrease in sampling frequency, owed to considerations of the data rates, which, however, is not expected to deteriorate the performance of the system [285].

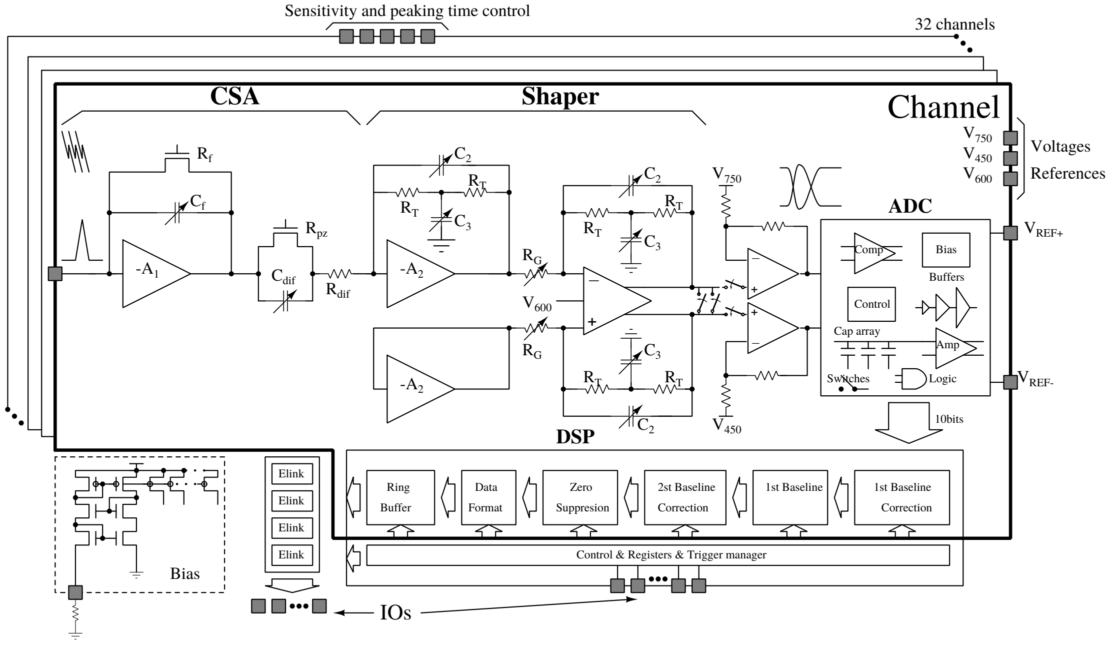

Figure 4.9: SAMPA block diagram [282]. See text for details.

---

[1] Application-Specific Integrated Circuit

[2] Complementary Metal-Oxide-Semiconductor

Table 4.4: Comparison of the specifications of the PASA and ALTRO [214], and the SAMPA [282, 283] in the configuration for the ALICE TPC.

		PASA/ALTRO (Run 1–2)	**SAMPA (Run 3)**
Signal polarity		positive	negative
System noise at 18.5 pF		670 e^-	580 e^-
Conversion gain	(mV/fC)	12.74	20 or 30
Shaping order		4th	4th
Shaper peaking time	(ns)	160	170
Return to baseline	(ns)	< 550	< 500
Non-linearity (CSA & Shaper)		$< 0.1\%$	$< 1\%$
ADC voltage range (differential)	(V)	2	2.2
ADC resolution		10-bit	10-bit
Sampling rate	(MHz)	10	5

4.2.4 Detector Readout and Online–Offline Processing with O^2

The FECs are organized in so-called *partitions*, as outlined in Table 4.5. For the OROC, the partitions reflect the division of the GEM stacks, while in the IROC the two partitions correspond to two rows of FECs. The partitions are further sub-divided into two pad regions and the data of one such region are streamed to and processed by one Common Readout Unit (CRU) [218]. The total data rate of all 3,276 FECs amounts to up to 3.28 TB/s demanding for significant online compression within the O^2 system [217–219] before the data can be stored. The CRUs are located off-detector and act as an interface between the on-detector FECs, the online and offine system O^2, and the central trigger processor. The CRUs are based on high-performance Field Programmable Gate Array processors and in the case of the TPC handle baseline restoration and zero suppression of the incoming raw data.

As shown schematically in Fig. 4.10, an initial data volume reduction to about 500 GB/s is conducted in a farm of about 250 parallel First Level Processors (FLP) computing nodes. In each FLP the continuous data stream of several CRUs is accumulated and split in slices of 20 ms, so-called *sub-time frames*. The width in time was chosen to minimize incomplete data of tracks that span across the boundaries. The sub-time frames are transferred to a farm of about 1500 Event Processing Nodes (EPN) equipped with Graphics Processing Units, where all parts belonging to the same time frame are accumulated on one node to a full time frame with a size

Table 4.5: Summary of the readout electronics attached to the TPC [214].

Partition	**# FECs**	**# SAMPAs**	**# channels**	**# CRUs**
IROC 1	15	75	2,400	2
IROC 2	18	90	2,880	2
OROC 1	18	90	2,880	2
OROC 2	20	100	3,200	2
OROC 3	20	100	3,200	2
Sector	91	455	14,560	10
Total	3,276	16,380	524,160	360

of about 10 GB. At this stage, full track reconstruction and a partial calibration of the data is conducted synchronously with data taking. For the case of the TPC, the cluster and track finding is conducted on the EPNs. The size of the time frame is thus reduced to about 2 GB yielding a data rate of about 100 GB/s to persistent storage. The overall compression of the TPC data is expected to amount to about a factor of 20 with respect to the zero-suppressed raw data size of Run 2 [286]. At a later point in time, asynchronously to the data taking, the EPN farm is used to reprocess these data using final calibration procedures.

This implies that there is no more division into Online and Offline computing, since both share the same algorithms – hence the name O^2 for the project and the common software framework. The latter incorporates the code for the reconstruction, calibration, simulation, and analysis [217, 219], and is based on Root [197], ALFA [288], and FairRoot [289], where the two latter provide the underlying communication layer. Since technology and CPU frequency scaling are not as beneficial as in the past, massive effort is conducted to gain extra performance by parallelization of the code.

The overall increase in the number of collected events is also reflected in the need for significantly larger samples of simulated events, by almost a factor of 20 [217]. Therefore, efficient use of the available computing resources is a mandatory ingredient of the re-design of the particle transport, detector response, and digitization code.

4.2.5 Prototypes

In the course of the R&D program for the GEM upgrade of the ALICE TPC, several small and full-size readout chamber prototypes have been assembled and operated to optimize the HV configuration and validate the working point of the upgrade. The former has been accomplished employing small prototypes equipped with $10 \times 10\,\mathrm{cm}^2$ GEM foils for optimization of

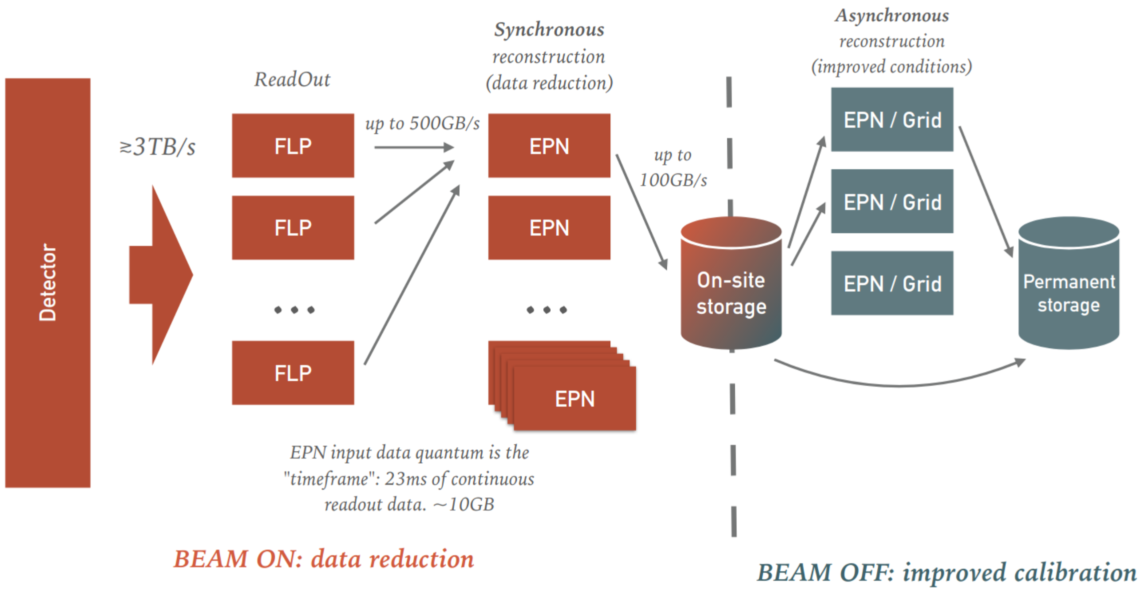

Figure 4.10: The computing architecture of ALICE in Run 3 [287]. See text for details.

the performance of the detectors with respect to energy resolution, *IB*, and operational stability, investigating various GEM structures and field configurations. An exemplary result of the measurement campaign is shown in Figs. 4.7 and 4.8. Additionally, several test beam campaigns with full-size IROC prototypes have been conducted in the course of the R&D phase.

In order to assess the PID performance of the 4-GEM system, beam tests with full-size IROCs have been conducted with secondary pions and electrons provided by the CERN Proton Synchrotron [290]. These tests were conducted with a first prototype of the 4-GEM system in 2014 [213, 215, 291] and with a chamber from the pre-production in 2017 [292]. The readout of the test beam in 2014 was based on EUDET FECs [293] with a sampling frequency of 20 MHz and a shaping time of 120 ns. In contrast to that, for the test in 2017 a first version of the SAMPA was employed with the sampling frequency at 5 MHz. Results from both test beam campaigns are shown in Fig. 4.11, with the separation power defined as

$$S_{\pi-\mathrm{e}} = \frac{|\mu_\mathrm{e} - \mu_\pi|}{0.5 \cdot (\sigma_\mathrm{e} + \sigma_\pi)}, \tag{4.3}$$

where μ and σ correspond to the mean value and the resolution of the $\mathrm{d}E/\mathrm{d}x$ of pions and electrons. The performance of different HV configurations corresponding to different values of $\sigma(^{55}\mathrm{Fe})$ and *IB* has been assessed in the course of these studies. The HV configurations are summarized in Table 4.6 for the 2014 and in Table 4.7 for the 2017 test beam.

As expected, the $\mathrm{d}E/\mathrm{d}x$ resolution decreases as the energy resolution degrades, even though the dependence is rather shallow and no sudden breakdown is observed. The results from the test in 2014 demonstrate that the resolution is well within the expectations of the current TPC [185] and prove that the 4-GEM configuration fulfills the requirements of the upgrade program. Microscopic simulations conducted with AliRoot yield a fairly good description of the trend [213, 291]. For the results obtained in 2017, the degradation of the separation power can be attributed to the short drift length of about 5 cm which, in combination with the sampling frequency of 5 MHz, leads to a significant loss of information in this particular configuration [292]. For the operation of the full TPC this effect is not relevant and therefore is not expected to affect the performance.

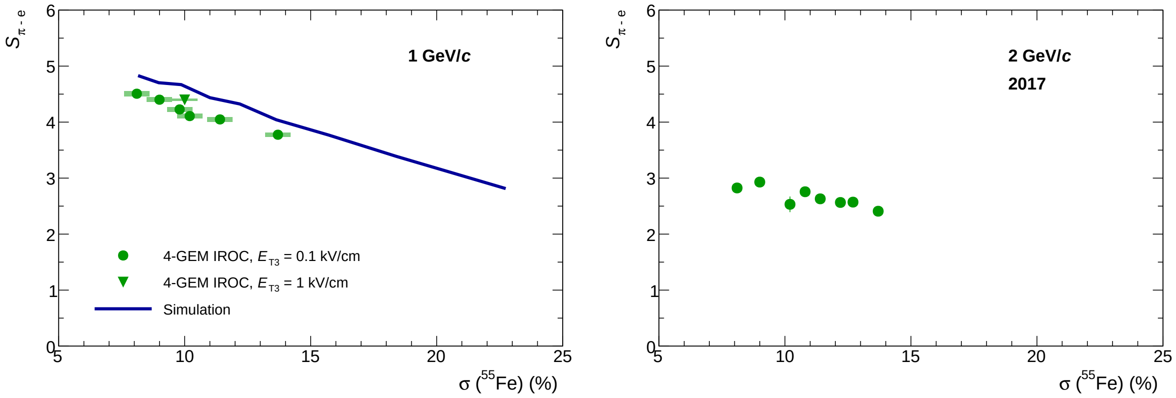

Figure 4.11: (*Left*) Separation power of pions and electrons at 1 GeV/c as a function of $\sigma(^{55}\mathrm{Fe})$ measured with a prototype IROC [213, 291]. The blue curve shows the result of a simulation with AliRoot. (*Right*) The performance of an pre-production IROC equipped with SAMPA-based FECs at 2 GeV/c. Reproduced from Ref. [292].

Table 4.6: HV configurations employed during the 2014 test beam [213, 215]. The absolute uncertainties are 0.1% and 0.5% on the measurements of IB and $\sigma(^{55}\mathrm{Fe})$.

IB (%)	$\sigma(^{55}\mathrm{Fe})$ (%)	$\Delta U_{\mathrm{GEM\,1}}$ (V)	E_{T1} (kV/cm)	$\Delta U_{\mathrm{GEM\,2}}$ (V)	E_{T2} (kV/cm)	$\Delta U_{\mathrm{GEM\,3}}$ (V)	E_{T3} (kV/cm)	$\Delta U_{\mathrm{GEM\,4}}$ (V)	E_{ind} (kV/cm)
0.5	13.7	225	4	235	2	304	0.1	382	4
0.7	11.4	255	4	235	2	292	0.1	364	4
0.8	10.2	275	4	235	2	284	0.1	345	4
1.2	9.0	305	4	235	2	271	0.1	339	4
2.5	8.1	315	4	285	2	240	0.1	300	4
1.1	9.8	275	4	235	2	308	0.1	323	4
2.0	9.9	275	2	240	3	254	1.0	317	4

Table 4.7: HV configurations employed during the 2017 test beam [281, 292]. The absolute uncertainties are 0.1% and 0.5% on the measurements of IB and $\sigma(^{55}\mathrm{Fe})$. The last five settings have also been tested in 2014.

IB (%)	$\sigma(^{55}\mathrm{Fe})$ (%)	$\Delta U_{\mathrm{GEM\,1}}$ (V)	E_{T1} (kV/cm)	$\Delta U_{\mathrm{GEM\,2}}$ (V)	E_{T2} (kV/cm)	$\Delta U_{\mathrm{GEM\,3}}$ (V)	E_{T3} (kV/cm)	$\Delta U_{\mathrm{GEM\,4}}$ (V)	E_{ind} (kV/cm)
0.7	12.7	270	4	230	4	288	0.1	359	4
1.1	10.8	270	3.5	230	3.5	320	0.1	320	3.5
1.0	12.2	250	2	215	4	332.5	0.1	332.5	4
1.1	12.1	245	2	220	4	324	0.1	324	4
1.6	12.3	235	2	240	4	304.5	0.1	304.5	4
0.9	12.0	240	2	225	4	337	0.1	337	4
0.5	13.7	225	4	235	2	304	0.1	382	4
0.7	11.4	255	4	235	2	292	0.1	364	4
0.8	10.2	275	4	235	2	284	0.1	345	4
1.2	9.0	305	4	235	2	271	0.1	339	4
2.5	8.1	315	4	285	2	240	0.1	300	4

5 Simulation Tools for GEM-based Detectors

Detector simulations are an essential ingredient of modern high-energy physics. On the one hand, simulated events, treated in the same way as measured data, are a commonly employed tool for data analysis and interpretation. The applications range from estimations of the detector resolution and reconstruction efficiencies to the comparison of physical observables to the output of event generators or theoretical models. On the other hand, detailed simulations make it possible to assess and improve the detector performance during the design phase and are instrumental for optimization. At the same time, calibration and commissioning strategies can be developed and improved already during early phases of the detector development, significantly shortening the start-up phase of an experiment. Additionally, dedicated simulations of individual physical processes inside a detector can be employed to understand and mitigate undesired effects.

This Chapter discusses two approaches to the simulation of different aspects of GEM-based detectors. The first part deals with the implementation of the full chain of processes for the signal formation in the ALICE GEM TPC, permitting the application of the same reconstruction algorithms as for the measured data. The second part focuses on dedicated simulations of the development of the conditions leading to the formation of discharges in GEM-based detectors, as discussed in Sec. 4.1, which enable the prediction of the stability in a given radiation environment.

5.1 Digitization for the ALICE TPC with O^2

The typical workflow of the simulation of a high-energy physics experiment starts with the event generator, providing the kinematic information of all particles produced in the primordial particle collision. The outgoing particles are then tracked through the detector material and electromagnetic and hadronic interactions with matter are simulated employing transport codes such as GEANT [205, 206]. The particles are transported in steps determined by physics processes and the detector geometry, with a *hit* corresponding to a localized energy deposit occurring after each step. The following processes leading to the formation of a measureable signal in the detector are typically not considered in the particle transport but are simulated in a separate step called *digitization*. The latter results in a data format identical to the output of the real detector, thus allowing the processing of the simulated data in the same way as real data by the calibration and reconstruction algorithms.

In general, the production of large samples of MC simulations takes a sizable fraction of the computing resources of modern high-energy physics experiments [294]. Indeed, about 70% of the overall computing resources allocated to ALICE are spent on MC productions [217]. Particle transport within the current simulation framework AliRoot [196] amounts to about 55% thereof, while about 35% are spent in the digitization with the largest part consumed by the TPC code [295].

The need for large simulation samples grows in line with the data samples collected during the LHC Run 3 and beyond. With an increase of the data volume by two orders of magnitude for ALICE, the requirements for simulated data samples increase by a factor of 20 [217]. Therefore, the performance of the simulation and digitization code is considered crucial [294–296].

The software for the ALICE experiment for Run 3 and beyond is organized in the O^2 framework [217, 219], as discussed in Sec. 4.2.4. The upgrade of the TPC readout and the requirements for continuous data taking and an efficient simulation procedure require a re-design of the full digitization code of the ALICE TPC, which is described in the following.

5.1.1 Workflow

The digitization of the TPC starts with the *hits*, which are simulated with GEANT [205, 206] and specify the spatial information and the energy deposit of the individual interactions of the incident particle with the detector medium. The task of the digitization is to simulate all relevant physics processes leading to the signal formation in the TPC. The data input of the hits and output of the final digits is provided by the O^2 Data Processing Layer [287, 297], into which the TPC digitization task is fully integrated. For reasons of flexibility and maintainability, the code is divided so that one `C++` class incorporates one physics process. The source code can be found at Ref. [219].

Figure 5.1 sketches the overall work flow. First of all, the drift of the individual ionization electrons in the detector gas towards the readout chambers is simulated. The charges are amplified by the GEM stack and the signal induction on the readout anode and signal processing in the FECs is simulated. The resulting *digits* are then written to disk and available for further processing.

The detailed implementation and description of the processes are discussed in the following, while the remainder of this Section is devoted to technical aspects of the overall workflow and data handling. The relevant parameters used in the full digitization chain are summarized in Table 5.1 and explained throughout this Section.

The main challenge of the implementation of the TPC digitization concerns the requirements of continuous data taking. The integration time of the TPC is defined by the electron drift time of about 100 µs. Therefore, at interaction rates of 50 kHz in Pb–Pb collisions, on average five collisions will accumulate within its active volume. Similarly, the tracks of 100 pp collisions will pile-up for the envisaged 1 MHz interaction rate in this system. The event generator and the simulation of the energy loss in the detector medium do not require information about events in the past or the future and can accordingly be processed on an event-by-event basis. Due to saturation and threshold effects, however, the long integration time in the TPC introduces correlations among consecutive events. For this reason, the simulation of the continuous readout is implemented at the stage of the digitization. The resulting amount of accumulated data per processing step is defined by the 20 ms length of a time frame, as discussed in Sec. 4.2.4. Considering the 5 MHz sampling frequency and the 524,160 pads of the TPC, one such time frame contains about 52.4×10^9 voxels. The resulting data size is significantly too large for the physical memory of a typical grid node. Therefore, several measures are implemented to reduce the memory footprint of the digitization and accordingly the computational requirements on the nodes.

The signal from individual electrons is buffered during processing in a pad row–pad matrix for a given time bin, as depicted in Fig. 5.1. Correlations among the digits produced from the hits of different events can only occur within the integration time of 100 µs. Since the events are processed time-ordered, this significantly reduces the time interval to be kept in memory for processing. In particular, the digits in time bins prior to the time stamp of the processed collision cannot be correlated with the present event. Therefore, before processing the hits from a new event, such digits are written to disk and the corresponding memory is freed. In

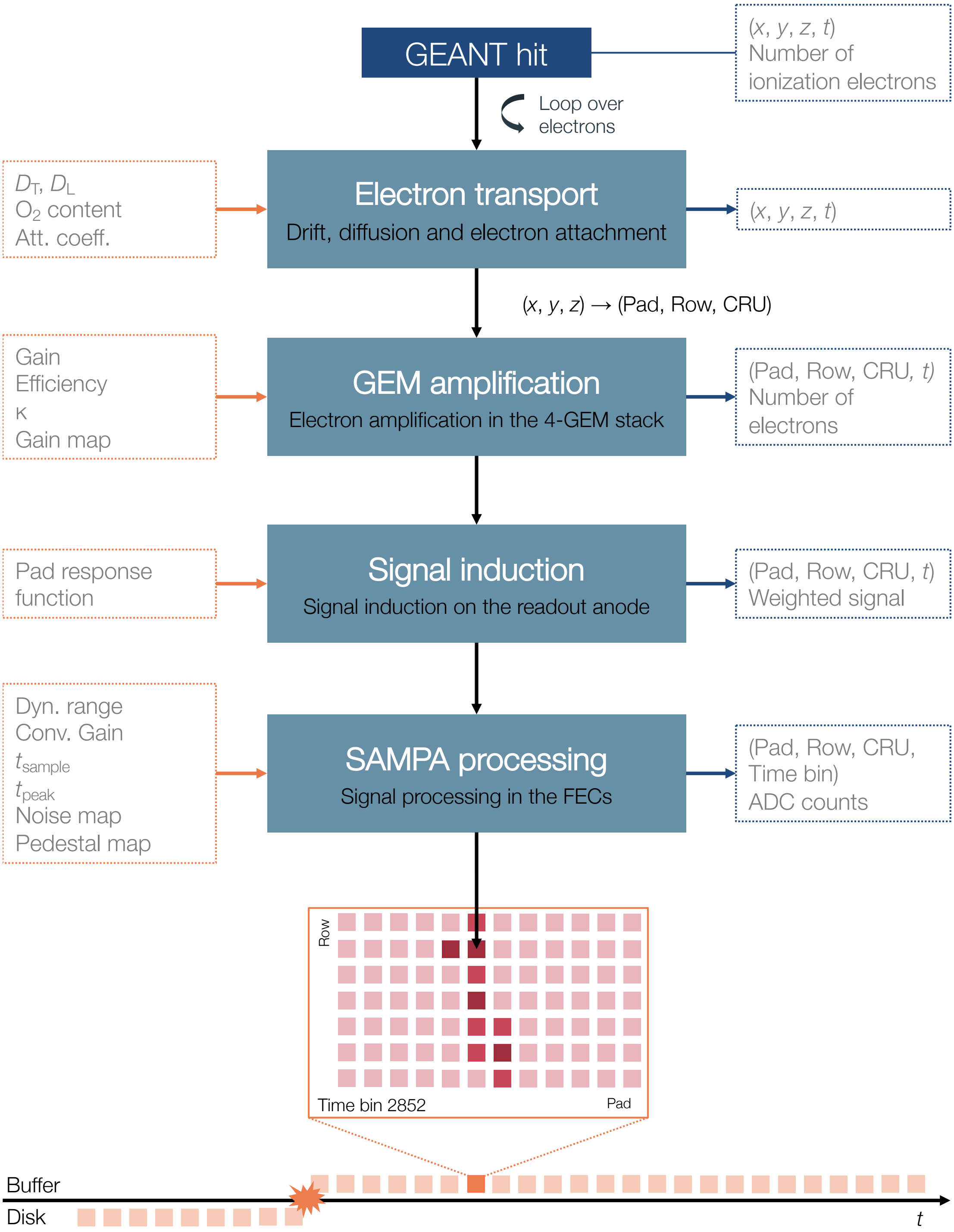

Figure 5.1: Work flow of the implementation of the TPC digitization in O^2. Each ionization electron subsequently undergoes the relevant physics processes. The resulting signal is stored in an intermediate buffer. Digits from events in the past that can no longer be correlated with the present event, denoted by the star, are dumped to disk. The left column depicts the employed parameters and de-calibration objects in the corresponding processes, while the right column refers to the output of a given physics process.

Table 5.1: Relevant parameters for the TPC digitization in O^2. The properties of the gas mixture employed for the ALICE TPC Ne-CO_2-N_2 (90-10-5) are evaluated at 400 V/cm [214].

Parameter		**Value**
Gas parameters		
Primary electrons per cm for MIP		14.0
Total number of electrons per cm for MIP		36.1
Effective ionization potential W_{ion}	(eV)	37.2
Drift velocity v_{d}	(cm/µs)	2.58
Longitudinal diffusion constant D_{L}	($\sqrt{\mathrm{cm}}$)	0.0221
Transverse diffusion constant D_{T}	($\sqrt{\mathrm{cm}}$)	0.0209
Larmor frequency $\omega\tau$ ($B = 0.5\,\mathrm{T}$)		0.32
O_2 content	(ppm)	5
Attachment coefficient	(s^{-1})	250
Single-electron response κ		1.64
GEM parameters		
Gain G		2000
Effective single-electron response κ_{eff}		1.205
Single-electron detection efficiency $\varepsilon_{\mathrm{eff}}$		0.528
Electronics parameters		
Dynamic range	(V)	2.2
Shaping time	(ns)	170
Conversion gain	(mV/fC)	20 (30)
Sampling frequency	(MHz)	5

order to additionally enable parallelization of the data processing, the digitization is conducted individually for each sector of the TPC, which covers 20° in azimuth. Space charge distortions and the widening of the charge cloud due to diffusion can lead to charge leakage from one sector to another. Therefore, one sector processes hits within an azimuthal interval of 40°, leaving a margin of 10° to either side of the ROC. The unnecessary processing of hits is prevented by further pre-selections discussed in Sec. 5.1.2. With these measures, the maximal memory consumption of the digitization of one TPC sector typically does not exceed 2 GB, even in the case of digitizing Pb–Pb collisions simulated with the HIJING [203] event generator.

In order to reduce the file size of the output, only digits containing actual signals are written to disk. Empty voxels are filled on-the-fly with noise and pedestal values during the cluster finding. The corresponding treatment of the signal digits is described in Sec. 5.1.6.

5.1.2 Electron Transport

The digitization starts with the energy deposit of the *hits*, which is converted to a number of electrons employing the effective ionization potential W_{ion}, as depicted in Table 5.1. The resulting ionization electrons are guided towards the readout chambers on both endplates by the applied electric drift field of the TPC. Microscopically, the drift of charge carriers in a gaseous medium can be described by a series of elastic collisions with the gas compounds. Each collision results in a randomization of the trajectory and a loss of energy. The external electric field leads to a directed acceleration of the charge carriers described by the *Langevin* equation [179]

$$m\frac{\mathrm{d}\mathbf{v}}{\mathrm{d}t} = e\mathbf{E} + e(\mathbf{v} \times \mathbf{B}) - K\mathbf{v}, \tag{5.1}$$

where m, e, and $\mathbf{v}$ are the mass, electric charge, and velocity of the particle. The collisions with the gas components are incorporated as a resistive force $K\mathbf{v}$, where $K = m/\tau$ with the mean time τ between two successive collisions. For the case $t \gg \tau$, the combination of both effects, deceleration by successive collisions and re-acceleration in the electric field, leads to an equilibrium in which the charge carriers move with a *macroscopically* constant drift velocity $\mathbf{v}_\mathrm{d}$. Therefore, the measured drift time of the electrons in the TPC can be directly converted to a position in z. In the ideal case, the electric and magnetic field in the TPC are parallel. Slight deviations from the ideal case, however, lead to a circular motion of the charge carriers around their nominal path with *Larmor* frequency $\omega = -(e/m)B$.

Additionally, the energy exchange with the gas components via elastic collisions and the resulting randomization of the momenta leads to an effective broadening of the charge cloud. In the absence of external fields, this results in a thermalization of the charge carriers' energy and an isotropic spread in all spatial dimensions. The introduction of an external field, however, causes a preferred direction of motion. Thus, the spread longitudinal and transverse to the movement differs. The effect of *diffusion* is simulated by smearing the point-like electron cluster with a Gaussian distribution with a width given by

$$\sigma_{\mathrm{T,\,L}} = D_{\mathrm{T,\,L}} \cdot \sqrt{L_\mathrm{drift}}, \tag{5.2}$$

where D_T and D_L are the corresponding diffusion coefficients and L_drift the drift length. The relevant gas parameters for the simulation of the electron transport in the TPC are quoted in Table 5.1. An exemplary point-like electron cloud placed close to the central electrode of the TPC accordingly obtains a width of about 3.5 mm in transverse and longitudinal direction after the full drift length of 2.5 m. Figure 5.2 depicts the effect of the electron transport on a few tracks of pions in the $x-y$ and the $r-z$ plane of the TPC. It can be seen that hits at larger z are less affected by the diffusion due to the shorter drift length.

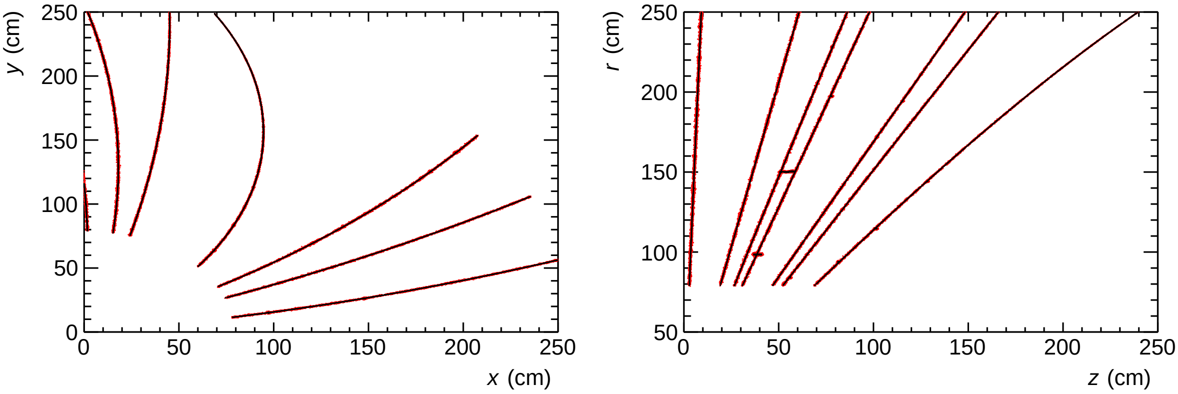

Figure 5.2: Position of the hits in the $x-y$ (*left*) and $r-z$ (*right*) plane before (*black*) and after the electron transport (*red*). The figures show the upper quadrant of the TPC. The central electrode is located at $z = 0$ cm.

The ionization electrons created by a single hit are tracked individually in the simulation. In order to avoid unnecessary processing, the electrons are only processed when the hit is localized inside the active area of the processed sector within $3\sigma_T$ of the expected transverse diffusion.

In addition, the electrons may be absorbed by electronegative gas components during the drift towards the readout chambers. In particular, residual O_2 or H_2O contaminations can lead to such losses. Since the energy resolution strongly depends on the amount of primary ionization, the purity of the employed gas medium is crucial. This effect is considered in the simulation by randomly removing electrons based on the corresponding drift time and the absorption probability.

The implementation of a more evolved simulation of the electron drift paths in the distorted drift field, due to the accumulation of space charge, is beyond the scope of this work and discussed in Ref. [298].

5.1.3 GEM Amplification

The individual electrons are multiplied by the gain of the GEM stack at the amplification stage. In general, gas amplification occurs in strong electric fields of the order of kV/cm in which single electrons achieve sufficient energy to undergo successive ionizing collisions within a short distance. The resulting electrons experience the same field and therefore an electron avalanche arises. The increase in number of electrons n per distance $\mathrm{d}x$ is

$$\mathrm{d}n = n\alpha\mathrm{d}x, \tag{5.3}$$

where α is the first *Townsend coefficient*, determined by the relevant ionization and excitation cross sections of the gas mixture [179]. Therefore, typically simulation methods with e.g. MAGBOLTZ [263] have to be employed to compute α. In general, the integration of Eq. 5.3 yields only average quantities for the amplified number of electrons. In reality, the amplification is a stochastic process with characteristic fluctuations. Since the number of primary electrons is rather low, these fluctuations have a driving impact on the energy resolution of the detector [299] and therefore need to be considered accordingly in the simulation.

The probability density function for single-electron amplification in a GEM stack can be described by the Polya distribution [299],

$$P(n) = \frac{1}{s \cdot \Gamma(\kappa)} \cdot \left(\frac{n}{s}\right)^{\kappa-1} \cdot e^{-n/s}, \tag{5.4}$$

where $s = G/\kappa$ is the slope parameter incorporating the gain G and the deviation from an exponential distribution $\kappa = (\sigma/\mu)^{-2}$. Figure 5.3 depicts the resulting distribution for a gain $G = 10$ and different values of κ. For larger values of κ, a clear deviation from the exponential behavior can be observed.

Indeed, measurements of the single-electron response for the gas to be used in the ALICE TPC, Ne-CO_2-N_2 (90-10-5), at low GEM gains have yielded $\kappa = 1.64 \pm 0.05$ [300]. As depicted in Fig. 5.4, such deviations from the exponential form are also observed in other gases and believed to be caused by avalanche saturation effects [301–303]. Such saturation effects can arise in GEMs since the single-electron avalanche is confined into a single GEM hole. The corresponding restriction of the lateral size, given by the diameter of the hole, reduces the fluctuations [302]. Simulation

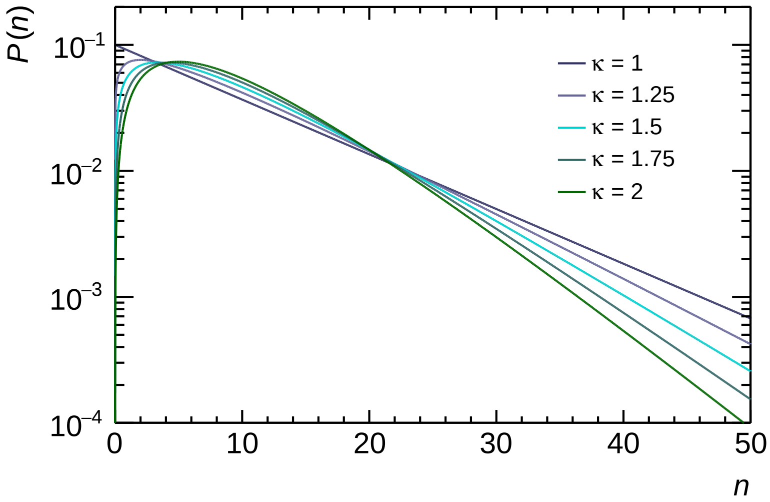

Figure 5.3: Polya distribution for different values of κ at a gain of 10.

studies employing GARFIELD [263] indicate that the single-electron distribution approaches the exponential form for moderate GEM gains, while deviating for very large gains [304]. Measurements of the single-electron response of multi-GEM systems demonstrate that the overall single-electron response can be described by an exponential distribution [301–303]. However, slight deviations towards a Polya distribution arise depending on the gas mixture [302, 303].

In order to consider random fluctuations of the gain and the collection and extraction efficiencies, two different models can be applied in the TPC digitization within O^2 – a subsequent simulation of all relevant processes occurring in the GEM stack and an effective model implemented for performance considerations. Since the pad size is significantly larger than the hole pitch of the GEMs, the latter is neglected in the simulation. The resulting signal is a convolution of single-electron avalanches.

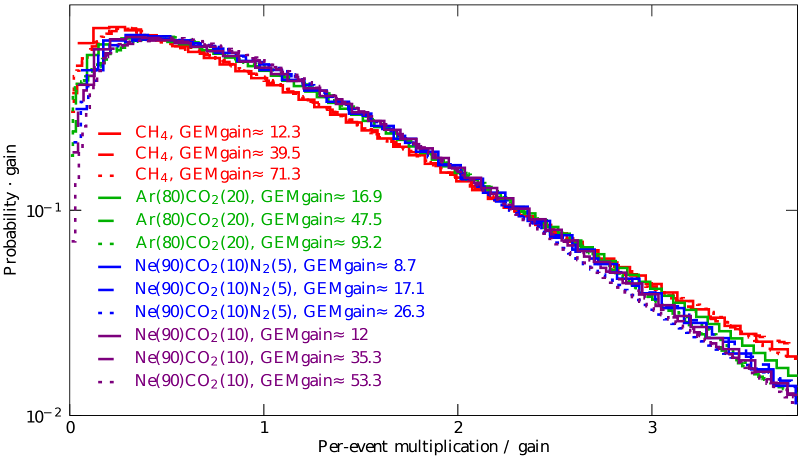

Figure 5.4: Single-electron multiplication distribution measured with a GEM setup in different gas mixtures and effective GEM gains. Modified from Ref. [300]. A clear deviation from the exponential shape is observed in the low amplitude region.

Table 5.2: Electron transport and amplification properties of an S-LP-LP-S configuration operated with the so-called *TDR setting* [214, 215]. The transfer and induction fields are, in decreasing order, 4, 2, 0.1, 4 kV/cm. The *IB* performance of the HV configuration is about 0.6% at an energy resolution of around 12% [214].

	ΔU_{GEM} (V)	$\varepsilon_{\text{coll}}$	M	$\varepsilon_{\text{extr}}$	G
GEM 1	270	1	14	0.65	9.1
GEM 2	250	0.2	8	0.55	0.88
GEM 3	270	0.25	53	0.12	1.6
GEM 4	340	1	240	0.6	144
Total					1830

Full Treatment In the full implementation of the GEM response, the electron avalanche is subsequently transported through the GEM stack considering charge collection, amplification and extraction in each GEM. For the statistics of collection and extraction, binomial distributions are assumed. However, this requires detailed knowledge about the transport properties within the 4-GEM stack extracted from measurements or simulations. Table 5.2 displays the relevant transport properties obtained using GARFIELD++ [305] simulations for an exemplary HV configuration of the TPC Upgrade [214]. Accordingly, the number of collected and extracted electrons is randomly sampled.

Fluctuations of the amplification process in the GEM itself are considered by sampling from a Polya distribution, considering the multiplication factor of the respective GEMs and the experimentally determined value of $\kappa = 1.64$ [300]. Since the GARFIELD++ simulation arrives only at a total 4-GEM stack gain of about 1830, the gain in GEM 4 is scaled up to achieve an overall gain of 2000. Using the last amplification stage in the stack ensures that the overall energy resolution remains unaffected. The resulting single-electron response is depicted in the left panel of Fig. 5.5. A slight deviation from the purely exponential shape can be observed.

Due to the finite collection and extraction efficiencies, in particular of the intermediate, ion-blocking layers of the stack where also the effective gain is low, the probability that the electron avalanche is completely lost during the transport is rather large. Indeed, the electron detection

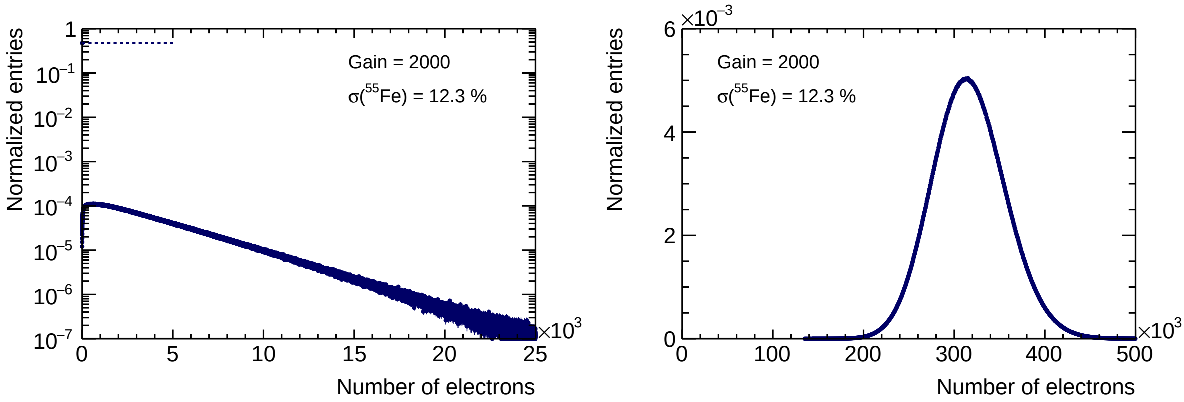

Figure 5.5: (*Left*) The single-electron response determined with the full amplification model. The dashed line highlights the case in which the avalanche created by the incoming electron is lost during the transport through the stack. (*Right*) The response of the system to the energy deposit caused by a ^{55}Fe photon in Ne-CO_2-N_2.

efficiency of the system is only about 53%, while in about 47% of the cases the electron avalanche is lost, as highlighted by the dashed line in Fig. 5.5. The electron detection efficiency is driving the energy resolution. Experimentally, the energy resolution is typically evaluated with a ^{55}Fe source. The energy deposit caused by the 5.9 keV photon liberates on average about 158 electrons in Ne-CO_2-N_2 (90-10-5). The resulting response of the GEM simulation is obtained by summing the result of 158 single-electron avalanches and depicted in the right panel of Fig. 5.5. The energy resolution is extracted from a fit to the data and found to be in good agreement with experimental characterization of this HV configuration.

It should be noted, that the full treatment has two disadvantages. First of all, the transport and amplification properties of the HV configuration need to be known. This requires either measurements or simulations of the charge dynamics at each stage of the GEM stack. In reality, however, the operation of the detector often requires adjustments of the voltages in order to fine-tune the performance or improve the stability of a given ROC by reducing the overall gain. Such situations are difficult to accommodate with the given setup. Furthermore, the simulation of the full charge transport and amplification at each step through the 4-GEM stack is unnecessarily complicated and time consumptive. In order to improve the performance, the sampling of random numbers is conducted from a circular buffer filled before the actual simulation. Considering the ionization density of minimum ionizing particles, the track length in the TPC, and a multiplicity of 1×10^4 in Pb–Pb collisions, about 60×10^6 electrons need to be processed in a typical event. Accordingly, the GEM amplification takes a considerable amount of processing time. Nevertheless, the full amplification model can be used as a benchmark and for testing purposes.

Effective Model for the Amplification Since computing performance is a crucial aspect of the TPC digitization, an effective model for the single-electron response of the 4-GEM stack is implemented. The consecutive simulation of the amplification and the loss of charge carriers due to the efficiencies of each GEM stage are combined to a single, effective electron amplification stage. The overall electron detection efficiency $\varepsilon_{\mathrm{eff}}$ of the whole system steers the probability that the avalanche is lost. Similarly, the deviation of the overall single-electron response of the system is incorporated into a single parameter, κ_{eff}. In this scenario, however, there is no longer the possibility to employ simulated or measured efficiencies of individual elements to constrain the GEM response. Therefore, the corresponding *effective* parameters κ_{eff} and $\varepsilon_{\mathrm{eff}}$ have to be tuned to experimental data, as discussed in Sec. 5.1.7.

Figure 5.6 depicts the resulting energy resolution $\sigma(^{55}\mathrm{Fe})$, determined by the response of the system to 158 incoming electrons for the parameter phase space of κ_{eff} and $\varepsilon_{\mathrm{eff}}$. As expected, the energy resolution deteriorates with decreasing effective electron detection efficiency $\varepsilon_{\mathrm{eff}}$. Deviating from the exponential shape of the single-electron response $\kappa_{\mathrm{eff}} = 1$ considerably improves the energy resolution. This reflects well the reduced spread of the Polya distribution for larger values of κ, as depicted in Fig. 5.3.

The best description of the single-electron response of the full treatment is obtained for $\kappa_{\mathrm{eff}} = 1.205$ and $\varepsilon_{\mathrm{eff}} = 52.8\%$, yielding consistent values for the gain and the energy resolution. The optimization of the response for different HV configurations must be conducted in a data-driven way. As discussed in Sec. 5.1.7, the charge distributions on the cluster level are insensitive to the actual value of κ_{eff}. This is not surprising considering the total ionization of a minimum ionizing particle, which liberates on average 36.1 e^-/cm in Ne-CO_2-N_2 (90-10-5). Accordingly,

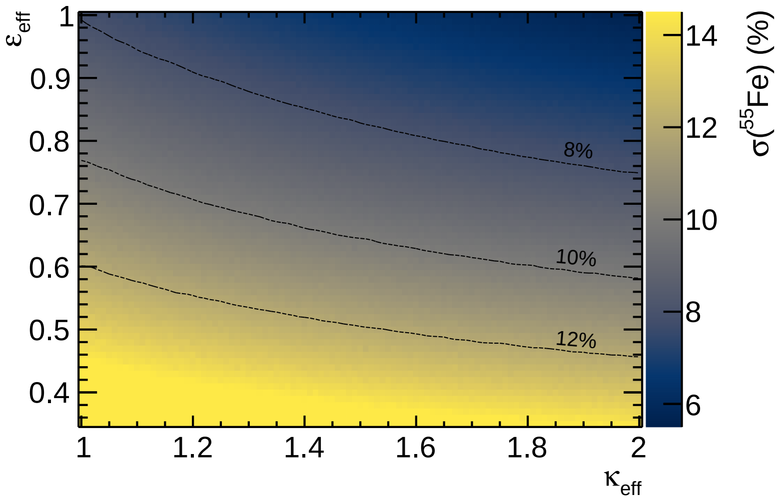

Figure 5.6: The energy resolution determined with the effective amplification model for different values of $\varepsilon_{\mathrm{eff}}$ and κ_{eff}.

on the pad level many single-electron avalanches are integrated and the actual shape of the single-electron response is no longer relevant due to the central limit theorem. Therefore, the realization of a given value of $\sigma(^{55}\mathrm{Fe})$ is accomplished by tuning $\varepsilon_{\mathrm{eff}}$. The simulation of the effective single-electron response is about a factor of 22 faster than the full simulation. Therefore, it is used as the default in the digitization.

5.1.4 Signal Induction on the Readout Anode

After the amplification in the GEM stack, the resulting charge cloud is drifting towards the readout anode in the induction field. The Coulomb field of the moving charges causes the induction of mirror charges on the anode, which leads to a current flow registered by the front-end electronics. The Coulomb potential is proportional to $1/r$ and therefore a perceivable charge is induced also on pads located further away from the center of the electron cloud. This effect is folded with the diffusion of the charge cloud while traversing the 4-GEM stack. Accordingly, the charge distribution drifting towards the anode is effectively broadened and a signal is induced as well on adjacent pads. The pad response function (PRF) incorporates the effect of diffusion in the GEM stack and signal induction and returns a weight for the signal as a function of the start position of the electron cloud.

In this work, the PRF for a 4-GEM stack is computed following the procedures discussed in Ref. [306]. The instantaneous current on the grounded pad of interest induced by a point charge approaching it on the trajectory $\mathbf{x}(t)$ is given by the Shockley-Ramo theorem [307, 308]

$$I(t) = -E_{\mathrm{weight}}[\mathbf{x}(t)] \cdot q \cdot \dot{\mathbf{x}}(t), \tag{5.5}$$

with the velocity $\dot{\mathbf{x}}(t)$, the charge q of the particles, and the weighting field E_{weight}. The weighting field is obtained by applying a potential of 1 V to the pad of interest with all other elements grounded. The geometry of the pad plane is implemented in the finite element method (FEM) software COMSOL® Multiphysics [309]. The GEM foil is simplified as a flat, homogeneous electrode. A two-dimensional projection of the weighting field E_{weight} in the center of the pad of an IROC is depicted in Fig. 5.7.

Before entering the induction field, the Coulomb field of the moving charges in the GEM stack is shielded by the GEM 4 electrodes. Therefore, the total charge induced on the pad is obtained by integration over the full drift time T in the induction field [179]

$$Q_{\text{induced}} = -\int_0^T \mathrm{d}t\ I(t) = -\int_0^T \mathrm{d}t\ E_{\text{weight}}[\mathbf{x}(t)] \cdot q \cdot \dot{\mathbf{x}}(t). \tag{5.6}$$

The total induced charge is therefore independent of the trajectory of the charges and depends only on their endpoints. This means, that the total charge induced on a given pad is equal to the number of charges arriving on it. For pads that receive no charges, the induced signal is bipolar.

The velocity of the drifting charges is obtained by simulating their movement with the COMSOL® software. The starting points and velocities of the electrons amplified in a 4-GEM stack and entering the induction field are obtained from GARFIELD++ simulations [305, 310] applying the baseline HV configuration [214]. The resulting charge cloud created at a distance of 100 µm below the GEM 4 bottom electrode has a width of about 250 µm in x and y direction. The velocities follow a Gaussian distribution with a mean (width) of about 50 µm/ns (35 µm/ns) in x and y and about 80 µm/ns (25 µm/ns) in z.

The starting points and velocities of 2000 electrons, chosen according to the nominal gain of the 4-GEM stack, are randomly sampled from these distributions. The induction field is computed using the same geometry as for the weighting field $E_{\text{weight}}[\mathbf{x}(t)]$, however applying nominal voltage to the GEM 4 bottom electrode. The trajectories of the electrons drifting in this field are computed considering additionally the influence of the 0.5 T magnetic field in z direction. The effect of diffusion is incorporated by simulating collisions among the electrons and the constituents of the detector gas with a rate of 7.4×10^{11} Hz, obtained from GARFIELD simulations [263].

The starting position of the electron avalanche is varied in x and y in steps of 250 µm between

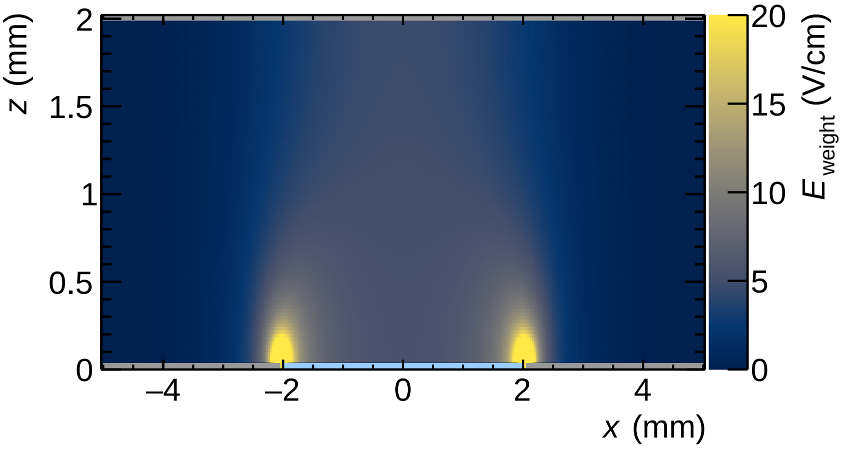

Figure 5.7: Weighting field of the ALICE IROC computed with COMSOL®. The gray elements depict the grounded readout pads (*bottom*) and GEM 4 bottom (*top*). A voltage of 1 V is applied to the blue pad in the center.

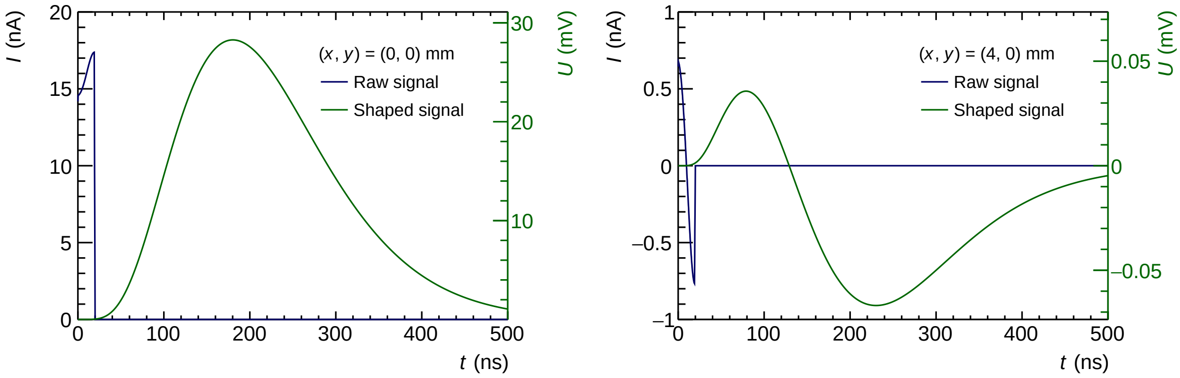

Figure 5.8: The instantaneous current induced on a pad as a function of the time with the avalanche starting directly above the center of the pad (*left*) and 4 mm left of the pad in x, corresponding to the center of the neighboring pad (*right*). The blue curve depicts the induced current on the pad, while the green curve displays the result of the signal processing in the SAMPA.

0 mm and 10 mm from the center of the pad. For each configuration, the position and velocity of each electron is stored for 100 steps between the bottom of the GEM 4 electrode and the readout anode. The instantaneous current can then be computed from Eq. 5.5 with these information. Figure 5.8 depicts the resulting instantaneous current for two different starting points of the avalanche. The length of the signal of about 20 ns corresponds to the electron drift in the induction gap. As expected, when the avalanche starts directly above the center of the pad (*left panel*), the induced signal is uni-polar. When the center of the avalanche is on the adjacent pad (*right panel*), no charges find their way onto the pad of interest. Correspondingly, the total inducted charge is zero and the signal purely bipolar.

It should be noted, that in the further processing of the signals in the readout chain of ALICE only an enhancement with respect to the baseline is considered, while the undershoot exhibited by the bipolar signal is not used. Therefore, the induced signal on the readout pad is folded with the effect of the signal processing in the SAMPA, as outlined in Sec. 5.1.6, for a realistic treatment. Furthermore, only the positive part of the signal is taken into account. The resulting total induced charge is then computed by summing up the positive parts of the signal. Finally, the pad response is obtained by normalizing the sum to the maximally achievable value obtained when the electron cloud starts above the center of the pad.

The resulting PRF for the three different pad sizes of IROC, OROC 1, OROC 2, and OROC 3 are shown in Figs. 5.9, 5.10, and 5.11. It is clearly visible, that the PRF is equal to unity on the surface of the pad and falls off rapidly at its borders. A comparison to experimental data from a test beam with an IROC prototype, discussed in Sec. 5.1.7, reveals that the inclusion of the PRF is essential to reproduce measured charge distributions and therefore serves as a benchmark for this calculation. A more detailed analysis can be conducted employing the track residuals measured with the full-size TPC once fully installed.

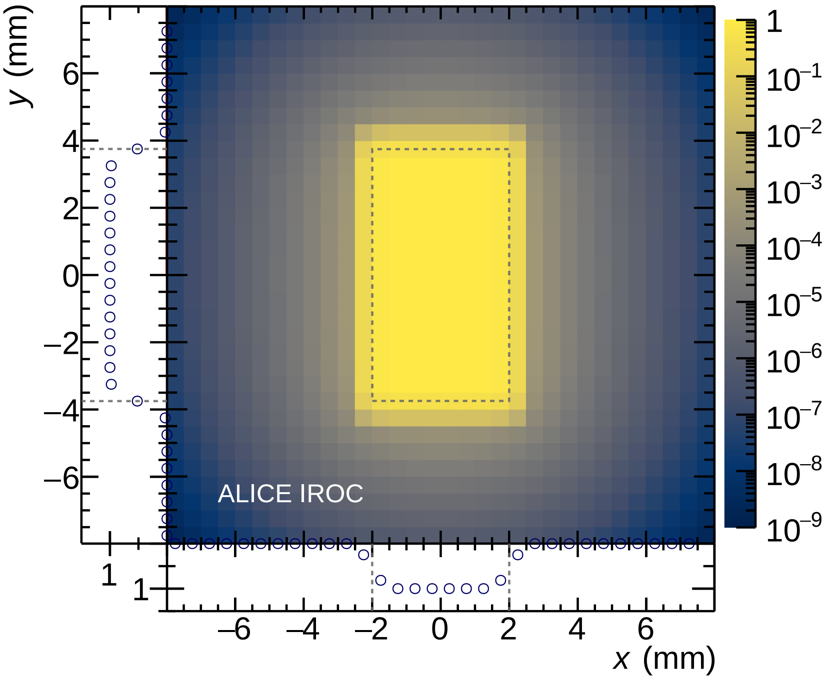

Figure 5.9: Pad response function of the ALICE IROC. The bottom and left panels depict the projection in x and y at the center of the pad and the dashed lines depict the outer profile of the pad.

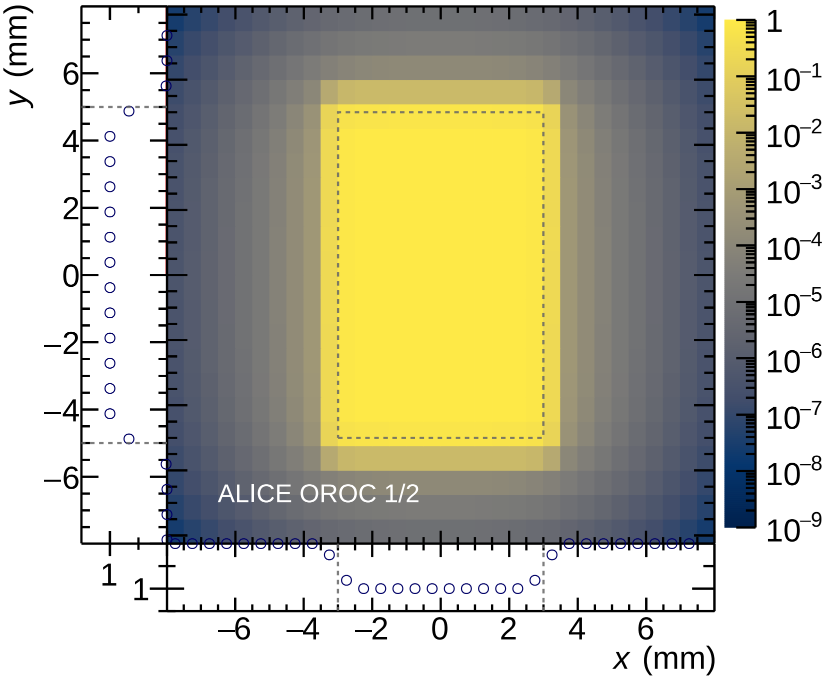

Figure 5.10: Pad response function of the ALICE OROC 1/2. The bottom and left panels depict the projection in x and y at the center of the pad and the dashed lines depict the outer profile of the pad.

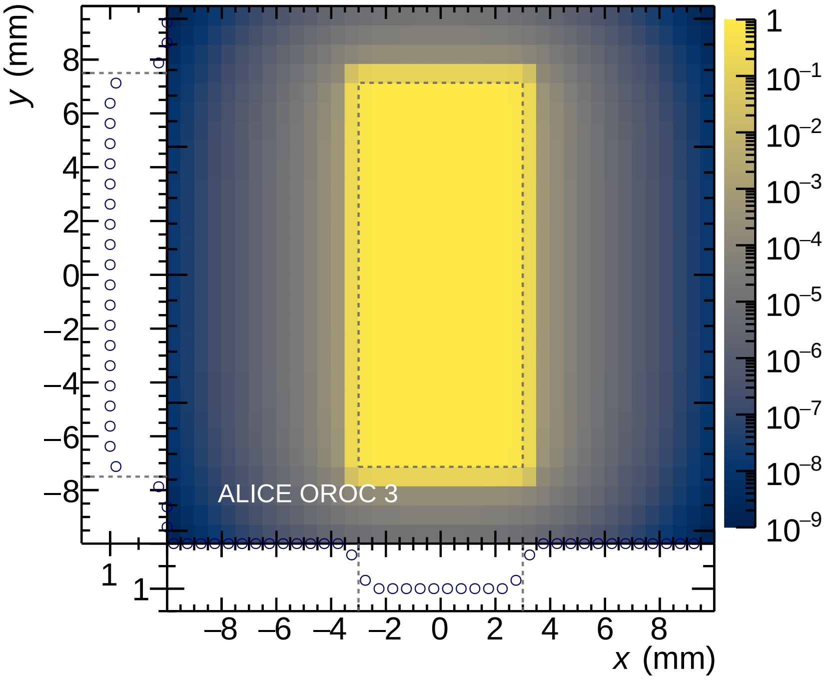

Figure 5.11: Pad response function of the ALICE OROC 3. The bottom and left panels depict the projection in x and y at the center of the pad and the dashed lines depict the outer profile of the pad.

5.1.5 Common Mode Effect

Capacitive coupling of the amplification structure to the readout anode leads to another contribution to the signal, the so-called *Common Mode* effect. Since the bottom electrode of GEM 4 is unsegmented, capacitive coupling occurs within a full ROC. Hence, the coupling causes a signal of opposite polarity on all pads of the same ROC for a given signal induced by a charge avalanche. The common mode signal resulting from a given current $I(t)$ induced on an individual readout pad can be computed as

$$I_{\text{common mode}}(t) = -I(t) \cdot \frac{C_{\text{pad}}}{C_{\text{total}}}, \tag{5.7}$$

where $C_{\text{pad}} = 0.1\,\text{pF}$ is the capacitance between an individual readout pad and the GEM 4 bottom electrode. The total capacitance $C_{\text{total}} = N_{\text{pads}} \cdot C_{\text{pad}} + C_{\text{external}}$ considers the number of pads per ROC and possible external capacitors in the system, that would be used to reduce the effect of the common mode. Since the introduction of external capacitors in the powering scheme of GEMs is known to significantly decrease the stability with respect to secondary discharges [280], no such elements are employed. Therefore, the computation of the common mode signal simplifies to

$$I_{\text{common mode}}(t) = -\frac{I(t)}{N_{\text{pads}}}. \tag{5.8}$$

Accordingly, the common mode effect amounts to about 10^{-4} of all induced charges in a given ROC. Recent measurements indicate that realistic values amount to about 40% of that for the ALICE TPC due to external parasitic capacitances in the HV system and charge dynamics in the induction gap [281]. This can be accounted for by introducing an additional scaling parameter

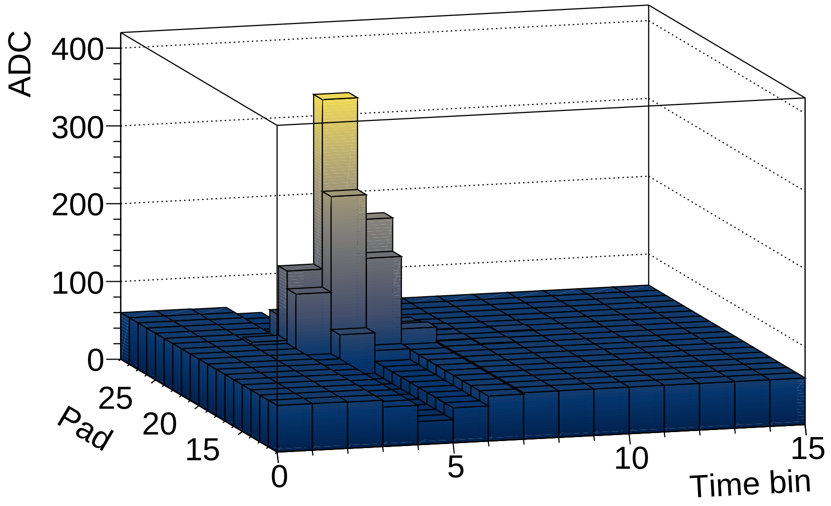

Figure 5.12: Exemplary signal of 1000 electrons after 2.5 m drift, with the corresponding common mode signal induced on all pads within the same ROC and time bin. A constant pedestal value of 60 is assumed for better visibility. For the same reason, the common mode values are scaled up by a factor of 100.

once the effect is fully understood. Figure 5.12 depicts an exemplary charge signal and the effect of the resulting common mode on all other pads within that time bin. For isolated charge depositions, as depicted in Fig. 5.12, the common mode signal is rather small and for this reason scaled up for better visibility. In the expected high-multiplicity Pb–Pb collisions, however, the common mode can lead to a temporary effective reduction of the baseline and therefore to an additional noise contribution causing a deterioration of the $\mathrm{d}E/\mathrm{d}x$ resolution.

During the data taking, the common mode values are computed and corrected for in the CRU, i.e. only for a subset of a ROC. The resulting precision of the common mode correction, however, is found to be sufficient [285]. For the sake of simplicity and in order to reduce the overhead, the common mode values are stored only for a given ROC and time bin in the simulation.

5.1.6 Signal Processing in the SAMPA

The induced charge signal of the avalanche Q is shaped in the analogue part of the SAMPA with a so-called *Gamma4* function,

$$S(t) = \mathcal{N} \cdot Q \cdot e^{-4 \cdot \frac{t-t_0}{t_{\mathrm{peak}}}} \cdot \left(\frac{t - t_0}{t_{\mathrm{peak}}} \right)^4 , \tag{5.9}$$

where t_0 corresponds to the arrival time of the electrons and $t_{\mathrm{peak}} = 170\,\mathrm{ns}$ to the peaking time of the shaper. The normalization constant $\mathcal{N}$ is equal to 55 and assures that the peak value of the signal corresponds to the input charge.

Output signals of the analogue part of the SAMPA are generated upon injection of a voltage step into a capacitor connected in series with the input [282, 283, 311]. Figure 5.13 depicts an

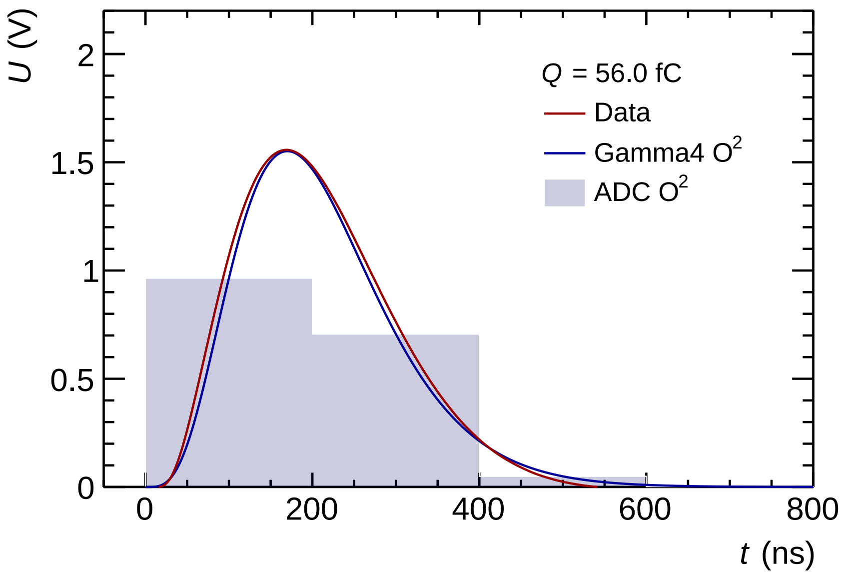

Figure 5.13: Exemplary charge signal processed with the analogue part of the SAMPA with a conversion gain of 30 mV/fC. The data are obtained by injecting a delta input charge of $Q = 56\,\mathrm{fC}$ to the chip [311]. The comparison with the implementation of O^2 yields good agreement. The filled area schematically depicts the result of the ADC sampling with 5 MHz.

exemplary result of these tests with an input charge of $Q = 56\,\mathrm{fC}$. The implementation of the response of the shaper according to Eq. 5.9 is in good agreement with the data. In order to improve the performance of the simulation SIMD[1] vectorization with Vc [312] is employed.

The resulting signal is then sampled with 5 MHz, as schematically depicted in Fig. 5.13, and converted to a 10-bit digital signal in the ADC. The voltage information of the shaper stage is transformed according to the dynamic range (2.2 V) and the conversion gain of $20(30)\,\mathrm{mV/fC}$, as outlined in Table 5.1.

Analyses of the system performance during a test beam campaign demonstrated that the noise performance of the readout system is fully within the requirements. The overall noise figure is about 1 ADC channel, with an average pedestal value of about 72 ADC counts [313]. This is accordingly incorporated in the simulation where the noise (pedestal) values are sampled on a pad-by-pad basis from a Gaussian distribution with a mean of 1 (72.5) and a width of 0.05 (9) ADC counts.

Cross-talk among neighboring channels occurs mainly in the flexible Kapton cable connecting the pad plane with the FECs. It is typically below 0.1% and therefore for performance reasons not included in the O^2 simulations.

The final ADC values of the digits are then stored alongside with the spatial information of the digit for further processing. Since only signal digits are written to disk, empty voxels are filled on-the-fly during the cluster finding procedure with noise, pedestal, and common mode values. In order to facilitate the procedure, the pedestal, noise and common mode values are subtracted from the signal after considering saturation effects. However, also the full digitized values can be passed further in the processing chain.

---

[1] Single Instruction Multiple Data

5.1.7 Validation

The results obtained from the test beam campaigns with 4-GEM Inner ReadOut Chambers in 2014 and 2017, described in Sec. 4.2.5, can be employed to validate and fine-tune the TPC digitization. These data are a good benchmark of the full simulation and digitization procedure, because details of the implementation of the signal formation, such as diffusion, gain variations, and the pad response, have been demonstrated to significantly influence the particle identification performance [314, 315]. Details of the analysis procedure of the test beam data can be found in Refs. [213, 291, 292].

The simulation is adopted so that the main characteristics of the experimental data are well reproduced. This concerns in particular the track geometry of the test beam data with a short drift length of 2 cm to 7 cm. In the following, the performance of the full digitization is benchmarked against the test beam data of 2017, where a pre-series of the SAMPA-based FECs were employed. The measured and simulated data are processed employing the reconstruction algorithms of O^2 [219]. Adjacent digits in time and space are combined to clusters. The total charge contained in the cluster is denoted by Q_{tot}, while the maximal signal contributing to the cluster by Q_{max}. The track finding procedure is then applied to the clusters [286]. At the employed sampling frequency of 5 MHz, the short drift length is known to significantly alter the particle identification capabilities [292]. Therefore, the performance is additionally compared to the results from the 2014 test beam with different FECs and 20 MHz sampling frequency at the end of this Section.

The simulated data are compared to an exemplary run of the 2017 test beam at an electron and pion beam momentum of 2 GeV/c, obtained from Ref. [292]. The applied HV configuration yields an $IB = 0.9\%$ and an energy resolution $\sigma(^{55}\mathrm{Fe}) = 12.0\%$ [281]. In the following, results for pions are shown. While the agreement of all relevant observables for electrons is similarly good, the required gain to describe the measured electron spectra is about 2% lower than the one employed for pions. This indicates that the parameters for the Bethe-Bloch equation as in Eq. 2.4 need further fine-tuning. This task, however, cannot be conducted with the test beam data at hand, but instead needs to be done with identified V^0 child tracks from the full TPC once installed.

First of all, the straggling functions obtained with Q_{max} and Q_{tot} for 2 GeV/c pions are compared in the left and right panel of Fig. 5.14. The full TPC simulation chain yields a good description of the measured spectra. In order to obtain a better description of the $Q_{\mathrm{max}}/Q_{\mathrm{tot}}$ ratio, the peaking

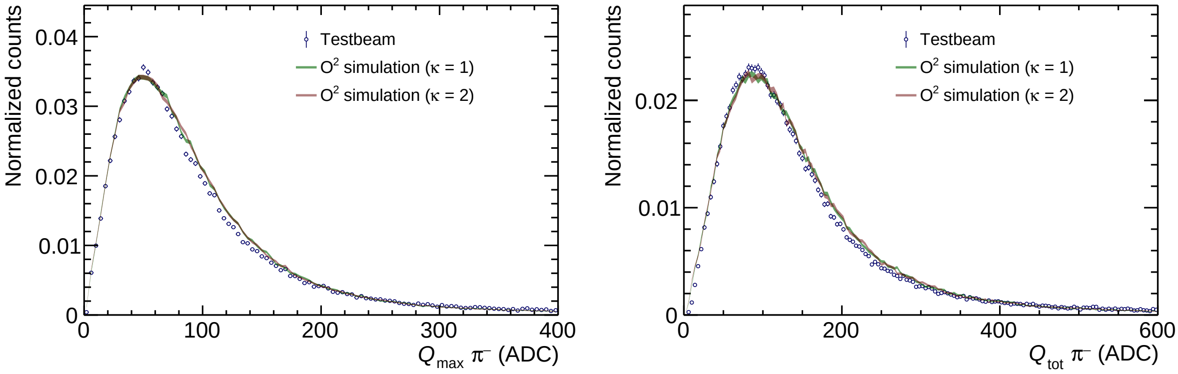

Figure 5.14: Straggling functions of pions at 2 GeV/c for the maximal cluster charge Q_{max} (*left*) and the total cluster charge Q_{tot} (*right*) for two extreme values of $\kappa_{\mathrm{eff}} = 1,\ 2$.

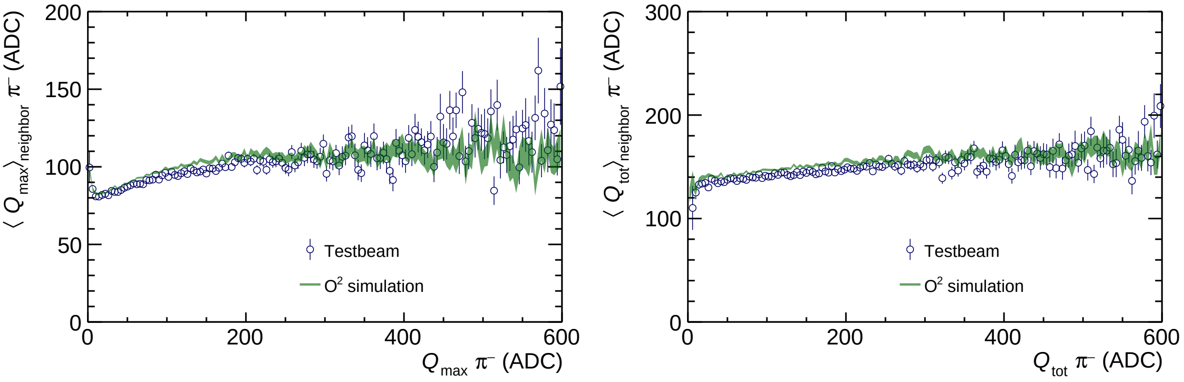

Figure 5.15: Correlations of the maximal Q_{max} (*left*) and the total cluster charge Q_{tot} (*right*) among neighboring clusters measured with pions at 2 GeV/c.

time of the employed FECs has been adjusted in the simulation. The effective model for the GEM amplification is employed in order to retain the flexibility to compare different HV configurations and to study the dependence on the κ_{eff} parameter. The effective electron detection efficiency ε_{eff} is tuned to always reproduce the local energy resolution $\sigma(^{55}\text{Fe}) = 12\%$ of the employed HV configuration. The simulation is conducted for two extreme values of $\kappa_{\text{eff}} = 1,\ 2$. The resulting cluster charge distributions for Q_{tot} and Q_{max} are insensitive to the value of κ_{eff} and the same holds for all observables. This is not surprising since the cluster incorporates many single-electron avalanches. Correspondingly, the actual shape of the single-electron response is no longer relevant because of the central limit theorem. For the sake of simplicity, a value of $\kappa = 1$ corresponding to the purely exponential case is chosen in the following.

Correlations among clusters in neighboring rows can arise from charge leakage due to diffusion and the pad response. The occurrence of such correlations can be measured by monitoring the average charge of the neighboring clusters as a function of the charge in a given pad row. In case of no correlations, the resulting distribution is flat. The left and right panel of Fig. 5.15 depict the measured and simulated distribution of Q_{max} and Q_{tot} for 2 GeV/c pions, respectively. The average values of Q_{max} and Q_{tot} recorded on the neighboring rows clearly exhibit a decrease for low cluster charges, demonstrating the influence of the pad response and diffusion. The simulation yields a good description of the experimental distributions, indicating that the diffusion and the pad response are properly described in the digitization.

This conclusion is underlined when conducting the simulation with a purely projective pad response instead of the PRF computed in Sec. 5.1.4. Figure 5.16 compares the measured straggling function of Q_{tot} and the corresponding row couplings to the full TPC digitization and to a purely projective pad response. As expected, the full treatment of the pad response leads to a significant improvement of the description of both observables. The row couplings are especially sensitive to the pad response and demonstrate that a purely projective pad response function is an oversimplification and incompatible with the experimental data.

The figure of merit of the TPC is the particle identification performance, determined by the resolution of the measurement of the specific ionization energy loss. The cluster charge distributions of Q_{max} and Q_{tot} reflect the distribution underlying the energy loss of charged particles, with a tail towards high energy deposits. Accordingly, the mean value is biased towards larger values and therefore not a good estimator of the specific ionization energy loss. For this reason, the dE/dx

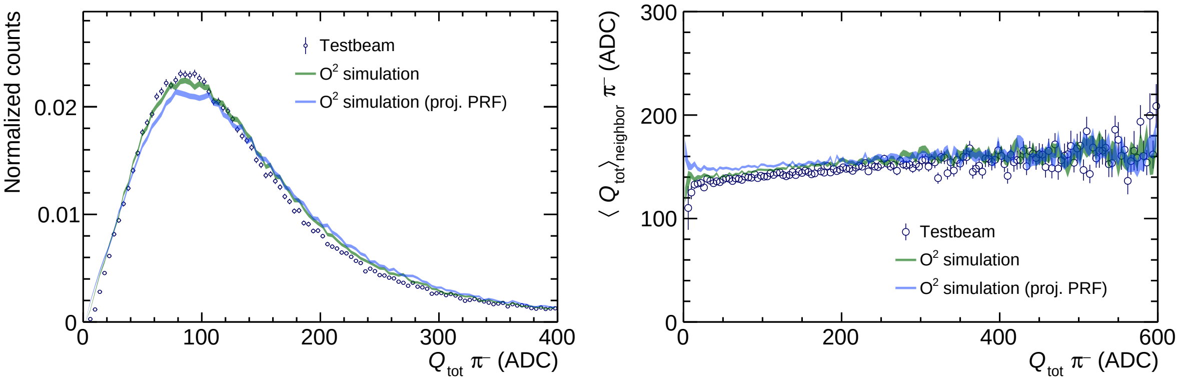

Figure 5.16: Comparison between the full simulation including the PRF computed in Sec. 5.1.4 (*green*) and a purely projective PRF (*light blue*) for the straggling function of Q_{tot} (*left*) and the corresponding row couplings (*right*) of pions at 2 GeV/c.

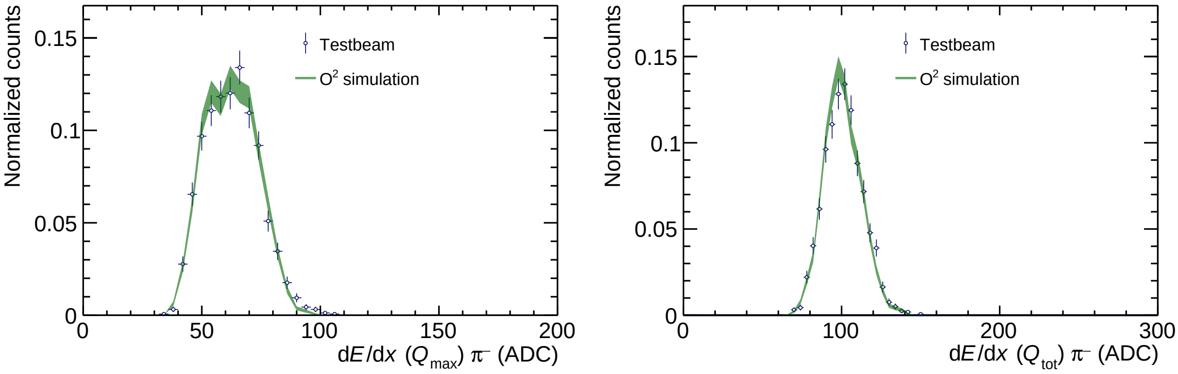

Figure 5.17: dE/dx distribution for Q_{max} (*left*) and Q_{tot} (*right*) of pions at 2 GeV/c.

distribution of the tracks is extracted as the truncated mean by discarding the largest 30% of the cluster charges per track. The resulting dE/dx distributions for Q_{max} and Q_{tot} are shown in the left and right panel of Fig. 5.17. The dE/dx distribution computed with the maximum charge contained within a cluster Q_{max} exhibits a broad structure. This is an artifact caused by the short drift length in conjunction with the sampling frequency and has been investigated in detail in Ref. [292]. The O^2 simulation reproduces both the Q_{max} dE/dx and the Q_{tot} dE/dx rather well. The corresponding dE/dx resolution is computed as σ/μ, where μ and σ correspond to the mean value and the width of a Gaussian fitted to the dE/dx distributions. The dE/dx resolution in the simulation is slightly better than the one extracted from the test beam data. It should be noted, however, that due to the short drift length and the sampling frequency of 5 MHz the detector response is mainly driven by details of the signal treatment in the FECs. For the test beam campaign in 2017 only a pre-series of the FECs were available, which could not be fully characterized. Therefore, details of the FEC response may not be properly handled in the simulation resulting in the observed difference. Nevertheless, the comparison with the test beam data of 2017 indicates a good description of all relevant physics processes for the signal formation. The final validation of the digitization can only be conducted with the full TPC installed within the ALICE detector and cosmic or collision data, which at this point are not available.

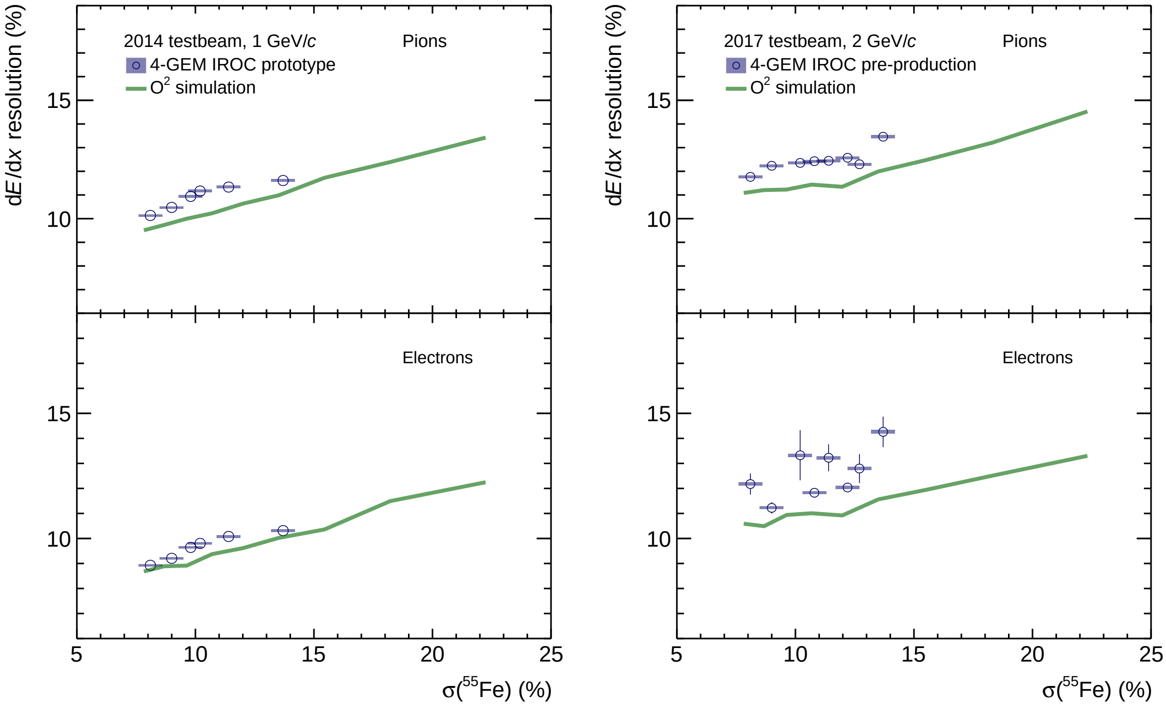

Figure 5.18: dE/dx resolution measured for different HV configurations with pions (*top*) and electrons (*bottom*) during the 2014 (*left*) and 2017 (*right*) test beam. The data points of the 2014 test beam are from Refs. [213, 291] and the ones from 2017 from Ref. [292]. Statistical uncertainties are represented by lines, while systematical uncertainties are represented by boxes. The uncertainties of the O^2 simulation are smaller than the line width.

Several HV configurations were tested during the test beam campaigns of 2014 and 2017 in order to assess the impact of the local energy resolution $\sigma(^{55}\text{Fe})$ on the particle identification performance and to identify possible limits of the system. The employed HV configurations are summarized in Table 4.6 for the 2014 and in Table 4.7 for the 2017 test beam. The resulting dE/dx resolutions are shown in Fig. 5.18 for electrons and pions. In all cases, the degradation of the dE/dx resolution with the local energy resolution is rather shallow.

A direct comparison of the experimental results of the two test beams, however, is for several reasons not possible. In contrast to the test beam in 2017, where the relevant measurements were conducted at a beam momentum of 2 GeV/c, in 2014 a beam momentum of 1 GeV/c was chosen. Due to a faulty GEM segment in 2014, the resolution is obtained with on average 46 space points, while in 2017 on average 55 clusters per track were available. Additionally, in 2014 the SAMPA-based FECs were not available yet. For this reason, the readout of the test beam in 2014 was based on EUDET FECs [293] with a sampling frequency of 20 MHz and a shaping time of 120 ns. Due to the short drift length, the significantly enhanced sampling frequency with respect to the nominal SAMPA-based FECs has a driving impact on the particle identification performance. Therefore, it is not surprising that the 2014 data demonstrate a significantly better dE/dx resolution.

The corresponding FEC parameters can be adjusted in the O^2 simulation to additionally use the 2014 data to validate the performance of the digitization. As demonstrated in Fig. 5.18, the overall agreement of the combined test beam data with the simulation is reasonable. In general, the dE/dx resolution obtained from the O^2 simulation slightly overpredicts the experimental performance. The discrepancy is larger for the 2017 data, where the pre-series SAMPA-based FECs were not fully characterized. As mentioned above, it may well be that details of the FEC response are not properly handled in the simulation. Furthermore, it should be noted that the employed detectors were produced during the prototyping and pre-commissioning phase of the project and therefore not subject to the final QA and production procedures. For this reason, the observed discrepancies should not be overestimated.

The corresponding separation power $S_{\pi-\mathrm{e}}$ of pions and electrons, defined in Eq. 4.3, is shown in Fig. 5.19. As for the dE/dx resolutions, in all cases a shallow deterioration of the separation power with the local energy resolution is observed. The O^2 simulation yields a consistent description of the behavior, albeit slightly overpredicting the performance of the 2017 test beam. As mentioned above, however, the observed mild discrepancies should not be overestimated.

Therefore, it can be concluded that the implementation of the TPC digitization in the O^2 framework yields a consistent description of the performance of large-size detector prototypes. A final validation will be conducted employing data measured with the full TPC and tracks from cosmic particle or collision data once fully installed within the ALICE detector.

5.1.8 Performance

The validated simulation in O^2 can be employed to obtain projections of the performance of the ALICE GEM TPC in Run 3 and beyond. Figure 5.20 depicts the simulated dE/dx spectrum in the TPC with particles generated by the heavy-ion version of the Pythia 8 event generator [201] at $\sqrt{s_{\mathrm{NN}}} = 5.02$ TeV. Albeit not a quantitative measurement, it demonstrates the particle identification performance of the system over a wide kinematic range.

A more quantitative estimate can be obtained by simulating electrons and pions at 2 GeV/c emitted in parallel to the pad plane close to the nominal interaction vertex in the center of the

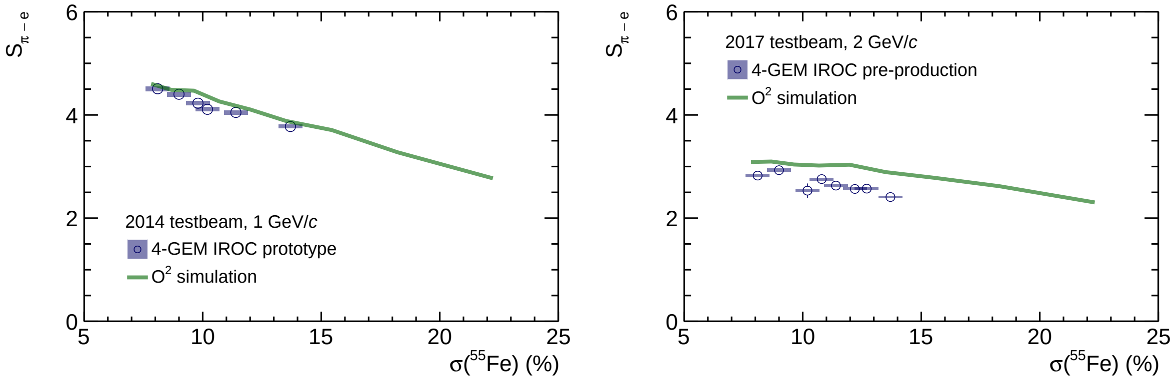

Figure 5.19: Separation power $S_{\pi-\mathrm{e}}$ of pions and electrons measured for different HV configurations during the 2014 (*left*) and 2017 (*right*) test beam. The data points of the 2014 test beam are from Refs. [213, 291] and the ones from 2017 from Ref. [292]. Statistical uncertainties are represented by lines, while systematical uncertainties are represented by boxes. The uncertainties of the O^2 simulation are smaller than the line width.

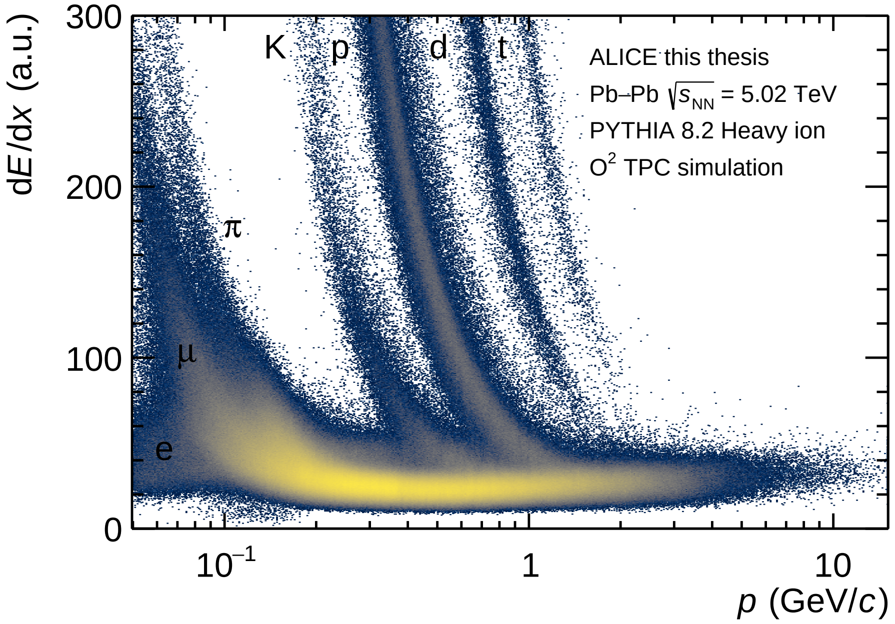

Figure 5.20: Specific energy loss dE/dx in the TPC as a function of the momentum of the incident particle in Pb–Pb collisions at $\sqrt{s_{\mathrm{NN}}} = 5.02$ TeV simulated with the PYTHIA event generator [201].

TPC. In contrast to the test beam data, the ionization electrons are transported through the full 2.5 m drift field and the tracks extend over the full length of one TPC sector. The resulting separation power $S_{\pi-\mathrm{e}}$ as a function of the local energy resolution is shown in the left panel of Fig. 5.21. The truncated mean of the specific energy loss is obtained from about 146 space points. The separation power is significantly improved in comparison to the test beam results, owed to the longer drift and the larger number of clusters per track. This demonstrates that the excellent particle identification performance of the detector is retained after the upgrade. Similar conclusions hold for the dE/dx resolution of electrons, depicted in the right panel of Fig. 5.21.

The simulation can additionally be employed to obtain valuable information about the performance of the TPC with a different gas mixture. One particular concern about the stability of the

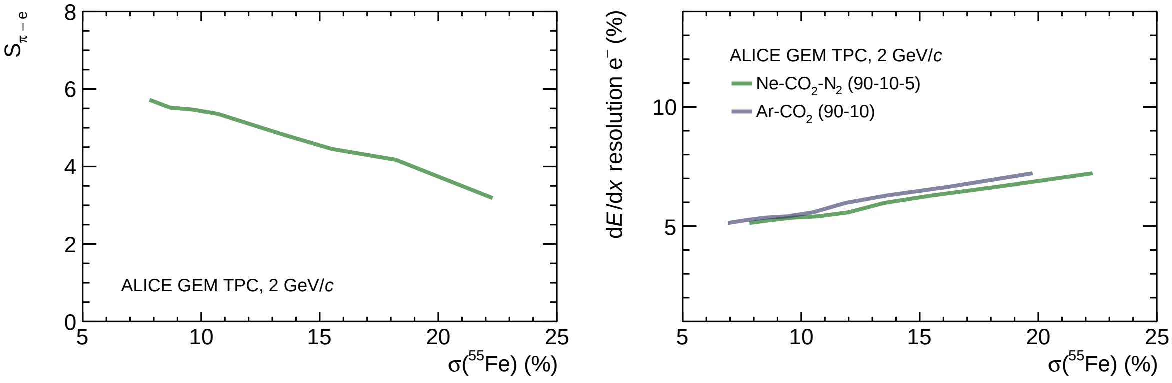

Figure 5.21: (*Left*) Separation power $S_{\pi-\mathrm{e}}$ of pions and electrons at a momentum of 2 GeV/c for a drift length of 2.5 m and on average 146 space points and (*right*) the dE/dx resolution for electrons in the full TPC with the nominal gas mixture and Ar-CO$_2$ (90-10).

GEM-based readout chambers with respect to secondary discharges are the rather large values for the transfer and induction fields of maximally 3.5 kV/cm [279], as discussed in Sec. 4.2.2. The onset for secondary discharges is at significantly higher fields in Argon-based gas mixtures than for Neon [279]. Therefore, the former are promising candidates in case the regular operation of the full TPC in the harsh LHC environment cannot be conducted in a stable manner with the baseline gas mixture Ne-CO_2-N_2 (90-10-5). In particular, Ar-CO_2 (90-10) might be a suitable choice. One downside of this mixture, however, is that the ion mobility is lower compared to Neon [316]. Accordingly, the field distortions caused by the ion leakage from the amplification stage are expected to be larger. In order to mitigate large field distortions, the applied HV configuration needs to be tuned to a lower *IB*, resulting in a better ion blocking. This, in turn, means operation at a deteriorated local energy resolution $\sigma(^{55}\mathrm{Fe})$. The gas properties of Ar-CO_2 (90-10) are significantly different with respect to Ne-CO_2-N_2 (90-10-5), with a lower effective ionization potential of 28.8 eV [214]. Accordingly, the amount of ionization electrons is enhanced by about 30%. Therefore, the correspondence between the local energy resolution $\sigma(^{55}\mathrm{Fe})$ and the particle identification performance might be different.

As shown in the right panel of Fig. 5.21, this is not the case. The $\mathrm{d}E/\mathrm{d}x$ resolution of electrons, measured within a full TPC sector, in Ar-CO_2 (90-10) is fully compatible with the performance of the nominal gas mixture. In particular, the deterioration with increasing $\sigma(^{55}\mathrm{Fe})$ is identical. Therefore, operating the TPC at a similar working point regarding the *IB* suppression in Ar-CO_2 (90-10) leads to a deterioration of the PID performance. Accordingly, a simple change of gas mixture is not sufficient as a back-up solution for the mitigation of secondary discharges.

5.2 Study of the Conditions for Discharge Formation

The prevention of the occurrence of electrical discharges is crucial to ensure stable long-term operation of GEM-based detectors, as discussed in Sec. 4.1. The energy released in a spark, initiated by the transition of an avalanche to a streamer, can lead to permanent damage of the detector ranging from enhanced leakage currents to irreversible short circuits that effectively render the detector blind. For this reason, the used HV configurations have been highly optimized, in particular for Ar-based tracking detectors employing 3-GEM stacks [256, 257, 269].

The overall discharge probability is significantly reduced when cascading several GEMs in a stack. In such a case, the total gain of the stack is shared among several elements with accordingly reduced gains of the individual elements and the charge density approaching each amplification stage becomes diluted due to diffusion. The importance of the latter point is underlined by measurements as a function of the inclination angle of the incident α particle, which indicate that charge deposition in the close vicinity of the GEM foil leads to significantly enhanced discharge rates [269]. This suggests that the overall discharge probability is driven by a convolution of the GEM gain and contained charge density. Nevertheless, when additionally optimizing the performance for other parameters, such as the *IB*, the overall detector stability may be significantly altered and become unpredictable. Indeed, as discussed in Sec. 4.2.2, for such cases significant R&D efforts are necessary and further measures need to be considered to assure safe operation.

In any case, the overall stability is always related to the breakdown limits of the individuals GEMs. Accordingly, systematic measurements of the single-GEM discharge probability could be employed to extrapolate to the stability of an arbitrary stack of GEMs under any HV configuration. By disentangling external influences such as the transfer fields and diffusion within the stack, the influence of the charge dynamics close to and inside the GEM hole on the discharge probability can be assessed. Dedicated studies of the discharge probabilities in single-GEM detector, however, have not been conducted prior to this work.

Comparing the discharge rates upon irradiation with x-rays to those caused by heavily ionizing particles [267, 269, 271] the maximal sustainable charge density seems to be consistent with the *Raether limit* [270] of about $10^7 - 10^8$ electron-ion pairs for parallel-plate detectors. Beyond such charge densities the space charge resulting from the amplification modifies the electric field and initiates a self-sustained charge avalanche. Due to diffusion phenomena and photon-feedback the streamer can then propagate through the full gas gap and lead to electrical breakdown. Qualitative simulations of the modification of the electric fields inside single GEM holes upon application of a large potential difference and implantation of charges point indeed towards a fast breakdown via a streamer [317, 318].

While the breakdown itself occurs on a time scale of a few ns [317, 318] it may take significantly longer to develop the conditions necessary for its formation. This is the idea underlying the herewith presented simulations, which investigate the conditions for discharge ignition in a more systematic way than previous studies conducted with MICROMEGAS [319] and GEMs [320].

The work presented in this Section was published in Ref. [321]. The simulations are accompanied by dedicated measurements of the discharge probability which constrain free parameters of the model. The measurement procedures themselves are not discussed in detail. Therefore, in the following the most important analysis steps of the simulation and the interpretation of the combined results is revised. An extension of this study for THGEMs has been conducted in Ref. [322].

5.2.1 Detector Simulation

The geometry of the detector is implemented to consistently describe the experimental setup [321], and shown in Fig. 5.22. The detector is irradiated with α particles from a coin-like mixed nuclide source containing ^{239}Pu, ^{241}Am and ^{244}Cm [278]. The associated energies and relative intensities are given in Table 5.3. The radioactive elements are deposited on an area with a diameter of 8 mm. This defines the energies and the geometric extension of the particle gun, which is mounted on top of the drift cathode, a 1.5 mm thick PCB with a copper coating on one side that allows the application of HV to define the 400 V/cm drift field. The distance between the drift cathode and the GEM stack is systematically varied from 1.3 cm to 7.1 cm in the course of the measurements. The detector gas and the GEM plane are irradiated with the α particles through a 7.8 mm diameter hole in the middle of the cathode plane. Relevant for this study is only the energy deposit in the detector gas, hence the material of the GEM plane and the anode is not simulated. Four different gas mixtures are employed and are accordingly considered in the simulation: Ar-CO_2 (70-30) as a reference to previous works [269], Ar-CO_2 (90-10), Ne-CO_2 (90-10), and the ALICE TPC mixture Ne-CO_2-N_2 (90-10-5). The properties of the respective gas mixture relevant for this study are summarized in Table 5.4. Notable are the low drift velocity and diffusion constants for Ar-CO_2 (70-30), and the significant difference in the effective ionization potential W_{ion} between Neon-based and Argon-based gas mixtures.

For the simulation of the energy deposit in the active detector medium, the latest version of GEANT4 [206] available at the time of conducting these studies was used (4.10.2). The description of the processes leading to the energy loss of the incident particle are summarized in the so-called physics list. For the case of this application, where low-energetic α particles are employed, the `G4EmLivermorePhysics` physics list was chosen as it extends the range of validity of the modeled particle interactions to lower energies [324]. The particle transport is then conducted step-wise, with the distance between the interactions being randomly sampled from the mean free path of the particle. In order to suppress too large distances between adjacent hits, the step length is fixed to 10 µm and the position of the hits smeared according to a flat distribution. In total 500×10^6 events have been simulated for each investigated gas mixture.

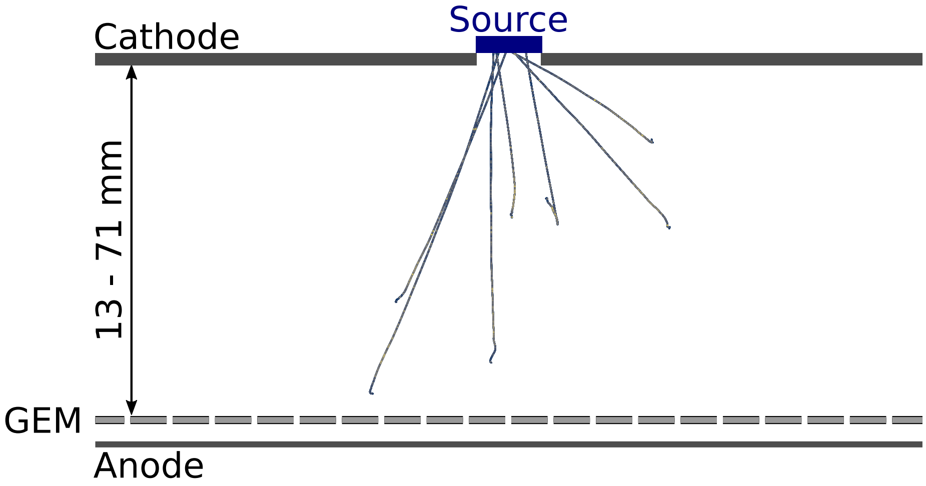

Figure 5.22: Schematic view of the detector setup implemented in the simulation with a few exemplary tracks of α particles traversing Ar-CO_2 (90-10). The color of the hits denotes the corresponding energy deposit.

Table 5.3: Energies and relative intensities of the α particles emitted from the mixed nuclide source [278].

Parent nucleus	Energy (MeV)	Relative intensity (%)
^{239}Pu	5.105	11.5
	5.143	15.1
	5.155	73.4
^{241}Am	5.388	1.4
	5.442	12.8
	5.486	85.2
^{244}Cm	5.763	23.3
	5.805	76.7

Table 5.4: Properties of the different gas mixtures employed in this study. The electron drift velocity, diffusion coefficients and the effective ionization potential are evaluated under Normal Temperature and Pressure conditions (20 °C, 1 atm) at the nominal drift field of 400 V/cm using the MAGBOLTZ software [263, 323]. The maximal range of α particles r_α from the mixed nuclide source is extracted using the GEANT simulations. Slight differences with respect to the values quoted in Table 5.1 are due to detailed settings of the used programs.

Gas		v_d (cm/µs)	D_L ($\sqrt{\mathrm{cm}}$)	D_T ($\sqrt{\mathrm{cm}}$)	W_i (eV)	r_α (cm)
Ar-CO_2	(70-30)	0.932	0.0138	0.0145	28.1	4.2
Ar-CO_2	(90-10)	3.26	0.0244	0.0268	28.8	4.8
Ne-CO_2	(90-10)	2.66	0.0223	0.0219	38.1	6.8
Ne-CO_2-N_2	(90-10-5)	2.52	0.0218	0.0224	37.3	6.9

The specific energy loss of the α-particles emitted from the mixed nuclide source is shown in Fig. 5.23. The contribution of the three different nuclides is clearly visible. As expected, the energy deposit varies with the penetration depth and reaches a distinctive maximum at the end of the trajectory of the α particle, the so-called *Bragg peak*. The curves reflect the expected Z dependence of the energy loss and accordingly the α particles looses more energy per path length in Argon-based mixtures and the penetration depth is shorter. At the same time, the effective ionization potential W_i in Argon is significantly lower compared to Neon resulting in an enhanced charge density along the particle's trajectory.

According to the working hypothesis, the number of accumulated charges inside single GEM holes is the driving factor for the formation of discharges. Since diffusion over a longer path length results in a dilution of the electron charge density arriving at the GEM plane, the figure of merit is the energy deposit of the incident particles in the closest vicinity of the GEM foil. The time scale of the formation of the conditions igniting the discharge is not yet known, while the actual development of the streamer and subsequent discharge takes place on $\mathcal{O}(\mathrm{ns})$ [317]. A quantitative result on the discharge formation time yields insights to the mechanisms underlying its creation, and might be able to differentiate among different scenarios, such as e.g. the accumulation of ionic space charge. Accordingly, the discharge formation time t_int is introduced as a parameter of the model.

The energy deposit of the hits is converted into number of electrons by employing the effective

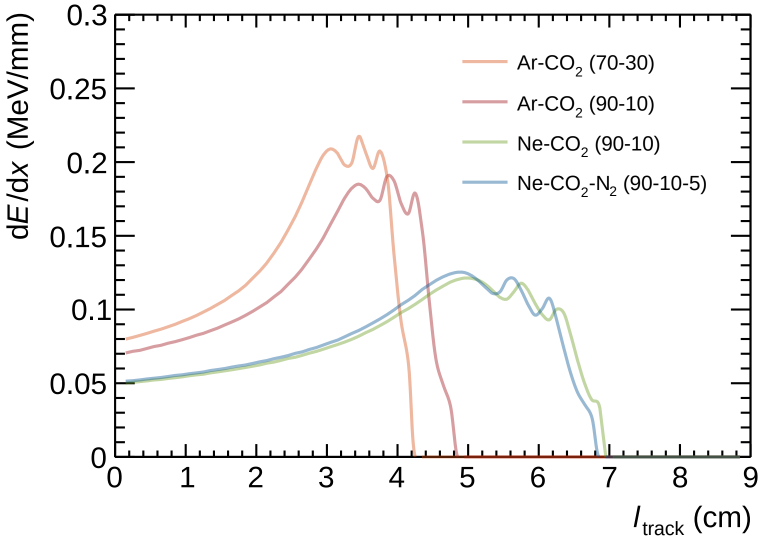

Figure 5.23: Bragg curves for the mixed nuclide source in the different gas mixtures obtained employing the GEANT simulations.

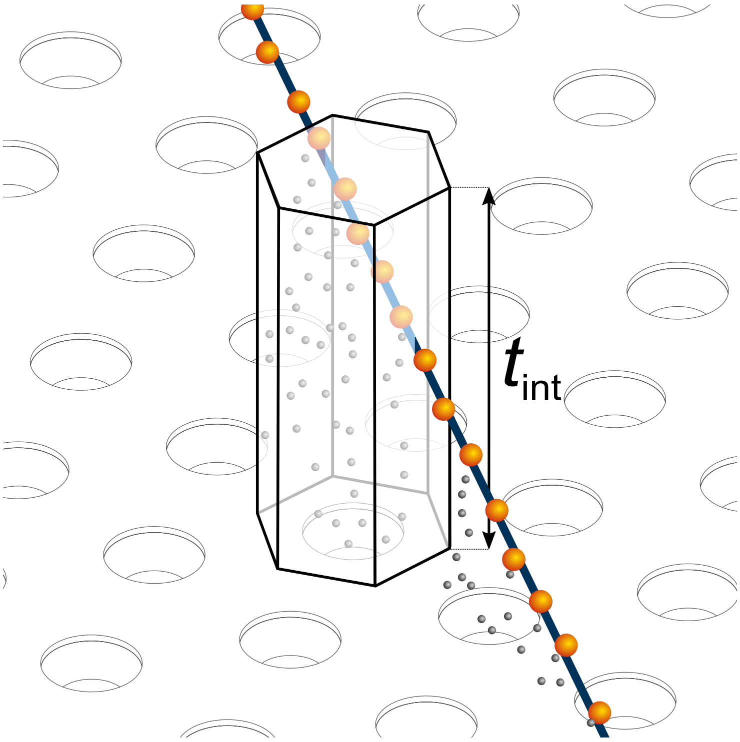

Figure 5.24: Schematic view of the honeycomb grid containing the volume of interest around a single GEM hole [321]. The trajectory of the incident alpha particle is shown as the blue line, and the corresponding GEANT hits are depicted by the yellow spheres. The resulting ionization electrons (gray spheres) are drifting towards the GEM-foil. The height of the volume defines the integration time t_{int} for ionization events considered for the formation of discharges in the corresponding GEM hole.

ionization potential W_{ion}, where only hits located $d_{\mathrm{int}} = t_{\mathrm{int}} \cdot v_{\mathrm{drift}}$ above the GEM plane are considered in the analysis. For this reason the formation time of the discharge t_{int} is also referred to as the integration time. The ionization electrons are then individually transported by the 400 V/cm drift field to the GEM plane. In order to consider the effect of longitudinal and transverse diffusion, the spatial coordinates of each electron are randomly sampled from a Gaussian distribution according to the corresponding gas parameters and the drift length as discussed in Sec. 5.1.2. On the GEM plane, the electrons are sorted in the honeycomb-like grid of the GEM holes assuming 100% collection efficiency, which is well justified for this choice of drift field and GEM potential [325]. The full process of the electron transport is sketched in Fig. 5.24. The typical resulting electron distribution inside individual GEM holes is shown in Fig. 5.25. In few cases a large amount of electrons created by a single α particle is accumulated inside single GEM holes.

In order to be able to compare to the results of the measurements, the resulting number of electrons accumulated inside the individual GEM holes is then multiplied by the absolute gain of the GEM. As discussed in the previous Section, fluctuations of the amplification process of single electrons can be described by a Polya distribution [300]. As shown in Fig. 5.25, however, the average number of electrons entering the GEM hole is much larger than just one. Therefore, following the central limit theorem, the fluctuations are expected to follow a Gaussian distribution. Since the latter is symmetric, the discharge probability remains on average unaffected. Therefore, fluctuations of the gain are neglected in the model.

Since the formation process of the discharge and its dependence on the charge density within the GEM hole is unknown, a fixed threshold of accumulated charges Q_{crit} is introduced. This rather crude assumption mimics a situation similar to the *Raether limit* [270] for parallel plate detectors. A discharge is then defined as an event in which this critical charge limit Q_{crit} is exceeded in one of the GEM holes. The final discharge probability is given by the number of events in which this threshold is exceeded, normalized only to the total number of simulated events. Since in the experimental setup a discharge leads to a rapid decrease of the potential across the GEM, the

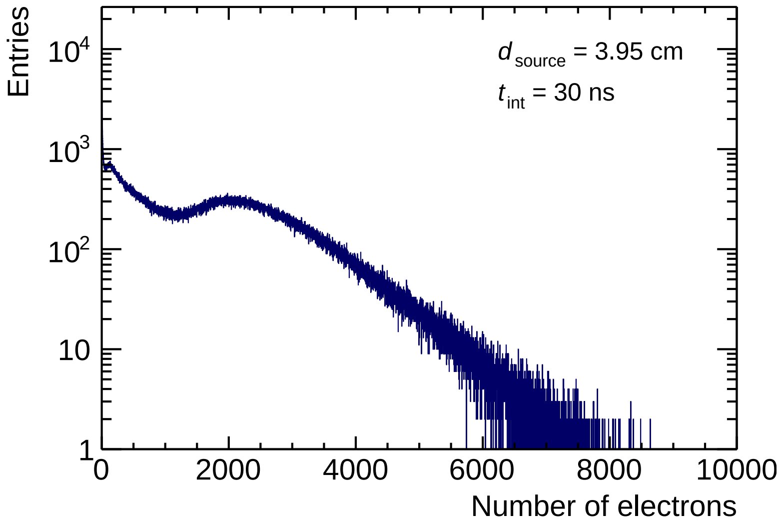

Figure 5.25: Distribution of the electrons accumulated in individual GEM holes in Ar-CO_2 (90-10) at $d_{\mathrm{source}} = 3.95\,\mathrm{cm}$ and a $t_{\mathrm{int}} = 30\,\mathrm{ns}$.

formation of more than one discharge per incident α particle is not possible. The same situation is adapted in the simulation.

The drift field in the experimental setup is only defined by the potentials applied to the cathode and the top side of the GEM foil. Due to the lack of field-defining elements in-between, the electric field within the active volume in the detector is distorted in particular for larger distances between the GEM and the source d_{source}. Distortions of the drift field are reflected in modifications of the drift velocity both with respect to magnitude and direction and would therefore demand for a more sophisticated treatment of the constant integration time t_{int}. The magnitude of the distortions has been studied using finite element calculations using the COMSOL® Multiphysics software [309]. For the integration times of interest in this study, the variations of the drift field are well below 1%, and can hence be neglected. Additional systematic effects might stem from the choice of the step length and the physics list. In particular for small integration times the step length might be larger than d_{int}, resulting in hits not being considered in the analysis. In order to assess the effect of the choice of the step size, the latter is systematically varied between 1 µm to 1000 µm. The results are only impacted by very large step lengths $\mathcal{O}(100\,\mu\text{m})$ and therefore the choice of 10 µm is sound. The choice of a different physics list suited for low-energy applications, `G4EmStandardPhysics_option4`, does not affect the results.

5.2.2 Comparison to Experimental Data

The experimental results for the discharge probability are displayed in Fig. 5.26 as a function of the absolute gain and in Fig. 5.27 as a function of the distance between the GEM and the source d_{source}. It is clearly visible that the measured values of the discharge probability cover several orders of magnitude. For discharge rates larger than about 1 Hz the dead-time of the readout system is becoming a limiting factor for the measurement and may lead to an underestimation

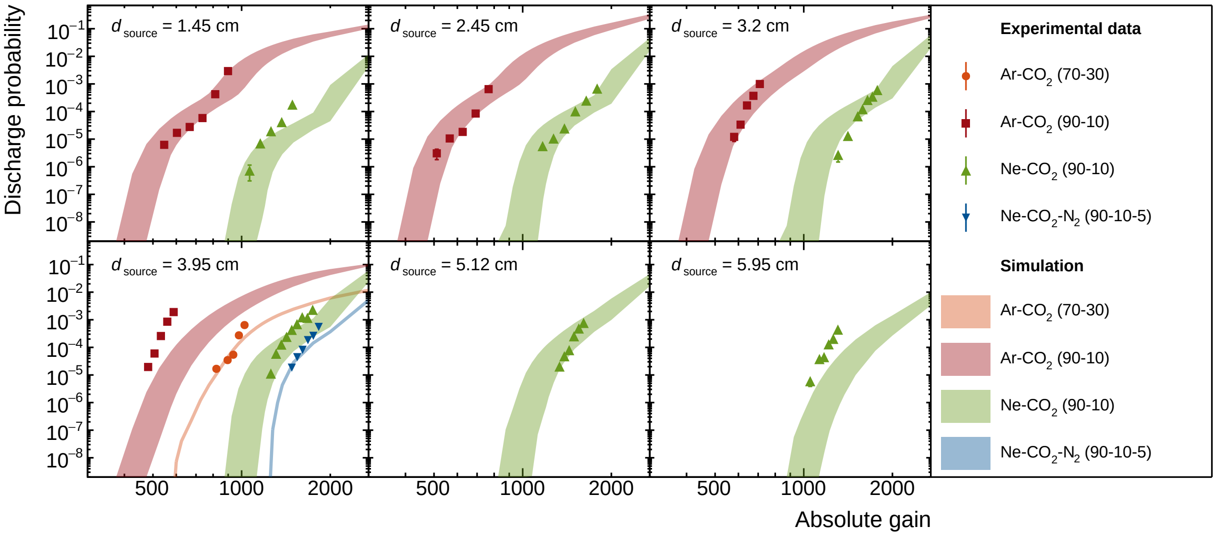

Figure 5.26: The discharge probability as a function of the absolute GEM gain for different gases and values of d_{source} [321]. The integration time in the simulation is 50 ns for Ne-CO_2 (90-10), 30 ns for Ar-CO_2 (90-10) and 40 ns for Ar-CO_2 (70-30) and Ne-CO_2-N_2 (90-10-5). The width of the corresponding bands is related to the uncertainty on Q_{crit}.

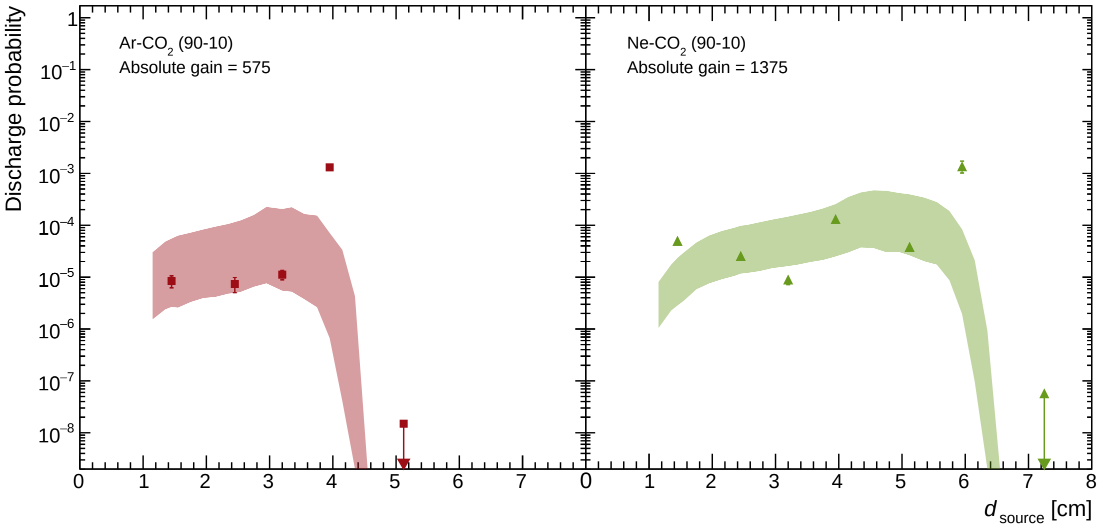

Figure 5.27: The discharge probability as a function of the distance between the source and the GEM d_{source} for two different gases [321].The integration time in the simulation is 50 ns for Ne-CO$_2$ (90-10) and 30 ns for Ar-CO$_2$ (90-10). The width of the corresponding bands is related to the uncertainty on Q_{crit}.

of the discharge probability. On the other hand, for significantly lower discharge probabilities the rate of the source of about 600 Hz implies long measurements during which variations of the gain due to changing atmospheric conditions may become relevant. These two factors define the boundaries of experimentally accessible discharge rates.

The influence of the gas mixture on the discharge probability becomes most obvious when comparing Ar-CO$_2$ (90-10) and Ne-CO$_2$ (90-10), for which the type and amount of quencher is the same. The measurements have been conducted for four different values of d_{source}. It is clearly visible that the discharge probability in Ar-CO$_2$ is enhanced by several orders of magnitude. The reason for this difference are basic properties of the noble gases. As shown in Fig. 5.23, the range of the α particles in the Argon-based mixture is reduced by about 40% compared to Neon, leading to larger energy deposits along the particle's trajectory. In addition to that, the effective ionization potential is smaller compared to Neon leading to an enhanced number of ionization electrons. As expected, these two effects lead to higher local charge densities that eventually cause the formation of a discharge a lower gains in Argon than in Neon.

For $d_{\text{source}} = 3.95$ cm the discharge probability was measured for all gas mixtures. As expected, the Argon-based mixtures have a significantly enhanced discharge probability compared to Neon-based ones. As shown in Table 5.4, the effective ionization potential and the range of the α particles and thus the local charge density, does not depend on the amount of quencher in the two Argon-based mixtures. The observed increase of the stability with the addition of quencher can therefore be assigned to the transport properties of the gas, which modify the charge density arriving at the GEM plane. Adding a small fraction of Nitrogen to Ne-CO$_2$ (90-10) does not alter the transport properties of the gas [326], while improving the overall stability.

The discharge probability as a function of d_{source} for Ar-CO$_2$ (90-10) and Ne-CO$_2$ (90-10) is shown in Fig. 5.27 for an absolute gain of 575 and 1375, respectively. The curves in Fig. 5.26 are extra-/interpolated using an exponential function in order to obtain the discharge probability at a fixed absolute gain. For both gas mixtures the discharge probability exhibits a monotonic increase with d_{source}. Beyond the approximate range of the α particles, however, the discharge probability drops significantly so no discharges can be measured within a reasonable amount of time with the given source rate and only upper limits could be measured. In this case, the ionization electrons can still reach the GEM foil due to the charge transport in the drift field, however the charge density is diluted by diffusion. Therefore, the discharge probability is significantly reduced. On the other hand, when the charge deposit of the incident α occurs in the closest vicinity of the GEM foil or inside the GEM hole itself, much larger local charge densities can be reached. Therefore, the discharge probability increases towards the end of the trajectory of the α particle.

In order to compare the results of the measurements to the discharge probability obtained from the simulation, the parameter phase space is scanned for values of d_{source} in steps of 2 mm and for values of the absolute gain of the GEM in steps of 50 for multiplication factors smaller than 1500 and in steps of 250 above that. Additionally, the two free parameters of the model t_{int} and Q_{crit}, are varied from 2 ns to 400 ns for t_{int} and between 1×10^5 and 1.25×10^7 electrons for Q_{crit}. The shape of the discharge probability as a function of the range of the particle demonstrates a significant sensitivity on variations of t_{int}, as shown in Fig. 5.28. Variations of Q_{crit} only lead to a shift of the absolute values of discharge probability, while not modifying the overall shape. Therefore, this observable can be used to constrain t_{int}.

For Ar-CO$_2$ (90-10) and Ne-CO$_2$ (90-10) the discharge probability is probed over the whole range of the α particles. The two parameters of the model t_{int} and Q_{crit} are varied, as mentioned above, for the two gases independently. Each combination yields a specific discharge curve, which is compared to the experimental data. The degree of consistency χ^2/NDF for a given combination of t_{int} and Q_{crit} is evaluated and the best values of both parameters are obtained using a χ^2 minimisation procedure. As shown in Fig. 5.29, the lowest values of χ^2 are achieved for integration times ranging from 20 ns to 90 ns for Ne-CO$_2$ (90-10) and 15 ns to 50 ns for Ar-CO$_2$ (90-10). The overall best description of the data is obtained with t_{int} of 50 ns for Ne-CO$_2$ (90-10) and 30 ns for Ar-CO$_2$ (90-10). The resulting critical charge limit Q_{crit} varies only by about 10% over the whole range of t_{int}.

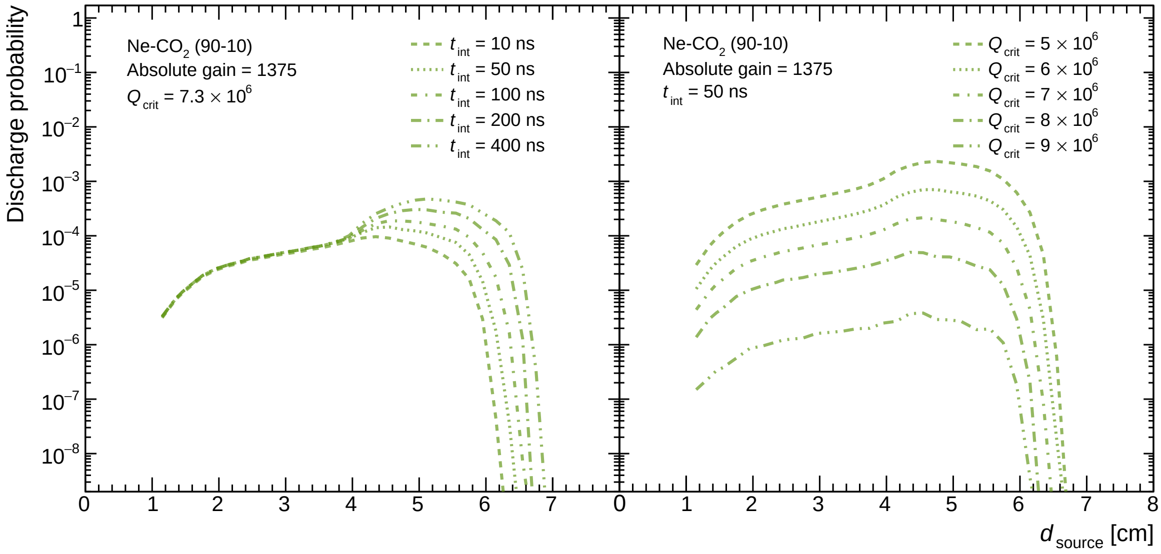

Figure 5.28: Dependence of the shape of the discharge probability on the integration time t_{int} (*left*) and the critical charge limit Q_{crit} (*right*).

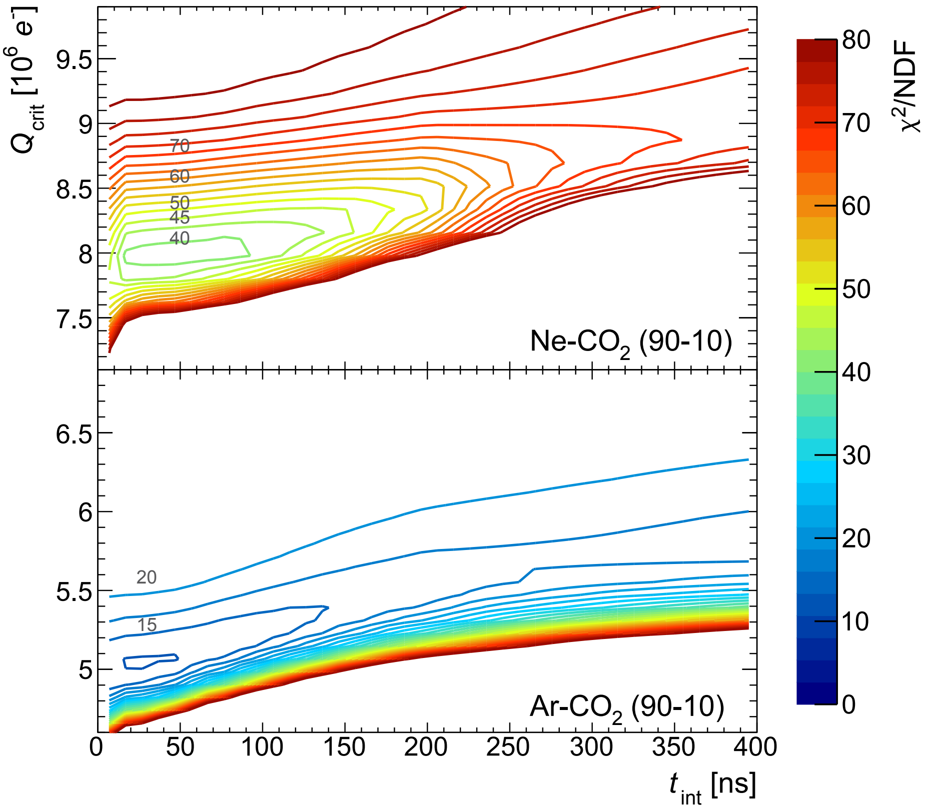

Figure 5.29: The contour lines of the degree of consistency (χ^2/NDF) of the experimental data with the simulated curves in the parameter space of the model [321].

An additional constraint can be obtained by including also the data of Fig. 5.26. In this case, the χ^2 minimization yields slightly different values of Q_{crit} for the different values of d_{source}. The resulting variations, however, are also around 10%. Hence, the uncertainty of the values for Q_{crit}, as quoted in Table 5.5, is given by the RMS. This is reflected by the bands shown in Fig. 5.26 and Fig. 5.27. In order to constrain Q_{crit} for the two gases where the measurements were conducted at only one d_{source}, Ar-CO$_2$ (70-30) and Ne-CO$_2$-N$_2$ (90-10-5), an integration time of 40 ns is chosen. This represents a good compromise between the values found above. It should also be noted that the critical charge limit Q_{crit} depends only mildly on t_{int}. Accordingly, the values obtained for Q_{crit} are 5×10^6 for Ar-CO$_2$ (70-30) and 9×10^6 for Ne-CO$_2$-N$_2$ (90-10-5), which agrees well with the results found for the other two gases shown in Table 5.5.

Table 5.5: Critical charge Q_{crit} for different gas mixtures and an integration time t_{int} of 50 ns for Ne-CO$_2$ (90-10) and 30 ns for Ar-CO$_2$ (90-10) [321].

Gas	Q_{crit}
Ar-CO$_2$ (90-10)	$(4.7 \pm 0.6) \times 10^6$
Ne-CO$_2$ (90-10)	$(7.3 \pm 0.9) \times 10^6$

5.2.3 Conclusions from the Model

The model yields a reasonable agreement of the experimental data. This demonstrates that basic gas properties modifying the ionization electrons from the incident particle and the rather basic assumption of a fixed threshold of charges contained inside a single GEM hole are sufficient to describe the discharge ignition in GEM-based detectors.

The obtained values for the critical charge limit Q_{crit} are in line with the Raether limit [270] and the values presented in Ref. [267]. It is not surprising that a modest dependence on the gas mixture is found. In general, Neon-based mixtures can withstand slightly larger charge densities than Argon-based ones and an increased amount of quencher seems to enhance Q_{crit} as well.

The values obtained for the integration time t_{int} permit to study how the charge accumulation inside the GEM holes leads to the ignition of the discharge. In the large electric fields inside the GEM holes, the transfer time of the electrons is $\mathcal{O}(\text{ns})$ [327]. Since the values found for t_{int} are much larger than that, a simple accumulation of electrons is not a satisfactory description for the discharge ignition process. The transfer time of the ions produced in the avalanche process in the GEM hole to the top GEM electrode is of the order of a few tens of ns [327]. Therefore, one possible explanation is that the accumulating ionic space charge modifies the amplification field inside the GEM hole, proceeding to the development of a streamer. This is in line with the findings of Ref. [317], where the electric field inside the GEM hole in the presence of charges is computed using finite element methods. In this study, the ion density inside the GEM hole was identified to lead to the streamer formation preceding the discharge.

Therefore, the herewith presented findings support the hypothesis of ions accumulating inside the GEM hole and subsequently leading to the ignition of the discharge. Additionally, the model can be employed to predict the stability of GEM-based detectors in a given radiation environment to ensure and optimize safe operation of the setup.

6 Summary

This work presents the first direct measurement of the p–Σ^0 interaction, studied via the femtoscopy method in high-multiplicity pp collisions at $\sqrt{s} = 13$ TeV measured by the ALICE detector at the LHC.

The excellent tracking and particle identification capabilities of the ALICE detector over the full momentum range down to low transverse momenta are essential for this measurement. The Σ^0 is reconstructed via the dominant electromagnetic decay to $\Lambda\gamma$. The short lifetime of the Σ^0 renders the decay products indistinguishable from primordial particles. The Λ is identified via the subsequent decay to $\mathrm{p}\pi^-$. The energy of the photon is driven by the mass difference of $77\,\mathrm{MeV}/c^2$ between the Σ^0 and the Λ and is therefore typically only a few hundred MeV. Accordingly, the photon reconstruction cannot be conducted with the calorimeters of the ALICE detector. For this reason, the identification relies on the detection of photon conversions to $\mathrm{e}^+\mathrm{e}^-$ pairs in the detector material. Owing to the low energy of the photons, however, the reconstruction efficiency for the Σ^0 is found to be on the sub percent level, which demonstrates the challenge of the measurement. In total, about 115×10^3 Σ^0 and 110×10^3 $\overline{\Sigma^0}$ candidates are found with a purity of 34.6%, which is due to the large number of uncorrelated primordial $\Lambda\gamma$ pairs.

A total number of 587 p–Σ^0 and 539 $\overline{\mathrm{p}}$–$\overline{\Sigma^0}$ pairs contribute to the correlation function in the low relative momentum regime relevant for studies of the final-state interaction. Because of the modest purity of the Σ^0 sample, the measured p–Σ^0 correlation function features a significant contribution from the p–$(\Lambda\gamma)$ baseline, where $(\Lambda\gamma)$ refers to combinations of uncorrelated Λ and γ particles. The resulting p–$(\Lambda\gamma)$ correlation function reflects the pattern of an attractive interaction, presumably due to residual p–Λ correlations smeared by the γ. The limited data sample, however, does not allow for a more detailed analysis. The shape of the p–$(\Lambda\gamma)$ correlation function defines the baseline of the measurement of the p–Σ^0 interaction and is therefore considered accordingly.
The p–Σ^0 correlation function is consistent with the p–$(\Lambda\gamma)$ baseline within $(0.2 - 0.8)\sigma$, indicating the presence of a shallow potential of the strong interaction in the p–Σ^0 channel. Accordingly, the data are found to be sensitive to the p–Σ^0 interaction. This demonstrates for the first time the feasibility of femtoscopic measurements in the N–Σ sector, where experimental constraints on the interaction are extremely scarce and typically exhibit large uncertainties.
The experimental correlation function is compared to state-of-the-art theoretical predictions for the interaction. The tested approaches include chiral effective field theory, two versions of the Nijmegen meson-exchange models, and a constituent quark model. The modeled correlation functions are defined by the interplay of the four involved spin and isospin channels and found to be sensitive to the strong interaction. Owing to the small mass difference and the same relevant quantum numbers, a strong effect of the coupled channel n–$\Sigma^+ \rightarrow$ p–Σ^0 is expected, while the influence of the coupling p–$\Lambda \rightarrow$ p–Σ^0 is less pronounced. The predictions for the p–Σ^0 correlation function differ significantly among the models. This indicates that this experimental technique has the potential to provide unprecedented constraints on the N–Σ interaction in vacuum. The precision of the experimental correlation function, however, does not yet allow a discrimination among different models. Nevertheless, it should be noted that the same holds for all presently available scattering, Σ atomic, and hypernuclear data.
This pioneering work proves the feasibility of femtoscopic measurements in the N–Σ sector. More detailed studies will be possible with the large data samples expected from future runs of

the LHC. Indeed, the p–Σ^0 correlation function can be studied in greater detail employing the anticipated data samples from the upcoming LHC Run 3 and Run 4.

The collection of these data samples can only be accomplished by increasing the interaction rates provided by the LHC and the rate capability of the ALICE detector. For this reason, significant upgrades of the main systems of ALICE are under way. In particular, the envisaged continuous operation does not conform with the readout system of the large TPC, which is the main detector for tracking and particle identification in the central barrel of ALICE. The previously used gated Multi-Wire Proportional Chambers imply an intrinsic rate limitation to about 3 kHz, which is significantly below the anticipated interaction rates of 50 kHz in Pb–Pb and 1 MHz in pp collisions. Therefore, the new readout chambers are equipped with a stack of four large-size Gas Electron Multiplier (GEM) foils as amplification stage. This arrangement, under a specific high-voltage configuration, has proven to fulfill the design specifications in terms of ion backflow and stable operation under LHC conditions, while retaining the excellent particle identification capabilities. This work contributes in manifold ways to the upgrade of the ALICE TPC. In the course of the service task for the ALICE Collaboration, the mechanical and electrical design of the large-size GEM foils has been finalized and supplied to the manufacturer.

The upgrade of the TPC and the requirements for continuous data taking require a re-design of the full simulation code of the ALICE TPC, which is incorporated in the new O^2 framework. In general, detector simulations are an essential ingredient to modern high-energy physics, since the output of event generators can only be compared to measured data when detector effects are properly accounted for. For the analyses of correlation functions, Monte Carlo simulations are an essential ingredient to assess single-particle purities and primary fractions, reconstruction efficiencies, and kinematic features of the correlation function. In order to enable such studies for future analyses, the simulation of the full chain of processes relevant for the signal formation in the ALICE GEM TPC, the so-called *digitization*, is implemented in the O^2 framework, with particular focus on computing performance.
Starting point are the localized energy deposits caused by the incident particles in the detector medium, which are provided by transport codes such as GEANT. The first step of the digitization is the transport of the resulting ionization electrons in the electric drift field to the readout chambers of the TPC, including the effect of diffusion and attachment to residual electronegative gases. In the readout chambers, the charges are subsequently amplified in the 4-GEM stack. Particularly relevant for the energy resolution of the detector and therefore the particle identification performance are statistical fluctuations of the amplification process. Two different versions of the amplification process are implemented – a full-scale simulation of all relevant processes occurring in the GEM stack and an effective model implemented for performance considerations. After the amplification stage, the electrons induce a signal on the segmented readout anode. The effect of the signal induction is computed with COMSOL® simulations and the resulting pad response function is necessary to obtain a consistent description of experimental observables. Finally, the induced signal is processed by the shaper stage of the SAMPA chip and converted to a digital signal for further processing. The full simulation chain is benchmarked against and validated with experimental data obtained with large-size prototypes equipped with a 4-GEM stack. The O^2 simulation yields good agreement with the performance of the prototypes. The digitization code will be used for all Monte Carlo simulation productions in ALICE for Run 3 and Run 4.

The collection of the envisaged large data samples is only possible when efficiently operating all sub-systems of ALICE. One particular aspect limiting the operational stability of gaseous detectors, such as the TPC, is the occurrence of electrical discharges. The mitigation of such events is crucial, however, requires a solid understanding of the underlying physical processes. Therefore, the conditions for discharge ignition in a single-GEM detector are studied with GEANT4-based simulations of the energy deposit of an α source in the detector gas and the subsequent charge collection and amplification. The working hypothesis is that a discharge ensues when the charge accumulated inside a single GEM hole exceeds a critical threshold Q_{crit} within the discharge formation time t_{int}. The two parameters of the model are constrained by comparison to experimental data. For two commonly used gas mixtures, Ar-CO_2 (90-10) and Ne-CO_2 (90-10), the values of the charge threshold Q_{crit} are $(4.7 \pm 0.6) \times 10^6$ and $(7.3 \pm 0.9) \times 10^6$ electrons per GEM hole. The slight difference among the two values indicates an additional influence of gas properties on the discharge ignition process. The time scale of the discharge formation is found to be within 15 ns to 90 ns. Two important conclusions can be drawn from these findings. First of all, the drift length corresponding to t_{int} is only a few mm. The diffusion over a longer drift length sufficiently dilutes the charge density and leads to a spread over copious GEM holes. This indicates that discharges occur mainly due to large energy deposits in the closest vicinity of GEM holes. Secondly, the time scale is significantly longer than the time it takes electrons to cross the GEM. This supports the hypothesis of ionic space charge accumulating inside the GEM hole and subsequently leading to the ignition of the discharge. The model can be employed to predict the stability of GEM-based detectors in a given radiation environment.

This work proves the feasibility of femtoscopic measurements in the N–Σ sector and contributes to the development of the required simulation tools for future analyses of the p–Σ^0 and other correlation functions. At the same time, an improved understanding of the occurrence of discharges ensures stable operation of the TPC and thus efficient data taking. The resulting data samples envisaged to be collected in pp collisions are expected to increase the number of pair candidates of the p–Σ^0 correlation function by about a factor of $40 - 50$. Accordingly, a decisive statement about the nature of the interaction in vacuum may be within reach.

A List of Relevant Publications

A.1 Relevant Publications

The author has contributed to the following publications, with the highlighted ones being subject of this work.

- **ALICE** Collaboration, S. Acharya *et al.*, "Investigation of the p–Σ^0 interaction via femtoscopy in pp collisions", *Phys. Lett.* **B805** (2020) 135419. *(Chair of the paper committee)*
- **ALICE TPC** Collaboration, M. M. Aggarwal *et al.*, "Particle identification studies with a full-size 4-GEM prototype for the ALICE TPC upgrade", *Nucl. Instrum. Meth.* **A903** (2018) 215. *(Chair of the paper committee and corresponding author)*
- P. Gasik, A. Mathis, L. Fabbietti, and J. Margutti, "Charge density as a driving factor of discharge formation in GEM-based detectors", *Nucl. Instrum. Meth.* **A870** (2017) 116. *(Co-author with P. Gasik and corresponding author)*
- **ALICE** Collaboration, S. Acharya *et al.*, "p–p, p–Λ and Λ–Λ correlations studied via femtoscopy in pp reactions at $\sqrt{s} = 7$ TeV ", *Phys. Rev.* **C99** (2019) 024001.
- **ALICE** Collaboration, S. Acharya *et al.*, "Study of the Λ–Λ interaction with femtoscopy correlations in pp and p–Pb collisions at the LHC", *Phys. Lett.* **B797** (2019) 134822.
- A. Deisting *et al.*, "Secondary discharge studies in single- and multi-GEM structures", *Nucl. Instrum. Meth.* **A937** (2019) 168.
- **ALICE** Collaboration, S. Acharya *et al.*, "Search for a common baryon source in high multiplicity pp collisions at the LHC", *submitted to Phys. Lett.* **B** (2020).
- **ALICE** Collaboration, S. Acharya *et al.*, "First observation of an attractive interaction between a proton and a multi-strange baryon", *Phys. Rev. Lett.* **123** (2019) 112002.

A.2 Additional Contributions

The following denote the most relevant side projects carried out during this work.

- Extraction of the experimental p–p, p–Λ, and Λ–Λ correlation functions from the pp collision data sample at $\sqrt{s} = 13$ TeV, collected with the minimum bias trigger.
- Mechanical and electrical design of the large-size GEM foils for the upgrade of the ALICE TPC (ALICE Service task *GEM foil design – from prototype to production*).
- Implementation and validation of the NanoAOD data format for femtoscopic analyses.
- Co-development and maintenance of the `FemtoDream` analysis and the `GentleFemto` post-processing framework.

A.3 Supervised Theses

The following theses were conducted under the supervision of the author.

- T. Klemenz, "$\mathrm{d}E/\mathrm{d}x$ Resolution Studies of a Pre-Production Read-Out Chamber with GEMs for the ALICE TPC", Master's thesis, Technische Universität München, 2019.
- E. Chizzali, "First Measurement of the ϕ-Proton Correlation Function with ALICE in pp Collisions at $\sqrt{s} = 13$ TeV, Bachelor's thesis, Technische Universität München, 2019.
- M. Korwieser, "Study of the photon identification in pp at $\sqrt{s} = 13$ TeV in ALICE for the Σ^0 reconstruction", Bachelor's thesis, Technische Universität München, 2018.
- F. Dufter, "Study of propagating discharges in GEM-based detectors", Bachelor's thesis, Technische Universität München, 2016.

B Appendix to the p–Σ^0 Analysis

This Section contains supplementary material for the reconstruction of the Σ^0 and the construction of the p–Σ^0 correlation function.

B.1 Σ^0 Reconstruction

The Σ^0 ($\overline{\Sigma^0}$) candidates are constructed by combining the Λ ($\overline{\Lambda}$) and γ candidates within the same event. In case a child track is employed to construct two γ, Λ, and $\overline{\Lambda}$ candidates, or a combination thereof, the one with the smaller CPA is removed from the sample. As depicted in Figs. B.1 and B.2 the rejection acts on the sub-percent level for all involved particle species.

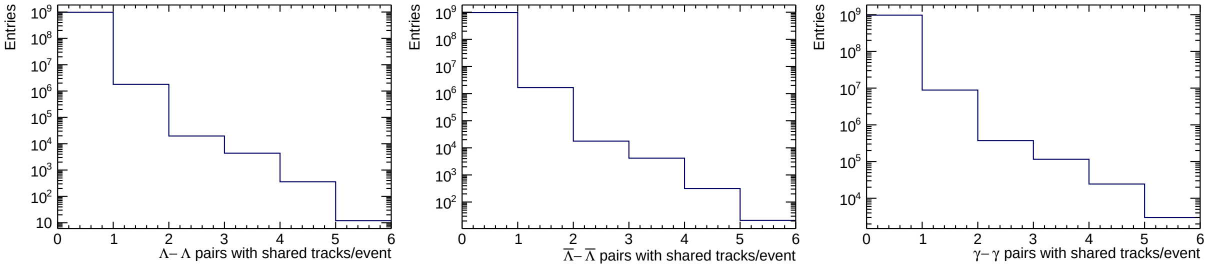

Figure B.1: Λ–Λ (*left*), $\overline{\Lambda}$–$\overline{\Lambda}$ (*middle*) and γ–γ (*right*) pairs that share a decay child per event.

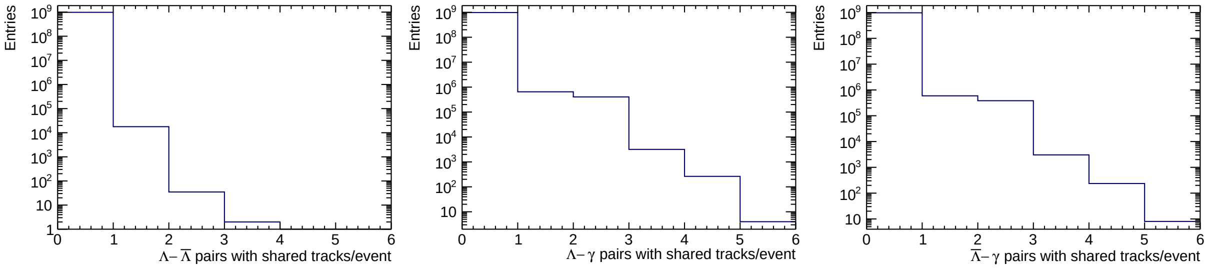

Figure B.2: Λ–$\overline{\Lambda}$ (*left*), Λ–γ (*middle*) and $\overline{\Lambda}$–γ (*right*) pairs that share a decay child per event.

B.2 p–Σ^0 Correlation Function

When the track of a primary proton is also employed as the child track of the γ or the Λ, the corresponding Σ^0 candidate is rejected. This is also the case for the construction of the $(\Lambda\gamma)$ candidates. As shown in Fig. B.3, B.4 and B.5 this happens in less than one per mille of the cases.

For the construction of the p–$(\Lambda\gamma)$ baseline correlation function the ratio of the baryon–baryon and antibaryon–antibaryon correlation function is consistent with unity. The same holds for the case of the correlation function up and down of the Σ^0 peak, as depicted in Fig. B.6.

The systematic uncertainties for the p–p and the p–$(\Lambda\gamma)$ correlation function are of the order of 2.5% in the respective first bin, and are shown in Figs. B.7 and B.8.

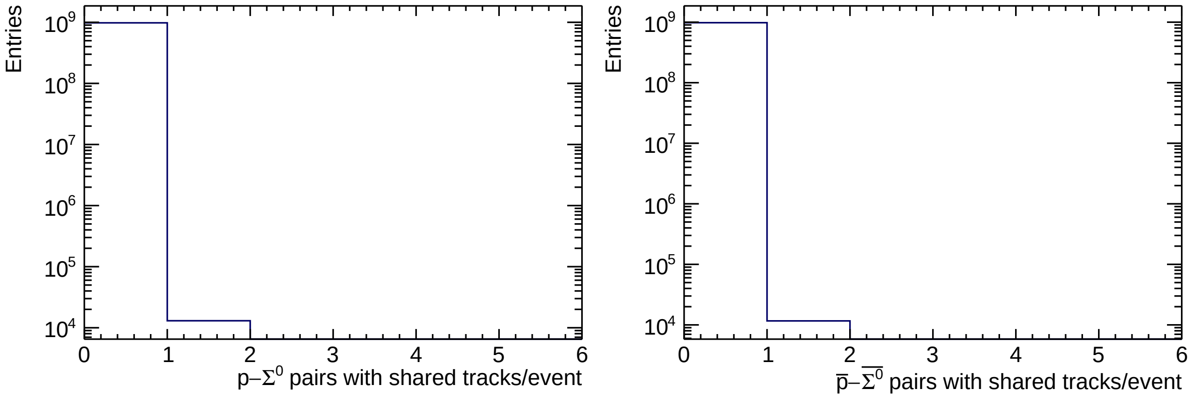

Figure B.3: p–Σ^0 (*left*) and $\overline{\text{p}}$–$\overline{\Sigma^0}$ (*right*) pairs that share a track per event.

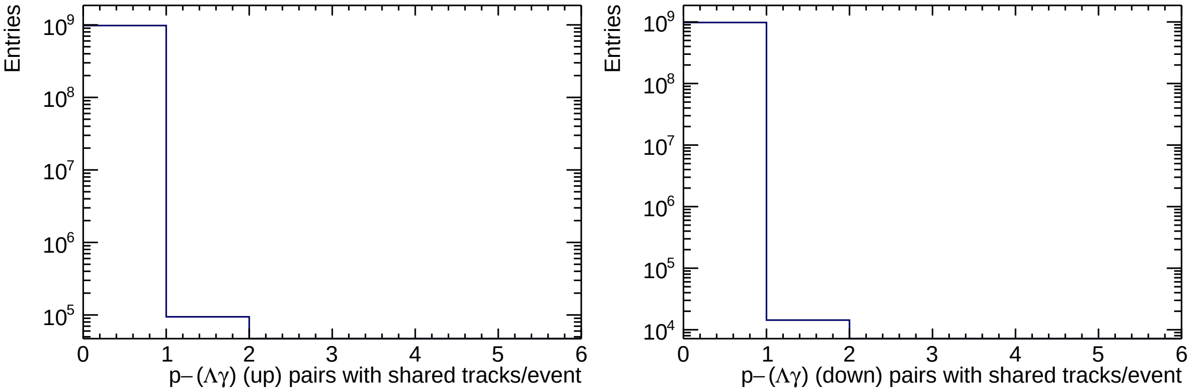

Figure B.4: p–$(\Lambda\gamma)$ pairs up (*left*) and down (*right*) of the Σ^0 peak that share a track per event

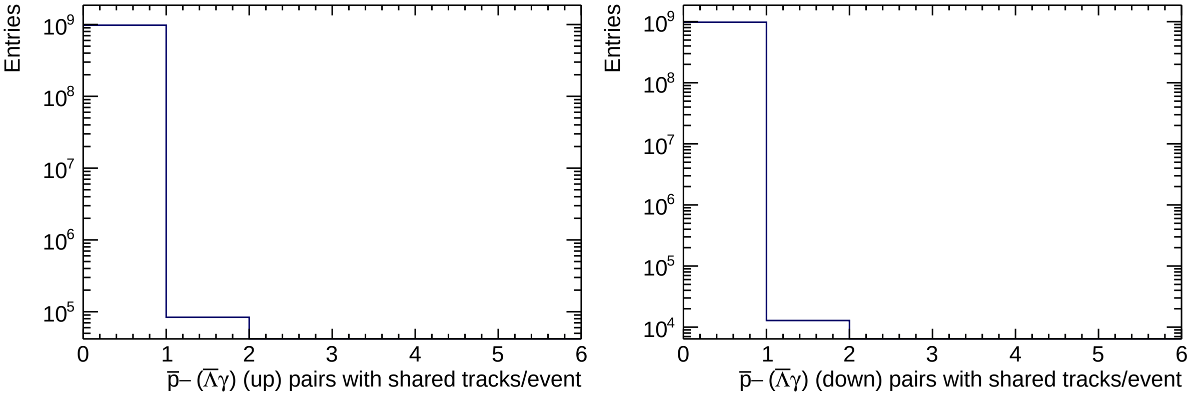

Figure B.5: $\overline{\text{p}}$–$(\overline{\Lambda}\gamma)$ pairs up (*left*) and down (*right*) of the $\overline{\Sigma^0}$ peak that share a track per event

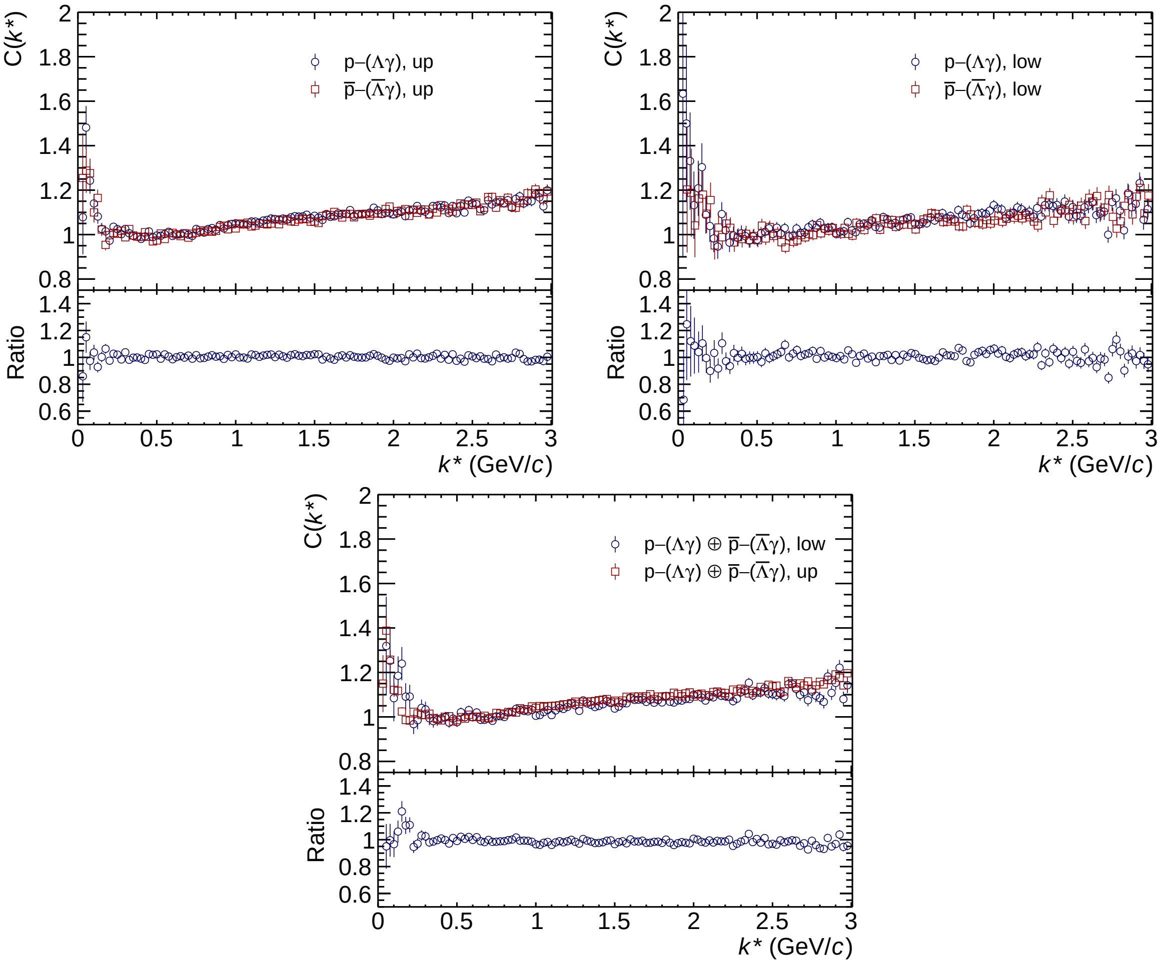

Figure B.6: The measured p–$(\Lambda\gamma)$ and $\overline{\mathrm{p}}$–$(\overline{\Lambda}\gamma)$ correlation functions with the corresponding ratio up (*top left*) and down (*top right*) of the Σ^0 peak. The bottom panel depicts the combination of the correlation functions up and down of the Σ^0 peak.

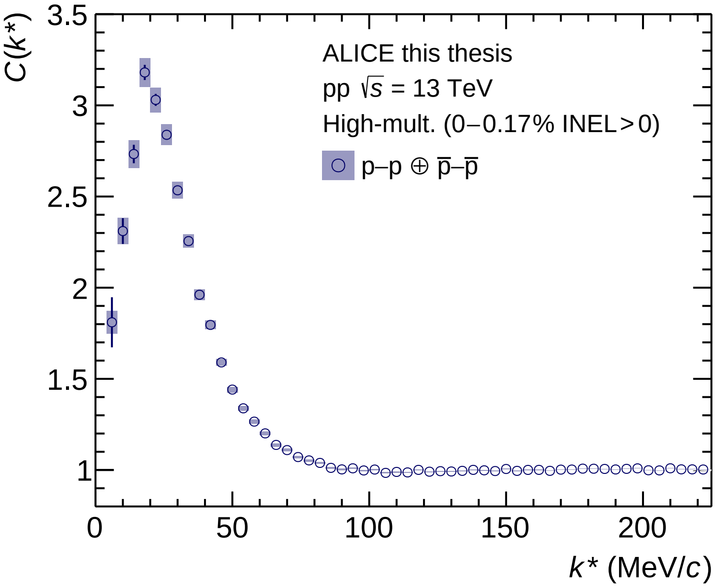

Figure B.7: Experimental p–p $\oplus$ $\overline{\text{p}}$–$\overline{\text{p}}$ correlation function with systematic uncertainties.

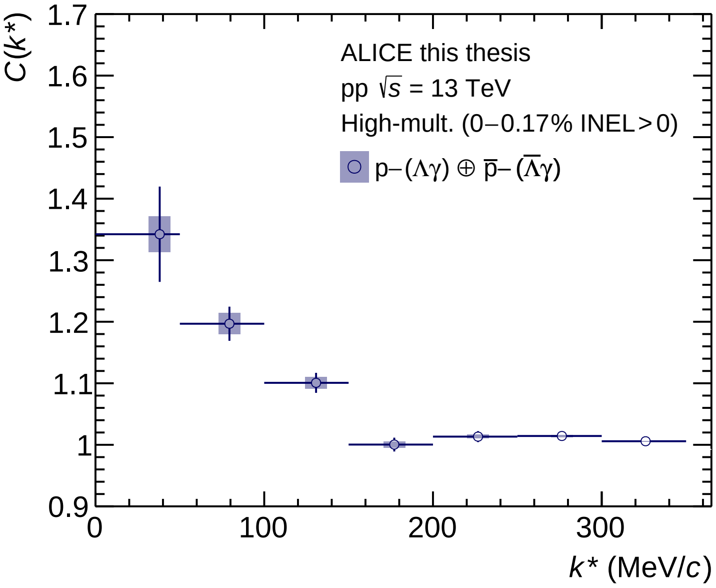

Figure B.8: Experimental p–$(\Lambda\gamma)$ $\oplus$ $\overline{\text{p}}$–$(\overline{\Lambda}\gamma)$ correlation function with systematic uncertainties.

List of Figures

List of Tables

Bibliography

[1] D. J. Gross and F. Wilczek, "Ultraviolet Behavior of Non-Abelian Gauge Theories," *Phys. Rev. Lett.* **30** (1973) 1343.

[2] S. Weinberg, "Non-Abelian Gauge Theories of the Strong Interactions," *Phys. Rev. Lett.* **31** (1973) 494.

[3] H. Fritzsch, M. Gell-Mann, and H. Leutwyler, "Advantages of the Color Octet Gluon Picture," *Phys. Lett.* **B47** (1973) 365.

[4] C. D. Roberts, "Three Lectures on Hadron Physics," *J. Phys.* **706** (2016) 022003.

[5] F. Halzen and A. D. Martin, *Quarks and Leptons: An Introductory Course in Modern Particle Physics*. Wiley, New York, 1984.

[6] D. J. Griffiths, *Introduction to elementary particles*. Wiley, New York, 2008.

[7] **Particle Data Group** Collaboration, M. Tanabashi *et al.*, "Review of Particle Physics," *Phys. Rev.* **D98** (2018) 030001.

[8] E. Epelbaum, H.-W. Hammer, and U.-G. Meißner, "Modern Theory of Nuclear Forces," *Rev. Mod. Phys.* **81** (2009) 1773.

[9] S. Petschauer, J. Haidenbauer, N. Kaiser, U.-G. Meißner, and W. Weise, "Hyperon-nuclear interactions from SU(3) chiral effective field theory," *Theory. Front. Phys.* **8** (2020) 12.

[10] P. Higgs, "Broken symmetries, massless particles and gauge fields," *Phys. Lett.* **12** (1964) 132.

[11] P. Higgs, "Broken symmetries and the masses of gauge bosons," *Phys. Rev. Lett.* **13** (1964) 508.

[12] F. Englert and R. Brout, "Broken Symmetry and the Mass of Gauge Vector Mesons," *Phys. Rev. Lett.* **13** (1964) 321.

[13] R. Rapp, J. Wambach, and H. van Hees, "The Chiral Restoration Transition of QCD and Low Mass Dileptons," *Landolt-Bornstein* **23** (2010) 134.

[14] S. Klimt, M. Lutz, and W. Weise, "Chiral phase transition in the SU(3) Nambu and Jona-Lasinio model," *Phys. Lett.* **B249** (1990) 386.

[15] M. Gell-Mann, "The Eightfold Way: A Theory of strong interaction symmetry,".

[16] Y. Ne'eman, "Derivation of strong interactions from a gauge invariance," *Nucl. Phys.* **26** (1961) 222.

[17] V. Hepp and H. Schleich, "A New Determination of the Capture Ratio $r(c) = \Sigma^- p \to \Sigma^0 n / ((\Sigma^- p \to \Sigma^0 n) + (\Sigma^- p \to \Lambda n))$, the Λ^0-Lifetime and $\Sigma^- \Lambda^0$ Mass Difference," *Z. Phys.* **214** (1968) 71.

[18] M. Abdel-Bary *et al.*, "Production of Λ and Σ^0 hyperons in proton-proton collisions," *Eur. Phys. J.* **A46** (2010) 27.

[19] **HADES** Collaboration, J. Adamczewski-Musch *et al.*, "Σ^0 production in proton nucleus collisions near threshold," *Phys. Lett.* **B781** (2018) 735.

[20] M. W. Sullivan *et al.*, "Measurement of the ratio of Σ^0 to Λ^0 inclusive production from 28.5-GeV/c protons on beryllium," *Phys. Rev.* **D36** (1987) 674.

[21] H. Albrecht *et al.*, "Observation of octet and decuplet hyperons in e^+e^- annihilation at 10 GeV centre-of-mass energy," *Phys. Lett.* **B183** (1987) 419.

[22] **L3** Collaboration, M. Acciarri *et al.*, "Inclusive Σ^+ and Σ^0 production in hadronic Z decays," *Phys. Lett.* **B479** (2000) 79.

[23] B. S. Yuldashev *et al.*, "Neutral-strange-particle production in p^{20}Ne and pN interactions at 300 GeV," *Phys. Rev.* **D43** (1991) 2792.

[24] **STAR** Collaboration, G. Van Buren, "The Σ^0/Λ ratio in high energy nuclear collisions," *J. Phys.* **G31** (2005) S1127.

[25] **ALICE** Collaboration, A. Borissov, "Production of Σ^0 hyperons at LHC with ALICE," *EPJ Web Conf.* **222** (2019) 02002.

[26] R. J. Oakes, "Baryon-Baryon Interactions and the Eightfold Way," *Phys. Rev.* **131** (1963) 2239.

[27] P. D. DeSouza, G. A. Snow, and S. Meshkov, "*S*-Wave Hyperon-Nucleon Interactions and SU_3 Symmetry," *Phys. Rev.* **135** (1964) B565.

[28] C. B. Dover and H. Feshbach, "Unitary symmetry in baryon baryon scattering," *Annals Phys.* **198** (1990) 321–357.

[29] V. G. J. Stoks, R. A. M. Klomp, M. C. M. Rentmeester, and J. J. de Swart, "Partial wave analaysis of all nucleon-nucleon scattering data below 350 MeV," *Phys. Rev.* **C48** (1993) 792.

[30] H. Yukawa, "On the Interaction of Elementary Particles I," *Proc. Phys. Math. Soc. Jap.* **17** (1935) 48.

[31] L. Tolos and L. Fabbietti, "Strangeness in Nuclei and Neutron Stars," *Prog. Part. Nucl. Phys.* **112** (2020) 103770.

[32] A. Gal, E. V. Hungerford, and D. J. Millener, "Strangeness in nuclear physics," *Rev. Mod. Phys.* **88** (2016) 035004.

[33] A. Feliciello and T. Nagae, "Experimental review of hypernuclear physics: recent achievements and future perspectives," *Rep. Prog. Phys.* **78** (2015) 096301.

[34] P. Bydžovský, J. Mareš, and A. Gal, *Topics in Strangeness Nuclear Physics*. Lecture Notes in Physics. Springer, Berlin, 2007.

[35] E. Friedman and A. Gal, "In-medium nuclear interactions of low-energy hadrons," *Phys. Rept.* **452** (2007) 89.

[36] R. Engelmann, H. Filthuth, V. Hepp, and E. Kluge, "Inelastic $\Sigma^- p$-interactions at low momenta," *Phys. Lett.* **21** (1966) 587.

[37] F. Eisele, H. Filthuth, W. Foehlisch, V. Hepp, and G. Zech, "Elastic $\Sigma^+ p$ scattering at low energies," *Phys. Lett.* **B37** (1971) 204.

[38] J. Kadyk, G. Alexander, J. Chan, P. Gaposchkin, and G. Trilling, “Λp interactions in momentum range 300 to 1500 MeV/c,” *Nucl. Phys.* **B27** (1971) 13.

[39] B. Sechi-Zorn, B. Kehoe, J. Twitty, and R. A. Burnstein, “Low-Energy Λ-Proton Elastic Scattering,” *Phys. Rev.* **175** (1968) 1735.

[40] G. Alexander, U. Karshon, A. Shapira, G. Yekutieli, R. Engelmann, H. Filthuth, and W. Lughofer, “Study of the $\Lambda - N$ System in Low-Energy $\Lambda - p$ Elastic Scattering,” *Phys. Rev.* **173** (1968) 1452.

[41] T. Hasegawa *et al.*, “Spectroscopic study of ${}^{10}_{\Lambda}$B, ${}^{12}_{\Lambda}$C, ${}^{28}_{\Lambda}$Si, ${}^{89}_{\Lambda}$Y, ${}^{139}_{\Lambda}$La, and ${}^{208}_{\Lambda}$Pb by the (π^+,K^+) reaction,” *Phys. Rev.* **C53** (1996) 1210.

[42] H. Hotchi *et al.*, “Spectroscopy of medium-heavy Λ hypernuclei via the (π^+, K^+) reaction,” *Phys. Rev.* **C64** (2001) 044302.

[43] O. Hashimoto and H. Tamura, “Spectroscopy of Λ hypernuclei,” *Prog. Part. Nucl. Phys.* **57** (2006) 564.

[44] R. L. Jaffe, “Perhaps a stable dihyperon,” *Phys. Rev. Lett.* **38** (1977) 195.

[45] J. Ahn *et al.*, “Measurement of the Ξ^--p scattering cross sections at low energy,” *Phys. Lett.* **B633** (2006) 214.

[46] S. Aoki *et al.*, “Quasifree p(K$^-$,K$^+$)Ξ^- reaction in nuclear emulsion,” *Nucl. Phys.* **A644** (1998) 365.

[47] K. Nakazawa *et al.*, “The first evidence of a deeply bound state of Ξ^--^{14}N system,” *Prog. Theor. Exp. Phys.* **2015** (2015) 033D02.

[48] H. Takahashi *et al.*, “Observation of a ${}^{6}_{\Lambda\Lambda}$He Double Hypernucleus,” *Phys. Rev. Lett.* **87** (2001) 212502.

[49] H. A. Rubin and R. A. Burnstein, “Low-Energy (Σ^+, p) and (Σ^-, p) Elastic Scattering,” *Phys. Rev.* **159** (1967) 1149.

[50] **KEK-PS E289** Collaboration, J.Kondo *et al.*, “$\Sigma^- p$ elastic-scattering in the region of $400 \leq p_{\Sigma^-} \leq 700\mathrm{MeV}/c$ with a scintillating-fiber active target,” *Nucl. Phys.* **A676** (2000) 371.

[51] **KEK-PS E289** Collaboration, J. Ahn *et al.*, “$\Sigma^+ p$ elastic scattering cross sections in the region of $350 \leq p_{\Sigma^+} \leq 750\mathrm{MeV}/c$ with a scintillating fiber active target,” *Nucl. Phys.* **A761** (2005) 41.

[52] J. Ahn *et al.*, “$\Sigma^+ p$ elastic scattering in the region of $300 \leq p_{\Sigma} \leq 600\mathrm{MeV}/c$ with a scintillating fiber target,” *Nucl. Phys.* **A648** (1999) 263.

[53] G. Alexander, Y. Gell, and I. Stumer, “Low-Energy ΣN Scattering Parameters: K-Matrix Analysis,” *Phys. Rev.* **D6** (1972) 2405.

[54] **J-PARC E40** Collaboration, Y. Nakada *et al.*, “A Σp Scattering Experiment at J-PARC and the Analysis Status,” *JPS Conf. Proc.* **26** (2019) 023024.

[55] C. J. Batty, “Exotic Atoms: A Review,” *Sov. J. Part. Nucl.* **13** (1982) 71.

[56] C. J. Batty, E. Friedman, and A. Gal, “Strong interaction physics from hadronic atoms,” *Phys. Rept.* **287** (1997) 385.

[57] G. Backenstoss *et al.*, “Observations of Σ hyperonic atoms,” *Phys. Lett.* **B33** (1970) 230.

[58] C. Batty *et al.*, “Measurement of strong interaction effects in Σ atoms,” *Phys. Lett.* **B74** (1978) 27.

[59] R. J. Powers *et al.*, “Strong-interaction effect measurements in Σ hyperonic atoms of W and Pb,” *Phys. Rev.* **C47** (1993) 1263.

[60] C. Batty, E. Friedman, and A. Gal, “Density dependence of the Σ nucleus optical potential derived from Σ^- atom data,” *Phys. Lett.* **B335** (1994) 273.

[61] C. J. Batty, E. Friedman, and A. Gal, “Density Dependence in Σ^- Atoms and Implications for Σ Hypernuclei,” *Prog. Theor. Phys. Suppl.* **117** (1994) 227.

[62] J. Mareš, E. Friedman, A. Gal, and B. K. Jennings, “Constraints on Σ nucleus dynamics from Dirac phenomenology of Σ^- atoms,” *Nucl. Phys.* **A594** (1995) 311.

[63] A. Gal and C. B. Dover, “Narrow Σ-hypernuclear states,” *Phys. Rev. Lett.* **44** (1980) 379.

[64] T. Nagae *et al.*, “Observation of a $^4_\Sigma$He Bound State in the ^{4}He(K^-, π^-) Reaction at 600 MeV/c,” *Phys. Rev. Lett.* **80** (1998) 1605.

[65] R. S. Hayano *et al.*, “Observation of a Bound State of $^4_\Sigma$He Hypernucleus,” *Phys. Lett.* **B231** (1989) 355.

[66] T. Harada, S. Shinmura, Y. Akaishi, and H. Tanaka, “Structure of the $^4_\Sigma$He hypernuclear bound state,” *Nucl. Phys.* **A507** (1990) 715.

[67] J. Dąbrowski, “Isospin dependence of the single-particle potential of the Σ hyperon in nuclear matter,” *Phys. Rev.* **C60** (1999) 025205.

[68] H. Noumi *et al.*, “Sigma-Nucleus Potential in $A = 28$,” *Phys. Rev. Lett.* **89** (2002) 072301.

[69] P. K. Saha *et al.*, “Study of the Σ-nucleus potential by the (π^-, K^+) reaction on medium-to-heavy nuclear targets,” *Phys. Rev.* **C70** (2004) 044613.

[70] T. Harada and Y. Hirabayashi, “Is the Σ−nucleus potential for Σ^- atoms consistent with the Si-28(π^-, K^+) data?,” *Nucl. Phys.* **A759** (2005) 143.

[71] J. Hüfner, S. Y. Lee, and H. A. Weidenmüller, “The Formation of Hypernuclei by K^- Capture,” *Nucl. Phys.* **A234** (1974) 429.

[72] T. Harada and Y. Hirabayashi, “Σ^- production spectrum in the inclusive (π^-, K^+) reaction on Bi-209 and the Σ−nucleus potential,” *Nucl. Phys.* **A767** (2006) 206.

[73] M. Kohno, Y. Fujiwara, Y. Watanabe, K. Ogata, and M. Kawai, “Strength of the Σ single-particle potential in nuclei from semiclassical distorted wave model analysis of (π^-, K^+) inclusive spectrum,” *Prog. Theor. Phys.* **112** (2004) 895.

[74] M. Kohno, Y. Fujiwara, Y. Watanabe, K. Ogata, and M. Kawai, “Semiclassical distorted wave model analysis of the (π^-, K^+) Σ formation inclusive spectrum,” *Phys. Rev.* **C74** (2006) 064613.

[75] B. Holzenkamp, K. Holinde, and J. Speth, “A Meson Exchange Model for the Hyperon Nucleon Interaction,” *Nucl. Phys.* **A500** (1989) 485.

[76] J. Haidenbauer and U.-G. Meißner, "Jülich hyperon-nucleon model revisited," *Phys. Rev.* **C72** (2005) 044005.

[77] P. M. M. Maessen, T. A. Rijken, and J. J. de Swart, "Soft-core baryon-baryon one-boson-exchange models. II. Hyperon-nucleon potential," *Phys. Rev.* **C40** (1989) 2226.

[78] T. A. Rijken, V. G. J. Stoks, and Y. Yamamoto, "Soft-core hyperon–nucleon potentials," *Phys. Rev.* **C59** (1999) 21.

[79] T. A. Rijken and Y. Yamamoto, "Extended-soft-core baryon-baryon model. II. Hyperon-nucleon interaction," *Phys. Rev.* **C73** (2006) 044008.

[80] T. A. Rijken, M. M. Nagels, and Y. Yamamoto, "Baryon-Baryon Interactions: Nijmegen Extended-Soft-Core Models," *Prog. Theor. Phys.* **185** (2010) 14.

[81] M. M. Nagels, T. A. Rijken, and Y. Yamamoto, "Extended-soft-core baryon–baryon model ESC16. II. Hyperon–nucleon interactions," *Phys. Rev. C* **99** (2019) 044003.

[82] H. Polinder, J. Haidenbauer, and U.-G. Meißner, "Hyperon–nucleon interactions – a chiral effective field theory approach," *Nucl. Phys.* **A779** (2006) 244 – 266.

[83] J. Haidenbauer, S. Petschauer, N. Kaiser, U. G. Meißner, A. Nogga, and W. Weise, "Hyperon–nucleon interaction at next-to-leading order in chiral effective field theory," *Nucl. Phys.* **A915** (2013) 24.

[84] J. Haidenbauer, U. G. Meißner, and A. Nogga, "Hyperon–nucleon interaction within chiral effective field theory revisited," *Eur. Phys. J.* **A56** (2020) 91.

[85] Y. Fujiwara, Y. Suzuki, and C. Nakamoto, "Baryon–baryon interactions in the SU(6) quark model and their applications to light nuclear systems," *Prog. Part. Nucl. Phys.* **58** (2007) 439.

[86] Y. Tang, M. LeMere, and D. Thompsom, "Resonating-group method for nuclear many-body problems," *Phys. Rep.* **47** (1978) 167.

[87] Y. Fujiwara, C. Nakamoto, and Y. Suzuki, "Effective meson-exchange potentials in the SU_6 quark model for NN and YN interactions," *Phys. Rev.* **C54** (1996) 2180.

[88] Y. Fujiwara, T. Fujita, M. Kohno, C. Nakamoto, and Y. Suzuki, "Resonating-group study of baryon-baryon interactions for the complete baryon octet: NN interaction," *Phys. Rev.* **C65** (2001) 014002.

[89] **HAL QCD** Collaboration, T. Inoue *et al.*, "Two-baryon potentials and H-dibaryon from 3-flavor lattice QCD simulations," *Nucl. Phys.* **A881** (2012) 28.

[90] **NPLQCD** Collaboration, S. R. Beane *et al.*, "Hyperon–nucleon scattering from fully-dynamical lattice QCD," *Nucl. Phys.* **A794** (2007) 62.

[91] **HAL QCD** Collaboration, H. Nemura, "Hyperon-nucleon interaction from lattice QCD at $(m_\pi, m_K) \approx (146, 525)$ MeV," *AIP Conf. Proc.* **2130** (2019) 040005.

[92] **HAL QCD** Collaboration, S. Aoki *et al.*, "Lattice quantum chromodynamical approach to nuclear physics," *Prog. Theor. Exp. Phys* **2012** (2012) 01A105.

[93] **NPLQCD** Collaboration, S. R. Beane *et al.*, "Hyperon-Nucleon Interactions from Quantum Chromodynamics and the Composition of Dense Nuclear Matter," *Phys. Rev. Lett.* **109** (2012) 172001.

[94] **HAL QCD** Collaboration, T. Inoue, “Strange Nuclear Physics from QCD on Lattice,” *AIP Conf. Proc.* **2130** (2019) 020002.

[95] Y. Yamamoto, T. Motoba, H. Himeno, K. Ikeda, and S. Nagata, “Hyperon nucleon and hyperon-hyperon interactions in nuclei,” *Prog. Theor. Phys. Suppl.* **117** (1994) 361.

[96] Y. Yamamoto, T. Motoba, and T. A. Rijken, “G-matrix approach to hyperon–nucleus systems,” *Prog. Theor. Phys. Suppl.* **185** (2010) 72.

[97] N. Kaiser, “Chiral dynamics of Σ hyperons in the nuclear medium,” *Phys. Rev.* **C71** (2005) 068201.

[98] N. Kaiser, “Σ-nuclear spin-orbit coupling from two-pion exchange,” *Phys. Rev.* **C76** (2007) 068201.

[99] S. Petschauer, J. Haidenbauer, N. Kaiser, U.-G. Meißner, and W. Weise, “Hyperons in nuclear matter from SU(3) chiral effective field theory,” *Eur. Phys. J.* **A52** (2016) 15.

[100] **HADES** Collaboration, J. Adamczewski-Musch *et al.*, “Probing dense baryon-rich matter with virtual photons,” *Nat. Phys.* **15** (2019) 1040.

[101] F. Özel and P. Freire, “Masses, Radii, and the Equation of State of Neutron Stars,” *Ann. Rev. Astron. Astrophys.* **54** (2016) 401.

[102] A. Schmitt, “Dense matter in compact stars: A pedagogical introduction,” *Lect. Notes Phys.* **811** (2010) 1.

[103] R. C. Tolman, “Static Solutions of Einstein’s Field Equations for Spheres of Fluid,” *Phys. Rev.* **55** (1939) 364.

[104] J. R. Oppenheimer and G. M. Volkoff, “On Massive Neutron Cores,” *Phys. Rev.* **55** (1939) 374.

[105] P. Demorest, T. Pennucci, S. Ransom, M. Roberts, and J. Hessels, “Shapiro Delay Measurement of A Two Solar Mass Neutron Star,” *Nature* **467** (2010) 1081.

[106] J. Antoniadis *et al.*, “A Massive Pulsar in a Compact Relativistic Binary,” *Science* **340** (2013) 6131.

[107] E. Fonseca *et al.*, “The NANOGRAV nine-year data set: Mass and geometric measurements of binary millisecond pulsars,” *Astrophys. J.* **832** (2016) 167.

[108] H. Cromartie *et al.*, “Relativistic Shapiro delay measurements of an extremely massive millisecond pulsar,” *Nat. Astron.* **4** (2020) 72.

[109] **LIGO Scientific, Virgo** Collaboration, B. P. Abbott *et al.*, “GW170817: Observation of Gravitational Waves from a Binary Neutron Star Inspiral,” *Phys. Rev. Lett.* **119** (2017) 161101.

[110] **LIGO Scientific, Virgo** Collaboration, B. P. Abbott *et al.*, “GW170817: Measurements of neutron star radii and equation of state,” *Phys. Rev. Lett.* **121** (2018) 161101.

[111] V. A. Ambartsumyan and G. S. Saakyan, “The Degenerate Superdense Gas of Elementary Particles,” *Sov. Astron.* **4** (1960) 187.

[112] H. Đapo, B.-J. Schaefer, and J. Wambach, “Appearance of hyperons in neutron stars,” *Phys. Rev.* **C81** (2010) 035803.

[113] I. Vidaña, "Hyperons: the strange ingredients of the nuclear equation of state," *Proc. Roy. Soc.* **A474** (2018) 0145.

[114] J. Schaffner-Bielich, "Strangeness in Compact Stars," *Nucl. Phys.* **A835** (2010) 279.

[115] J. Schaffner and I. N. Mishustin, "Hyperon rich matter in neutron stars," *Phys. Rev.* **C53** (1996) 1416.

[116] S. Weissenborn, D. Chatterjee, and J. Schaffner-Bielich, "Hyperons and massive neutron stars: the role of hyperon potentials," *Nucl. Phys.* **A881** (2012) 62.

[117] S. Weissenborn, D. Chatterjee, and J. Schaffner-Bielich, "Hyperons and massive neutron stars: vector repulsion and SU(3) symmetry," *Phys. Rev.* **C85** (2012) 065802.

[118] J. Haidenbauer, U. G. Meißner, N. Kaiser, and W. Weise, "Lambda-nuclear interactions and hyperon puzzle in neutron stars," *Eur. Phys. J.* **A53** (2017) 121.

[119] D. Lonardoni, A. Lovato, S. Gandolfi, and F. Pederiva, "Hyperon Puzzle: Hints from Quantum Monte Carlo Calculations," *Phys. Rev. Lett.* **114** (2015) 092301.

[120] D. Gerstung, N. Kaiser, and W. Weise, "Hyperon-nucleon three-body forces and strangeness in neutron stars," `arXiv:2001.10563`.

[121] R. Hanbury Brown and R. Q. Twiss, "Correlation between Photons in two Coherent Beams of Light," *Nature* **177** (1956) 27.

[122] R. Hanbury Brown and R. Q. Twiss, "A Test of a New Type of Stellar Interferometer on Sirius," *Nature* **178** (1956) 1046.

[123] G. Goldhaber, S. Goldhaber, W.-Y. Lee, and A. Pais, "Influence of Bose-Einstein statistics on the anti-proton proton annihilation process," *Phys. Rev.* **120** (1960) 300.

[124] S. Pratt, "Pion Interferometry of Quark-Gluon Plasma," *Phys. Rev.* **D33** (1986) 1314.

[125] M. A. Lisa, S. Pratt, R. Soltz, and U. Wiedemann, "Femtoscopy in relativistic heavy ion collisions," *Ann. Rev. Nucl. Part. Sci.* **55** (2005) 357.

[126] U. Heinz and B. V. Jacak, "Two-Particle Correlations in Relativistic Heavy-Ion Collisions," *Ann. Rev. Nucl. Part. Sci.* **49** (1999) 529.

[127] U. A. Wiedemann and U. W. Heinz, "Particle interferometry for relativistic heavy ion collisions," *Phys. Rept.* **319** (1999) 145.

[128] O. W. Arnold, *Study of the hyperon-nucleon interaction via femtoscopy in elementary systems with HADES and ALICE.* PhD thesis, Technische Universität München, 2017. `https://mediatum.ub.tum.de/?id=1368097`.

[129] K. Morita, S. Gongyo, T. Hatsuda, T. Hyodo, Y. Kamiya, and A. Ohnishi, "Probing $\Omega\Omega$ and $p\Omega$ dibaryons with femtoscopic correlations in relativistic heavy-ion collisions," *Phys. Rev.* **C101** (2020) 015201.

[130] R. Lednický, "Finite-size effects on two-particle production in continuous and discrete spectrum," *Phys. Part. Nucl.* **40** (2009) 307.

[131] S. E. Koonin, "Proton pictures of high-energy nuclear collisions," *Phys. Lett.* **B70** (1977) 43.

[132] S. Pratt, T. Csörgő, and J. Zimányi, "Detailed predictions for two-pion correlations in ultrarelativistic heavy-ion collisions," *Phys. Rev.* **C42** (1990) 2646.

[133] R. Lednický and V. L. Lyuboshits, "Final State Interaction Effect on Pairing Correlations Between Particles with Small Relative Momenta," *Sov. J. Nucl. Phys.* **35** (1982) 770.

[134] R. B. Wiringa, V. G. J. Stoks, and R. Schiavilla, "Accurate nucleon-nucleon potential with charge-independence breaking," *Phys. Rev.* **C51** (1995) 38.

[135] D. L. Mihaylov, V. Mantovani Sarti, O. W. Arnold, L. Fabbietti, B. Hohlweger, and A. M. Mathis, "A femtoscopic Correlation Analysis Tool using the Schrödinger equation (CATS)," *Eur. Phys. J.* **C78** (2018) 394.

[136] A. Badalian, L. Kok, M. Polikarpov, and Y. Simonov, "Resonances in Coupled Channels in Nuclear and Particle Physics," *Phys. Rept.* **82** (1982) 31.

[137] J. A. Oller, "Coupled-channel approach in hadron-hadron scattering," *Prog. Part. Nucl. Phys.* **110** (2020) 103728.

[138] Y. Kamiya, T. Hyodo, K. Morita, A. Ohnishi, and W. Weise, "$K^- p$ correlation function from high-energy nuclear collisions and chiral SU(3) dynamics," *Phys. Rev. Lett.* **124** (2020) 132501.

[139] J. Haidenbauer, "Coupled-channel effects in hadron–hadron correlation functions," *Nucl. Phys.* **A981** (2019) 1.

[140] R. Lednický, V. V. Lyuboshitz, and V. L. Lyuboshitz *Phys. At. Nucl.* **61** (1998) 2950.

[141] F. Becattini, P. Castorina, A. Milov, and H. Satz, "Predictions of hadron abundances in pp collisions at the LHC," *J. Phys.* **G38** (2011) 025002.

[142] F. Wang and S. Pratt, "Lambda proton correlations in relativistic heavy ion collisions," *Phys. Rev. Lett.* **83** (1999) 3138.

[143] **E895** Collaboration, P. Chung *et al.*, "Comparison of Source Images for Protons, π^-'s, and Λ's in 6AGeV Au + Au Collisions," *Phys. Rev. Lett.* **91** (2003) 162301.

[144] **STAR** Collaboration, J. Adams *et al.*, "Proton-Λ correlations in central Au+Au collisions at $\sqrt{s_{NN}} = 200$ GeV," *Phys. Rev.* **C74** (2006) 064906.

[145] **HADES** Collaboration, G. Agakishiev *et al.*, "$\Lambda - p$ femtoscopy in collisions of Ar + KCl at 1.76A GeV," *Phys. Rev.* **C82** (2010) 021901.

[146] **NA49** Collaboration, T. Anticic *et al.*, "Proton-Λ correlations in central Pb+Pb collisions at $\sqrt{s_{NN}} = 17.3$ GeV," *Phys. Rev.* **C83** (2011) 054906.

[147] V. M. Shapoval, B. Erazmus, R. Lednický, and Y. M. Sinyukov, "Extracting $p\Lambda$ scattering lengths from heavy ion collisions," *Phys. Rev.* **C92** (2015) 034910.

[148] A. R. Bodmer, Q. N. Usmani, and J. Carlson, "Binding energies of hypernuclei and three-body ΛNN forces," *Phys. Rev.* **C29** (1984) 684–687.

[149] **ALICE** Collaboration, "ALICE Figure repository." `https://alice-figure.web.cern.ch/`. Accessed: 2020-02-23.

[150] D. L. Mihaylov, *Analysis techniques for femtoscopy and correlation studies in small collision systems and their applications to the investigation of* $p-\Lambda$ *and* $\Lambda-\Lambda$ *interactions with ALICE*. PhD thesis, Technische Universität München, 2020. in preparation.

[151] **HADES** Collaboration, J. Adamczewski-Musch *et al.*, "The Λp interaction studied via femtoscopy in p + Nb reactions at $\sqrt{s_{NN} = 3.18}$ GeV," *Phys. Rev.* **C94** (2016) 025201.

[152] **ALICE** Collaboration, S. Acharya *et al.*, "p-p, p–Λ and Λ–Λ correlations studied via femtoscopy in pp reactions at $\sqrt{s}$ = 7 TeV," *Phys. Rev.* **C99** (2019) 024001.

[153] **ALICE** Collaboration, S. Acharya *et al.*, "Study of the Λ–Λ interaction with femtoscopy correlations in pp and p–Pb collisions at the LHC," *Phys. Lett.* **B797** (2019) 134822.

[154] **STAR** Collaboration, L. Adamczyk *et al.*, "ΛΛ Correlation Function in Au + Au Collisions at $\sqrt{s_{NN}} = 200$ GeV," *Phys. Rev. Lett.* **114** (2015) 022301.

[155] K. Morita, T. Furumoto, and A. Ohnishi, "ΛΛ interaction from relativistic heavy-ion collisions," *Phys. Rev.* **C91** (2015) 024916.

[156] S. Gongyo *et al.*, "Most Strange Dibaryon from Lattice QCD," *Phys. Rev. Lett.* **120** (2018) 212001.

[157] P. Naidon and S. Endo, "Efimov Physics: a review," *Rept. Prog. Phys.* **80** (2017) 056001.

[158] T. Hatsuda, K. Morita, A. Ohnishi, and K. Sasaki, "$p\Xi^-$ Correlation in Relativistic Heavy Ion Collisions with Nucleon-Hyperon Interaction from Lattice QCD," *Nucl. Phys.* **A967** (2017) 856.

[159] **ALICE** Collaboration, S. Acharya *et al.*, "First observation of an attractive interaction between a proton and a multi-strange baryon," *Phys. Rev. Lett.* **123** (2019) 112002.

[160] B. Hohlweger, *First observation of the* $p-\Xi^-$ *interaction with the femtoscopy method*. PhD thesis, Technische Universität München, 2020. in preparation.

[161] **ALICE** Collaboration, S. Acharya *et al.*, "A new laboratory to study hadron-hadron interactions," *in preparation* (2020) .

[162] E. Chizzali, "First Measurement of the ϕ-Proton Correlation Function with ALICE in pp Collisions at $\sqrt{s} = 13$ TeV," Bachelor thesis, Technische Universität München, 2019. `https://www.das.ktas.ph.tum.de/DasDocs/Public/Bachelor_Theses/BachelorThesis_EmmaChizzali.pdf`.

[163] L. Evans and P. Bryant, "LHC Machine," *J. Instrum.* **3** (2008) S08001.

[164] E. Mobs, "The CERN accelerator complex. Complexe des accélérateurs du CERN,". `http://cds.cern.ch/record/2197559`.

[165] **ATLAS** Collaboration, G. Aad *et al.*, "The ATLAS Experiment at the CERN Large Hadron Collider," *J. Instrum.* **3** (2008) S08003.

[166] **CMS** Collaboration, S. Chatrchyan *et al.*, "The CMS experiment at the CERN LHC," *J. Instrum.* **3** (2008) S08004.

[167] **LHCb** Collaboration, A. A. Alves, Jr. *et al.*, "The LHCb Detector at the LHC," *J. Instrum.* **3** (2008) S08005.

[168] **TOTEM** Collaboration, G. Anelli *et al.*, “The TOTEM Experiment at the CERN Large Hadron Collider,” *J. Instrum.* **3** (2008) S08007.

[169] **LHCf** Collaboration, O. Adriani *et al.*, “The LHCf detector at the CERN Large Hadron Collider,” *J. Instrum.* **3** (2008) S08006.

[170] **MoEDAL** Collaboration, B. Acharya *et al.*, “The Physics Programme Of The MoEDAL Experiment At The LHC,” *Int. J. Mod. Phys.* **A29** (2014) 1430050.

[171] **ALICE** Collaboration, K. Aamodt *et al.*, “The ALICE experiment at the CERN LHC,” *J. Instrum.* **3** (2008) S08002.

[172] **ALICE** Collaboration, F. Carminati *et al.*, “ALICE: Physics Performance Report, Volume I,” *J. Phys* **G30** (2004) 1517.

[173] **ALICE** Collaboration, B. Alessandro *et al.*, “ALICE: Physics Performance Report, Volume II,” *J. Phys.* **G32** (2006) 1295.

[174] **ALICE** Collaboration, B. Abelev *et al.*, “Performance of the ALICE experiment at the CERN LHC,” *Int. J. Mod. Phys.* **A29** (2014) 1430044.

[175] C. Lippmann, “Particle identification,” *Nucl. Instrum. Meth.* **A666** (2012) 148.

[176] J. Engelfried, “Cherenkov light imaging—fundamentals and recent developments,” *Nucl. Instrum. Meth.* **A639** (2011) 1.

[177] A. Andronic and J. Wessels, “Transition radiation detectors,” *Nucl. Instrum. Meth.* **A666** (2012) 130.

[178] H. Bethe, “Zur Theorie des Durchgangs schneller Korpuskularstrahlen durch Materie,” *Annalen der Physik* **397** (1930) 325.

[179] W. Blum, W. Riegler, and L. Rolandi, *Particle detection with drift chambers*. Springer, Berlin, 2008.

[180] E. Fermi, “The Ionization Loss of Energy in Gases and in Condensed Materials,” *Phys. Rev.* **57** (1940) 485.

[181] J. Podolanski and R. Armenteros, “III. Analysis of V-events,” *Philos. Mag.* **45** (1954) 13.

[182] B. Adeva *et al.*, “The construction of the L3 experiment,” *Nucl. Instrum. Meth.* **A289** (1990) 35.

[183] **ALICE** Collaboration, K. Aamodt *et al.*, “Alignment of the ALICE Inner Tracking System with cosmic-ray tracks,” *J. Instrum.* **5** (2010) P03003.

[184] J. Alme *et al.*, “The ALICE TPC, a large 3-dimensional tracking device with fast readout for ultra-high multiplicity events,” *Nucl. Instrum. Meth.* **A622** (2010) 316.

[185] J. N. Marx and D. R. Nygren, “The Time Projection Chamber,” *Phys. Today* **31N10** (1978) 46.

[186] G. Charpak, R. Bouclier, T. Bressani, J. Favier, and C. Zupancic, “The Use of Multiwire Proportional Counters to Select and Localize Charged Particles,” *Nucl. Instrum. Meth.* **62** (1968) 262.

[187] A. Akindinov *et al.*, “Performance of the ALICE Time-of-Flight detector at the LHC,” *Eur. Phys. J. Plus* **128** (2013) 44.

[188] E. Cerron Zeballos *et al.*, "A New type of resistive plate chamber: The Multigap RPC," *Nucl. Instrum. Meth.* **A374** (1996) 132.

[189] A. Akindinov *et al.*, "The multigap resistive plate chamber as a time-of-flight detector," *Nucl. Instrum. Meth.* **A456** (2000) 16.

[190] **ALICE** Collaboration, E. Abbas *et al.*, "Performance of the ALICE VZERO system," *J. Instrum.* **8** (2013) P10016.

[191] S. van der Meer, "Calibration of the effective beam height in the ISR," Tech. Rep. CERN-ISR-PO-68-31, CERN, 1968. `https://cds.cern.ch/record/296752`.

[192] **ALICE** Collaboration, J. Adam *et al.*, "Determination of the event collision time with the ALICE detector at the LHC," *Eur. Phys. J. Plus* **132** (2017) 99.

[193] J. Wenninger, "Operation and Configuration of the LHC in Run 2,". `https://cds.cern.ch/record/2668326`.

[194] J. Jimenez *et al.*, "Observations, Analysis and Mitigation of Recurrent LHC Beam Dumps Caused by Fast Losses in Arc Half-Cell 16L2," in *9th International Particle Accelerator Conference (IPAC'18)*, p. MOPMF053. 2018.

[195] **ALICE** Collaboration, "ALICE QA repository." `http://aliqaevs.web.cern.ch/aliqaevs/`. Accessed: 2020-02-23.

[196] **ALICE** Collaboration, "AliRoot: ALICE Software Framework," 2020. `https://github.com/alisw/AliRoot`.

[197] R. Brun and F. Rademakers, "ROOT: An object oriented data analysis framework," *Nucl. Instrum. Meth.* **A389** (1997) 81–86.

[198] T. Sjostrand, S. Mrenna, and P. Z. Skands, "PYTHIA 6.4 Physics and Manual," *JHEP* **05** (2006) 026.

[199] P. Z. Skands, "Tuning Monte Carlo Generators: The Perugia Tunes," *Phys. Rev.* **D82** (2010) 074018.

[200] P. Skands, S. Carrazza, and J. Rojo, "Tuning PYTHIA 8.1: the Monash 2013 Tune," *Eur. Phys. J.* **C74** (2014) 3024.

[201] T. Sjöstrand *et al.*, "An Introduction to PYTHIA 8.2," *Comput. Phys. Commun.* **191** (2015) 159.

[202] S. Roesler, R. Engel, and J. Ranft, "The Monte Carlo event generator DPMJET-III," *Advanced Monte Carlo for radiation physics, particle transport simulation and applications* (2000) 1033.

[203] X.-N. Wang and M. Gyulassy, "HIJING: A Monte Carlo model for multiple jet production in pp, pA, and AA collisions," *Phys. Rev.* **D44** (1991) 3501.

[204] T. Pierog, I. Karpenko, J. M. Katzy, E. Yatsenko, and K. Werner, "EPOS LHC: Test of collective hadronization with data measured at the CERN Large Hadron Collider," *Phys. Rev.* **C92** (2015) 034906.

[205] R. Brun, F. Bruyant, M. Maire, A. C. McPherson, and P. Zanarini, "GEANT3," Tech. Rep. CERN-DD-EE-84-1, CERN, 1987.

[206] **GEANT4** Collaboration, S. Agostinelli *et al.*, "GEANT4: A Simulation toolkit," *Nucl. Instrum. Meth.* **A506** (2003) 250.

[207] M. Ivanov, I. Belikov, P. Hristov, and K. Safarik, "Track reconstruction in high density environment," *Nucl. Instrum. Meth.* **A566** (2006) 70.

[208] R. Frühwirth, "Application of Kalman filtering to track and vertex fitting," *Nucl. Instrum. Meth.* **A262** (1987) 444.

[209] **ALICE** Collaboration, "AliPhysics: ALICE Analysis Repository," 2020. `https://github.com/alisw/AliPhysics`.

[210] **ALICE** Collaboration, B. Abelev *et al.*, "Upgrade of the ALICE Experiment: Letter Of Intent," *J. Phys.* **G41** (2014) 087001.

[211] **ALICE** Collaboration, S. Acharya *et al.*, "ALICE upgrade physics performance studies for 2018 Report on HL/HE-LHC physics,". `https://cds.cern.ch/record/2661798`.

[212] **ALICE** Collaboration, B. Abelev *et al.*, "Technical Design Report for the Upgrade of the ALICE Inner Tracking System," *J. Phys.* **G41** (2014) 087002.

[213] **ALICE TPC** Collaboration, M. M. Aggarwal *et al.*, "Particle identification studies with a full-size 4-GEM prototype for the ALICE TPC upgrade," *Nucl. Instrum. Meth.* **A903** (2018) 215.

[214] **ALICE** Collaboration, B. Abelev *et al.*, "Upgrade of the ALICE Time Projection Chamber," Tech. Rep. CERN-LHCC-2013-020. ALICE-TDR-016, CERN, 2013. `https://cds.cern.ch/record/1622286`.

[215] **ALICE** Collaboration, J. Adam *et al.*, "Addendum to the Technical Design Report for the Upgrade of the ALICE Time Projection Chamber," Tech. Rep. CERN-LHCC-2015-002. ALICE-TDR-016-ADD-1, CERN, 2015. `https://cds.cern.ch/record/1984329`.

[216] F. Sauli, "GEM: A new concept for electron amplification in gas detectors," *Nucl. Instrum. Meth.* **A386** (1997) 531.

[217] **ALICE** Collaboration, P. Buncic, M. Krzewicki, and P. Vande Vyvre, "Technical Design Report for the Upgrade of the Online-Offline Computing System," Tech. Rep. CERN-LHCC-2015-006. ALICE-TDR-019, CERN, 2015. `https://cds.cern.ch/record/2011297`.

[218] **ALICE** Collaboration, P. Antonioli, A. Kluge, and W. Riegler, "Upgrade of the ALICE Readout & Trigger System," Tech. Rep. CERN-LHCC-2013-019. ALICE-TDR-015, CERN, 2013. `http://cds.cern.ch/record/1603472`.

[219] **ALICE** Collaboration, M. Richter *et al.*, "AliceO2Group/AliceO2: First stable release," 2018. `https://github.com/AliceO2Group/AliceO2`.

[220] **ALICE** Collaboration, S. Acharya *et al.*, "Investigation of the p–Σ^0 interaction via femtoscopy in pp collisions," *Phys. Lett.* **B805** (2020) 135419.

[221] **ALICE** Collaboration, J. Adam *et al.*, "Enhanced production of multi-strange hadrons in high-multiplicity proton-proton collisions," *Nat. Phys.* **13** (2017) 535.

[222] **ALICE** Collaboration, J. Adam *et al.*, "Insight into particle production mechanisms via angular correlations of identified particles in pp collisions at $\sqrt{s} = 7$ TeV," *Eur. Phys. J.* **C77** (2017) 569.

[223] **ALICE** Collaboration, S. Acharya *et al.*, "Measurement of the inclusive isolated photon production cross section in pp collisions at $\sqrt{s}$ = 7 TeV," *Eur. Phys. J.* **C79** (2019) 896.

[224] P. Aurenche, P. Chiappetta, M. Fontannaz, J. Guillet, and E. Pilon, "Next to leading order bremsstrahlung contribution to prompt-photon production," *Nucl. Phys.* **B 399** (1993) 34.

[225] **ALICE** Collaboration, V. I. Man'ko, W. Klempt, L. Leistam, J. De Groot, and J. Schukraft, "ALICE Photon Spectrometer (PHOS): Technical Design Report," Tech. Rep. CERN-LHCC-99-004, CERN, 1999. `https://cds.cern.ch/record/381432`.

[226] W. Williams, *Nuclear and Particle Physics*. Oxford University Press Inc., Oxford, 1997.

[227] J. W. Motz, H. A. Olsen, and H. W. Koch, "Pair production by photons," *Rev. Mod. Phys.* **41** (1969) 581.

[228] **ALICE** Collaboration, B. Abelev *et al.*, "Neutral pion and η meson production in proton–proton collisions at $\sqrt{s} = 0.9$ TeV and $\sqrt{s} = 7$ TeV," *Phys. Lett.* **B717** (2012) 162.

[229] **ALICE** Collaboration, S. Acharya *et al.*, "Neutral pion and η meson production in p-Pb collisions at $\sqrt{s_{\mathrm{NN}}} = 5.02$ TeV," *Eur. Phys. J.* **C78** (2018) 624.

[230] K. Koch, *Measurement of π^0 and η mesons with photon conversions in ALICE in proton-proton collisions at $\sqrt{s} = 0.9,\ 2.76$ and 7 TeV*. PhD thesis, Universität Heidelberg, 2011. `https://www.physi.uni-heidelberg.de/Publications/thesis_K-Koch-Dec2011.pdf`.

[231] F. Bock, "ALICE Capabilities for Studying Photon Physics with the Conversion Method at LHC Energies," Bachelor thesis, Universität Heidelberg, 2010. `https://www.physi.uni-heidelberg.de/Publications/Bock-Bachelorthesis.pdf`.

[232] T. Dahms, "Measurement of photons via conversion pairs in $\sqrt{s_{\mathrm{NN}}} = 200\,\mathrm{GeV}$ Au+Au collisions with the PHENIX experiment at RHIC," *Eur. Phys. J.* **C49** (2007) 249.

[233] **ALICE** Collaboration, J. Adam *et al.*, "One-dimensional pion, kaon, and proton femtoscopy in Pb-Pb collisions at $\sqrt{s_{\mathrm{NN}}}$=2.76 TeV," *Phys. Rev.* **C92** (2015) 054908.

[234] A. Stavinskiy, K. Mikhailov, B. Erazmus, and R. Lednický, "Residual correlations between decay products of $\pi^0\pi^0$ and $p\Sigma^0$ systems," `arXiv:0704.3290`.

[235] A. Kisiel, H. Zbroszczyk, and M. Szymański, "Extracting baryon-antibaryon strong-interaction potentials from $\mathrm{p}\overline{\Lambda}$ femtoscopic correlation functions," *Phys. Rev.* **C89** (2014) 054916.

[236] **ALICE** Collaboration, S. Acharya *et al.*, "Search for a common baryon source in high multiplicity pp collisions at the LHC," *Submitted to Phys. Lett.* **B** (2020) , `arXiv:2004.08018`.

[237] **ALICE** Collaboration, K. Aamodt *et al.*, "Femtoscopy of pp collisions at $\sqrt{s} = 0.9$ and 7 TeV at the LHC with two-pion Bose-Einstein correlations," *Phys. Rev.* **D84** (2011) 112004.

[238] N. Bock, *Femtoscopy of proton-proton collisions in the ALICE experiment*. PhD thesis, Ohio State U., 2011. `http://rave.ohiolink.edu/etdc/view?acc_num=osu1316184643`.

[239] **CMS** Collaboration, A. M. Sirunyan *et al.*, "Bose-Einstein correlations in pp, pPb, and PbPb collisions at $\sqrt{s_{NN}} = 0.9 - 7$ TeV," *Phys. Rev.* **C97** (2018) 064912.

[240] **PHENIX** Collaboration, A. Adare *et al.*, "Lévy-stable two-pion Bose-Einstein correlations in $\sqrt{s_{NN}} = 200$ GeV Au + Au collisions," *Phys. Rev.* **C97** (2018) 064911.

[241] J. P. Nolan, *Stable Distributions - Models for Heavy Tailed Data*. Birkhauser, Boston, 2018. In progress, Chapter 1 online at http://fs2.american.edu/jpnolan/www/stable/stable.html.

[242] T. Csörgő, S. Hegyi, and W. A. Zajc, "Bose-Einstein correlations for Lévy stable source distributions," *Eur. Phys. J.* **C36** (2004) 67.

[243] R. Metzler, E. Barkai, and J. Klafter, "Anomalous Diffusion and Relaxation Close to Thermal Equilibrium: A Fractional Fokker-Planck Equation Approach," *Phys. Rev. Lett.* **82** (1999) 3563.

[244] U. A. Wiedemann and U. Heinz, "Resonance contributions to Hanbury-Brown–Twiss correlation radii," *Phys. Rev.* **C56** (1997) 3265.

[245] Y. Sinyukov, V. Shapoval, and V. Naboka, "On m_T dependence of femtoscopy scales for meson and baryon pairs," *Nucl. Phys.* **A946** (2016) 227.

[246] **ALICE** Collaboration, K. Aamodt *et al.*, "Femtoscopy of pp collisions at $\sqrt{s} = 0.9$ and 7 TeV at the LHC with two-pion Bose-Einstein correlations," *Phys. Rev.* **D84** (2011) 112004.

[247] A. Kisiel, "Nonidentical-particle femtoscopy at $\sqrt{s_{NN}} = 200$ GeV in hydrodynamics with statistical hadronization," *Phys. Rev.* **C81** (2010) 064906.

[248] A. Kisiel, W. Florkowski, W. Broniowski, and J. Pluta, "Femtoscopy in hydrodynamics-inspired models with resonances," *Phys. Rev.* **C73** (2006) 064902.

[249] **ATLAS** Collaboration, G. Aad *et al.*, "Two-particle Bose–Einstein correlations in pp collisions at $\sqrt{s}$=0.9 and 7 TeV measured with the ATLAS detector," *Eur. Phys. J.* **C75** (2015) 466.

[250] **ALICE** Collaboration, B. Abelev *et al.*, "Charged kaon femtoscopic correlations in pp collisions at $\sqrt{s} = 7$ TeV," *Phys. Rev.* **D87** (2013) 052016.

[251] **ALICE** Collaboration, B. Abelev *et al.*, "$\mathrm{K}^0_\mathrm{S} - \mathrm{K}^0_\mathrm{S}$ correlations in pp collisions at $\sqrt{s} = 7$ TeV from the LHC ALICE experiment," *Phys. Lett.* **B717** (2012) 151.

[252] Z. Citron *et al.*, "Future physics opportunities for high-density QCD at the LHC with heavy-ion and proton beams," *CERN Yellow Reports* **7** (2019) 1159.

[253] A. Breskin, G. Charpak, F. Sauli, M. Atkinson, and G. Schultz, "Recent Observations and Measurements with High Accuracy Drift Chambers," *Nucl. Instrum. Meth.* **124** (1975) 189.

[254] F. Sauli and A. Sharma, "Micropattern Gaseous Detectors," *Ann. Rev. Nucl. Part. Sci.* **49** (1999) 341.

[255] Y. Giomataris, P. Rebourgeard, J. P. Robert, and G. Charpak, "MICROMEGAS: A High granularity position sensitive gaseous detector for high particle flux environments," *Nucl. Instrum. Meth.* **A376** (1996) 29.

[256] C. Altunbas *et al.*, "Construction, test and commissioning of the triple-GEM tracking detector for COMPASS," *Nucl. Instrum. Meth.* **A490** (2002) 177.

[257] G. Bencivenni *et al.*, "A triple GEM detector with pad readout for high rate charged particle triggering," *Nucl. Instrum. Meth.* **A488** (2002) 493.

[258] G. Bencivenni and D. Domenici, "An ultra-light cylindrical GEM detector as inner tracker at KLOE-2," *Nucl. Instrum. Meth.* **A581** (2007) 221.

[259] D. Abbaneo *et al.*, "Characterization of GEM Detectors for Application in the CMS Muon Detection System," in *IEEE Nuclear Science Symposium and Medical Imaging Conference*, p. 1416. 2010.

[260] M. G. Bagliesi *et al.*, "The TOTEM T2 telescope based on triple-GEM chambers," *Nucl. Instrum. Meth.* **A617** (2010) 134.

[261] M. Berger *et al.*, "A Large Ungated TPC with GEM Amplification," *Nucl. Instrum. Meth.* **A869** (2017) 180.

[262] F. V. Böhmer *et al.*, "First measurement of $\mathrm{d}E/\mathrm{d}x$ with a GEM-based TPC," *Nucl. Instrum. Meth.* **A737** (2014) 214.

[263] R. Veenhof, "Garfield - simulation of gaseous detectors," 1984 - 2010. `http://garfield.web.cern.ch`.

[264] F. V. Böhmer *et al.*, "Simulation of Space-Charge Effects in an Ungated GEM-based TPC," *Nucl. Instrum. Meth.* **A719** (2013) 101.

[265] M. Villa *et al.*, "Progress on large area GEMs," *Nucl. Instrum. Meth.* **A628** (2011) 182.

[266] F. Sauli, "The gas electron multiplier (GEM): Operating principles and applications," *Nucl. Instrum. Meth.* **A805** (2016) 2.

[267] A. Bressan *et al.*, "High rate behavior and discharge limits in micropattern detectors," *Nucl. Instrum. Meth.* **A424** (1999) 321.

[268] J. Merlin, "Study of discharges and their effects in GEM detectors." `https://indico.cern.ch/event/757322/contributions/3396501/attachments/1839468/3015160/JMerlin_MPGD2019_Discharge_Study_V1_23042019.pdf`. Micro Pattern Gaseous Detectors Conference 2019, 7.5.2019.

[269] S. Bachmann *et al.*, "Discharge mechanisms and their prevention in the gas electron multiplier (GEM)," *Nucl. Instrum. Meth.* **A479** (2002) 294.

[270] H. Raether, *Electron avalanches and breakdown in gases*. Butterworths, London, 1964.

[271] **RD51** Collaboration, V. Peskov and P. Fonte, "Research on discharges in micropattern and small gap gaseous detectors," `arXiv:0911.0463`.

[272] **ALICE** Collaboration, A. Mathis, "From gated to continuous readout - the GEM upgrade of the ALICE TPC," *PoS* **322 MPGD2017** (2019) 055.

[273] M. Ball, B. Ketzer, J. Ottnad, V. Ratza, and S. Urban, "Quality assurance of GEM foils for the upgrade of the ALICE TPC," *J. Instrum.* **12** (2017) C01081.

[274] **ALICE TPC Upgrade** Collaboration, J. E. Brücken and T. E. Hildén, "The GEM QA Protocol of the ALICE TPC Upgrade Project," *PoS* **322 MPGD2017** (2019) 073.

[275] **ALICE** Collaboration, P. Gasik, "Upgrade of the ALICE central barrel tracking detectors: ITS and TPC," *Nucl. Phys.* **A982** (2019) 943.

[276] S. Agosteo *et al.*, "A Facility for the test of large area muon chambers at high rates," *Nucl. Instrum. Meth.* **A452** (2000) 94.

[277] **ALICE TPC** Collaboration, P. Gasik, "Discharge probability studies with multi-GEM detectors for the ALICE TPC Upgrade," *PoS* **322 MPGD2017** (2019) 031.

[278] Eckert & Ziegler Nuclitec GmbH, 2020. `http://www.ezag.com`.

[279] A. Deisting *et al.*, “Secondary discharge studies in single- and multi-GEM structures,” *Nucl. Instrum. Meth.* **A937** (2019) 168.

[280] L. Lautner, L. Fabbietti, P. Gasik, and T. Klemenz, “High voltage scheme optimization for secondary discharge mitigation in GEM-based detectors,” *J. Instrum.* **14** (2019) P08024.

[281] P. Gasik. Private communication.

[282] S. Barboza *et al.*, “SAMPA chip: a new ASIC for the ALICE TPC and MCH upgrades,” *J. Instrum.* **11** (2016) C02088.

[283] J. Adolfsson *et al.*, “SAMPA chip: the new 32 channels ASIC for the ALICE TPC and MCH upgrades,” *J. Instrum.* **12** (2017) C04008.

[284] P. Moreira *et al.*, “The GBT Project,” in *Topical Workshop on Electronics for Particle Physics*. CERN, 2009.

[285] **ALICE** Collaboration, H. Appelshäuser, M. Arslandok, M. Ivanov, C. Lippmann, and J. Wiechula, “Readout scheme of the upgraded ALICE TPC,”. `https://cds.cern.ch/record/2231785`.

[286] **ALICE** Collaboration, D. Rohr, S. Gorbunov, M. O. Schmidt, and R. Shahoyan, “GPU-based Online Track Reconstruction for the ALICE TPC in Run 3 with Continuous Read-Out,” *EPJ Web Conf.* **214** (2019) 01050.

[287] **ALICE** Collaboration, G. Eulisse *et al.*, “Evolution of the ALICE Software Framework for Run 3,” *EPJ Web Conf.* **214** (2019) 05010.

[288] M. Al-Turany *et al.*, “ALFA: The new ALICE-FAIR software framework,” *J. Phys.* **664** (2015) 072001.

[289] M. Al-Turany *et al.*, “The FairRoot framework,” *J. Phys.* **396** (2012) 022001.

[290] D. Simon *et al.*, “Secondary beams for tests in the PS East experimental area,” Tech. Rep. CERN PS-PA-EP-Note-88-26, CERN, 1988. `http://cds.cern.ch/record/1665434`.

[291] A. Mathis, “Performance studies with a full-size GEM-based prototype for the ALICE TPC,” Master’s thesis, Technische Universität München, 2016. `https://www.das.ktas.ph.tum.de/DasDocs/Public/Master_Theses/Thesis_Mathis.pdf`.

[292] T. Klemenz, “dE/dx Resolution Studies of a Pre-Production Read-Out Chamber with GEMs for the ALICE TPC,” Master’s thesis, Technische Universität München, 2019. `https://www.das.ktas.ph.tum.de/DasDocs/Public/Master_Theses/MScThesis_tklemenz.pdf`.

[293] A. Kaukher, O. Schäfer, H. Schröder, and R. Wurth, “Status of TPC-electronics with Time-to-Digit Converters,” Tech. Rep. EUDET-Memo-2009-08, EUDET, 2009.

[294] V. D. Elvira, “Impact of detector simulation in particle physics collider experiments,” *Phys. Rep.* **695** (2017) 1.

[295] **HEP Software Foundation** Collaboration, J. Apostolakis *et al.*, “HEP Software Foundation Community White Paper Working Group - Detector Simulation,” `arXiv:1803.04165`.

[296] **HEP Software Foundation** Collaboration, J. Albrecht *et al.*, “A Roadmap for HEP Software and Computing R&D for the 2020s,” *Comput. Softw. Big Sci.* **3** (2019) 7.

[297] **ALICE** Collaboration, S. Wenzel, “A scalable and asynchronous detector simulation system based on ALFA,” *EPJ Web Conf.* **214** (2019) 02029.

[298] E. Hellbär. PhD thesis, Goethe-Universität Frankfurt, 2020. in preparation.

[299] G. Alkhazov, “Statistics of electron avalanches and ultimate resolution of proportional counters,” *Nucl. Instrum. Meth.* **89** (1970) 155.

[300] A. László, G. Hamar, G. Kiss, and D. Varga, “Single electron multiplication distribution in GEM avalanches,” *J. Instrum.* **11** (2016) P10017.

[301] J. Va’vra and A. Sharma, “Single electron detection in quadruple-GEM detector with pad readout,” *Nucl. Instrum. Meth.* **A478** (2002) 235.

[302] A. Buzulutskov, A. Breskin, R. Chechik, G. Garty, F. Sauli, and L. Shekhtman, “The GEM photomultiplier operated with noble gas mixtures,” *Nucl. Instrum. Meth.* **A443** (2000) 164.

[303] A. Buzulutskov, A. Breskin, R. Chechik, G. Garty, F. Sauli, and L. Shekhtman, “Further studies of the GEM photomultiplier,” *Nucl. Instrum. Meth.* **A442** (2000) 68.

[304] H. Schindler, *Microscopic Simulation of Particle Detectors*. PhD thesis, Technische Universität Wien, 2012.

[305] H. Schindler and R. Veenhof, “Garfield++ — simulation of ionisation based tracking detectors,” 2018. `http://garfieldpp.web.cern.ch/garfieldpp`.

[306] M. Berger, *Development, Commissioning and Spatial Resolution Studies of a new GEM based TPC*. PhD thesis, Technische Universität München, 2015. `http://mediatum.ub.tum.de/?id=1279050`.

[307] S. Ramo, “Currents Induced by Electron Motion,” *Proc. IRE* **27** (1939) 584.

[308] W. Shockley, “Currents to Conductors Induced by a Moving Point Charge,” *J. Appl. Phys.* **9** (1938) 635.

[309] COMSOL, “COMSOL Multiphysics®,” 1984 - 2010. `www.comsol.com`.

[310] T. Gunji. Private communication.

[311] M. Bregant. Private communication.

[312] M. Kretz and V. Lindenstruth, “Vc: A C++ library for explicit vectorization,” *Software: Practice and Experience* **42** (2012) 1409.

[313] H. Schulte, “Pedestal, Noise und Common Mode Effect Analyse an einem Kammerprototypen des ALICE TPC Run 3 Upgrade,” Master’s thesis, Goethe Universität Frankfurt am Main, 2019. `https://www.uni-frankfurt.de/77473040/Masterarbeit_Hendrik_Schulte_2019.pdf`.

[314] **ALICE TPC** Collaboration, D. Antonczyk *et al.*, “Performance studies with an ALICE TPC prototype,” *Nucl. Instrum. Meth.* **A565** (2006) 551.

[315] P. Christiansen *et al.*, “The influence of detector effects on TPC performance,” *Nucl. Instrum. Meth.* **A609** (2009) 149.

[316] A. Deisting, C. Garabatos, and A. Szabo, "Ion mobility measurements in Ar-CO_2, Ne-CO_2, and Ne-CO_2-N_2 mixtures, and the effect of water contents," *Nucl. Instrum. Meth.* **A904** (2018) 1.

[317] S. Franchino *et al.*, "Effects of High Charge Densities in Multi-GEM Detectors," in *IEEE Nuclear Science Symposium and Medical Imaging Conference*, p. 7581778. 2016.

[318] F. Resnati, *Modeling, design and first operation of the novel double phase LAr LEM-TPC detector*. PhD thesis, ETH Zürich, 2012.

[319] S. Procureur, J. Ball, P. Konczykowski, B. Moreno, H. Moutarde, and F. Sabatie, "A Geant4-based study on the origin of the sparks in a Micromegas detector and estimate of the spark probability with hadron beams," *Nucl. Instrum. Meth.* **A621** (2010) 177.

[320] J. Margutti, "Stability studies on triple-GEM detectors for the GEM upgrade of the ALICE TPC," Master's thesis, Technische Universität München, 2014.

[321] P. Gasik, A. Mathis, L. Fabbietti, and J. Margutti, "Charge density as a driving factor of discharge formation in GEM-based detectors," *Nucl. Instrum. Meth.* **A870** (2017) 116.

[322] L. Lautner, "Influence of the charge density on discharges in THGEM-based detectors," Master's thesis, Technische Universität München, 2019. `https://www.das.ktas.ph.tum.de/DasDocs/Public/Master_Theses/Master_Thesis_LukasLautner.pdf`.

[323] C. Garabatos. Private communication.

[324] **GEANT4** Collaboration, "Physics Reference Manual - geant4 10.2," 2015. `http://geant4-userdoc.web.cern.ch/geant4-userdoc/UsersGuides/PhysicsReferenceManual/BackupVersions/V10.2/fo/PhysicsReferenceManual.pdf`.

[325] S. Bachmann *et al.*, "Charge amplification and transfer processes in the gas electron multiplier," *Nucl. Instrum. Meth.* **A438** (1999) 376.

[326] C. Garabatos, "The ALICE TPC," *Nucl. Instrum. Meth.* **A535** (2004) 197.

[327] S. Dildick, "Gas gain in a single GEM: parameter space." `https://indico.cern.ch/event/158402/contributions/226201/attachments/178335/250833/GainSingleGemParamSpace.pdf`. RD51 mini-week, 23.11.2011.

Acknowledgements

The support of many people has contributed to the successful completion of the many projects conducted within the scope of this work.

First and foremost, I would like to express my gratitude to Prof. Laura Fabbietti for the incredible opportunity to carry out such a diverse and interesting thesis. Ever since I joined the group back in 2013, she has continuously supported me in numerous ways in developing my skills and knowledge. I thank her for her confidence and the freedom she gave me in running these different projects, and finally for enabling the many, great, and interesting trips to CERN, conferences, workshops, and summer schools. I am very proud of what we have accomplished within the last years!

I am deeply indebted to Piotr Gasik who has been a mentor and friend for many years. I'd like to thank him for all his fantastic advise, never ending enthusiasm and encouragement, and fruitful discussions over one beer or another in R1 at CERN, or elsewhere.

The femto adventure would not have been the same without the *femto gang*. Thanks a lot to Berhard Hohlweger, Dimitar Mihaylov, Valentina Mantovani Sarti, and Oton Vazquez Doce for the interesting and enlightening discussions we had over the years, the great support, intelligent advice, and all the fun. Especially a big thank you to my good friend and office comrade Bernie for all the chats, the coffee breaks, and all the *hummus* we encountered during our travels! A huge thanks to Vale, for answering all my questions about theory with endless patience and the great discussions working on the p–Σ^0 paper and in general, and to Dimitar for all the nice chats about physics and non-physics and sharing all his CATS-pertise! Of course I need to mention Oliver Arnold, whose pioneering work paved the way to the mass production of great results. And finally, all the best to the new generation of femtoscopists – Emma Chizzali, Stefan Heckel, Max Korwieser, and Bhawani Singh! In addition, Alexander Borissov and Friederike Bock have provided valuable input about the photon reconstruction for the Σ^0 identification. In general, I would like to express my acknowledgement to the ALICE Collaboration for all the input provided over the years, in particular from copious members of the Femto PAG. Many thanks to Johann Haidenbauer and Tom Rijken for enlightening discussions about theoretical aspects and providing their model calculations.

I am incredibly thankful to Jens Wiechula for all his constant support and brilliant input, which made the implementation and validation of the TPC digitization a truly delightful task! The analysis of the 2017 test beam data has been invaluable for the validation of the digitization – thanks a lot to Thomas Klemenz for doing such a great job, for all his input to the simulation and being such a great office companion. The optimization of the code could not have been conducted without the help and experience of Sandro Wenzel and Ruben Shahoyan. Invaluable input for the development and validation has been provided by Marco Bregant, Taku Gunji, and Christian Lippmann. The participation to test beams at CERN has always been a pleasure, in particular thanks to the excellent organization by Chilo Garabatos and Alexander Deisting.

Many thanks also to all members of the E62 group for the fantastic atmosphere and all the rest. Here I particularly need to mention my PhD colleagues Steffen Maurus and Joana Wirth and former group members Martin Berger and Robert Münzer for the support, the coffee breaks, and the trips taken together. I would like to thank all the students I had the privilege to supervise over the years – Emma Chizzali, Florian Dufter, Thomas Klemenz, Max Korwieser, and Jenny Padberg – for all their dedication, brilliant work, and curiosity. Thanks a lot to Petra Zweckinger and Sigrid Weichs for all their help with bureaucracy and to Ralf Lang for all his technial support. The invaluable comments from Bernie, Laura, Jens, Piotr, Stefan, Steffi, Thomas, and Vale have given the final touch to this work, thanks a lot for proofreading!

Special recognition goes out to my parents, for all their constant support, advice, and belief.

And above all, I would like to thank my wonderful wife Steffi for her incredible support in uncountable ways, her patience, and her love. We have shared this adventure, and I'm very much looking forward to what is yet to come.